**学位論文**

# A Study of Dusty Star-Forming Galaxies in the z=2-3 Protoclusters with Herschel and ALMA

# （ハーシェル宇宙望遠鏡とアルマ望遠鏡で探る 赤方偏移 2-3 原始銀河団における爆発的星形成銀河の研究）

平成 29 年 12 月博士 (理学) 申請

東京大学大学院理学系研究科
天文学専攻

加藤 裕太

# Abstract

Protocluster is a few tens of proper Mpc galaxy overdensity seen in the $z > 2$ Universe, which is a progenitor of local galaxy cluster. Although the formation of elliptical galaxies in local clusters is thought to be occurred at $z > 2$, the lack of far-infrared observation prevents us to search for their precursors, massive dusty star-forming galaxies (DSFGs). In protoclusters, simultaneous dusty star-formations through DSFGs are expected due to a frequent galaxy-galaxy merger induced by a rapid collapse of dark matter halos and/or a high potential of gas supply from the large scale structure.

We conducted *Herschel*/SPIRE survey to search for DSFGs in three protoclusters, 2QZCluster ($z = 2.2$), HS1700 ($z = 2.3$) and SSA22 ($z = 3.1$). We targeted these protoclusters with a few tens of proper Mpc filamentary, large scale structures with evidence for an enhancement of Active Galactic Nucleus (AGNs) fraction. In addition, all of the three protoclusters have blobs, which thought to be formation sites of massive galaxies. Based on the SPIRE colors of $S_{350}/S_{250}$ and $S_{500}/S_{350}$, we selected DSFGs potentially associated with the protoclusters.

By using a 6 comoving Mpc radius aperture, we found a $4\sigma$ overdensity of six SPIRE sources $4.5'$ ($\sim 2.0$ proper Mpc) west to a density peak of H$\alpha$ emitters (HAEs) at $z = 2.2$ in the 2QZCluster field. We found a $5\sigma$ overdensity of eight SPIRE sources around $2.1'$ ($\sim 1.0$ proper Mpc) north to a density peak of Lyman Break Galaxies (LBGs) at $z = 2.3$ in the HS1700 field. We found three 500 $\mu$m sources are concentrated $3'$ ($\sim$1.5 proper Mpc) east to a density peak of Ly$\alpha$ emitters (LAEs) at $z = 3.1$ in the SSA22 field. The inferred star-formation rate (SFR) densities of these three overdensities are possibly 100-1000 times higher than the average value at the same redshifts if all of the SPIRE sources are associated with protoclusters. This suggests that simultaneous bursting star-formation could be occurred in the $z \sim 2 - 3$ protoclusters. Simultaneously galaxy-galaxy mergers or much longer molecular gas depletion times in protoclusters are possible explanations to concentrations of DSFGs. Thus, the key observational challenge is to investigate the morphology (e.g., galaxy-galaxy mergers), measure molecular gas mass and molecular gas depletion time for DSFGs in protoclusters.

We conducted ALMA Band 7 and Band 3 observations for one of spectroscopically confirmed *Herschel*/SPIRE source SSA22-SPIRE394, which corresponds to SSA22-LAB18 (LAB18) at $z = 3.1$ SSA22 protocluster. LAB18 has the highest far infrared (FIR), Millimeter/Sub-millimeter flux densities and has a 100 kpc filamentary structure of Ly$\alpha$ emission in the $z = 3.1$ SSA22 protocluster. Subaru and *Hubble Space Telescope (HST)* revealed that diffuse ultraviolet (UV) continuum emission is also elongated within the LAB18, which is similar to satellite galaxies with inflowing gas accreting onto DSFGs predicted in the recent simulation for LABs.

In ALMA Cycle 2 Band 7 observations, we found that LAB18 consists of four 860 $\mu$m dust continuum sources above $5\sigma$ level, LAB18.a, LAB18.b, LAB18.c, and LAB18.d. We found that these four DSFGs are aligned with the 100 kpc filamentary structure of the Ly$\alpha$ emission in the LAB18.

In ALMA Cycle 4 Band 3 observations, we detected CO J=4-3 line from one of the DSFGs, LAB18.b. The CO based spectroscopic redshift is $z = 3.0936 \pm 0.0002$, which is blueshifted compared with the Ly$\alpha$ spectroscopy of $z = 3.014$. We found that LAB18.b has a FWHM of 5.6 kpc extended CO gaseous rotationally disk and a FWHM of 2.0 kpc central 860 $\mu$m dusty star-forming region. The velocity integrated CO J=4-

3 luminosity ($L'_{\rm CO(4-3)}$) is converted to molecular gas mass ($M_{\rm gas}$). We derived molecular gas mass of $M_{\rm gas} = (4.4 \pm 0.3) \times 10^9 M_\odot$ for LAB18.b. For CO non-detected ALMA sources, we derived $3\sigma$ upper limit of $M_{\rm gas} = 1.0 \times 10^9 M_\odot$ with same manner as LAB18.b. The $L'_{\rm CO(4-3)}$ of the four DSFGs in the LAB18 are relatively low compared with far infrared luminosity ($L_{\rm FIR}$), and they are outside from $1\sigma$ scatter of previous studies. For LAB18.b, the derived gas depletion time ($\tau_{\rm dep}$) is $22^{+14}_{-6}$ Myr with assuming CO to molecular gas mass conversion factor of $\alpha$=0.8. This is significantly lower than the average value of 558 Myr for normal star-forming galaxies at the same redshift and the average value of 100-200 Myr for typical DSFGs at the same redshift. Nonetheless LAB18.b is in the $z = 3.1$ Universe, $\tau_{\rm dep}$ of LAB18.b is also lower than the value of local ULIRGs ($\sim$50 Myr), and is between early stage mergers ($16^{+6}_{-4}$ Myr) and merging galaxies ($60^{+30}_{-20}$ Myr). Thus, LAB18.b could be an initial stage of merging galaxy, although there are no significant such signs from their morphology and kinematics.

In ALMA Cycle 4 Band 3 observations, we detected 2.85 mm dust continuum emission from four DSFGs in the LAB18. We estimated dust mass ($M_{\rm dust}$) of four DSFGs in the LAB18, and found that they have $M_{\rm dust} = (1.8 - 8.1) \times 10^7$ M$_\odot$. This corresponds to the usual range of $\delta_{\rm GDR}$, $\delta_{\rm GDR} = 12 - 90$. By combining *Herschel*/SPIRE 250 $\mu$m and ALMA Band 7 860 $\mu$m flux densities, we conducted far-infrared SED fitting by assuming optically thin modified black body radiation with free parameters of single dust temperature ($T_{\rm dust}$) and dust emissivity index ($\beta$). We found that four DSFGs in the LAB18 have ULIRGs class far-infrared luminosities of $L_{\rm FIR} = (1.7 - 4.2) \times 10^{12}$ L$_\odot$.

We also found that LAB18.b shows larger $\beta$ and smaller $T_{\rm dust}$ compared with the other ULIRGs class objects. The larger $\beta$ can be reproduced by recent astronomical experiment. The location of larger $\beta$ and smaller $T_{\rm dust}$ of LAB18.b in $\beta$ vs. $T_{\rm dust}$ plane is similar to the metal rich, gas poor early type galaxies and LIRGs. This situation is similar to the CO J=4-3 observation for LAB18.b, which indicates small gas fraction 8%. By combining our CO and dust observations, we may see the evolution from DSFGs to the early type galaxies. ALMA long wavelength multi-band continuum observation will reveal differences of $\beta$ among the galaxy populations and optical properties of interstellar dust grains.

By combining these results, we discuss possible origins of LAB18. Because of a one X-ray detection and a large total SFR of four DSFGs in LAB18, a photoionization is possible origin of LAB18. For the galactic superwind model, the 860 $\mu$m derived surface SFR densities of $\Sigma$SFRs suggest the four DSFGs in the LAB18 can drive galactic superwinds. Large velocity offset between CO J=4-3 and Ly$\alpha$ spectroscopy and one X-ray detection suggest possible existence of strong galactic superwinds. The blue component of CO J=4-3 of LAB18.b, which is extended toward south-east, possibly suggests turbulent motion and/or inflows/outflows. For the inflowing gas model, LAB18.b needs gas supply to evolve more massive ($\sim 10^{11}$ M$_\odot$) galaxies. Even if all of the gas mass of LAB18.b is converted to its stellar mass ($M_*$), the achieved stellar mass is only $M_* = 5.2 \times 10^{10}$. Diffuse UV continuum emission around LAB18.b might reflect a satellite galaxies with inflowing gas accreting onto DSFGs.

In protoclusters, simultaneously galaxy-galaxy mergers or much longer molecular gas depletion times are possible explanations to concentration of DSFGs. However, we found the LAB18.b has very low gas mass and gas depletion time. Further statistical samples are needed to investigate about these explanations.

# Declaration

The work in this thesis is baed on research carried out at the Department of Astronomy, the University of Tokyo, Japan. No part of this thesis has been submitted elsewhere for any other degree or qualification.

Yuta Kato
December 2018

# Acknowledgments

I am deeply grateful to Seiichi Sakamoto, my supervisor. He kindly accepted me to study galaxy evolution and formation in Chile Observatory at National Astronomical Observatory of Japan, and I received generous support from him in my life as a second degree of a Ph.D student. I would like to express the deepest appreciation to Yuichi Matsuda for sharing a large amount of time to discuss various matter related to this thesis. Originally he first accepted and guided me to the fantastic world of galaxy evolution and formation. He is a pioneer and professional in studying galaxies in protoclusters with various wavelengths. I learned severe attitude of science of galaxies and protoclusters. Not only the science, but also I really respect his man of character and appreciate that he saved me even if I was in "dark-side" of life. He kindly gave me a chance to study the science of astronomy again. He is also a good badminton and tennis player. I enjoyed playing them with him. I would like to thank the members of the Iono laboratory and colleagues in Chile Observatory who gave me a lot of stimulation and motivation: Kazuhiro Kiyokane, Chihomi Hara, Kosuke Fujii, Ayumu Matsuzawa, Satoshi Ohashi, Toshiki Saito, Kyoko Onishi, Minju Lee, Tomonari Michiyama, Misaki Ando, Jinshi Sai, Masayuki Yamaguchi.

I would like to thank ALMA staffs for their great effort. I would particularly like to express my gratitude to Norikazu Mizuno, the professor of Chile Observatory. He introduced me to the Chile Observatory as I was a undergraduate student, and he was my supervisor until I become second degree of a Ph.D student. I never forget that he gave me the chance to study of galaxy evolution and formation. I owe a very important debt to Ian Smail, James Geach, Bret Lehmer, David Alexander, Yoichi Tamura, Kotaro Kohno, Dawn Erb, and Charles Steidel who are the original members of getting *Herschel* data, providing me a great opportunity to study dusty star-forming galaxies using the map taken with SPIRE camera. I would like to offer my special thanks to the researchers of the SSA22 field and protoclusters: Toru Yamada, Koichiro Nakanishi, Hideki Umehata, Mariko Kubo, Mark Swinbank, Yiping Ao, Scott Chapman and Ichi Tanaka for sharing their data and/or giving me a comment. Ian Smail gave me insightful comments and suggestions from the various point of view as an expert of Sub-millimeter/Millimeter astronomy.

I want to thank my classmates at NAOJ and NAOJ Mitaka Stargazing colleague. I especially spent a lot of time with the members: Akio Taniguchi, Yutaka Hirai, Mitsuda Kazuma, Yuki Kashiwada, Megumi Kasuga, Fuko Baba, Masafusa Onoue, Haruka Baba, Tsuguru Ryu, and Koki Okutomi.

I owe my deepest gratitude to the members of my soft tennis team in Mitaka city: Ken Seino, Megumi Seino, Fuko Seino, Reina Toyosawa, Masashi Yoshinaga, Hiroya Kinjo, Ryosuke Ito, Hideki Maruyama, Hiroyuki Omiya, Kazuki Sakamoto, Fumihiro Kuroki, Hayato Tsukagoshi, Kota Hamada, Kenta Mori, Ryo Nishihara, Takuya Koda, Naoki Yuasa, Shotaro Oshima, Koji Matsuda, Miki Yoshida, Kensuke Iizuka, Takanobu Kawagishi and all of soft tennis players I met in Mitaka city.

I really appreciate the referees of this thesis: Masami Ouchi, Hideyuki Kobayashi, Masao Tanaka, Tadayuki Kodama and Tsutomu Takeuchi. Advice and comments given by them have been a grate help in improving this work.

Finally my deepest appreciation goes to my family, who have supported me all the times.

# Contents

# List of Figures

# List of Tables

# Chapter 1

# Introduction

## 1.1 Structure Evolution of the Universe

The distribution of dark matter halo is not uniform, but is concentrated at some place, makes large scale structure of the Universe. Galaxies in the dark matter halos are thus also not uniformly distributed, and significantly concentrated at some place. The mega parsec (Mpc) scale hundreds to thousands of galaxies and galaxies groups are called clusters. Clusters are located on the network of the large scale structure of the dark matter halos, and which are connecting smaller dark matter halos of individual galaxies and groups. Figure 1.1 shows 43 Mpc scale structure evolution of the cold dark matter model from $z = 30$ to $z = 0$. At $z = 30$, distribution of dark matter appears to be uniform. At $z = 10 - 5$, the fluctuation grows can be seen, and structure becomes to have clumps. Down to the $z = 5$, we can clearly see the filaments of large scale structures. This signature is remaining to $z = 0$. Thus, Figure 1.1 illustrates the complexities of the structure evolution, which is accretion of matter along filaments.

Astronomical observations also have revealed that the existence of a large scale structures over the cosmic time, and the questions of "when and how present-day galaxy clusters formed at the high redshift Universe" have driven extensive surveys in the past two decades. Such ancestor of clusters, are called as "protoclusters". Protocluster is an overdense region seen in the $z > 2$ Universe, which is a progenitor of local galaxy clusters (e.g., Steidel et al., 1998; Ouchi et al., 2005; Kodama et al., 2007; Daddi et al., 2009; Matsuda et al., 2011a; Walter et al., 2012; Toshikawa et al., 2017). At the Chiang, Overzier, & Gebhardt (2013), there are more than twenty $z > 2$ protoclusters are listed in. At the moment, protocluster search is more expanding. For instance, Toshikawa et al. (2017) reports 216 protocluster candidates at $z \sim 4$ by using Subaru/Hyper Suprime-Cam. In the coming years, their protocluster search will be extended to the 1400 deg$^2$ to probe cluster formation up to $z \sim 6$. Figure 1.2 is the schematic view of a cluster and protocluster from Figure 5 in Chiang & Senaha (2017). Figure 1.3 is observation and simulation examples of a protocluster at $z \sim 2$ from Figure 5 in Kodama et al. (2007) and Borgani & Kravtsov (2011). Figure 1.4 shows $z \sim 6$ large scale structure from Figure 4 in Ouchi et al. (2005).

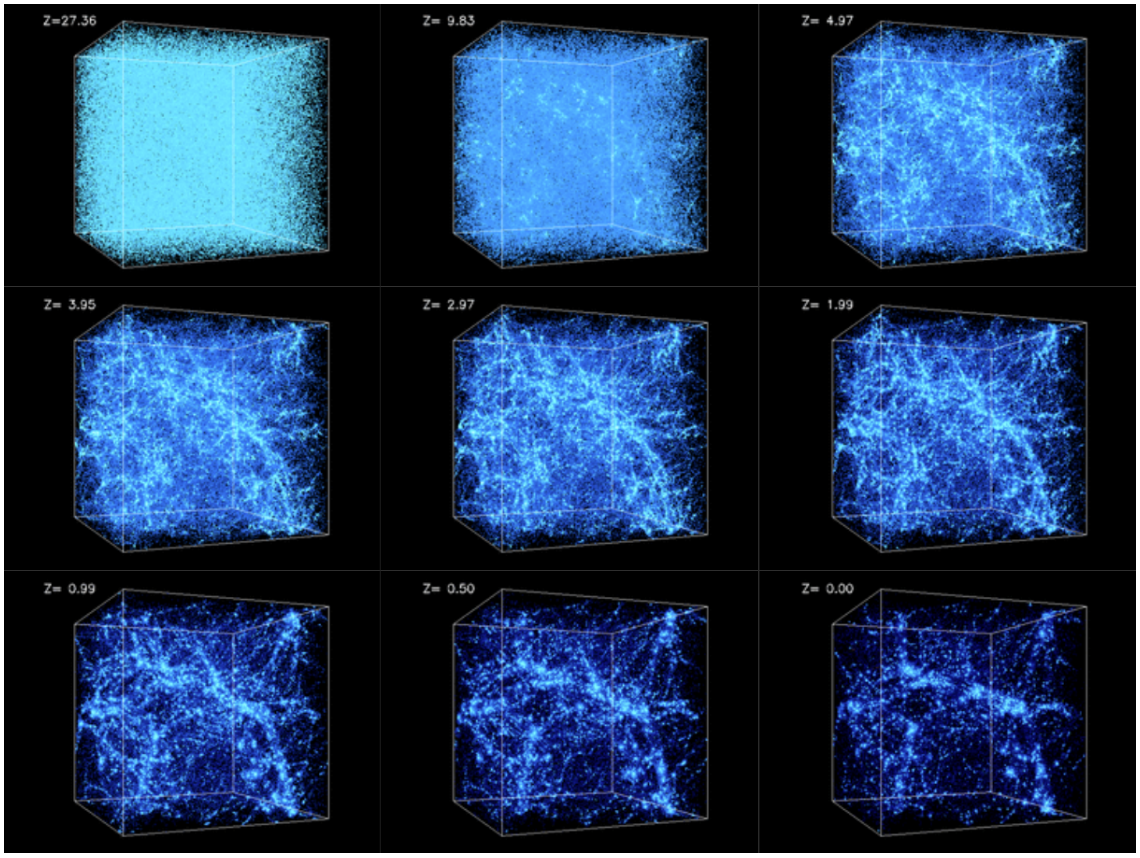


Figure 1.1: Structure evolution of a cold dark matter in the Universe from $z = 30$ to $z = 0$. The one side of box scale is 43 Mpc. Simulations were performed at the National Center for Supercomputer Applications by Andrey Kravtsov (The University of Chicago) and Anatoly Klypin (New Mexico State University). Visualizations by Andrey Kravtsov.

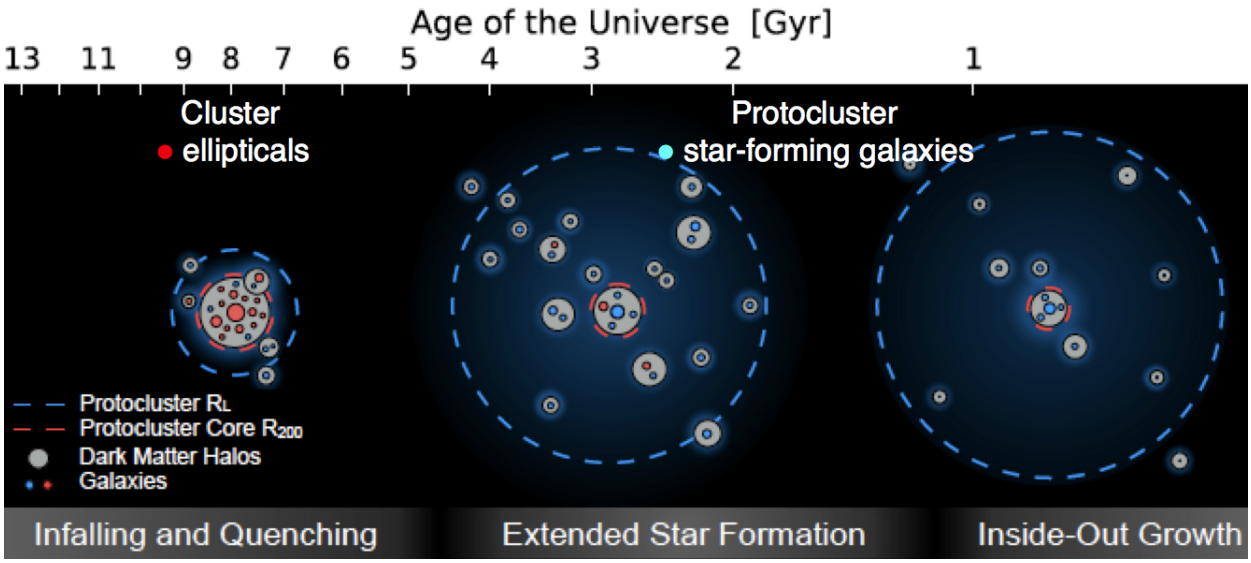


Figure 1.2: A schematic view of a local galaxy cluster and a high redshift protocluster from Figure 5 in Chiang & Senaha (2017). Local galaxy clusters are characteristic to their highly concentration of ellipticals, compared to distribution of many star-forming galaxies in extended region in high-$z$ protoclusters (Chiang & Senaha, 2017).

## 1.2 Galaxy Formation in Protoclusters

The galaxy formation and star-formation of field galaxies are thought to occur at $z < 2$ (Lilly et al., 1995), comparing to the star-formation of elliptical galaxies in local clusters are thought to occur at $z \geq 2$ (Ellis et al., 1997). This suggests accelerated galaxy formation is occurred in galaxy overdense region such protoclusters (e.g., Thomas et al., 2005; McDermid et al., 2015). Thus, the local clusters could be formed at $z > 2$ galaxy overdensities (i.e., protoclusters). Figure 1.5 shows the epochs of elliptical galaxy formation as a function of environment. The left and right panels show formation epoch of various stellar mass galaxies with distinction to a low galaxy number density region and a high galaxy number density region. We can see the formation epoch is less than $z = 2$ in low galaxy number density region, compared to the formation epoch is around $z = 5$ in a high galaxy number density region. This is the evidence for accelerated galaxy formation of protoclusters.

Why do $z > 2$ protoclusters experience accelerated galaxy formation? One of a possible explanation is more frequently and rapidly galaxy-galaxy mergers due to the more frequently and rapidly dark matter halo collisions at a high galaxy number density region in the early Universe (Governato et al., 1998). Another explanation is an inflowing gas along the large scale structure. A galaxy in a high galaxy number density region in the high-$z$ Universe is expected to be embedded into the intersection of the large scale structure. Such intersections have high potential to be supplied more amount of gas into galaxies from Inter Galactic Mediums (IGMs) (Dekel et al., 2009). Figure 1.6 shows a schematic view of these two possible explanations.

In this way, the both case could accelerate the galaxy formation, and probably induce dusty, bursting star-formation. Dusty star-forming galaxies (DSFGs) are massive strongly star-forming galaxies (star formation

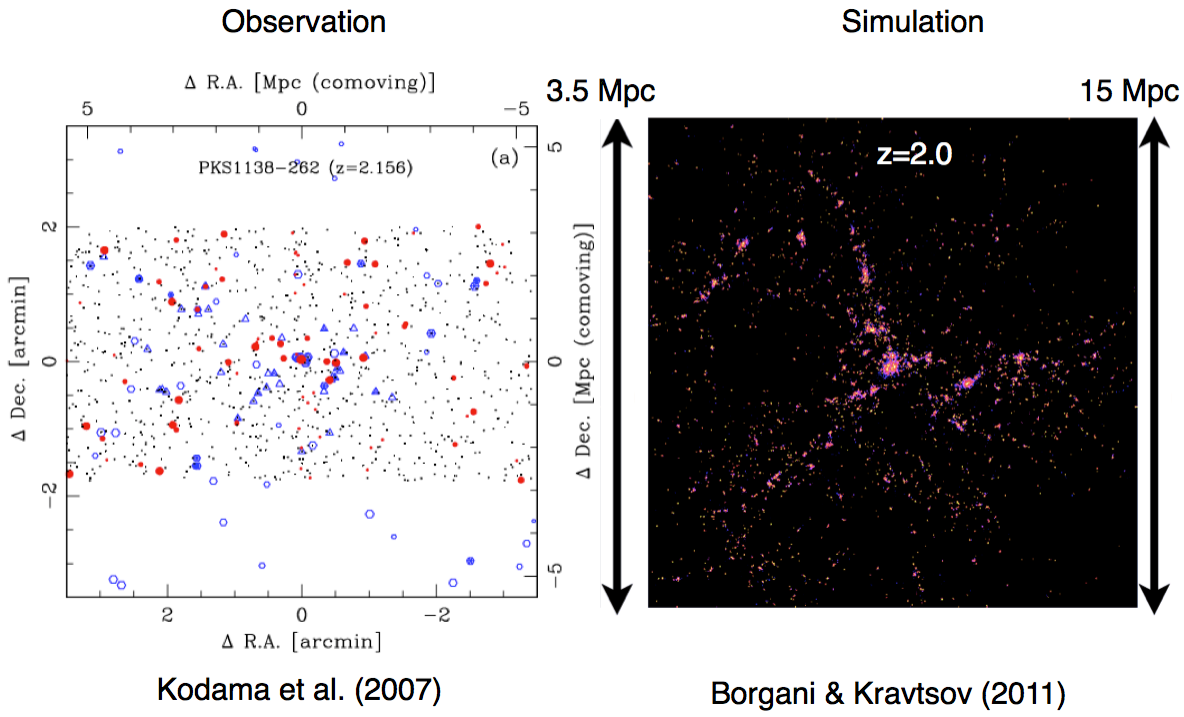


Figure 1.3: Observation and Simulation examples of a protocluster from Kodama et al. (2007) and Borgani & Kravtsov (2011). The left figure shows one of a protocluster at $z = 2.2$ (Kodama et al., 2007). The protocluster member galaxies are shown by red circles, blue circles, blue triangles and blue hexagons corresponding to distant red galaxies (DRGs), Ly$\alpha$ emitters (LAEs), H$\alpha$ emitters (HAEs), and Lyman break galaxies (LBGs) respectively. All other objects detected in the $K_s$ band are also shown by small dots. We can see the galaxies are distributed over Mpc scale and configure filamentary structure. The right figure shows a hydrodynamical simulation of a protocluster (Borgani & Kravtsov, 2011). We can see a filamentary large scale structure is spread over Mpc scale.

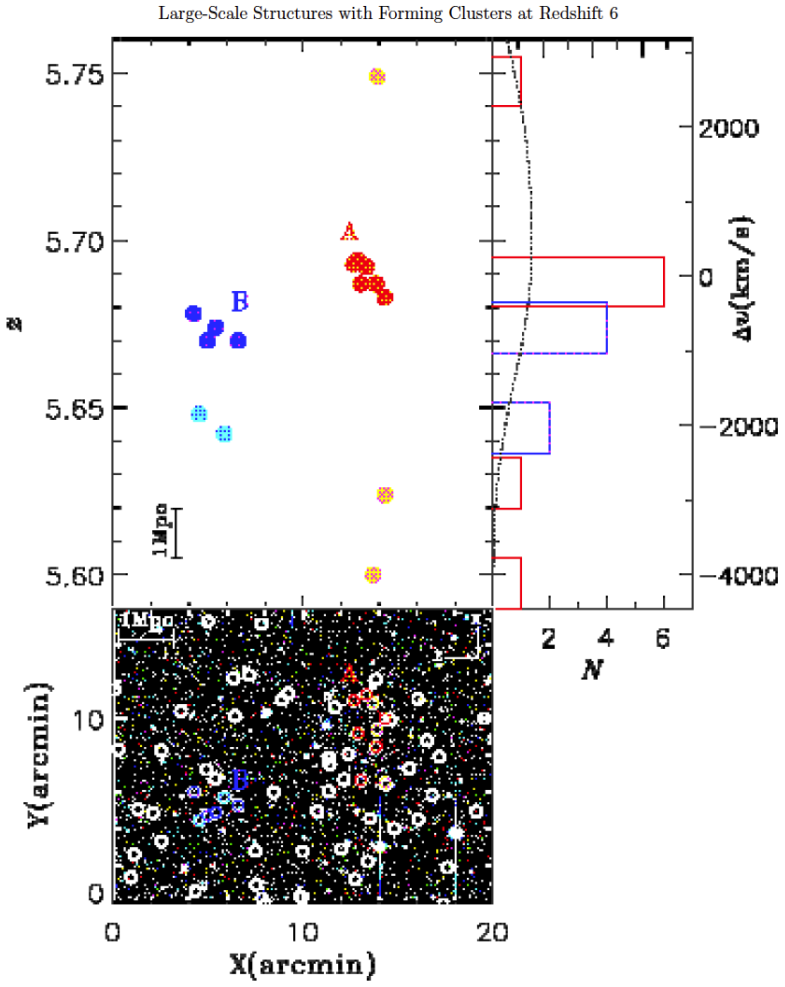


Figure 1.4: Forming clusters at $z = 6$ in the large scale structure (Ouchi et al., 2005, Figure 5). In the upper left panel, we show the LAEs distribution in redshift directions vs. East to West direction. In the bottom panel, we show the LAEs distribution in North to South direction vs. East to West direction. LAEs which are associated with the forming clusters A and B are shown as the red and blue circles. LAEs which are not associated with clusters are shown as the orange and cyan circles. LAEs without spectroscopic redshift are represented by the open white circles on the bottom panel. The redshift distribution of LAEs in the upper left panel are shown in the upper right panel. The red and blue histograms correspond to LAEs which are associated with forming clusters A and B, respectively.

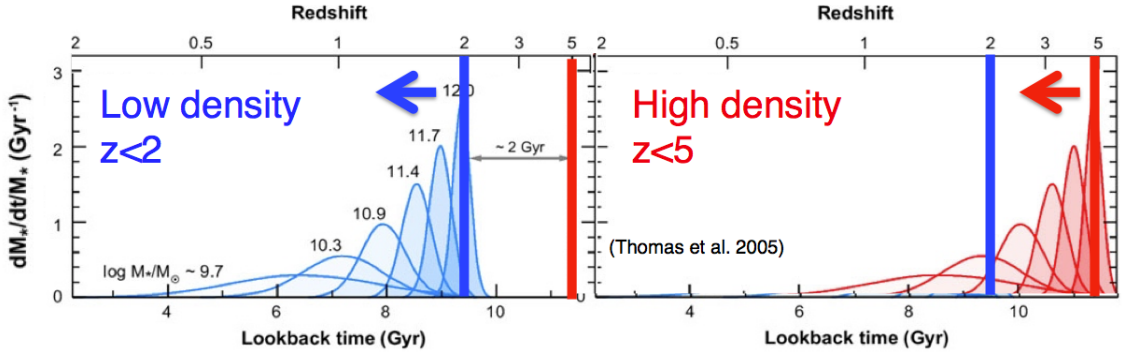


Figure 1.5: The epochs of elliptical galaxy formation as a function of environment from Thomas et al. (2005) are shown. The left and right panels show a formation epoch of various stellar mass galaxies with distinction to a low galaxy number density region and a high galaxy number density region. We can see the formation epoch is less than $z = 2$ in a low galaxy number density region, compared to the formation epoch is less than $z = 5$ in a high galaxy number density region. This is the evidence for accelerated galaxy formation of protoclusters (Thomas et al., 2005).

rate, SFR $\gtrsim 100 - 1000$ $M_\odot$ $yr^{-1}$) and have been proposed to ancestors of present-day ellipticals in local clusters (e.g., Lilly et al., 1998; Smail et al., 1998; Lutz et al., 2001; Ivison et al., 2013). Large hydrodynamical simulations predict intense bursting star-formation could be detectable as concentrations of DSFGs in protoclusters (e.g., Granato et al., 2015). Thus, studying the bursting star-formation in protoclusters through DSFGs is to study why protoclusters are experienced accelerated galaxy formation. Figure 1.7 shows the schematic view of searching for DSFGs in protoclusters.

The spectral energy distribution (SED) of DSFGs characterizes their strong emission at the longer part of infrared wavelength. In 1990s, the far-infrared (FIR) absolute energy spectrum of galaxies is first measured by COsmic Background Explorer (*COBE*). The *COBE* observation and optical wavelength observation revealed that the massive OB stars are formed in a dust rich region in galaxies. The ultraviolet (UV) radiation of OB stars in dusty regions heats dust grains, then the thermal emission leaves from the dust grains at FIR and sub-millimeter (sub-mm) wavelengths (from roughly 10-1000 $\mu$m). Figure 1.8 left shows a SED of bursting star-formation galaxy M82 and a cosmic background spectrum revealed by various telescope from UV to millimeter (Lagache, Puget, & Dole, 2005). Figure 1.8 right shows a schematic view of UV and FIR radiation in a dust rich region.

In the later 1990s, the observations with Sub-millimeter Common User Bolometer Array (SCUBA) equipped on James Clerk Maxwell Telescope (JCMT) first succeeded to detect far-infrared and sub-mm luminous galaxies in high-$z$ Universe (e.g., Smail et al. (1998)). The DSFGs have their far-infrared luminosity of $L_{\rm FIR} \gtrsim 10^{12} - 10^{13}$ $L_\odot$. Today, such far-infrared and/or sub-mm wavelength radiation from DSFGs thought to be contributed about $\sim 50\%$ of the energy densities from whole galaxies in the Universe. Figure 1.9 shows a comparison of a contribution for cosmic SFR density between ultraviolet (UV) and infrared (IR) (Takeuchi, Buat, & Burgarella, 2005; Madau & Dickinson, 2014). Moreover, the fraction of bursting star-formation is a strong function of stellar mass as shown in Figure 1.10 (Whitaker et al., 2017, Figure 2).

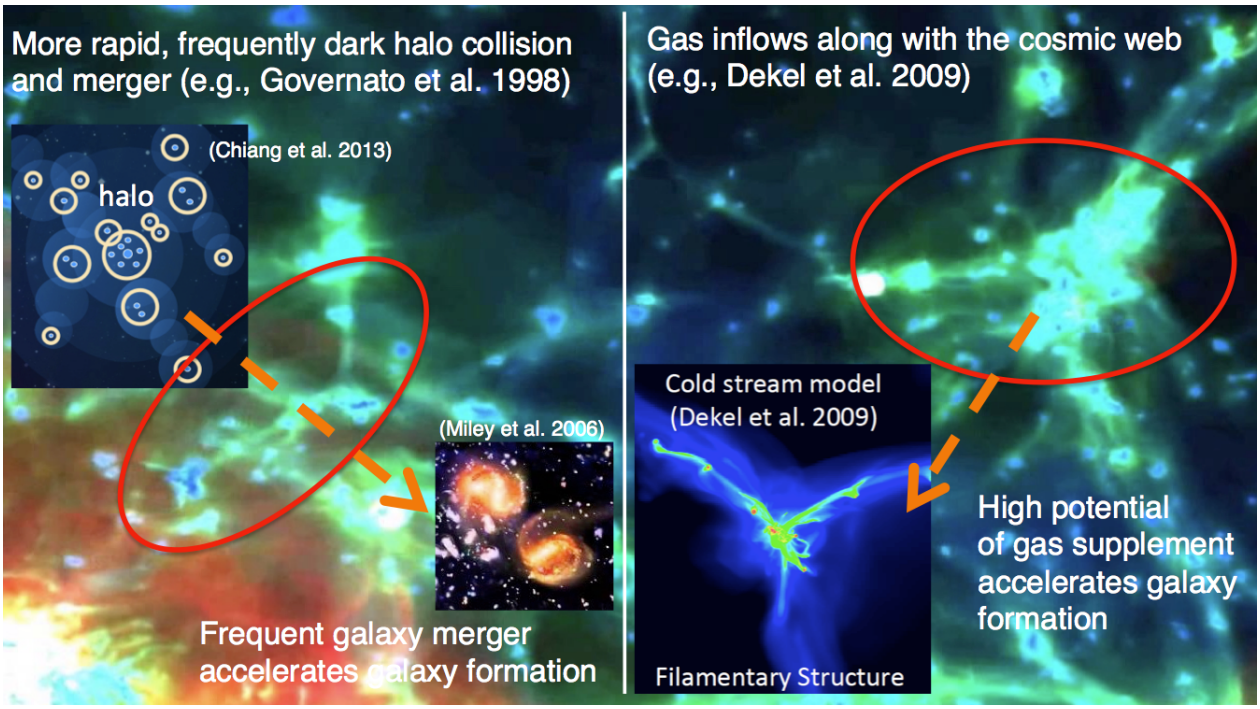


Figure 1.6: The possible explanations of an accelerated galaxy formation in protoclusters. The left panel shows more frequently dark matter halo collision which induce frequently and rapidly galaxy-galaxy mergers (e.g., Governato et al., 1998; Miley et al., 2006; Chiang, Overzier, & Gebhardt, 2013). The right panel shows inflowing gas along the large scale structure (e.g., Dekel et al., 2009). The galaxy in a high galaxy number density region in the high-$z$ Universe is expected to be embedded into the intersection of the large scale structure, which has high potential to be supplied more amount of gas into galaxy from IGMs. The background image is a cosmological simulation from illustris simulation from Vogelsberger et al. (2014). The both case of galaxy-galaxy mergers and inflowing gas could accelerate galaxy formations and induce bursting star-formations.

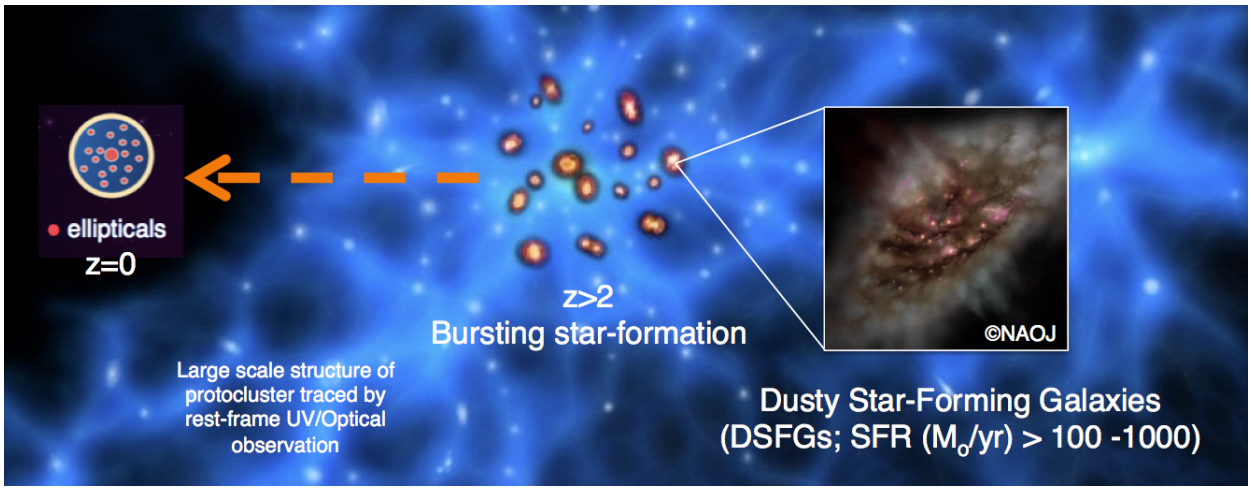


Figure 1.7: Schematic view of searching for DSFGs in protoclusters (©NAOJ). Through DSFGs, we study the bursting star-formation in protoclusters and investigate why protoclusters experience accelerated galaxy formation (Umehata et al., 2015).

Almost all of star-formations in massive galaxies ($M_* \gtrsim 10^{11}\ M_\odot$) come from IR wavelength (Whitaker et al., 2017). Thus, in terms of investigating the bursting star-formation and massive galaxy formation in protoclusters, we need to conduct far-infrared and sub-mm wavelength surveys in addition to the previous rest-frame UV/optical observations.

## 1.3 Scope of This Thesis

In this thesis, we report the results of DSFGs survey for three protoclusters, 2QZCluster, HS1700, and SSA22 at $z = 2.2$, 2.3, and 3.1 respectively. We used Spectral and Photometric Imaging Receiver (SPIRE; Griffin et al., 2010) on *Herschel Space Observatory* (*HSO*; Pilbratt et al., 2010). The three protoclusters have been found by rest-frame UV/optical selected galaxies, and consist filamentary large scale structures of these galaxies with more than 10 Mpc scales. These protoclusters are selected with evidence for enhancement of Active Galactic Nucleus (AGNs) fraction. In addition, these protoclusters have Ly$\alpha$ Blobs (LABs) and H$\alpha$ Blobs (HABs), which are huge nebulas tracing atomic hydrogen gas and thought to be sites of massive galaxy formation. We search for concentration of DSFGs in the three protoclusters and investigate whether the protoclusters are experiencing simultaneous dusty star-formation through DSFGs.

Then, we report results of our ALMA follow up observations for one of spectroscopically confirmed *Herschel*/SPIRE source SSA22-SPIRE394, corresponding to SSA22-LAB18 (hereafter, LAB18) in the $z = 3.1$ SSA22 protocluster. By using ALMA, we investigate why simultaneously, intensive bursting star-formation is occurred in LAB18 at $z = 3.1$ SSA22 protocluster.

The structure of this paper is following. In §2 we introduce the *Herschel*/SPIRE observations, the data processing, and our protocluster target. In §3 we present source detection methods, SPIRE sources number counts, and SPIRE color selection. In §4 we present our *Herschel*/SPIRE results. Then, we present ALMA

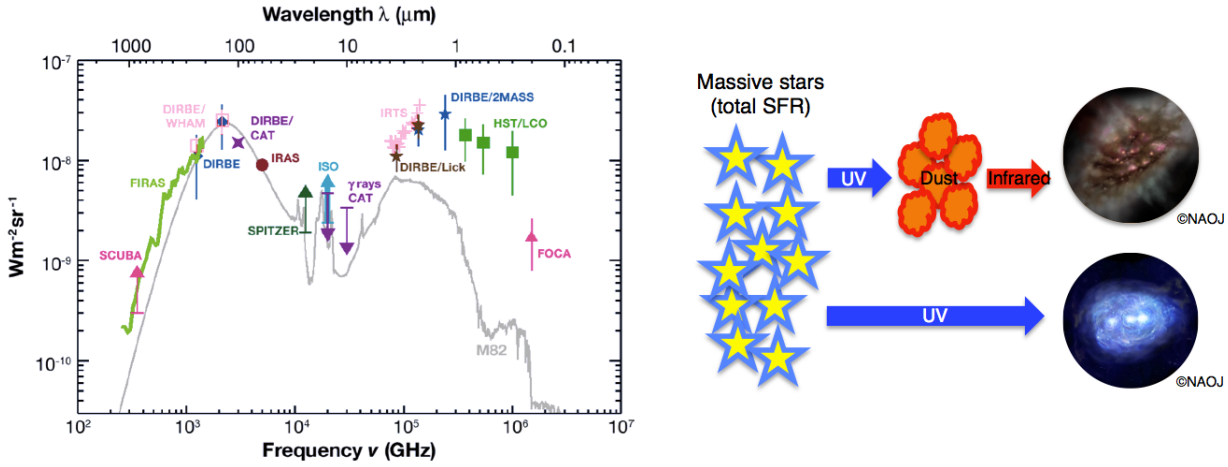


Figure 1.8: The SED of M82 and cosmic background spectrum, and a schematic view of a radiation in dust rich region are shown. The left figure shows a SED of dusty bursting star-formation galaxy M82 and the cosmic background spectrum revealed by various telescope from UV to millimeter wavelengths (Lagache, Puget, & Dole, 2005). The right figure shows a schematic view of a radiation in a dust rich region.

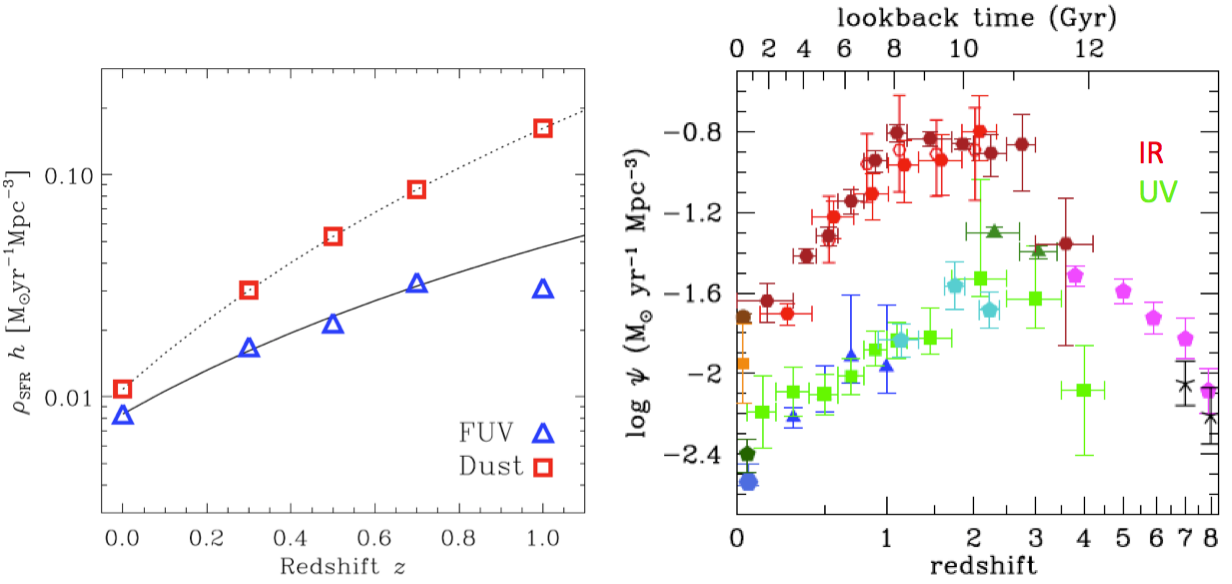


Figure 1.9: A comparison of UV and IR contribution to the cosmic SFR density (Takeuchi, Buat, & Burgarella, 2005; Madau & Dickinson, 2014). In the left figure from Takeuchi, Buat, & Burgarella (2005), the contribution of UV and IR is estimated from *GALEX* FUV luminosity function data and *IRAS* 60 $\mu$m luminosity function for local galaxies and *Spitzer* 15 $\mu$m for higher-$z$ galaxies. More than 70% of the star formation activity is obscured by dust at $0.5 \lesssim z \lesssim 1.2$. In the right figure from Madau & Dickinson (2014), determinations of the cosmic SFR density from UV data and IR data are listed in Table 1 in Madau & Dickinson (2014).

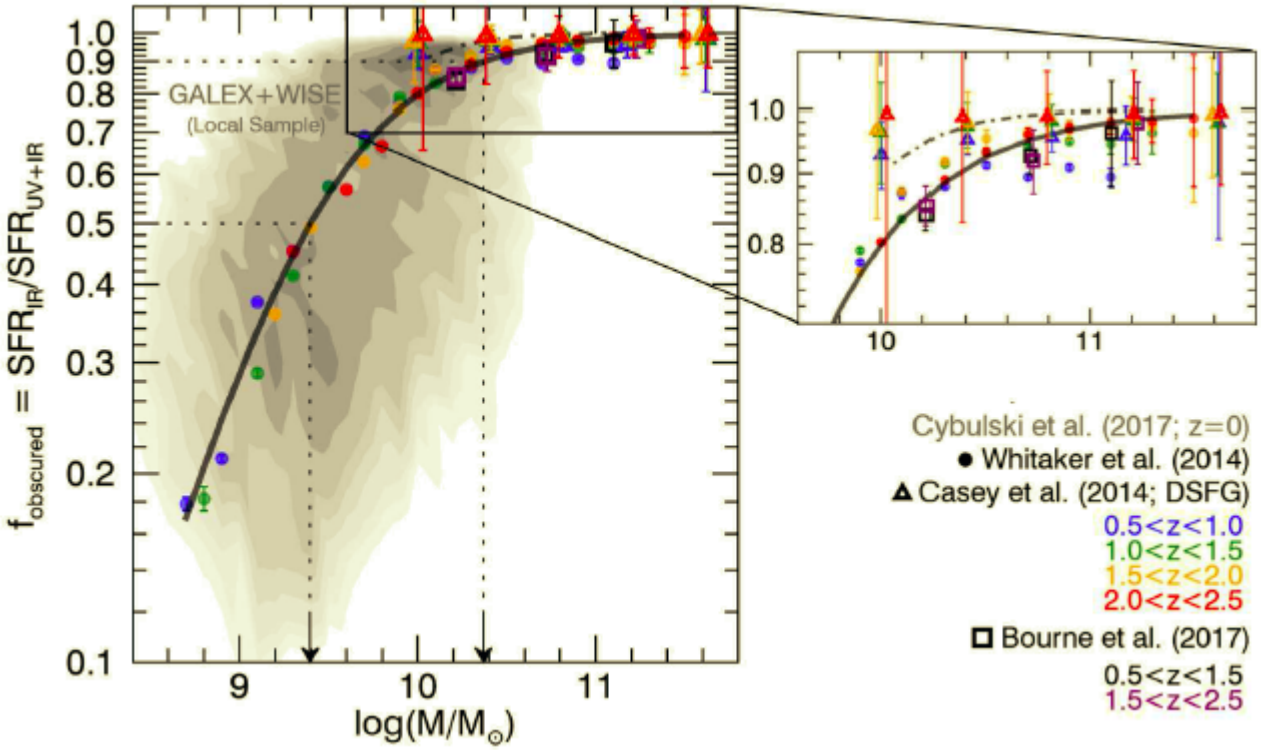


Figure 1.10: The figure 2 from Whitaker et al. (2017). The fraction of SFR from obscured dusty star-formation traced by IR radiation as a function of stellar mass. Almost all of star-formations in massive ($\log M_* \gtrsim 10$) galaxies are traced by IR wavelength.

follow up observation for LAB18 in §5. In §6, we summarize our main findings and future prospects. We use the following cosmological parameters in §2–§4: $\Omega_m = 0.3,\ \Omega_\Lambda = 0.7,\ h = 0.7$. In this cosmology, the Universe is 2.9, 2.8, and 2.0 Gyr old and $1.0''$ corresponds to 8.3, 8.2 and 7.6 kpc in physical length at $z = 2.2$, 2.3 and 3.1, respectively. We use the following cosmological parameters in §5: $\Omega_m = 0.315,\ \Omega_\Lambda = 0.685,\ h = 0.67$.

# Chapter 2

# Herschel Observations

## 2.1 Herschel/SPIRE Observations

*Herschel Space Observatory* (HSO; Pilbratt et al., 2010) was launched on 14 May 2009. It is built and operated by European Space Agency (ESA). It is the largest space telescope ever launched which have a 3.5 m Cassegrain antennae. It performs photometry and spectroscopy in 55-671 $\mu$m range. It continued to operate until April 2013, since *Herschel* ran out of coolant liquid helium. Figure 2.1 shows the image of *Herschel*.

Spectral and Photometric Imaging Receiver (SPIRE; Griffin et al., 2010) is a photometry camera and low to medium resolution spectrometer for wavelengths in the range 194-671 $\mu$m. SPIRE is one of three scientific instruments equipped on *Herschel*. It comprises an imaging photometer and a Fourier Transform Spectrometer (FTS), both of which use bolometer detector arrays.

SPIRE has a total of five arrays, three dedicated for photometry and two for spectroscopy. Its imaging photometer can simultaneously observe three wavelengths bands, whose central frequencies are 250 $\mu$m, 350 $\mu$m, and 500 $\mu$m. In Figure 2.2 left, we show photometer relative spectral response functions. The numbers of pixels are 139, 88 and 43 for 250 $\mu$m, 350 $\mu$m, and 500 $\mu$m respectively and the Field of View is $4' \times 8'$. The full width at half maximum (FWHM) of the SPIRE beam is $18.1''$, $24.9''$, and $36.6''$ at 250 $\mu$m, 350 $\mu$m, and 500 $\mu$m, respectively (Swinyard et al., 2010). High survey performance of *Herschel* increases of numbers of galaxies with far-infrared and sub-mm wavelengths, which allows for large statistical studies of a DSFGs which is a marked improvement over the original samples of galaxies discovered in the JCMT/SCUBA in the late 1990s.

We searched for dusty star-forming galaxies (DSFGs) in three $z = 2-3$ protoclusters with *Herschel*/SPIRE as part of the second Open Time (OT2) *Herschel* programs (PI: Y. Matsuda). We summarize the observations in Table 2.1. These environments are exceptionally rare, pre-virialised regions corresponding to peaks in the dark matter halo and located at the nodes of >10 Mpc large scale structures. They are the best candidates for the progenitors of the most massive clusters of galaxies ($\sim 10^{15}$ $M_{\odot}$) today. By using *Herschel*/SPIRE, we search for concentration of DSFGs and investigate whether or not the protoclusters are experiencing simultaneously dusty star-formation through DSFG.

Figure 2.1: The *Herschel Space Observatory*. It orbits around the L2 Earth-Sun equilibrium point and the largest (3.5 m) single telescope ever launched into space. It is capable of observing wavelengths from 55 to 671 $\mu$m. ©ESA

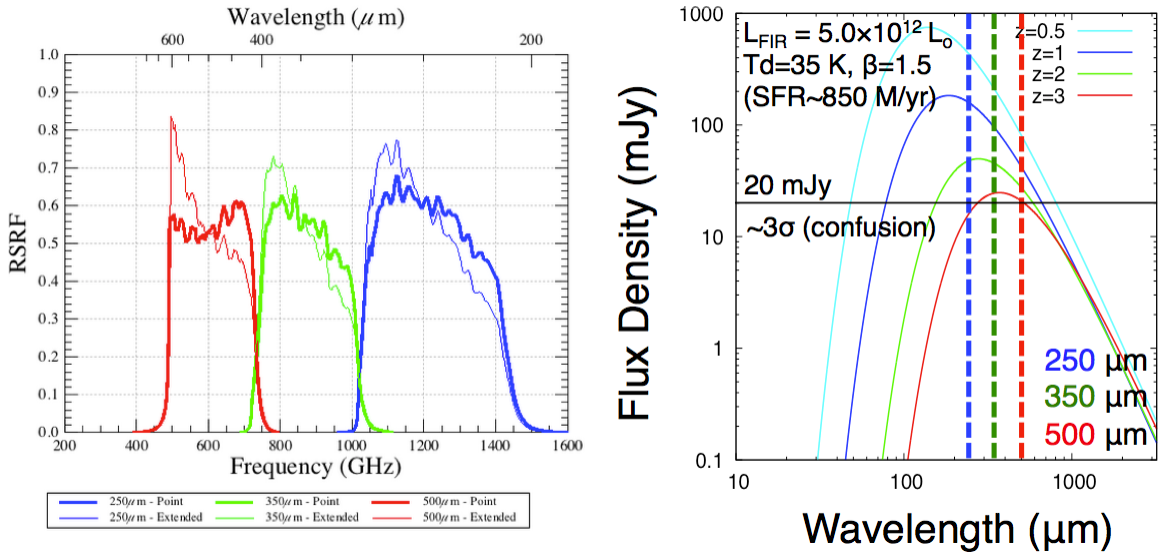


Figure 2.2: (left): Photometer Relative Spectral Response Functions (RSRFs) for SPIRE camera are shown. The full width half maximums (FWHMs) of the SPIRE beam are 18.1″, 24.9″, and 36.6″ at 250 $\mu$m, 350 $\mu$m, and 500 $\mu$m, respectively. The numbers of pixels are 139, 88 and 43 for 250 $\mu$m, 350 $\mu$m and 500 $\mu$m respectively. The Field of View is $4' \times 8'$. ©ESA (right): A single temperature, optically thin modified black body radiation from DSFGs at various redshift. We can detect DSFGs with SFR around 850 $M_\odot$ $yr^{-1}$ above ~20 mJy in each SPIRE band which is above $3\sigma$ level of source confusion at $z = 2 - 3$.

Table 2.1: *Herschel*/SPIRE observation parameters.

| Target | $z^a$ | R.A.$^b$ | Dec$^c$ | Area$^d$ | $t_{\rm int}{}^e$ | $\sigma_{\rm conf}{}^f$ | | | $\sigma_{\rm inst}{}^g$ | | |
|---|---|---|---|---|---|---|---|---|---|---|---|
| | | | | | | $S_{250}$ | $S_{350}$ | $S_{500}$ | $S_{250}$ | $S_{350}$ | $S_{500}$ |
| | | (J2000) | (J2000) | (arcmin$^2$) | (hours) | (mJy) | (mJy) | (mJy) | (mJy) | (mJy) | (mJy) |
| 2QZCluster | 2.230 ± 0.016 | 10h03m51s | +00d15m09s | 515 | 1.8 | 6.7 | 7.0 | 7.1 | 2.0–3.9 | 1.6–2.6 | 2.0–3.3 |
| HS1700 | 2.300 ± 0.015 | 17h01m15s | +64d14m03s | 497 | 1.5 | 7.3 | 7.4 | 7.5 | 2.0–3.7 | 1.6–2.7 | 2.0–3.2 |
| SSA22 | 3.090 ± 0.030 | 22h17m34s | +00d17m01s | 1076 | 3.7 | 7.7 | 7.8 | 8.0 | 1.9–3.2 | 1.6–2.4 | 1.9–3.0 |
| COSMOS | - | 10h00m37s | +02d11m26s | 3422 | 50.1 | 7.1 | 7.7 | 7.8 | 2.1–2.7 | 1.7–2.0 | 2.1–2.8 |

**Notes.** $(a)$: Redshift range of HAEs for 2QZCluster (Matsuda et al., 2011a), LBGs for HS1700 (Steidel et al., 2005) and SSA22 (Steidel et al., 1998, 2000) protocluster. $(b), (c)$: The center coordinates of the *Herschel*/SPIRE observations. $(d)$: The area where the integration time is greater than 30%. We used center of 3422 arcmin$^2$ area for COSMOS field. $(e)$: Total integration times. See Oliver et al. (2012) for the survey design of COSMOS field. $(f), (g)$: The confusion noise and instrumental noise are shown.

*Herschel*/SPIRE is the only instrument that can efficiently map these protoclusters and observe around the peak of dust thermal emission of protocluster member galaxies. The SPIRE wavelengths range of 250–500 $\mu$m corresponds to a dust thermal peak of $T_d \sim 25-50$ K at $z \sim 3$ and $T_d \sim 20-40$ K at $z \sim 2$ if we assume a single temperature of dust and an optically thin modified blackbody radiation with $\beta = 1.5$. In Figure 2.2 right, we show optically thin modified black body radiation from DSFGs at various redshift. We can detect DSFGs with SFR around 850 $M_\odot$ yr$^{-1}$ at $z \sim 2-3$ above ∼20 mJy in each SPIRE band, which is $3\sigma$ level of source confusion.

The observations have been done on the 22 June 2012 (2QZCluster), 4 March 2012 (HS1700), and 10 May 2012 (SSA22) with Large map mode (scan rate of $30''$ s$^{-1}$). The observations have been repeated 14 times for each field. The integration times are 1.8, 1.5 and 3.7 hours for 2QZCluster, HS1700 and SSA22, respectively. The covered area are $\sim 23' \times 23'$ (2QZCluster), $\sim 22' \times 22'$ (HS1700), and $\sim 33' \times 33'$ (SSA22) respectively. These coverages are sufficient to search for DSFGs around the density peak of protocluster member galaxies. These coverage correspond to $\sim 40-60$ comoving Mpc at the protocluster redshifts.

By using *Herschel* Interactive Processing Environment (HIPE, v11.0.0), we produced the maps following the standard data processing and map-making steps with destriping. The beam FWHMs of SPIRE are $18.1''$, $24.9''$ and $36.6''$ at 250, 350 and 500 $\mu$m, respectively (Swinyard et al., 2010). The pixel sizes of maps are $6''$, $10''$, and $14''$ at 250, 350, and 500 $\mu$m, respectively. The $1\sigma$ confusion noises ($\sigma_{\rm conf}$) are measured as map variances of flux density within effective area (Table 2.1), which are slightly higher than the values of blank fields (Nguyen et al., 2010). We measured the instrumental noises in our three map, which are about one-third of the confusion noises (Table 2.1).

## 2.2 Other Protocluster Surveys for DSFGs

The presence of DSFGs in $z < 2$ galaxy clusters have been confirmed (e.g., Brodwin et al., 2013; Smail et al., 2014; Ma et al., 2015; Webb et al., 2015), although confirming DSFGs at $z \gtrsim 2$ protoclusters are progressing (e.g., Tamura et al., 2009; Clements et al., 2014; Umehata et al., 2014, 2015, 2017a; Casey et al., 2015; Oteo

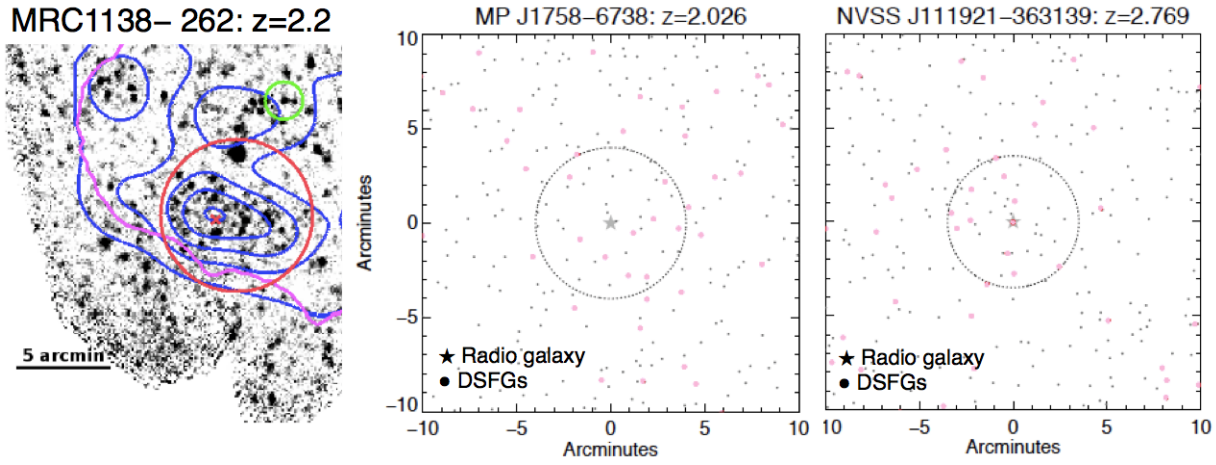


Figure 2.3: Examples of bursting star-formation around radio galaxies field. Some fraction of $z \sim 2$ protoclusters around radio galaxies indeed appear to be experienced bursting star-formation (Valtchanov et al., 2013, Dannerbauer et al., 2014, Rigby et al., 2014). (left): Figure from Valtchanov et al., (2014). The position of radio galaxy is shown as a green circe. Red circle shows the position of overdensity of DSFGs. The background is a *Herschel*/SPIRE 250 $\mu$m image. The blue contour is proportional to the 250 $\mu$m flux densities. (middle and right): Figure from Rigby et al., (2014). The positions of the radio galaxy and candidate DSFGs associated with radio galaxy filed are shown as central stars and red circles. They selected candidate DSFGs by using SPIRE color (see §3). The grey dots show the DSFGs which are not selected by SPIRE color. Only two nineteenth radio galaxy fields have concentration of DSFG. Radio galaxy selection could missed a period of dusty star-formation in Mpc scale structure.

et al., 2017b).

Some searches with far-infrared wavelengths have focused on radio galaxy fields (e.g., Stevens et al., 2003; Valtchanov et al., 2013; Rigby et al., 2014; Dannerbauer et al., 2014), and some fraction of $z \gtrsim 2$ protoclusters around radio galaxies indeed appear to be related to DSFGs (e.g., Ivison et al., 2000). Figure 2.3 shows examples possibly experienced bursting star-formation around radio galaxy.

Planck Collaboration et al. (2015) have investigated all sky to search for clusters and protoclusters undergoing dusty star-formation with *Planck* and *Herschel*/SPIRE. They have confirmed 234 candidate of clusters and protoclusters possibly experienced simultaneous dusty star-formation. However, such regions inversely need to search for large scale structures with galaxies selected by other techniques, and need to determine their precise redshifts. Clements et al., (2014) conducted follow-up studies for four candidate of clusters undergoing bursting star-formation at $z = 1 - 2$ in Planck Collaboration et al. (2015), and found that their clusters are indeed galaxy overdense region with red sequence of the galaxies, and their star-formation rate density is 100-1000 times higher than the cosmic averaged value. But is it also true for protoclusters confirmed with UV/optical-selected star-forming galaxies? It is needed to explore DSFGs in large-scale structures confirmed from UV/optical-selected star-forming galaxies to investigate bursting star-formation more generally.

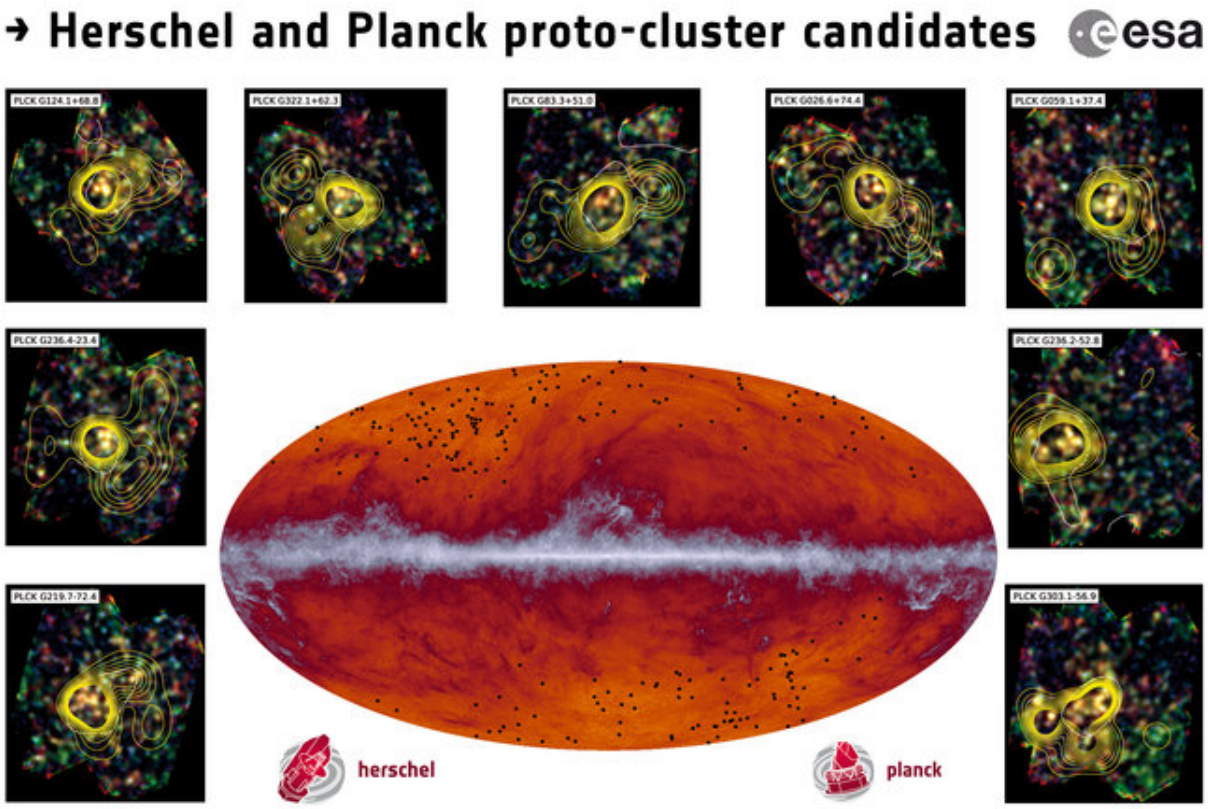


Figure 2.4: *Herschel* and *Planck* cluster/protocluster candidates possibly experiencing bursting star-formation. They investigated all sky to search for clusters/protoclusters undergoing bursting star-formation with *Planck* and *Herschel*. Planck Collaboration et al. (2015) have confirmed 234 candidate of clusters/protoclusters experienced bursting star-formation. However, whether or not these also have large scale structures of UV/optical selected star-forming galaxies or not is unclear. ©ESA

## 2.3 Our Protocluster Targets

We targeted three protoclusters, 2QZCluster ($z = 2.2$), HS1700 ($z = 2.3$) and SSA22 ($z = 3.1$) with a few tens of proper Mpc filamentary, large scale structures of galaxy overdensities and evidence for enhancement of AGNs fraction. In addition, all of the three protoclusters have Ly$\alpha$ blobs (LABs) and H$\alpha$ blobs (HABs), which thought to be sites of massive galaxy formation. We describe short summaries as following and in Figure 2.5 and 2.6, we summarize characteristic of targeted three protoclusters. We show the obtained *Herschel*/SPIRE maps in Figure 2.7.

### 2QZCluster

This protocluster was originally identified as a concentration of five Quasi Stellar Objects (QSOs) in a $\sim 1$ degree region at $z = 2.23$ from the 2dF Quasar Redshift survey (Croom et al., 2001, 2004). Four out of the five QSOs are even more strongly clustered in a $30 \times 30$ comoving Mpc patch. An H$\alpha$ narrow-band imaging revealed a filamentary large-scale structure of an over density of 22 HAEs connecting the QSOs (Matsuda et al., 2011a). A H$\alpha$ Blob is reported in this protocluster (Matsuda et al., 2011a). *Chandra*/ACIS-I 100 ks observations reported evidence for the Active Galactic Nucleus (AGNs) fraction is a factor of $\sim 3.5$ higher than blank fields (Lehmer et al., 2013).

### HS1700

This protocluster was originally discovered as a $\sim 7\times$ density contrast redshift spike of UV/optical-selected star forming galaxies (BX/BM) within a $\sim 25$ comoving Mpc region at $z = 2.30$ (Steidel et al., 2005). A Ly$\alpha$ narrowband imaging survey revealed six giant Ly$\alpha$ Blobs (LABs) consist filamentary large scale structures (Erb, Bogosavljević, & Steidel, 2011). *Chandra*/ACIS-I 200 ks observations reported tentative evidence of an enhancement of AGN fraction compared to the blanck field (Digby-North et al., 2010).

### SSA22

This protocluster was originally discovered as a $\sim 4 - 6\times$ density contrast in redshift distribution of Lyman Break Galaxies (LBGs) and Ly$\alpha$ emitters (LAEs) within a $\sim 20$ comoving Mpc region at $z = 3.09$ (Steidel et al., 1998, 2000). A wide-field Ly$\alpha$ narrowband imaging survey with Subaru Telescope revealed a filamentary large-scale structure of 283 LAEs, extended to at least $\sim 60$ comoving Mpc (Hayashino et al., 2004). 35 LABs with sizes of 30–150 kpc scale are reported (Steidel et al., 2000; Matsuda et al., 2004). *Chandra*/ACIS-I 400 ks observations reported that the AGN fraction of protocluster members is $\sim 3\times$ higher than that in the field environment (Lehmer et al., 2009a,b).

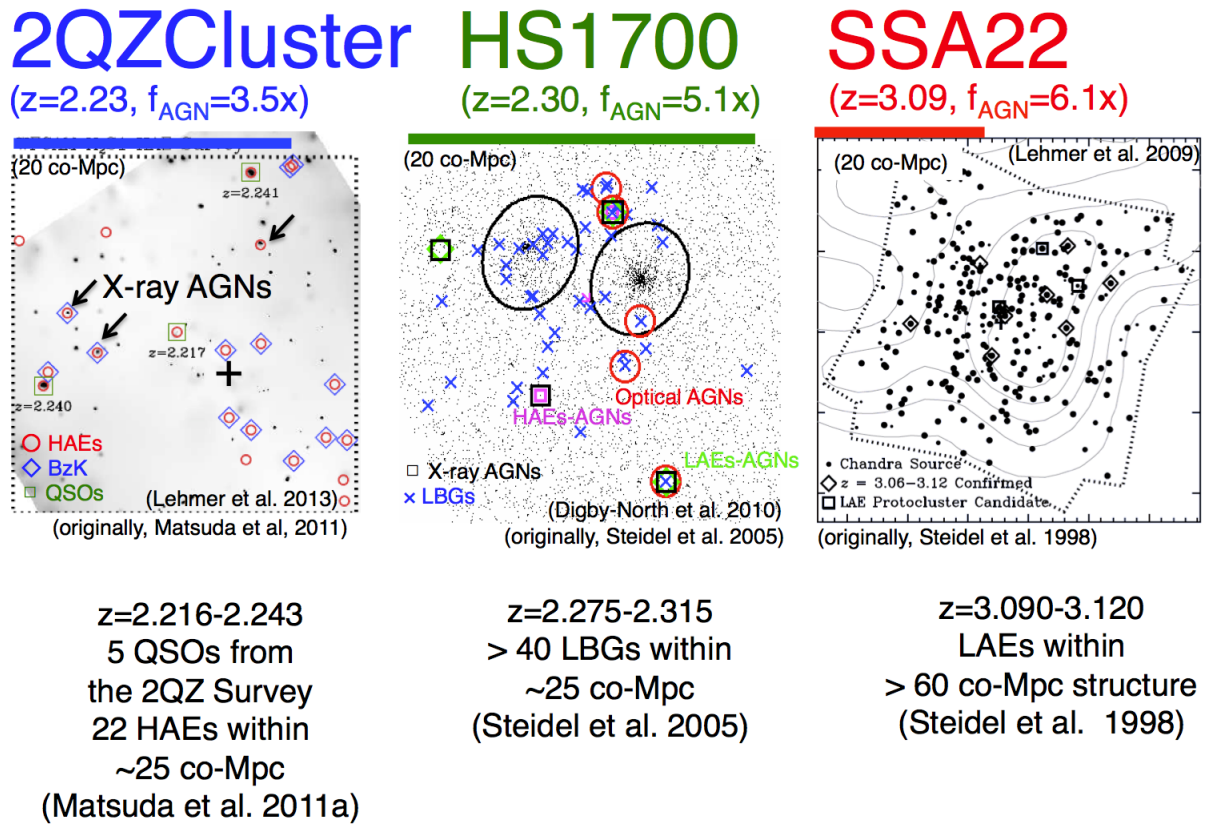


Figure 2.5: Our targeted three protoclusters. (left): 2QZCluster is a protocluster of QSOs and HAEs at $z = 2.23$, which makes ∼25 comoving Mpc structure. Red circles and green boxes show the position of HAEs and QSOs. We can see these galaxies are strongly concentrated and make a filamentary large scale structure. (middle): HS1700 is the protocluster of LBGs at $z = 2.30$, and has ∼25 comoving Mpc structure. Blue cross show the position of the LBGs at $z = 2.30$, we can see LBGs are strongly concentrated, and make a filamentary large scale structure. (right): SSA22 is the protocluster of largest structure at $z = 3.09$ which has ∼60 comoving Mpc structure of LAEs. The contour shows galaxy number density of LAEs. We can see a filamentary large scale structure traced by LAEs.

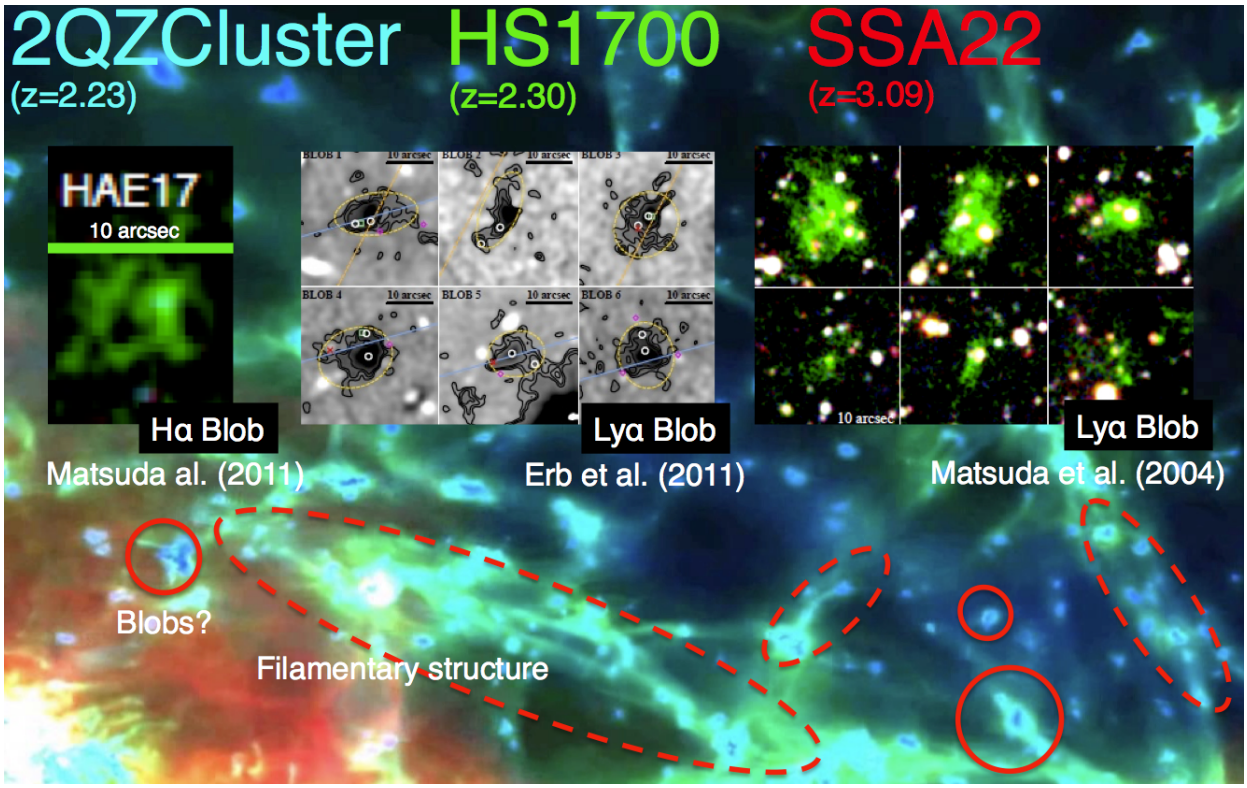


Figure 2.6: Summary of the characteristics of the targeted three protoclusters. We selected filamentary, large scale structures traced by the galaxy overdensities with evidence for enhancements of AGNs fraction. In addition, three targeted protoclusters have blobs. The upper figures are the examples of blobs. LABs and HABs thought to be atomic hydrogen gas embedded in the large scale structure and sites of massive galaxy formation. We show their expected counterpart in the background image from illustris simulation as red circles. We also show expected filamentary structures of protoclusters as red dashed circles in the background image from illustris simulation Vogelsberger et al. (2014).

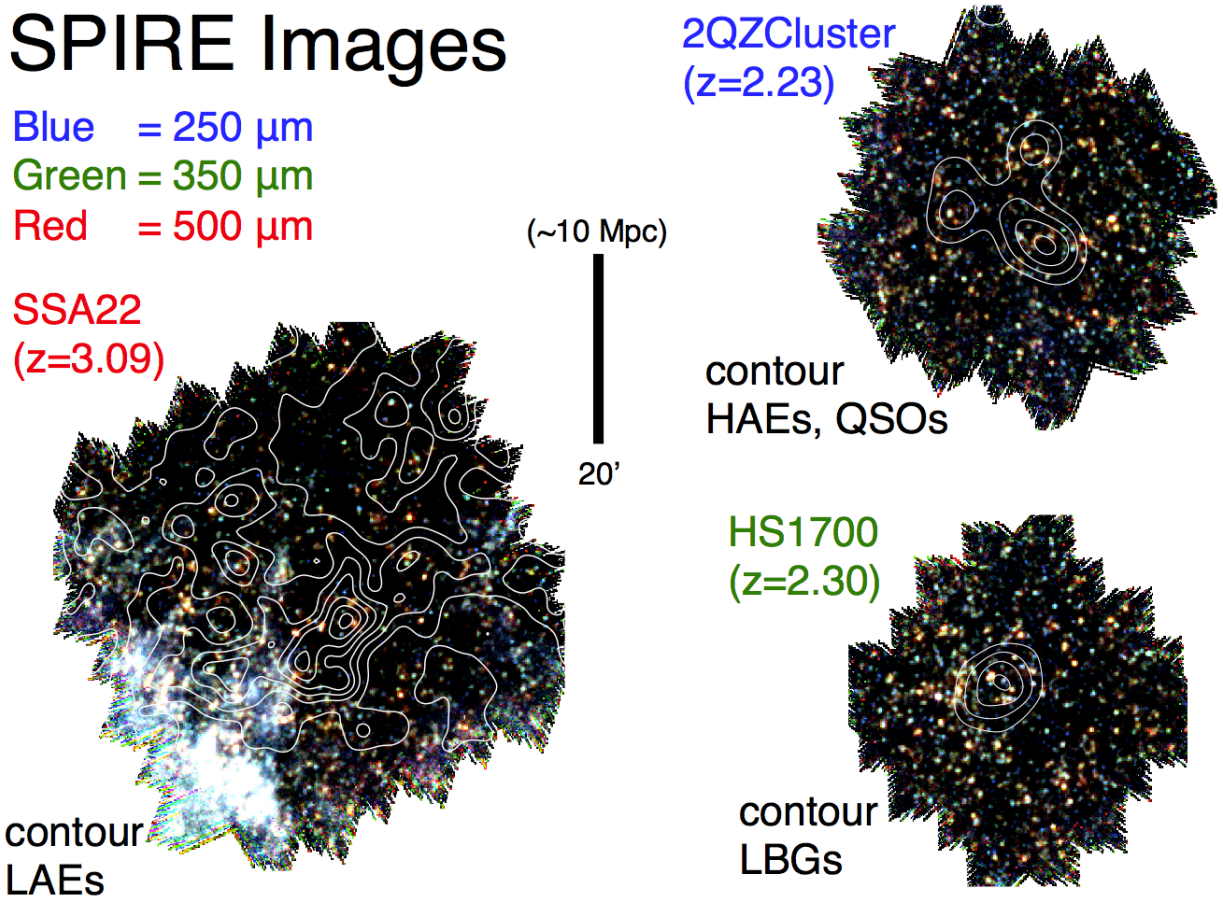


Figure 2.7: Obtained *Herschel*/SPIRE maps for three protoclusters. The contours show the galaxy number density of each protoclusters. The density of 19 HAEs and 3 QSOs (Matsuda et al., 2011a) are shown as contours for the 2QZCluster, 45 LBGs are shown as contours for HS1700 (Rudie et al., 2012; Steidel et al., 2014), and 742 LAEs are shown as contours for SSA22 (Yamada et al., 2012), respectively. The 1–4$\sigma$, 1–4$\sigma$, and 3–6$\sigma$ steps are shown for 2QZCluster, HS1700, and SSA22 with smoothed Gaussian kernel of a FWHM of 6 comoving Mpc. SPIRE coverages are enough large to search for DSFGs around the density peak of these protoclusters.

# Chapter 3

# Herschel Analysis

## 3.1 Number Counts of SPIRE Sources

Because of a better spatial resolution compared with longer *Herschel*/SPIRE wavelength bands, the source detection was conducted on the 250 $\mu$m maps. We caution that 500 $\mu$m detection causes a source blending and a large spatial uncertainty. In some case, even 250 $\mu$m map can deblend these. We detected sources with S/N $> 2$ in the 250 $\mu$m maps within the region where the integration time is greater than 30% of the deepest parts (515 arcmin$^2$ for 2QZCluster, 497 arcmin$^2$ for HS1700, 1076 arcmin$^2$ for SSA22, and 3422 arcmin$^2$ for COSMOS field). We used SUSSEXTRACTOR (Smith et al., 2012) for the source detection and the photometry.

We selected well-studied extragalactic field Cosmic Evolution Survey (COSMOS) to use as a blank field. The COSMOS field is observed as a part of *Herschel* Multi-tiered Extra-galactic survey, HerMES (Oliver et al., 2012). We reprocessed the maps of COSMOS field by limiting to depth by using $N_{\rm rep} = 14$ because of the deeper SPIRE maps in COSMOS field than our protocluster maps. We apply the same map making, and the source detection procedure in order to make sure that we match the depth of our observations. The final obtained values of instrumental noises and confusion noises are given in Table 2.1.

We measured 350 $\mu$m and 500 $\mu$m fluxes densities at the positions of 250 $\mu$m detections. Then we listed these 250 $\mu$m sources only if the flux density is above 12 mJy in at least one of the SPIRE bands. The full tables are available in online (`https://academic.oup.com/mnras/article/460/4/3861/2609134/Herschel-protocluster-survey-a-search-for-dusty#supplementary-data`, see also Table 3.6–3.8). This flux density limit of 12 mJy corresponds to $4\sigma$ of the instrumental noise and $2\sigma$ of the confusion noise in all three bands. For SSA22, we cut out the high background fluxes region due to the Galactic cirrus shown in Figure 4.1.

We compared *Herschel*/SPIRE number counts of the three protoclusters with those of COSMOS field. We show the completeness non corrected number counts in Figure 3.1 (See also Table 3.2–3.4). The number counts of three protoclusters are roughly consistent with those of COSMOS field at $> 20$ mJy bin at 250 $\mu$m and 350 $\mu$m SPIRE bands. Although they are within the error bars based on Poisson noise, the number counts at $S_{350} > 50$ mJy and $S_{500} > 40$ mJy show moderate excesses by a factor of 2–3 in the HS1700 field and the 2QZCluster field. The number counts in COSMOS field agree with that of HerMES survey data

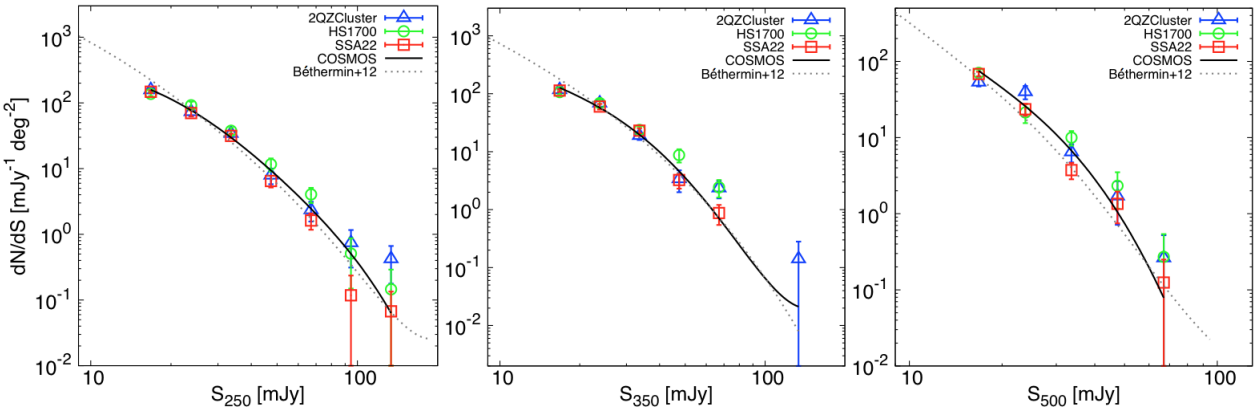


Figure 3.1: We show the number counts at *Herschel*/SPIRE 250, 350 and 500 $\mu$m in the 2QZCluster (blue), HS1700 (green) SSA22 (red), and COSMOS field (magenta). We detected sources with S/N $>$ 2 in the 250 $\mu$m maps because of the better spatial resolution. We measured the 350 $\mu$m and 500 $\mu$m fluxes densities at the positions of the 250 $\mu$m detections. We fitted a bézier curve for the data points of COSMOS filed (black solid lines). The number counts of the SPIRE sources in the three protoclusters averaged over their full fields are roughly consistent with those of COSMOS field. The number counts of the SPIRE sources in COSMOS field are also consistent with those of HerMES blank fields (Béthermin et al., 2012), suggesting that COSMOS field can be used as a control field.

Table 3.1: Number of sources which have fluxes above 12 mJy in each bands.

| | COSMOS | SSA22 | HS1700 | 2QZCluster |
|---|---|---|---|---|
| 250 $\mu$m | 2552 | 699 | 356 | 365 |
| 350 $\mu$m | 1944 | 529 | 259 | 260 |
| 500 $\mu$m | 961 | 252 | 133 | 116 |

(Béthermin et al., 2012), suggesting that COSMOS field can be used as a control blank field.

## 3.2 SPIRE Color Selection

We applied a color constraint to the SPIRE 250 $\mu$m detected sources to search for candidates of DSFGs possibly associated with the three protoclusters. The SPIRE colors of $S_{350}/S_{250}$ and $S_{500}/S_{350}$ were used with assuming single temperature, optically thin modified black body radiation. We assumed protocluster redshifts, dust temperatures of $T_d = 30-40$ K, and a dust emissivity index of $\beta = 1.5$. SPIRE-selected DSFGs typically have dust temperatures of $T_d = 20-60$ K Casey et al. (2012). The dust emissivity index is typically assumed $\beta = 1.0 - 2.0$ for DSFGs (Hildebrand, 1983). Different values of $\beta$ yield almost the same SPIRE colors. We included flux errors of $\pm$ 20% in estimating the uncertainties in the SPIRE colors. Figure 3.2 shows SPIRE $S_{500}/S_{350}$ vs. $S_{350}/S_{250}$ color-color diagram of the SPIRE sources in the three protoclusters.

We derived $L_{\rm FIR}$ $(8-1000$ $\mu$m) by fitting single temperature, optically thin modified black body radiation with free parameter of $T_d$ and fixed parameter of $\beta = 1.5$. We assumed all of the sources are associated with

Table 3.2: Number counts at 250 $\mu$m. The errors take into account the statistical uncertainties, including the Poisson noise.

| Central flux | Flux bin | Number counts ($dN/dS$) [mJy$^{-1}$ deg$^{-2}$] | | | |
|---|---|---|---|---|---|
| (mJy) | (mJy) | SSA22 | HS1700 | 2QZCluster | COSMOS |
| 16.8 | 12.0 – 21.6 | 148.1 ± 7.2 | 137.2 ± 10.2 | 157.1 ± 10.7 | 158.1 ± 4.2 |
| 23.8 | 21.6 – 26.0 | 70.0 ± 7.3 | 92.1 ± 12.3 | 73.0 ± 10.8 | 87.5 ± 4.6 |
| 33.6 | 26.0 – 41.2 | 31.5 ± 2.6 | 37.6 ± 4.2 | 34.0 ± 4.0 | 36.4 ± 1.6 |
| 47.4 | 41.2 – 53.6 | 6.5 ± 1.3 | 11.7 ± 2.6 | 7.9 ± 2.1 | 10.4 ± 0.9 |
| 67.0 | 53.6 – 80.4 | 1.6 ± 0.5 | 4.0 ± 1.0 | 2.3 ± 0.8 | 2.7 ± 0.3 |
| 94.6 | 80.4 – 108.8 | 0.12 ± 0.12 | 0.51 ± 0.36 | 0.74 ± 0.43 | 0.74 ± 0.17 |
| 133.7 | 108.8 – 158.6 | 0.07 ± 0.07 | 0.15 ± 0.15 | 0.42 ± 0.24 | 0.06 ± 0.04 |
| 188.8 | 158.6 – 219.0 | - | - | - | - |

Table 3.3: Number counts at 350 $\mu$m. The errors take into account the statistical uncertainties, including the Poisson noise.

| Central flux | Flux bin | Number counts ($dN/dS$) [mJy$^{-1}$ deg$^{-2}$] | | | |
|---|---|---|---|---|---|
| (mJy) | (mJy) | SSA22 | HS1700 | 2QZCluster | COSMOS |
| 16.8 | 12.0 – 21.6 | 113.6 ± 6.3 | 107.0 ± 9.0 | 116.4 ± 9.2 | 127.4 ± 3.7 |
| 23.8 | 21.6 – 26.0 | 60.1 ± 6.8 | 69.1 ± 10.7 | 68.3 ± 10.4 | 62.2 ± 3.9 |
| 33.6 | 26.0 – 41.2 | 23.1 ± 2.3 | 23.8 ± 3.4 | 18.8 ± 2.9 | 28.5 ± 1.4 |
| 47.4 | 41.2 – 53.6 | 3.2 ± 0.9 | 8.8 ± 2.3 | 3.4 ± 1.4 | 5.9 ± 0.7 |
| 67.0 | 53.6 – 80.4 | 0.9 ± 0.3 | 2.4 ± 0.8 | 2.3 ± 0.8 | 1.5 ± 0.2 |
| 94.6 | 80.4 – 108.8 | - | - | - | 0.04 ± 0.04 |
| 133.7 | 108.8 – 158.6 | - | - | 0.14 ± 0.14 | - |
| 188.8 | 158.6 – 219.0 | - | - | - | - |

Table 3.4: Number counts at 500 $\mu$m. The errors take into account the statistical uncertainties, including the Poisson noise.

| Central flux | Flux bin | Number counts ($dN/dS$) [mJy$^{-1}$ deg$^{-2}$] | | | |
|---|---|---|---|---|---|
| (mJy) | (mJy) | SSA22 | HS1700 | 2QZCluster | COSMOS |
| 16.8 | 12.0 – 21.6 | 68.3 ± 4.9 | 70.8 ± 7.3 | 53.1 ± 6.2 | 75.2 ± 2.9 |
| 23.8 | 21.6 – 26.0 | 23.6 ± 4.2 | 21.4 ± 5.9 | 39.7 ± 7.9 | 27.3 ± 2.6 |
| 33.6 | 26.0 – 41.2 | 3.7 ± 0.9 | 10.0 ± 2.2 | 6.4 ± 1.7 | 9.7 ± 0.8 |
| 47.4 | 41.2 – 53.6 | 1.3 ± 0.6 | 2.3 ± 1.2 | 1.7 ± 1.0 | 1.6 ± 0.4 |
| 67.0 | 53.6 – 80.4 | 0.1 ± 0.1 | 0.27 ± 0.27 | 0.26 ± 0.26 | 0.08 ± 0.06 |
| 94.6 | 80.4 – 108.8 | - | - | - | - |
| 133.7 | 108.8 – 158.6 | - | - | - | - |
| 188.8 | 158.6 – 219.0 | - | - | - | - |

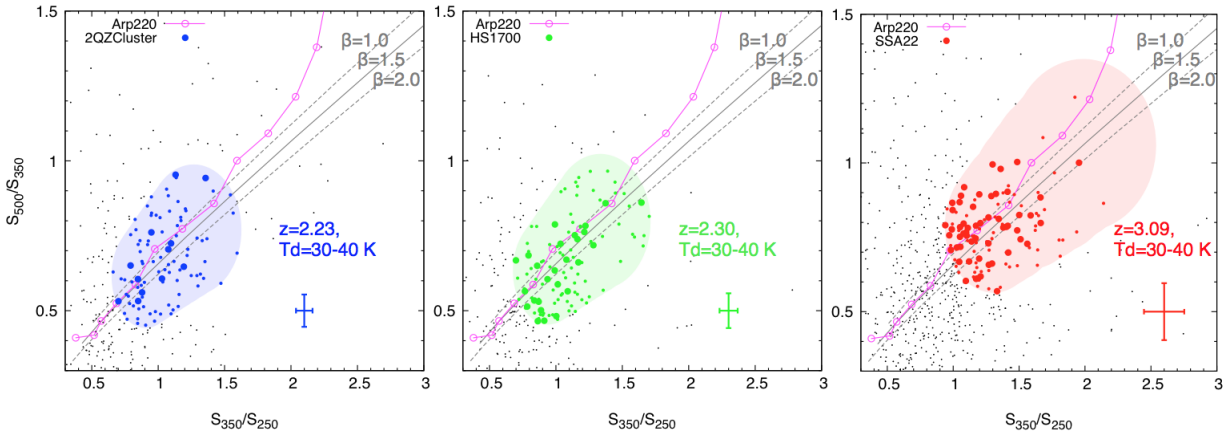


Figure 3.2: We show the SPIRE color-color ($S_{500}/S_{350}$ vs $S_{350}/S_{250}$) diagram for the 250 $\mu$m detected sources. From left to right, we show the results for 2QZCluster (blue), HS1700 (green), and SSA22 (red). We selected candidates of DSFGs which are possibly associated with the protoclusters by using consistent colors with single temperature, optically thin modified black body radiation. We included a photometric error of $\pm$ 20% (shaded regions) and assumed the protocluster redshifts, dust temperatures of $T_d = 30 - 40$ K and dust emissivity index of $\beta = 1.5$. The solid and dashed grey lines show tracks of different $\beta$. We also plotted the expected colors of Arp 220 as a function of redshifts (Polletta et al., 2007) for comparison. We plotted open magenta circles on track of Arp220 every $z = 0.5$ from $z = 0$ to $z = 5.5$. The small grey points show the sources with fluxes above 12 mJy in at least one SPIRE bands. The colored larger/smaller filled circles show the sources with $L_{\rm FIR}$ larger/smaller than $5.0 \times 10^{12}$ $L_{\odot}$. The average SPIRE color errors of color-selected bright SPIRE sources are shown in the bottom right with error bars. We finally used 2%, 5%, and 4% color-selected bright SPIRE sources in 2QZCluster, HS1700, and SSA22, respectively, to search for overdensities of DSFGs.

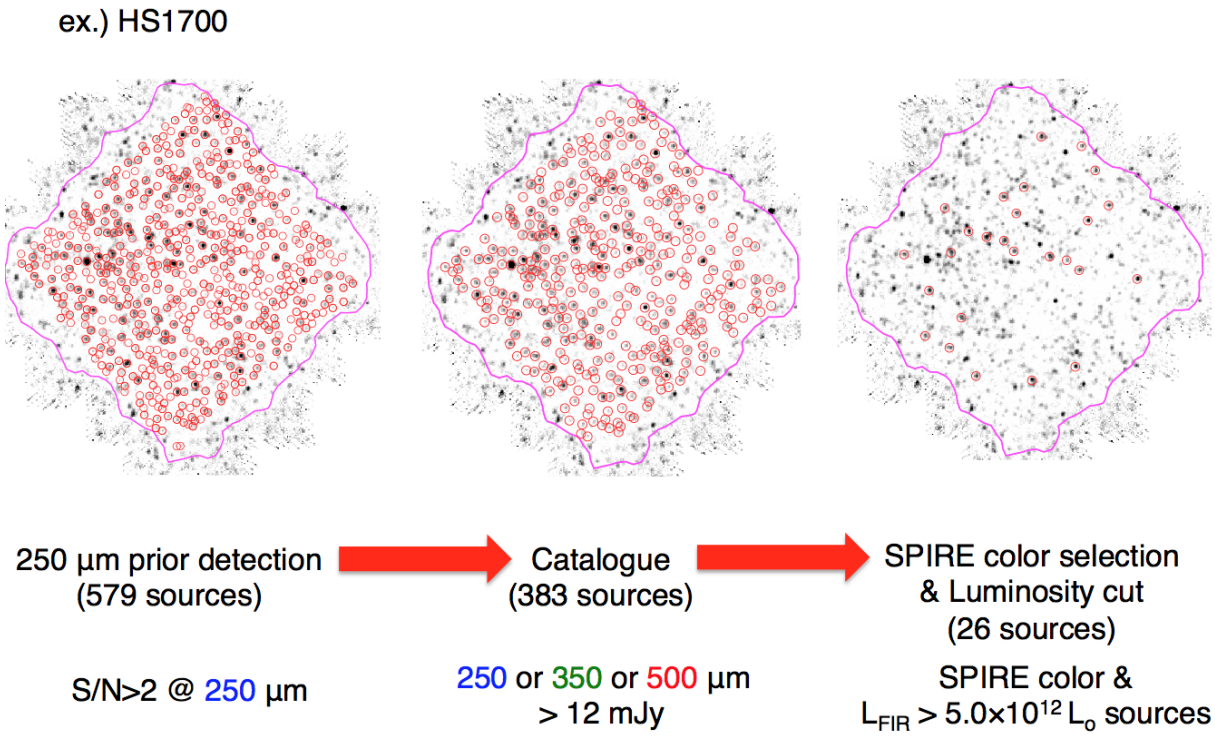


Figure 3.3: Summary of our SPIRE color selection.

each protocluster. We calculated $L_{\rm FIR}$ for the SPIRE sources by using following equation,

$$S_{\rm obs}\ ({\rm mJy}) = \frac{3.84\times10^{55} L_{\rm FIR} (\frac{h\nu_{\rm obs}(1+z)}{k_B T_{\rm dust}})^{(\beta+4)}}{4\pi\Gamma(\beta+4)\zeta(\beta+4) D_L^2 (\exp(\frac{h\nu_{\rm obs}(1+z)}{k_B T_{\rm dust}})-1)\nu_{\rm obs}} \tag{3.1}$$

Here we use $k_B = 1.38\ \times 10^{-23}$ J K$^{-1}$, h $= 6.62\ \times\ 10^{34}$ J s, $\pi = 3.14$, c $= 3.0\ \times\ 10^{8}$ m s$^{-1}$, and $\beta = 1.5$. $k_B$, $h$, and $\beta$ are Boltzmann constant, Planck's constant, and dust emissivity index respectively. $L_{\rm FIR}$ is in solar luminosity ($L_\odot = 3.84\times10^{33}$ erg s$^{-1}$), and 1 mJy $= 10^{-26}$ erg s$^{-1}$ cm$^{-2}$ Hz$^{-1}$. $\Gamma$ and $\zeta$ represent Gamma function and Zeta function respectively. $D_L^2$ is luminosity distance in cm, $\nu$ is frequency in Hz.

We further applied a FIR luminosity cut of $L_{\rm FIR} \geq 5.0\times10^{12}\ L_\odot$ for conservative searches for DSFGs. The lowest flux densities in our samples are (36.0, 30.0, 19.4) mJy for 2QZCluster, (28.8, 26.3, 15.2) mJy for HS1700, and (15.6, 19.2, 12.9) mJy for SSA22 in the SPIRE bands (250, 350, 500) $\mu$m, respectively. We finally obtained color-selected bright SPIRE sources by rejecting $\sim$ 95% of the 250 $\mu$m sources. Thus we selected just 12/643 (2%), 26/579 (5%), and 55/1253 (4%) color-selected bright SPIRE sources in 2QZCluster, HS1700, and SSA22, respectively. We applied the same SPIRE color selection and luminosity cut as the three protoclusters for the reference COSMOS field. We selected 111/4923 (2%), 140/4923 (3%), and 262/4923 (5%) color-selected bright SPIRE sources in COSMOS field for the references to 2QZCluster, HS1700, and SSA22 respectively (see also Table 3.5).

Table 3.5: Summary of *Herschel*/SPIRE sources in the three protoclusters.

| Field | Area[a] (arcmin$^{-2}$) | N[b] (prior) | N[c] (catalogued) | N[d] (selected) | N[e] | $\Sigma^f$ (arcmin$^{-2}$) | $\Sigma^g$ (arcmin$^{-2}$) | $\delta^h$ | $\sigma^i$ |
|---|---|---|---|---|---|---|---|---|---|
| 2QZCluster | 515 | 643 | 399 | 12 | 6 | 0.023 ± 0.007 | 0.132 ± 0.054 | 3.0 ± 1.7 | 3.9 ± 2.1 |
| HS1700 | 497 | 579 | 383 | 26 | 8 | 0.052 ± 0.010 | 0.186 ± 0.066 | 3.7 ± 1.7 | 5.0 ± 2.2 |
| SSA22 | 1076 | 1253 | 772 | 55 | 5 | 0.051 ± 0.007 | - | - | - |
| COSMOS (matched to 2QZCluster) | 3422 | 4923 | 2777 | 111 | 7 | 0.032 ± 0.003 | - | - | - |
| COSMOS (matched to HS1700) | 3422 | 4923 | 2777 | 140 | 7 | 0.041 ± 0.004 | - | - | - |
| COSMOS (matched to SSA22) | 3422 | 4923 | 2777 | 262 | 10 | 0.077 ± 0.005 | - | - | - |

**Notes.** ($a$): The area where the integration time is greater than 30%. ($b$): The numbers of S/N (250 $\mu$m) $> 2$ prior sources. ($c$): The numbers of catalogued sources which at least one SPIRE band flux is above 12 mJy. ($d$): The numbers of color-selected bright SPIRE sources. For SSA22, we excluded the sources in high background fluxes (see Figure 2.7). ($e$): The numbers of color-selected bright SPIRE sources within the overdensities. ($f$): The surface density of color-selected bright SPIRE sources. We assumed Poisson statistics for the errors. ($g$): The surface density of color-selected bright SPIRE sources in the overdensities, assume an area of the overdensities ($r = 3.8'$ for 2QZCluster, $r = 3.7'$ for HS1700). We assumed Poisson statistics for the errors. ($h$) – ($i$): The $\delta$ and $\sigma$ are calculated from $\delta_{\rm pc} = (n_{\rm pc} - n_{\rm ave})/n_{\rm ave}$ and $\sigma_{\rm pc} = (n_{\rm pc} - n_{\rm ave})/\sigma_{\rm ave}$. We assumed Poisson statistics for the errors.

Table 3.6: SPIRE sources catalogue of 2QZCluster. The full table is in appendix and available online.

| ID | R.A. (J2000) | Dec. (J2000) | $S_{250}$ (mJy) | $S_{350}$ (mJy) | $S_{500}$ (mJy) |
|---|---|---|---|---|---|
| 2QZCluster-SPIRE1 | 150.81846968368112 | 0.029424092103377656 | 127.0 ± 2.1 | 54.2 ± 1.9 | 24.6 ± 2.2 |
| 2QZCluster-SPIRE2 | 150.76480950482065 | 0.22501254698200338 | 139.1 ± 2.4 | 117.9 ± 1.8 | 71.4 ± 2.3 |
| 2QZCluster-SPIRE3 | 150.91517959664077 | 0.3909833462929028 | 111.4 ± 2.4 | 55.2 ± 1.8 | 21.2 ± 2.4 |
| 2QZCluster-SPIRE4 | 151.02463506680982 | 0.1206541823404277 | 97.4 ± 2.2 | 54.2 ± 1.8 | 26.5 ± 2.4 |
| 2QZCluster-SPIRE5 | 151.04455762206453 | 0.4047339937359634 | 93.6 ± 2.3 | 61.3 ± 1.8 | 24.2 ± 2.2 |
| 2QZCluster-SPIRE6 | 151.07930718745527 | 0.12006911913976963 | 84.1 ± 2.3 | 58.9 ± 1.8 | 31.3 ± 2.3 |
| 2QZCluster-SPIRE7 | 151.11225122198036 | 0.17674219593981788 | 66.1 ± 2.2 | 36.2 ± 2.1 | 13.2 ± 2.1 |
| 2QZCluster-SPIRE8 | 150.7066091154151 | 0.2830585502030584 | 67.4 ± 2.3 | 54.5 ± 1.8 | 18.4 ± 2.2 |
| 2QZCluster-SPIRE9 | 150.94968775985714 | 0.33116978814976 | 64.4 ± 2.2 | 22.2 ± 1.9 | 0.0 ± 2.1 |
| 2QZCluster-SPIRE10 | 150.91631977926835 | 0.3524558479517708 | 60.1 ± 2.1 | 64.7 ± 1.8 | 45.6 ± 2.0 |

Table 3.7: SPIRE sources catalogue of HS1700. The full table is in appendix and available online.

| ID | R.A. (J2000) | Dec. (J2000) | $S_{250}$ (mJy) | $S_{350}$ (mJy) | $S_{500}$ (mJy) |
|---|---|---|---|---|---|
| HS1700-SPIRE1 | 255.53646683056928 | 64.2060083253161 | 422.6 ± 3.1 | 181.4 ± 1.9 | 67.3 ± 2.4 |
| HS1700-SPIRE2 | 255.07094202680116 | 64.36337246187729 | 112.4 ± 2.2 | 49.0 ± 1.9 | 19.5 ± 2.2 |
| HS1700-SPIRE3 | 255.10511462429938 | 64.14686204692669 | 86.2 ± 2.4 | 51.5 ± 2.0 | 21.4 ± 2.1 |
| HS1700-SPIRE4 | 255.15806474143926 | 64.22916135482777 | 85.8 ± 2.5 | 60.5 ± 1.8 | 27.9 ± 2.2 |
| HS1700-SPIRE5 | 254.99437853070503 | 64.26410380634614 | 70.8 ± 2.1 | 76.4 ± 1.7 | 51.2 ± 2.2 |
| HS1700-SPIRE6 | 254.91863041158092 | 64.21174308418698 | 76.7 ± 2.4 | 44.4 ± 1.7 | 17.6 ± 2.3 |
| HS1700-SPIRE7 | 255.22359843297363 | 64.38646521955137 | 65.7 ± 2.2 | 21.3 ± 1.9 | 13.0 ± 2.3 |
| HS1700-SPIRE8 | 254.82938021291324 | 64.17873107989598 | 68.7 ± 2.3 | 59.4 ± 1.7 | 27.6 ± 2.2 |
| HS1700-SPIRE9 | 255.20168755944053 | 64.25859055126669 | 66.3 ± 2.2 | 35.3 ± 2.1 | 16.2 ± 2.2 |
| HS1700-SPIRE10 | 255.1823543841818 | 64.03153372522755 | 64.7 ± 2.2 | 64.8 ± 1.9 | 31.2 ± 2.1 |

Table 3.8: SPIRE sources catalogue of SSA22. The full table is in appendix and available online.

| ID | R.A. (J2000) | Dec (J2000) | $S_{250}$ (mJy) | $S_{350}$ (mJy) | $S_{500}$ (mJy) |
|---|---|---|---|---|---|
| SSA22-SPIRE1 | 334.264444128561 | 0.6764415586203842 | 135.3 ± 2.2 | 71.3 ± 1.9 | 30.4 ± 2.3 |
| SSA22-SPIRE2 | 334.57160684240256 | 0.49219161422544583 | 93.3 ± 2.2 | 76.7 ± 1.7 | 48.7 ± 2.3 |
| SSA22-SPIRE3 | 334.344178441303 | 0.3528652232847903 | 79.2 ± 2.2 | 34.4 ± 1.9 | 10.4 ± 2.2 |
| SSA22-SPIRE4 | 334.34457572927244 | 0.607307593915126 | 79.7 ± 2.4 | 56.9 ± 1.7 | 21.9 ± 2.0 |
| SSA22-SPIRE5 | 334.69745115684617 | 0.3983836901706686 | 72.9 ± 2.2 | 29.8 ± 1.9 | 12.8 ± 2.1 |
| SSA22-SPIRE6 | 334.392819716858 | 0.3042332652494624 | 68.9 ± 2.1 | 33.2 ± 1.8 | 0.0 ± 2.1 |
| SSA22-SPIRE7 | 334.23836274598824 | 0.40194158606064945 | 61.8 ± 2.1 | 45.8 ± 1.8 | 8.8 ± 2.1 |
| SSA22-SPIRE8 | 334.55462830631444 | 0.47701863826781765 | 62.9 ± 2.1 | 33.3 ± 1.8 | 18.3 ± 2.0 |
| SSA22-SPIRE9 | 334.3848999033597 | 0.2912395866246295 | 57.5 ± 2.1 | 49.6 ± 1.7 | 45.7 ± 2.2 |
| SSA22-SPIRE10 | 334.58002216598203 | 0.35006798763473185 | 64.3 ± 2.3 | 51.3 ± 2.0 | 30.6 ± 2.3 |

# Chapter 4

# Herschel Results

## 4.1 Overdensities of DSFGs in the Protoclusters

We searched for overdensities of DSFGs by using an aperture with a radius of 6 comoving Mpc. This comoving scale corresponds to $3.8'$, $3.7'$, and $3.2'$ radius for $z = 2.2, 2.3$, and 3.1. The corresponding proper scale is $\sim 1.5-2$ Mpc radius for each protocluster redshift, matching the size of the searches for DSFGs overdensities around radio galaxies field (e.g., Rigby et al., 2014; Dannerbauer et al., 2014). We counted the number of color-selected bright SPIRE sources ($L_{\rm FIR} \geq 5.0 \times 10^{12}\ L_{\odot}$) within each 6 comoving radius aperture every $10''$ for the SPIRE maps of three protoclusters field and the COSMOS field.

In the 2QZCluster and HS1700 fields, we found $3.9\sigma$ and $5.0\sigma$ overdensities respectively. We did not find any significant ($> 3\sigma$) overdensities in the SSA22 field. We show the overdensities of the color-selected bright SPIRE sources in Figure 4.1. We measured $1\sigma$ standard deviation of numbers of color-selected bright SPIRE sources in the COSMOS field. We measured the significance level of overdensity by $\sigma_{\rm pc} = (n_{\rm pc} - n_{\rm ave})/\sigma_{\rm ave}$, where $n_{\rm pc}$ is the number of color-selected bright SPIRE sources in overdense region of the protocluster fields, $n_{\rm ave}$ is the average number within search apeartures for COSMOS field, and $\sigma_{\rm ave}$ is the standard deviation of $n_{\rm ave}$. In case for 10% and 30% flux error boundaries in Figure 3.2, we also searched for overdensities of color-selected bright SPIRE sources to make sure the results. First, we found that 10% boundary is not suitable because the number of color-selected bright SPIRE sources are too small to search for overdensities. Second, we found the results did not change for 20% and 30% boundaries. We found 30% boundary shows same overdensities of color-selected bright SPIRE sources compared with that of 20% boundary in the 2QZCluster field and the HS1700 field.

We plotted the density distribution of the color-selected bright SPIRE sources for the 2QZCluster field and the HS1700 field in Figure 4.2. We searched for overdensities of the color-selected bright SPIRE sources in the COSMOS field as same as the protocluster fields, and plotted the density distribution for COSMOS fields in Figure 4.2. Figure 4.2 shows the histograms of the distributions of the number of color-selected bright SPIRE sources within a 6 comoving Mpc aperture. We found that the fraction of the apertures which have no sources is about two times higher in the 2QZCluster field compared with the COSMOS field. This could be a void like structure while there is an overdensity in the 2QZCluster field. In contrast to the 2QZCluster

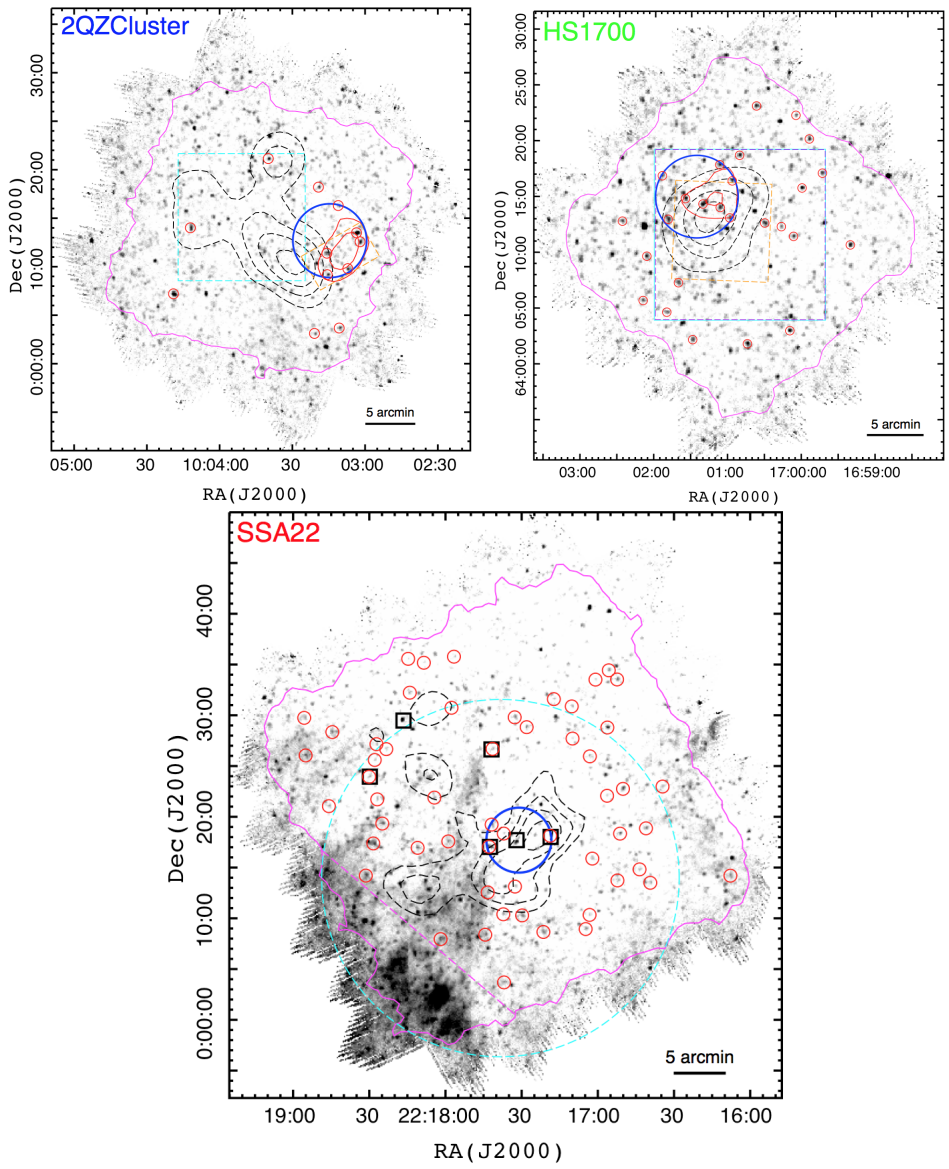


Figure 4.1: Sky distributions of color-selected bright 250 $\mu$m sources are shown as open red circles over the SPIRE 250 $\mu$m maps. The magenta contours correspond to the 30% depth coverage. The number density of 19 HAEs and 3 QSOs (Matsuda et al., 2011a) for the 2QZCluster, 45 LBGs for HS1700 (Rudie et al., 2012; Steidel et al., 2014), and 742 LAEs for SSA22 (Yamada et al., 2012) protoclusters are shown as dashed black contours, respectively. Their steps show 1–4$\sigma$ for 2QZCluster and HS1700, and 3–6$\sigma$ for SSA22 protocluster with smoothed Gaussian FWHM of 6 comoving Mpc. The number density of color-selected bright SPIRE sources in 2QZCluster and HS1700 are shown as red contours with 3–4$\sigma$, 4–5$\sigma$ steps with smoothed Gaussian FWHM of 6 comoving Mpc. The overdensity of color-selected bright 250 $\mu$m detected sources for 2QZCluster and HS1700, and color-selected bright 500 $\mu$m detected sources for SSA22 using filtering a radius of 6 comoving Mpc are shown as blue circles. We found a 4$\sigma$ and 5$\sigma$ overdensity of color-selected bright 250 $\mu$m detected sources in the 2QZCluster and HS1700 fields. We didn't find significant ($> 3\sigma$) overdensities of 250 $\mu$m detected sources in SSA22, but we found six color-selected bright 500 $\mu$m detected sources (black squares), and three sources are concentrated 3′ ($\sim$1.4 Mpc) east to the LAEs overdensity.

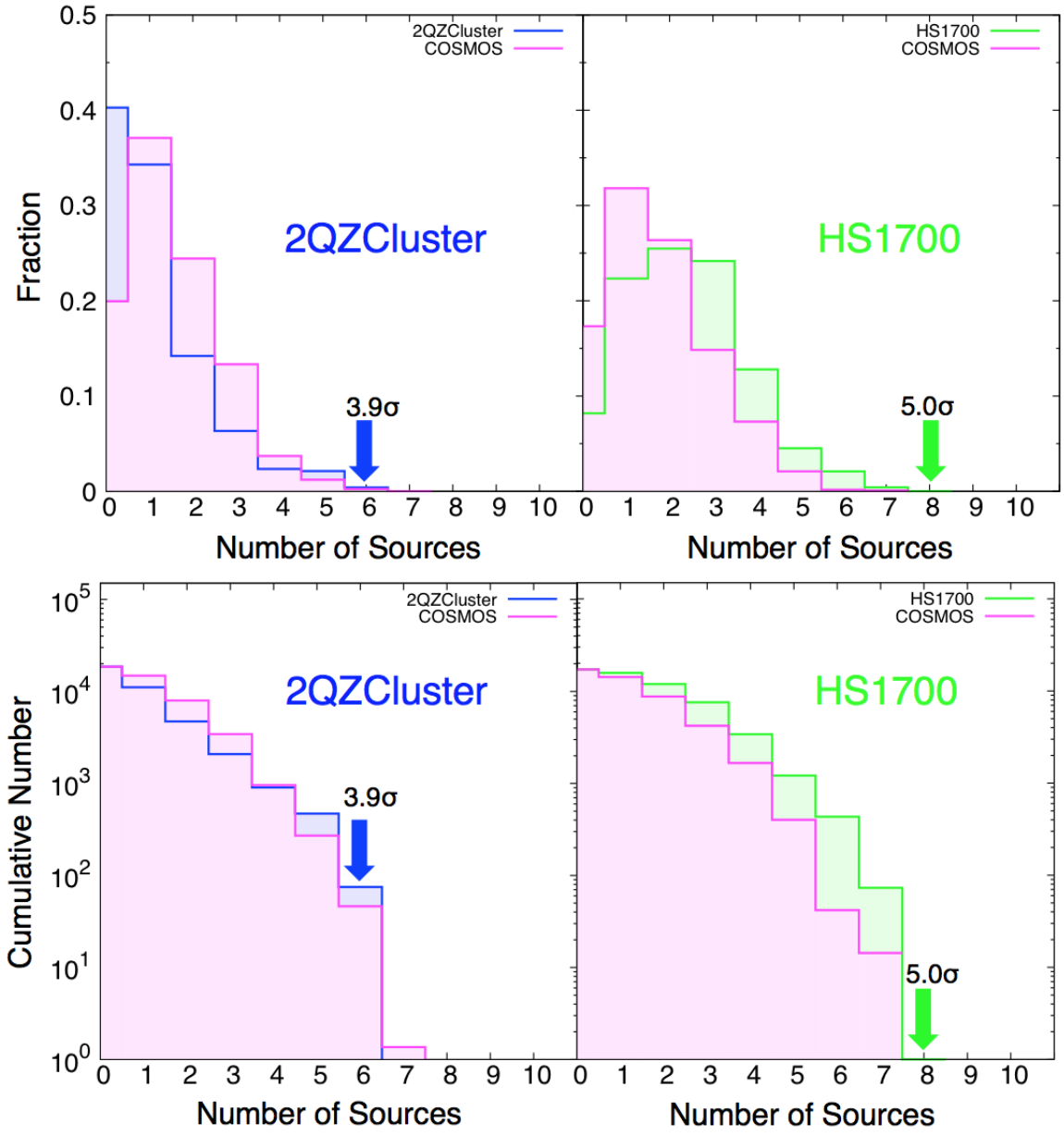


Figure 4.2: (*Upper*). The distributions of the number of the color-selected bright SPIRE sources in the 2QZ-Cluster field (left column) and the HS1700 field (right column) within an aperture radius of 6 comoving Mpc. We found that 2QZCluster tends to have lower density of color-selected bright SPIRE sources compared with COSMOS field. In contrast, HS1700 tends to have higher number of the color-selected bright SPIRE sources. (*Lower*). Cumulative numbers of the apertures with a radius of 6 comoving Mpc, which we normalized the cumulative numbers of the COSMOS field to the each protocluster.

field, the HS1700 field shows large number of color-selected bright SPIRE sources.

We also plotted the cumulative numbers in Figure 4.2. We normalized the cumulative numbers of the reference COSMOS field to the protoclusters. We found that the normalized cumulative numbers with $> 3.9\sigma$ overdensities in the 2QZCluster field is about two times higher than that of the COSMOS field. In the reference COSMOS field for the HS1700 field, there are no overdensities which contain eight color-selected bright SPIRE sources. These results suggest that such overdensities are preferentially located in the protoclusters.

## 4.2 Counterparts Identifications for the 2QZCluster field

In the 2QZCluster field, an overdensity of color-selected bright SPIRE sources were found $4.5'$ ($\sim$2.2 Mpc) west to the HAEs overdensity.

We searched for counterparts of SPIRE sources for HAEs and QSOs in 2QZCluster, although the SPIRE overdensity were not covered with UKIRT/WFCAM observation (see Figure 4.1). In total, 19 HAEs and 3 QSOs are within the 174 arcmin$^2$ overlap region (Matsuda et al., 2011a). We defined the following quality criteria, $p$-value, which is based on Downes et al. (1986) to assess the robustness of counterparts identification. The sources with $p \leq 0.05$ are classified as secure counterparts, and those with $0.05 < p \leq 0.10$ are classified as tentative counterparts. The $p$-value is defined by $p = 1 - \exp(-\pi \mathrm{n} \theta^2)$, where $n$ is a source density, and $\theta$ is an angular offset. The counterparts were searched within $11''$ radius from the position of the SPIRE 250 $\mu$m detections. This corresponds to $\sim$40% beam response in SPIRE 250 $\mu$m band.

One optically luminous QSOs, 2QZC-C1-HAE2 (Matsuda et al., 2011a), coincides with one of our color-selected bright SPIRE source 2QZCluster-SPIRE10 ($2.7''$ offset). The estimated $p$-value of 2QZC-C1-HAE2 is lower than 0.01, suggesting that this source is classified as a secure counterpart. The $p$-value means a probability of chance association of counterparts. Thus the probability of chance association of 2QZC-C1-HAE2 and 2QZCluster-SPIRE10 is less than 1%. 2QZ-C1-HAE3 also coincides with our SPIRE source 2QZCluster-SPIRE124 ($5.6''$ offset) as a secure counterpart. Such optically luminous FIR bright QSOs are thought to be in a transient phase between DSFGs and QSOs (Simpson et al., 2012). No other HAEs counter parts for the color-selected bright SPIRE sources were found in the 2QZCluster field. We then repeated this process using all 250 $\mu$m catalogued sources which is at least one SPIRE band has above 12 mJy. We found five secure HAEs counterparts for catalogued 250 $\mu$m sources (see Table 4.1).

We conducted Subaru/MOIRCS follow-up observations of NB H$\alpha$ imaging to search for new HAEs in the SPIRE overdense region ($4' \times 7'$; dashed orange box in Figure 4.1) on May 5, 2015. The total exposure times of $K_\mathrm{s}$ and NB data are 1.5 and 2.4 kilo seconds, respectively. The $5\sigma$ detection limit is almost the same as the previous HAE search depth, NB $< 19.8$ (Vega) compared to NB $< 19.9$ in Vega in Matsuda et al. (2011a).

We found no new HAEs within the SPIRE overdense region. This might suggest that the region is actually a little under-dense in terms of bright HAEs. From Matsuda et al. (2011a), we estimate an HAEs average field count of 0.09 per arcmin$^2$. This means we can expect that we find 2–3 HAEs in this observation, although such void like structures adjacent to protocluster have been reported (e,g., Koyama et al., 2013; Saito et al., 2015).

Table 4.1: SPIRE sources which have HAEs counterparts in 2QZCluster.

| ID (SPIRE) | R.A. (J2000) | Dec (J2000) | $S_{250}$ (mJy) | $S_{350}$ (mJy) | $S_{500}$ (mJy) | Counterpart | R.A. (J2000) | Dec (J2000) | Sepa.[a] (arcsec) | $p$-value[b] | Member[c] |
|---|---|---|---|---|---|---|---|---|---|---|---|
| color-selected bright SPIRE sources | | | | | | | | | | | |
| 2QZCluster-SPIRE10 | 150.916320 | 0.352456 | 60.1 ± 2.1 | 64.7 ± 1.8 | 45.6 ± 2.0 | QZC-C1-HAE02(QSO) | 150.915790 | 0.353000 | 2.73 | <0.01 | Secure |
| at least one SPIRE band above 12 mJy sources | | | | | | | | | | | |
| 2QZCluster-SPIRE124 | 150.965998 | 0.249463 | 21.9 ± 2.2 | 14.2 ± 1.8 | 9.7 ± 2.2 | QZC-C1-HAE03(QSO) | 150.964920 | 0.250583 | 5.60 | <0.01 | Secure |
| 2QZCluster-SPIRE239 | 151.069470 | 0.310488 | 15.4 ± 2.2 | 4.1 ± 1.8 | 6.9 ± 2.3 | QZC-C1-HAE20 | 151.069750 | 0.309167 | 4.86 | <0.01 | Secure |
| 2QZCluster-SPIRE251 | 150.885551 | 0.168325 | 15.5 ± 2.2 | 6.8 ± 2.0 | 3.7 ± 2.3 | QZC-C1-HAE09 | 150.887370 | 0.167917 | 6.71 | <0.01 | Secure |
| 2QZCluster-SPIRE261 | 150.852526 | 0.155903 | 15.8 ± 2.3 | 13.8 ± 1.8 | 12.1 ± 2.2 | QZC-C1-HAE05 | 150.854380 | 0.155694 | 6.72 | <0.01 | Secure |
| 2QZCluster-SPIRE353 | 150.916183 | 0.187292 | 14.4 ± 2.7 | 12.1 ± 1.8 | 3.0 ± 2.1 | QZC-C1-HAE16 | 150.915750 | 0.187722 | 2.20 | <0.01 | Secure |
| 2QZCluster-SPIRE372 | 150.935267 | 0.238716 | 10.2 ± 2.2 | 16.2 ± 1.8 | 14.0 ± 2.1 | QZC-C1-HAE15 | 150.932670 | 0.238944 | 9.39 | 0.01 | Secure |

**Notes.** ($a$): Separation between SPIRE sources and counterparts. ($b$): The $p$-values Downes et al. (1986). ($c$): We classified sources with $p \leq 0.05$ as secure counterparts, and those with $0.05 < p \leq 0.10$ as tentative counterparts.

## 4.3 Counterparts Identifications for the HS1700 field

In the HS1700 field, an overdensity of color-selected bright SPIRE sources were found 2.1′ (∼1.0 Mpc) north to the LBGs overdensity.

We searched for the counterparts of SPIRE sources using UV-selected (BX/BM) star-forming galaxies (LBGs), HAEs, LAEs, and DRGs in the SPIRE overdense region. There are 3010 LBGs within 256 arcmin$^2$ from KBSS (Keck Baryonic Structure Survey; Rudie et al., 2012; Steidel et al., 2014), 123 LAEs are within 219 arcmin$^2$ from Milan Bogosavljević 's Ph.D thesis (Bogosavljević, 2010), 83 HAEs and 75 DRGs are within 72 arcmin$^2$. Detailed properties of LBGs and LAEs are described in Shapley et al. (2005), Erb, Bogosavljević, & Steidel (2011), Kulas et al. (2013), and Erb et al. (2014). We used Palomar/WIRC Br$\gamma$ filter (center wavelength 2.17 $\mu$m, FWHM=297 Å) for the H$\alpha$ narrow band (NB) imaging. We used narrow band selection criteria of NB $< 20.5$ (Vega) and NB $-K_s \leq -0.75$. We have selected DRGs with $J - K > 2.3$ to a limit of $K_s = 21$ (Vega). We defined the quality criteria of $p$-value as described in the previous section, and classified sources. We calculated the number density of spectroscopically confirmed 45 protocluster member LBGs in the redshift spike of $z = 2.285 - 2.315$ separately from remaining 2965 LBGs outside of redshift spike. We searched for counterparts of SPIRE sources counterparts within 11″ radius from the position of the SPIRE 250 $\mu$m detection.

Three color-selected bright SPIRE sources within SPIRE overdensities have been found that they were secure counterparts (see Table 4.2). However, we found that one of the LAEs "BNB1" indicates an extremely odd spectrum. We identified it as a " Lo-BAL " QSO and it is more likely to have $z \sim 2.00$. We do not treat as it is a protocluster member galaxy.

One LAE and LBG are secure, and one DRG and LAE were found that they were tentative counterparts of color-selected faint (i.e., $L_{\rm FIR} < 5.0 \times 10^{12}\ L_{\odot}$) SPIRE source. We found two secure LAEs, three secure HAEs, and one tentative HAE were counterparts of the catalogued SPIRE sources (at least one SPIRE band flux density above 12 mJy). Totally, we found that seven SPIRE sources in the SPIRE overdensity have secure counterparts of protocluster member galaxies (see Table 4.2).

We compared the results of counterparts identifications for color-selected bright/faint SPIRE sources with

Table 4.2: SPIRE sources which have emitter counterparts within overdensity in HS1700.

| ID (SPIRE) | R.A. (J2000) | Dec (J2000) | $S_{250}$ (mJy) | $S_{350}$ (mJy) | $S_{500}$ (mJy) | ID (Count.) | R.A. (J2000) | Dec (J2000) | $z^a$ | Sepa.$^b$ (arcsec) | $p$-value$^c$ | Member$^d$ |
|---|---|---|---|---|---|---|---|---|---|---|---|---|
| color-selected bright SPIRE sources | | | | | | | | | | | | |
| HS1700-SPIRE21 | 255.3951 | 64.2484 | $52.5 \pm 2.2$ | $41.2 \pm 1.7$ | $21.1 \pm 2.2$ | BNB1 | 255.3953 | 64.2479 | $\sim 2.00^e$ | 1.63 | $< 0.01$ | Secure |
| | | | | | | BX980 | 255.3987 | 64.2490 | - | 6.13 | 0.32 | Not |
| HS1700-SPIRE42 | 255.2428 | 64.2196 | $40.0 \pm 2.3$ | $46.4 \pm 1.8$ | $34.3 \pm 2.1$ | DRG46 | 255.2419 | 64.2195 | - | 1.37 | $< 0.01$ | Secure |
| | | | | | | HaNB2 | 255.2417 | 64.2196 | - | 1.75 | $< 0.01$ | Secure |
| HS1700-SPIRE24 | 255.3349 | 64.2403 | $51.5 \pm 2.3$ | $63.0 \pm 2.0$ | $49.3 \pm 2.2$ | DRG53 | 255.3378 | 64.2395 | $\sim 2.3^f$ | 5.36 | 0.03 | Secure |
| | | | | | | HaNB10* | 255.3399 | 64.2384 | 2.289(abs) | 10.43 | 0.10 | Tentative |
| | | | | | | BX913* | 255.3399 | 64.2385 | 2.289(abs), 2.291(neb) | 10.29 | 0.05 | Tentative |
| | | | | | | BX928 | 255.3318 | 64.2405 | 2.755(Ly$\alpha$) | 4.92 | 0.22 | Not |
| color-selected faint SPIRE sources | | | | | | | | | | | | |
| HS1700-SPIRE321 | 255.2732 | 64.2046 | $13.7 \pm 2.4$ | $20.2 \pm 1.8$ | $15.9 \pm 2.1$ | BNB41* | 255.2688 | 64.2027 | 2.287(abs) | 9.64 | 0.05 | Secure |
| | | | | | | MD109* | 255.2687 | 64.2026 | 2.293(abs,neb) | 10.09 | 0.02 | Secure |
| | | | | | | DRG38$^+$ | 255.2669 | 64.2032 | 2.286(emi) | 10.98 | 0.10 | Tentative |
| | | | | | | BNB16$^+$ | 255.2670 | 64.2033 | 2.290(emi) | 10.53 | 0.05 | Tentative |
| at least one SPIRE band above 12 mJy sources | | | | | | | | | | | | |
| HS1700-SPIRE70 | 255.2827 | 64.2586 | $31.1 \pm 2.2$ | $21.4 \pm 1.9$ | $11.0 \pm 2.0$ | BNB155 | 255.2811 | 64.2574 | 2.290(Ly$\alpha$) | 5.13 | 0.01 | Secure |
| | | | | | | HaNB27 | 255.2873 | 64.2578 | - | 7.81 | 0.06 | Tentative |
| HS1700-SPIRE78 | 255.4358 | 64.2607 | $30.3 \pm 2.2$ | $16.9 \pm 1.7$ | $6.0 \pm 2.1$ | BNB139 | 255.4331 | 64.2622 | - | 6.85 | 0.02 | Secure |
| HS1700-SPIRE142 | 255.2668 | 64.2469 | $22.7 \pm 2.2$ | $12.0 \pm 1.8$ | $1.8 \pm 2.2$ | HaNB83 | 255.2653 | 64.2487 | - | 6.67 | 0.04 | Secure |
| | | | | | | HaNB76 | 255.2661 | 64.2461 | - | 3.06 | 0.01 | Secure |
| HS1700-SPIRE179 | 255.3768 | 64.1988 | $19.8 \pm 2.2$ | $9.4 \pm 1.8$ | $0.5 \pm 2.2$ | HaNB45 | 255.3796 | 64.1996 | - | 5.41 | 0.03 | Secure |

**Notes.** ($a$): Redshift of counterparts. ($b$): Separation between SPIRE sources and counterparts. ($c$): Estimated $p$-value (Downes et al., 1986). ($d$): We classified sources with $p \leq 0.05$ as secure counterparts, and those with $0.05 < p \leq 0.10$ as tentative counterparts. ($e$): BNB1 is identified as a " Lo-BAL " QSO. ($f$): Photometric redshift is given in Chapman et al. (2015).

the catalogued SPIRE sources (i.e., not color-selected, but at least one SPIRE band flux density is above 12 mJy) lying within SPIRE overdensity in order to assess the success rate of the SPIRE color selection. We assumed that all spectroscopically not confirmed HAEs and LAEs are also associated with the protocluster except for BNB1. However, we should note that the HAEs without spectroscopic follow-up are much less likely than spectroscopic confirmed HAEs to be at the protocluster redshift because of its sensitivity. We found that the success rates for the secure counterparts within SPIRE overdensities are 2/7(29%) for color-selected bright SPIRE sources, 1/5(20%) for color-selected faint SPIRE sources, and 4/28(14%) for catalogued SPIRE sources, respectively. This comparison suggests that SPIRE color selection can select possible protocluster members with two times higher probability compared to catalogued SPIRE sources.

There are several foreground galaxy groups in the HS1700 field. A $z = 0.453$ group is very close to the position of HS1700-SPIRE24. Peter et al. (2007) found that BX913 is lensed by the group. We estimated a magnification factor by using GLAFIC (Oguri, 2010). We used a halo mass of $M/h = 1 \times 10^{14}\ M_\odot$ (Israel et al., 2014) and a concentration parameter of c=6 (Bhattacharya et al., 2013). We found that the second nearest SPIRE source at $1.5'$ away from group center was affected $\sim$5% magnification, and the HS1700-SPIRE24 flux could be affected by lensing.

## 4.4 Counterparts Searches for the SSA22 field

We found that the maximum number of color-selected bright SPIRE sources within 6 comoving Mpc aperture was five. This corresponds to a $1.6\sigma$ overdensity, suggesting that SSA22 doesn't have significant overdensities of 250 $\mu$m detected color-selected bright SPIRE sources. However, because DSFGs at higher redshift would start to drop out at 250 $\mu$m, this could be a problem for SSA22 at $z = 3.1$. Thus we searched for an overdensity of color-selected bright 500 $\mu$m detected SPIRE sources with the same color selection and the same luminosity cut in §3.2. We found that six 500 $\mu$m detected color-selected bright SPIRE sources in the SSA22 field, and three sources were concentrated $3'$ ($\sim$1.4 Mpc) east to the LAEs overdensity (Figure 4.1). We also searched for an overdensity of 350 $\mu$m detected color-selected bright sources, and did not find significant overdensities as same as 250 $\mu$m detected sources.

We searched for AzTEC 1.1 mm counterparts in Umehata et al. (2014, 2015) for the five 500 $\mu$m detected color-selected bright SPIRE sources within $\sim$800 arcmin$^2$ overlapped region (Figure 4.1). We used a search radius of $14''$ (half of AzTEC 1.1 mm FWHM). We found that 4/5 sources have been matched (SSA22-AzTEC1, 2, 5, and 34). Thus 80% 500 $\mu$m detected color-selected bright SPIRE sources are matched with AzTEC 1.1 mm sources.

## 4.5 Star Formation Rate Density of the Protoclusters

We searched for dusty star-forming galaxies (DSFGs) possibly associated with the three protoclusters at $z = 2-3$ (2QZCluster, HS1700, SSA22) with *Herschel*/SPIRE observation. We found $4\sigma$ and $5\sigma$ overdensities of the color-selected bright SPIRE sources on a scale of 6 comoving Mpc radius in the 2QZCluster filed and HS1700 field. We did not find any significant overdensities of 250 $\mu$m detected color-selected bright SPIRE sources, but we found that three 500 $\mu$m detected color-selected bright SPIRE sources were concentrated on a scale of 6 comoving Mpc radius in the SSA22 field. These results suggest simultaneous dusty star-formation is possibly occurred in three protoclusters at $z \sim 2-3$.

We integrated star-formation rate (SFR) of DSFGs in the 2QZCluster, HS1700 and SSA22 within SPIRE overdensities. The SFR of DSFGs is converted from far-infrared luminosity ($L_{\rm FIR}$), although the conversion from $L_{\rm FIR}$ to SFR is not straightforward and relies on the dust composition and initial mass function (IMF). Most works on DSFGs assume the conversion given by (Kennicutt, 1998),

$$\mathrm{SFR}\ (\mathrm{M/yr^{-1}}) = 4.5\times\ 10^{44}\ L_{\rm FIR}\ (\mathrm{erg\ s^{-1}}) = 1.7\times\ 10^{10}\ L_{\rm FIR}\ (L_\odot) \tag{4.1}$$

where $L_{\rm FIR}$ is the integrated luminosity of $8-1000$ $\mu$m. This conversion takes the radiative transfer models of Leitherer & Heckman (1995) and a Salpeter IMF (Salpeter, 1955).

By assuming all of the color-selected bright SPIRE sources in the SPIRE overdensities are associated with the protoclusters, we estimated the integrated SFR densities. We included SPIRE sources within a radius of 1 Mpc (proper scale) following Clements et al. (2014) analysis of *Planck* clumps with *Herschel*/SPIRE observation. We adjusted the position of the smaller 1 Mpc aperture to contain as many color-selected bright SPIRE sources as possible within search radius of 6 comoving Mpc ($\sim 1.5-2$ Mpc in proper scale). The $1\sigma$ instrumental noise of Clements's work is similar to our survey, which range from $2.5-2.8$ mJy at 250 $\mu$m,

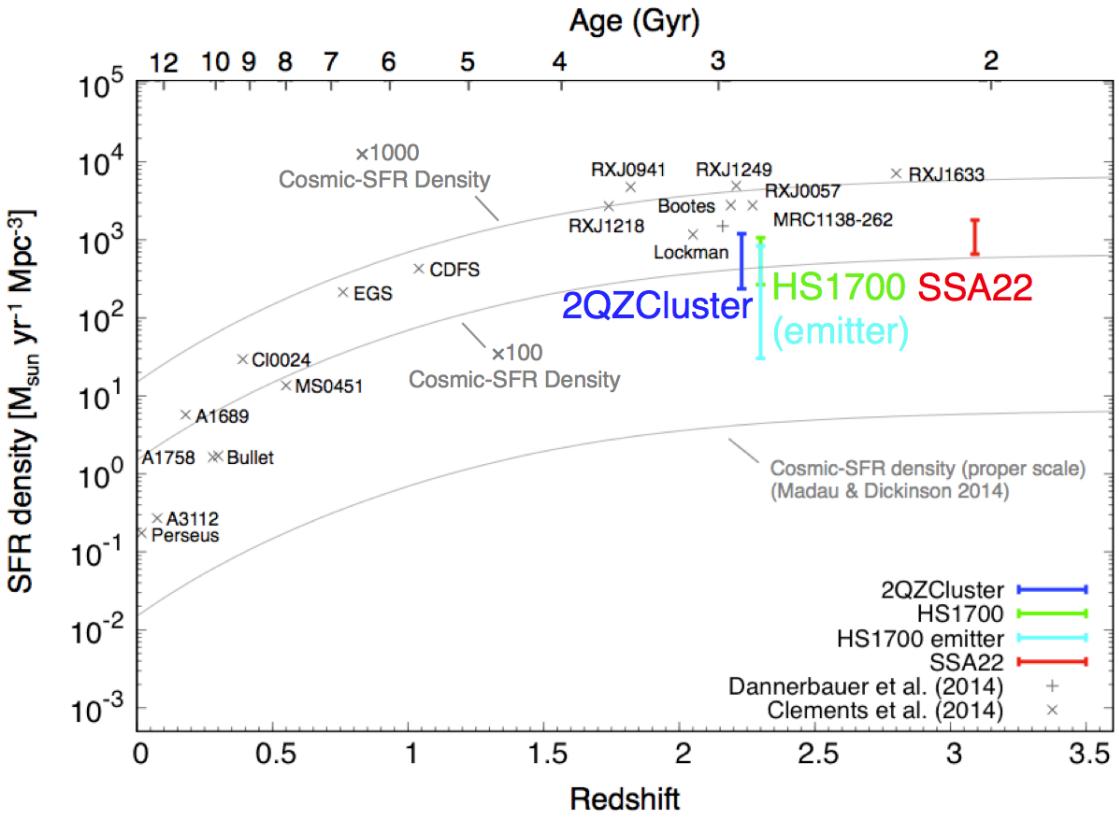


Figure 4.3: The SFR density of clusters and protoclusters. If all of the SPIRE sources are associated with each protocluster, the inferred SFR densities of our protoclusters are possibly 100–1000 times higher than the global SFR density (Madau & Dickinson, 2014). At that moment, we show the SFR density of the SSA22 protocluster, which is at the highest redshift. We also show the SFR density of SPIRE sources, which have LAEs, HAEs, and LBGs secure counterparts for the HS1700 protocluster. We show the compilation from Dannerbauer et al. (2014) and data from Clements et al. (2014), which original literature are following; *IRAS* measurements of Perseus from Meusinger, Brunzendorf, & Krieg (2000), BLAST measurements of A3112 from Braglia et al. (2011), *ISO* measurements of A1689 from Fadda et al. (2000), and *Spitzer* measurements of A1758 from Haines et al. (2009), Bullet cluster from Chung et al. (2010), Cl0024+16 and MS0451-03 from Geach et al. (2006). RXJ0057, RXJ0941, RXJ1218, RXJ1249 and RXJ1633 are based on JCMT/SCUBA from Stevens et al. (2010).

Table 4.3: Estimated SFR and assumed volume for Figure 4.3.

| Field | $z$ | SFR$^a$ ($M_\odot$ yr$^{-1}$) | $r^b$ (Mpc) | $V^c$ (Mpc$^3$) | SFR$_{\rm min}{}^d$ ($M_\odot$ yr$^{-1}$) |
|---|---|---|---|---|---|
| All sources | | | | | |
| 2QZCluster | $2.230 \pm 0.016$ | 5000 | 1.0 | 4.2 | 150 |
| HS1700 | $2.300 \pm 0.015$ | 4500 | 1.0 | 4.2 | 280 |
| (emitter) | $2.300 \pm 0.015$ | 3500 | 1.0 | 4.2 | 320 |
| SSA22 | $3.09 \pm 0.03$ | 7500 | 1.0 | 4.2 | 310 |
| Field corrected values | | | | | |
| 2QZCluster | $2.230 \pm 0.016$ | 1000 | 1.0 | 4.2 | - |
| HS1700 | $2.300 \pm 0.015$ | 1100 | 1.0 | 4.2 | - |
| SSA22 | $3.09 \pm 0.03$ | 2800 | 1.0 | 4.2 | - |

**Notes.** $(a)$: Integrated SFR derived from SPIRE sources. $(b) - (c)$: Used radius and volume to calculate SFR density. $(d)$: Minimum SFR of SPIRE source which is included in integrated SFR.

$2.1 - 2.3$ mJy at 350 $\mu$m, and $3.0 - 3.3$ mJy at 500 $\mu$m, respectively (Clements et al., 2014). We fitted single temperature, optically thin modified black body radiation with fixed $T_d = 35$ K, $\beta = 1.5$, and the protocluster's redshifts to derive $L_{\rm FIR}$ for all SPIRE sources with S/N $> 2$ in all three SPIRE bands within a 1 Mpc radius. We found that *Spitzer*/Mips 24 $\mu$m flux densities of color-selected bright SPIRE sources in HS1700 are consistent with that of typical high-$z$ star-forming galaxies except for one color-selected bright SPIRE source HS1700-SPIRE30. We excluded this source from this discussion because it is very close to $z = 0.08$ SDSS galaxy, and its *Spitzer*/MIPS 24 $\mu$m flux density is very high ($\sim 200$ $\mu$Jy). 2QZCluster does not have any *Spitzer* images.

Figure 4.3 shows results of estimations of integrated SFR of DSFGs in SPIRE overdensities. Following Clements et al. (2014) analysis, we estimated SFR with Bell (2003)'s $L_{\rm FIR}$ correction. If all of the SPIRE sources are associated with each protocluster, the derived SFR densities are possibly 100–1000 times higher than the global SFR density seen in Madau & Dickinson (2014). The enhancement of dusty star-formation activity in our three protoclusters is consistent with Clements et al. (2014). Dannerbauer et al. (2014) also presents results based on APEX/LABOCA 870 $\mu$m observations around MRC1138−262 at $z = 2.16$. They found that at least six DSFGs are likely part of the protocluster, and the SFR density reaches $\sim$ 1500 $M_\odot$ yr$^{-1}$ Mpc$^{-3}$. This is similar to Clements et al. (2014) and our protoclusters study. The error bars in Figure 4.3 shows the case for including all sources in 1 Mpc radius (upper limit) and the case for subtracting field average values (lower limit). We estimated field values by calculating average number of sources and average luminosity in 1 Mpc radius apertures in the COSMOS field.

We summarized the estimated SFR and assumed volume in Table 4.3. We also calculated SFR density in an aperture using a radius of 6 comoving Mpc in the same manner to make sure the results. These radii are 1.9, 1.8 and 1.5 Mpc in proper scale units for 2QZCluster, HS1700 and SSA22, respectively. We found that the results didn't change and the same for the case for using radius of 1 Mpc.

## 4.6 Discussions of Concentration of DSFGs in the Protoclusters

Why simultaneously, intensive dusty star-formations are occurred in protoclusters? One possible explanation to this is frequent galaxy-galaxy mergers. For instance, by using *HST* H-band imaging data, the fraction of irregular and interacting galaxies among the LBGs and DSFGs in a protocluster at $z = 2.5$ is 2.4 times higher than in the field (Casey et al., 2015). Dusty, bursting star-formation at the center of a $z = 1.7$ cluster is being driven by galaxy-galaxy interaction, involving a far-infrared luminous Bright Cluster Galaxy (Webb et al., 2015). Progenitors of galaxy groups and cluster halos at $z > 2$ have $3 - 5\times$ higher major merger rates than isolated halos in N-body simulation (Gottlöber, Klypin, & Kravtsov, 2001). The facts that the color-selected bright SPIRE sources are significantly concentrated in three protoclusters would support such major galaxy-galaxy merging phenomenon. To investigate this, we need spatially and spectroscopically resolved observations for DSFGs in protoclusters.

Alternatively, duration of dusty star-formation would be much longer than prior measurements suggest in protoclusters. For instance, if the inflowing gas stream continuously feeds to DSFGs, it appears to fuel the dusty star-formation phase much longer time. The inflowing gas along the large scale structure could play a very important role at $z = 2 - 3$ as the peak epoch of cosmic SFR density. From cosmological simulation, it is suggested that the peak epoch of gas accretion is at $z = 3$, and their amount is about five times higher than the mergers (Kereš et al., 2005; Dekel et al., 2009). In addition, the galaxy volume density of DSFGs is consistent with their simulated galaxies which have 100-1000 $M_\odot$ $yr^{-1}$ gas accretion rate (Dekel et al., 2009). From cosmological hydrodynamic zoom galaxy formation simulations, Narayanan et al. (2015) suggests that DSFGs in the massive dark matter halo can be kept for a long time ($\sim$1 Gyr) by their own stellar feedback and gas recycling. To investigate these, we need to measure molecular gas mass and molecular gas depletion time, and search for the extended gaseous structure such outflows and/or inflows of DSFGs in protoclusters.

## 4.7 Herschel Observations Summary

Protocluster is a few tens of Mpc galaxy overdensity seen in the $z > 2$ Universe, which is thought to be a progenitor of local galaxy clusters. Although protoclusters are expected to be observed many DSFGs, the lack of far-infrared observation prevent us to search for their precursors, massive dusty star-forming galaxies (DSFGs).

We conducted *Herschel*/SPIRE surveys to search for DSFGs in three protoclusters, 2QZCluster ($z = 2.2$), HS1700 ($z = 2.3$) and SSA22 ($z = 3.1$). We targeted these protoclusters as following criteria, (1). few tens of proper Mpc filamentary, large scale structures with galaxy overdensities, (2). an enhancement of AGNs fraction, and (3). existences of Ly$\alpha$ blobs (LABs) or H$\alpha$ blobs (HABs). Based on the SPIRE colors of $S_{350}/S_{250}$ vs. $S_{500}/S_{350}$, we selected DSFGs potentially associated with the protoclusters. Main conclusions are as follows:

- By using 6 comoving Mpc radius aperture, we found a $4\sigma$ overdensity of six SPIRE sources around $4.5'$ ($\sim$ 2 proper Mpc) east to a density peak of HAEs at $z = 2.2$ in the 2QZCluster field. In the HS1700 field, we found a $5\sigma$ overdensity of eight SPIRE sources $2.1'$ ($\sim$ 1 proper Mpc) north to a density

peak of LBGs at $z = 2.3$. We found three 500 $\mu$m detected color selected bright SPIRE sources are concentrated $3'$ ($\sim$1.5 proper Mpc) east to a density peak of LAEs at $z = 3.1$ in the SSA22 field.

- If all of the SPIRE sources in these three overdensities are associated with protoclusters, the inferred star-formation rate densities are possibly 100-1000 times higher than the average value at the same redshifts. This suggests that simultaneously, intensive bursting dusty star-formation could be occurred in the $z \sim 2-3$ protoclusters. We see the intensively formation scene of local elliptical galaxies through bursting dusty star-formation of massive DSFGs in the protoclusters.

- Simultaneously galaxy-galaxy mergers or much longer molecular gas depletion times are possible explanations to this. The key observational challenge is to investigate the morphology (i.e., to see whether DSFGs show signatures of galaxy-galaxy merger or not), measure molecular gas mass and molecular gas depletion time, and search for the extended gaseous structure such outflow and/or inflow for DSFGs in protoclusters.

To investigate these, we conducted ALMA observation for one of spectroscopically confirmed *Herschel*/SPIRE source SSA22-SPIRE394, which corresponds to SSA22-LAB18 (hereafter; LAB18) at $z = 3.1$ SSA22 protocluster (following section §5). LAB18 is previously known about the highest FIR, Millimeter/Sub-millimeter wavelengths flux densities (e.g., Chapman et al., 2001, 2004; Geach et al., 2005, 2014; Tamura et al., 2013; Hine et al., 2016b; Ao et al., 2018) and its morphology of the highest filamentarity of Ly$\alpha$ emission (Matsuda et al., 2011b) in the SSA22 protocluster. In Figure 4.4, we show *Herschel*/SPIRE image of LAB18 and its location in the SPIRE color-color diagram (see also Figure 3.2).

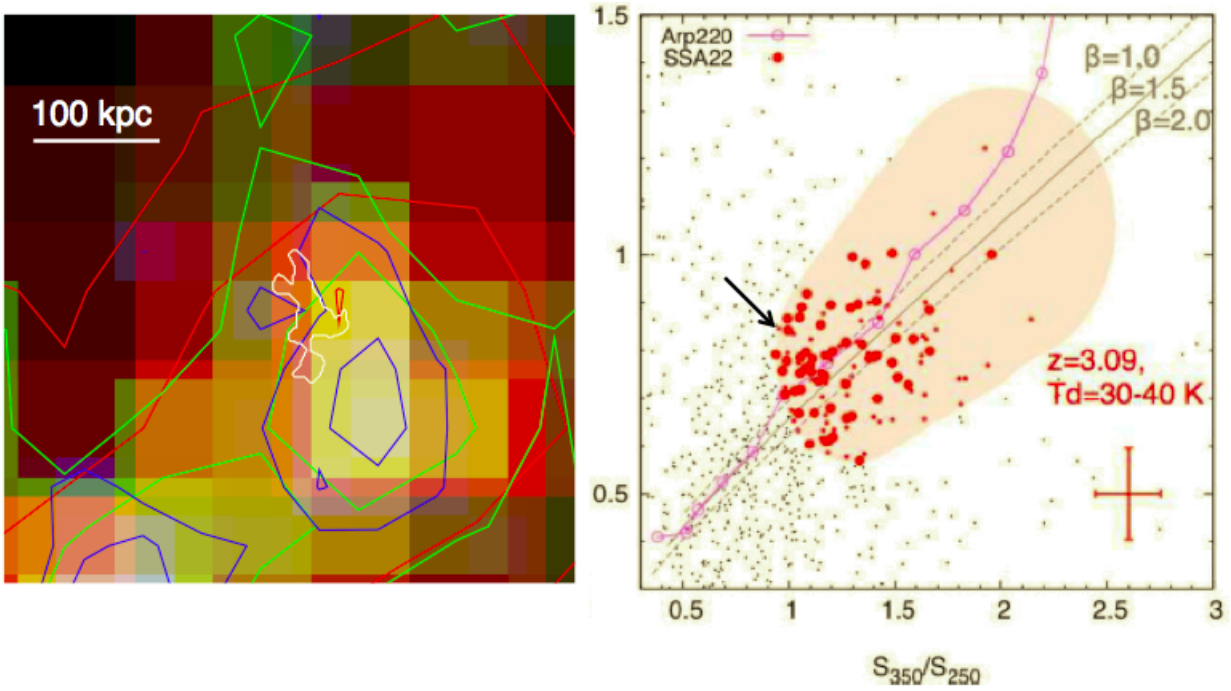


Figure 4.4: One of spectroscopically confirmed *Herschel*/SPIRE source SSA22-SPIRE394 (LAB18) and its location in the SPIRE color-color diagram. (left): SSA22-SPIRE394 is one of spectroscopically confirmed source, LAB18. The flux densities are 250 $\mu$m = 18.1 $\pm$ 2.3 mJy, 350 $\mu$m = 18.0 $\pm$ 1.8 mJy, 500 $\mu$m = 15.5 $\pm$ 2.2 mJy respectively. The white contour indicates isophotal apertures with a threshold of Ly$\alpha$ emission of $1.4 \times 10^{-18}$ erg s$^{-1}$ cm$^{-2}$ arcsec$^{-2}$, which shows the filamentary structure of Ly$\alpha$ emissions of the LAB18 in the $z = 3.1$ SSA22 protocluster (Matsuda et al., 2011b). Blue, green, and red color show *Herschel*/SPIRE 250, 350, and 500 $\mu$m emissions, respectively. The contour is 1, 2, 3$\sigma$ level from the confusion noise (see also §3). LAB18 is know to the highest FIR and sub-mm flux densities (e.g., Chapman et al., 2001, 2004; Geach et al., 2005, 2014; Tamura et al., 2013; Hine et al., 2016b; Ao et al., 2018). (right): The location of SSA22-SPIRE394 in the SPIRE color-color diagram as pointed as a black allow. We successfully selected LAB18 at $z = 3.1$ as SSA22-SPIRE394 by SPIRE color-color diagram.

# Chapter 5

# ALMA Observations for LAB18

## 5.1 Ly$\alpha$ Blobs

Ly$\alpha$ Blobs (LABs) are $\sim$10-100 kpc scale Ly$\alpha$ emitting gas nebula primarily found at high-$z$ protoclusters (e.g., Steidel et al., 2000; Matsuda et al., 2004; Dey et al., 2005; Matsuda et al., 2011b; Barger, Cowie, & Wold, 2012). Figure 5.1 shows examples of LABs found in SSA22 protocluster at $z = 3.1$ and Figure 5.2 shows sky distribution of LABs in the SSA22 protocluster at $z = 3.1$.

At least three possible mechanisms are proposed for the origins of LABs; photoionization, galactic superwind, and inflowing gas along the large scale structure. In the photoionization model, the origin of LABs is attributed to central bursting dusty star-formation and small satellite galaxies in the sub halo structure within LABs (Geach et al., 2016). Geach et al. (2016) used a high resolution cosmological zoom simulation of a $10^{13}$ $M_{\odot}$ halo at $z = 3$ including a stellar, dust and Ly$\alpha$ radiative transfer. They successfully model the observations, which Ly$\alpha$ photons escaping from the central bursting dusty star-formation are expected to resonantly scatter in neutral hydrogen. In the galactic superwind model, the origin of LABs is attributed to bursting star-formation induced by such galaxy-galaxy mergers/interactions (e.g., Taniguchi & Shioya, 2000; Mori & Umemura, 2006), which also often hosts optical luminous continuum sources (e.g., Uchimoto et al., 2012; Yajima, Umemura, & Mori, 2012; Kubo et al., 2015). In the inflow gas model, accretion of large amount of cold hydrogen gas ($\lesssim 10^4$ K) is expected from large scale structures (Kereš et al., 2005; Dekel et al., 2009). Figure 5.3 illustrates above three models.

It was shown that some fraction of LABs in SSA22 are bright in submillimeter/millimeter (submm/mm) wavelengths by using various single-dish telescopes in the past decades (Chapman et al., 2001, 2004; Geach et al., 2005; Beelen et al., 2008; Tamura et al., 2013; Geach et al., 2014; Hine et al., 2016b; Ao et al., 2018), suggesting that LABs are the formation site of DSFGs. However, the lack of sufficient spatially and spectroscopic information prevent us to discuss relation between DSFGs and LABs.

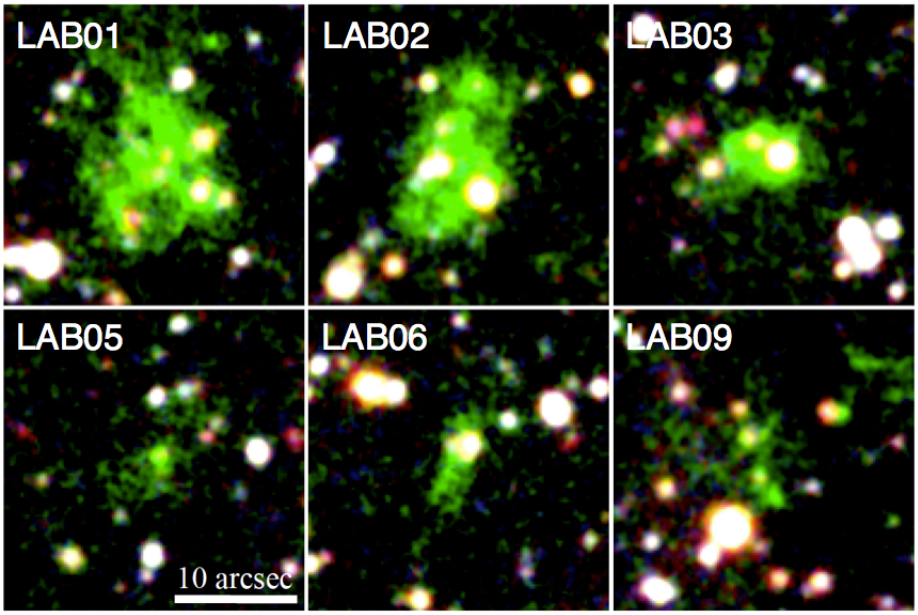


Figure 5.1: Examples of LABs in the $z = 3.09$ SSA22 protocluster (Matsuda et al., 2004). We show Subaru/Suprime-cam $B, NB497, V$-band images as blue, green, and red, respectively. The each panel is $25'' \times 25''$ ($\sim$200 $\times$ 200 kpc$^2$).

## 5.2 SSA22-LAB18

SSA22-LAB18 (hereafter, LAB18) was identified from a narrowband imaging survey at $z = 3.1$ (Steidel et al., 2000; Matsuda et al., 2004). LAB18 has Ly$\alpha$ luminosity of $(0.8 \pm 0.2) \times 10^{43}$ erg s$^{-1}$ and physical sizes of $100 \times 30$ kpc (Hayashino et al., 2004; Matsuda et al., 2004). In Matsuda et al. (2011b), the Ly$\alpha$ spectroscopic redshift is $z_{\mathrm{Ly}\alpha} = 3.104$. This LAB is known to be the filamentary structure of the Ly$\alpha$ emission within Matsuda et al. (2011b) samples and sub-millimeter detections with Submillimeter Common User Bolometer Array (SCUBA) on the James Clerk Maxwell Telescope (JCMT) (Chapman et al., 2001, 2004; Geach et al., 2005). The 850 $\mu$m flux densities are measured with JCMT/SCUBA-2 (Geach et al., 2014; Hine et al., 2016b; Ao et al., 2018). Tamura et al. (2013) reports ASTE/AzTEC 1.1 mm detections at the level around $3\sigma$ although they conclude they are not significant detections. LAB18 has a X-ray Active Galactic Nuclei (AGN), and its rest-frame near-infrared color of LAB18 is consistent with a power-law continuum associated with warm dust emission due to the AGN (Geach et al., 2009; Webb et al., 2009). LAB18 shows diffuse UV emission along the extent of the LAB with Multiple Mirror Telescope (MMT)/Megacam $r'$-band (Webb et al., 2009). Similar extended emission is seen in the Karl G. Jansky Very Large Array (VLA) 3 GHz continuum (Ao et al., 2018). Subaru/Suprime-cam $R$-band shows similar rest frame UV diffuse emissions (Matsuda et al., 2004). In Figure 5.4, we show the Subaru/Suprime-Cam Ly$\alpha$ image, ALMA Band7 860$\mu$m image, HST/ACS F814W image, and Subaru/Suprime-Cam $R$-band image of LAB18. These features are very similar to the recent hydrodynamical cosmological simulation, which suggests that DSFGs in the massive dark matter halo can be kept for a long time ($\sim$1 Gyr) due to recycling inflowing gas blowed out by their own stellar feedback

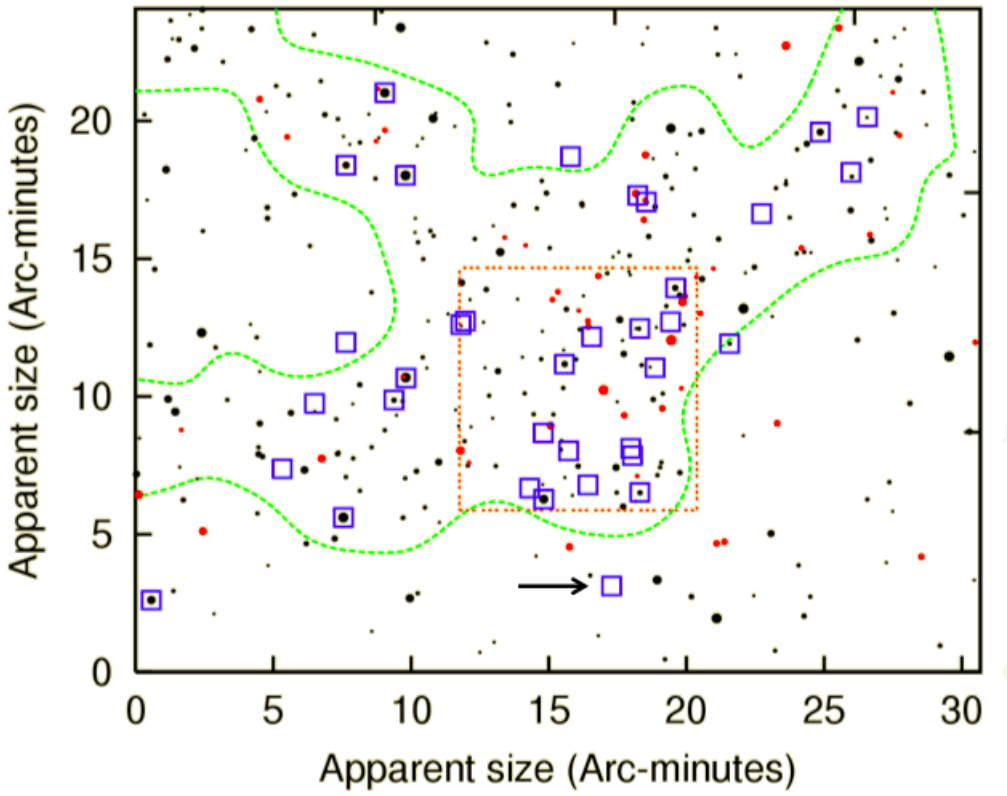


Figure 5.2: The sky distribution of 35 LABs in the $z = 3.09$ SSA22 protocluster, adopted from Figure 4 in Matsuda et al. (2004). The blue boxes show the position of the LABs. The black points show the 283 LAEs (Hayashino et al., 2004). The dashed square shows the sub-field where 24 LBGs was discovered (Steidel et al., 1998). The Ly$\alpha$ absorbers are shown as red points. The contours show the number density of the LAEs. LAB18 is located at slightly outside of the structure of SSA22. We show the position of the LAB18 as black allow.

(Narayanan et al., 2015). Geach et al. (2016) also suggests these extended UV emissions are satellite galaxies with the inflowing gas accreting onto a DSFGs from hydrodynamical cosmological simulation.

## 5.3 ALMA Observations

We conducted Atacama Large Millimeter/submillimeter Array (ALMA) observations to investigate DSFGs in LAB18 with sufficient spatial and spectroscopic information.

### ALMA Cycle 2 project

We observed LAB18 as an ALMA Cycle 2 project (2013.1.00704.S). Originally we targeted four LABs in the SSA22 protocluster, LAB01, LAB02, LAB05, and LAB18 while we focus on the LAB18 in this thesis which

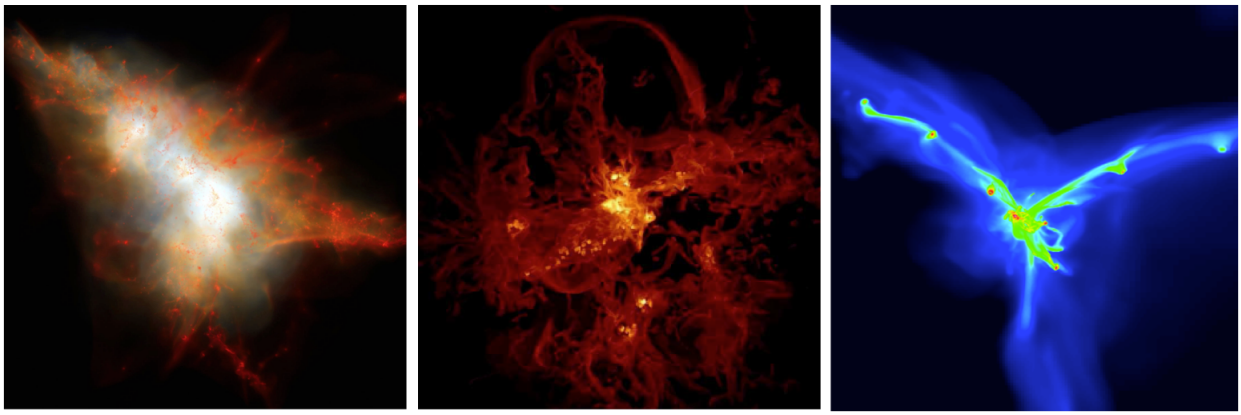

Figure 5.3: Simulation of photoionization, galactic superwind, and inflowing gas model. (left): Photoionization model from (Geach et al., 2016). The panel scale is ∼100 kpc. The distribution of gas within the dark matter halo is shown. Red and white color show cold ($\lesssim 10^4$ K) and hot gas ($\gtrsim 10^4$ K) respectively. (middle): Galactic superwind model from (Mori & Umemura, 2006). The panel scale is ∼150 kpc. The projected distribution of the Ly$\alpha$ emission from gas component for the simulated galaxy is shown. (right): Inflowing gas model from Dekel et al. (2009). The panel scale is ∼300 kpc. Gas density in the streams feeding the galaxy is shown.

we observed CO J=4-3 line in Cycle 4 project. Detail discussions for the other three LABs are, for instance, found in Martin et al. (2014); Geach et al. (2014, 2016); Alexander et al. (2016); Umehata et al. (2017b). Physical extents of all four LABs are larger than 100 kpc (Steidel et al., 2000; Matsuda et al., 2004).

The ALMA Band 7 continuum observations (rest frame $\sim 210$ $\mu$m) were carried out in three separated runs on 10 and 14 June 2015 with $37-41$ antennas with the baseline lengths of $21.4-918$ m ($\sim 25-1100\,\mathrm{k}\lambda$) in the dual-polarization setup. The center map coordinates are listed in Table 5.1. The total on-source integration time was 36 minutes per target. We used the correlator in the time division mode (TDM) at a central frequency of 350 GHz (860 $\mu$m). Ceres was observed as a flux calibrator. The absolute accuracy of flux calibration is ∼10% for Ceres. The bandpass and phase were calibrated with J2232+1143 and J2206−0031, respectively.

We reduced the data using the Common Astronomy Software Applications (CASA; McMullin et al., 2007) 4.2.2 package in a standard manner. From the calibrated data from the pipeline, we made continuum maps with the CLEAN algorithm with natural weighting (Figure 5.5). In this procedure, we placed a CLEAN box around $> 5\sigma$ peaks and CLEANed these down to a depth of $1\sigma$. The pixel size is set to $0.1''$. The image size is set to $36''$. The achieved synthesized beamsize (full-width at half maximum, FWHM) is $0.35'' \times 0.33''$ ($\sim 2.7$ kpc at $z = 3.1$) with PA$= -46$ deg. The continuum maps have an rms noise of 0.11 mJy beam$^{-1}$.

### ALMA Cycle 4 project

We observed LAB18 as an ALMA Cycle 4 project (#2016.1.01101.S) to detect CO J=4-3 line and 2.85 mm continuum emission. The ALMA Band 3 observations were carried out from 12th to 14th in November 2016 with 39–41 antennas with the baseline lengths of 15.1–1039 m ($\sim$4–290 k$\lambda$) in the dual-polarization setup. The total on-source integration time was 296.4 minutes. We set four spectral windows to cover 97–101 GHz and 109-113 GHz, which later one contains CO J=4-3 line from protocluster redshift of $z = 3.09 \pm 0.03$. J2148+0657 and J0006–0623 were observed as flux calibrators. The absolute accuracies of flux calibrations are $\sim$5% for these. The bandpass and phase were calibrated with J2148+0657 and J2226+0052, respectively.

We reduced the data with the CASA (McMullin et al., 2007) 4.7.2 package in a standard manner. From the calibrated data with pipeline, we made a primary beam corrected continuum subtracted spectral data cube with 20 km s$^{-1}$ resolution with the CLEAN algorithm with natural weighting. The achieved typical synthesized beamsize (full-width at half maximum, FWHM) is $1.07'' \times 0.99''$ with PA=76 deg. The typical $1\sigma$ noise is 2.5 mJy beam$^{-1}$ km s$^{-1}$. The $1\sigma$ noises are measured where the primary beam sensitivity is larger than 90%. The pixel size is set to $0.1''$ for all image. The image size is set to $60''$.

The 2.85 mm natural-weighted continuum images are also made by using all spectral windows, 99–103 GHz and 109–113 GHz bandwidth with CO J=4-3 line free channels. The achieved synthesized beamsize is $1.15'' \times 1.06''$ with PA=72 deg. The $1\sigma$ noises of 2.85 mm continuum image is 4.9 $\mu$Jy beam$^{-1}$. The $1\sigma$ noises are measured where the primary beam sensitivity is larger than 90%. The pixel size is set to $0.1''$ for all image. The image size is set to $60''$.

## 5.4 Results of 860 $\mu$m Dust Continuum Observations

We performed an ALMA Cycle 2 Band 7 860 $\mu$m (rest-frame 210 $\mu$m at $z = 3.1$) dust continuum observation.

### Detections of four 860 $\mu$m dust continuum emissions from LAB18

We used SExtractor 2.19.5 (Bertin & Arnouts, 1996) for source detection. We performed source detection on the natural-weighted maps before primary beam correction, detecting four sources (LAB18.a, LAB18.b, LAB18.c, LAB18.d) with peak flux densities $\geq 5\sigma$ (or $S_{860} \geq 0.55\,\mathrm{mJy\,beam^{-1}}$) within the field of view where the primary beam sensitivity is larger than 30%. We show 860 $\mu$m image of the LAB18 in Figure 5.4. We could not detect any $\geq 5\,\sigma$ sources on the inverted maps.

We performed flux and size measurements on the primary beam corrected maps by two-dimensional Gaussian fitting using IMFIT. The results of the flux density and source size measurements of these four DSFGs are shown in Table 5.1. The four DSFGs of LAB18,a,b,c and d are fully resolved, and the beam deconvolved source size is listed here. The four thumbnails are shown in Figure 5.5.

All four DSFGs are expected to be associated with the LAB18. The minimum integrated flux density of the ALMA 860 $\mu$m sources is $\sim 1\,\mathrm{mJy}$, whereas the expected number density of 860 $\mu$m sources with $\geq 0.5\,\mathrm{mJy}$ is $\sim 1 \times 10^4\,\mathrm{deg^{-2}}$ (e.g., Simpson et al., 2015; Oteo et al., 2016; Aravena et al., 2016). The field area within the 30% primary beam sensitivity is $380\,\mathrm{arcsec^2}$, so that the expected number of unrelated source

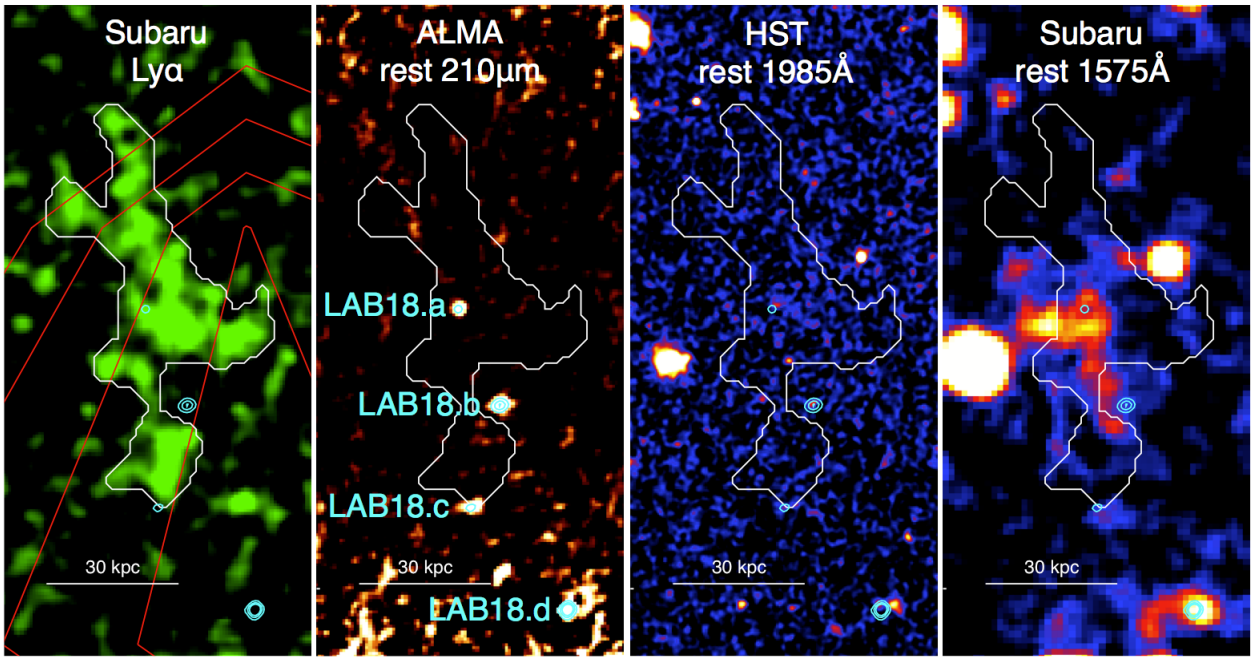


Figure 5.4: (left): LAB18 has a projected major axis size of 100 kpc, the highest filamentarity of the Ly$\alpha$ emission (Matsuda et al., 2011b) and has the highest FIR, Millimeter/Sub-millimeter flux densities in the SSA22 protocluster (e.g., Chapman et al., 2001, 2004; Geach et al., 2005, 2014; Tamura et al., 2013; Hine et al., 2016b; Ao et al., 2018). The white contour indicates isophotal apertures with a threshold of Ly$\alpha$ emission of $1.4 \times 10^{-18}$ erg s$^{-1}$ cm$^{-2}$ arcsec$^{-2}$. The cyan contour shows 5,10,15$\sigma$ level of ALMA 860 $\mu$m image in the left middle panel. We also show *Herschel*/SPIRE 500 $\mu$m emission from 16 mJy to 19 mJy as red contours. (left middle): ALMA 860 $\mu$m dust continuum image. We can see the four significant detections. The cyan contour shows 5,10,15$\sigma$ level of ALMA 860 $\mu$m image. From top to bottom, we defined four sources, LAB18.a, LAB18.b, LAB18.c, and LAB18.d in the following section. (right middle): *Hubble Space Telescope (HST)*/Advanced Camera for Surveys (ACS) F814W filter image of LAB18. (right): Subaru/Suprime-Cam $R$-band image of LAB18.

Table 5.1: Flux and size measurement of four 860 $\mu$m dust continuum sources in the LAB18

| ID | RA(J2000) (h:m:s) | Dec(J2000) (d:m:s) | $S^{a}_{860,\mathrm{int}}$ (mJy) | Major Axis$^{b}$ (arcsec) | Minor Axis$^{b}$ (arcsec) | PA (deg) |
|---|---|---|---|---|---|---|
| LAB18.a | 22:17:29.03 | +00:07:50.2 | $1.15 \pm 0.03$ | $0.19 \pm 0.02$ | $0.17 \pm 0.02$ | $43 \pm 50$ |
| LAB18.b | 22:17:28.94 | +00:07:47.0 | $2.61 \pm 0.03$ | $0.26 \pm 0.01$ | $0.15 \pm 0.01$ | $98 \pm 3$ |
| LAB18.c | 22:17:29.01 | +00:07:43.5 | $1.15 \pm 0.09$ | $0.27 \pm 0.05$ | $0.19 \pm 0.06$ | $95 \pm 38$ |
| LAB18.d | 22:17:28.79 | +00:07:40.1 | $4.69 \pm 0.09$ | $0.24 \pm 0.01$ | $0.14 \pm 0.01$ | $162 \pm 5$ |

**Notes**. $^{a}$The integrated flux densities have been primary beam corrected. $^{b}$The intrinsic full width of half maximum of the major axis and minor axis have been beam deconvolved.

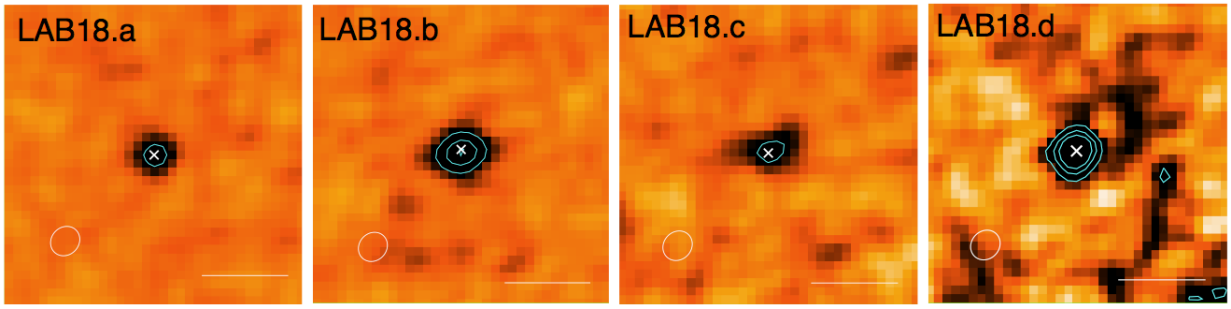


Figure 5.5: ALMA 860 $\mu$m natural weighted dust continuum images for LAB18.a, LAB18.b, LAB18.c and LAB18.d. Each image has size of $3.5'' \times 3.5''$ ($\sim$27 $\times$27 kpc$^2$). The white x-crosses represent the peaks of 860 $\mu$m dust continuum emissions. The contours on the 860 $\mu$m image show 5,10,15$\sigma$ level. The ellipses at the bottom-left corner represent the naturally-weighted beam size of ALMA ($0.35'' \times 0.33''$). The horizontal bars in the bottom right corner show $1''$ scale (7.6 kpc). The pixel size is set to $0.1''$.

is only $\sim 0.3$ in 380 arcsec$^2$ area. Thus, these four DSFGs are possibly associated with LAB18 in the $z = 3.1$ SSA22 protocluster.

## 5.5 Results of CO J=4-3 Line Observations

We performed an ALMA Cycle 4 Band 3 observation to detect CO J=4-3 line emissions.

### Detection of CO J=4-3 line from LAB18.b

The CO J=4-3 line emission is detected at a significance of 11$\sigma$ (peak flux density from the map variance) at the position of the LAB18.b in the velocity integrated flux intensity map (Figure 5.7 left & middle left). We integrated over $-110$ to $+70$ km s$^{-1}$ with respect to the 20 km s$^{-1}$ center narrow component. The spectrum of LAB18.b shows double peak structure and its single fitted Gaussian FWHM shows 123 $\pm$ 27 km s$^{-1}$ (Figure 5.7 left). We made images of the redshifted ($10 < v < 70$ km s$^{-1}$) and blueshifted ($-110 < v < -10$ km s$^{-1}$) components respect to the central narrow ($-10 < v < 10$ km s$^{-1}$) component. FWHMs of the red and blue component are $43 \pm 8$ km s$^{-1}$ and $79 \pm 5$ km s$^{-1}$, respectively. The center velocities of red and blue

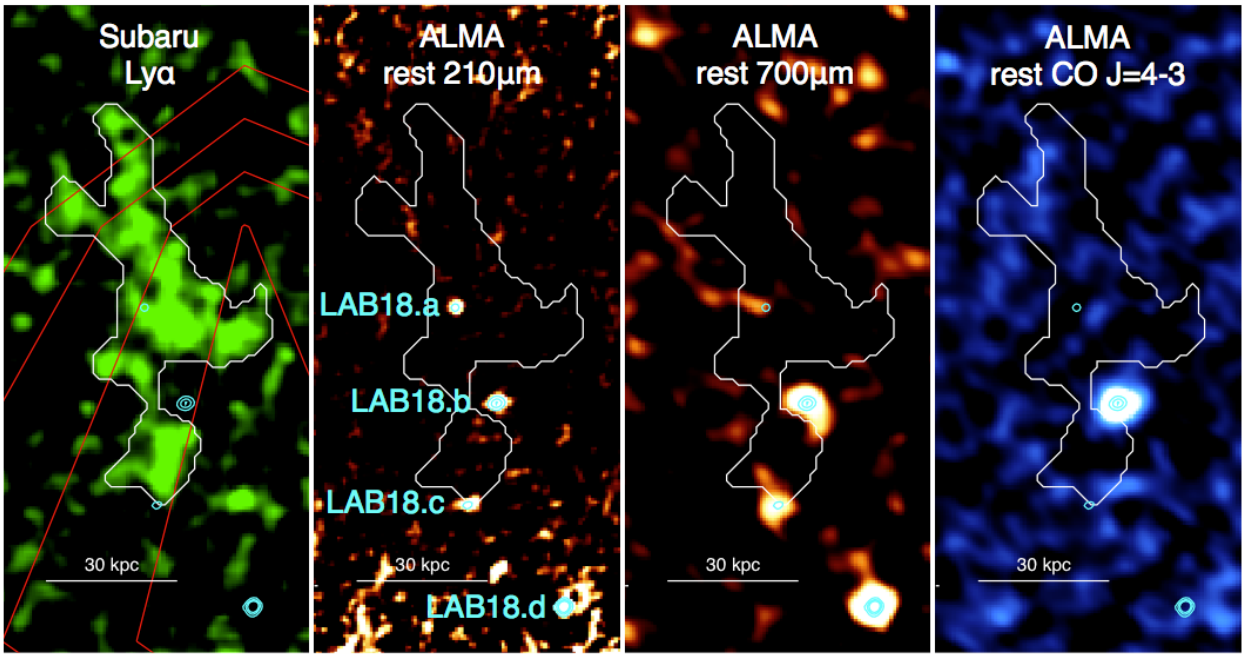


Figure 5.6: (left): Subaru/Suprime-Cam $NB497 - BV$ (Ly$\alpha$) image of LAB18. (left middle): ALMA Band 7 860 $\mu$m dust continuum emission image of LAB18. (right middle): ALMA Band 3 3 mm dust continuum emission image of LAB18 (right): ALMA Band 3 CO J=4-3 line. White contours show Ly$\alpha$ emission of $1.4 \times 10^{-18}$ erg s$^{-1}$ cm$^{-2}$ arcsec$^{-2}$ for all images. Cyan contours show the positions of the LAB18.a, LAB18.b, LAB18.c, and LAB18.d (from top to bottom) whose steps are 5, 10, 15$\sigma$ level ($1\sigma$ = 0.11 mJy beam$^{-1}$) for all images. The red contour in the Ly$\alpha$ image shows *Herschel*/SPIRE 500 $\mu$m dust continuum emission, whose steps are 16–19 mJy.

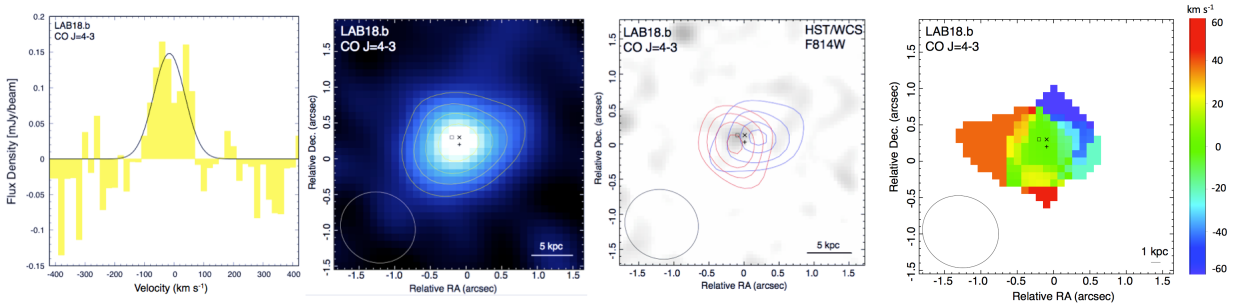


Figure 5.7: (left). The spatially integrated CO J=4-3 line spectrum of LAB18.b. The velocity resolution is 20 km s$^{-1}$. The center velocity is corresponding to the frequency of 112.6245 GHz, which is 20 km s$^{-1}$ narrow component of the line emission. The best-fit Gaussian profile for the CO J=4-3 line is overlaid as a black line. We spatially integrated its flux densities with 2D Gaussian by using IMFIT task over the aperture of 2.5″ diameter. The velocity FWHM is 123 ± 27 km s$^{-1}$. (middle left). The velocity integrated ALMA CO J=4-3 intensity map of LAB18.b. We integrated over −110 to +70 km s$^{-1}$ for the LAB18.b with respect to the 20 km s$^{-1}$ center narrow component. The yellow contour shows 3–6$\sigma$ level. (middle right). Red and blue contours show the redshifted ($10 < v < 70$ km s$^{-1}$) and blueshifted ($-110 < v < -10$ km s$^{-1}$) components with 3–6$\sigma$ and 3, 4, 5, 5.5$\sigma$ level, respectively. The background is *HST*/ACS F814W filter image. The box, cross and x-cross show the peak positions of 2.85 mm continuum, CO and 860 $\mu$m continuum, respectively. The image size is 3.5″ × 3.5″ (∼27×27 kpc$^2$). The ellipse at the bottom-left corner represents the naturally-weighted CO beam size of ALMA (1.07″ × 0.99″). (right). The CO moment one map of LAB18.b with 3$\sigma$ clipping. The inset color bar shows relative velocity to the center narrow component of 20 km s$^{-1}$. The box, cross and x-cross show the peak positions of 2.85 mm continuum, CO and 860 $\mu$m continuum, respectively.

components are $39 \pm 3$ km s$^{-1}$ and $-38 \pm 2$ km s$^{-1}$. The derived systematic redshift is $z_{\rm CO} = 3.0936 \pm 0.0002$, whose error comes from the center narrow component of the spectrum of CO.

Beam-deconvovled CO J=4-3 line emission of LAB18.b is spatially resolved, and the FWHM source size with approximated 2D Gaussian using IMFIT is estimated to be $0.73'' \times 0.24''$, corresponding to a physical scale of $5.57 \times 1.83$ kpc$^2$. In Figure 5.7 middle right panel and right panel, we show the velocity integrated red and blue components image, and the moment one velocity map of LAB18.b.

## Estimation of $L'_{\rm CO_{(4-3)}}$ of LAB18

We measure the total flux density of the CO J=4-3 line emission by fitting to a 2D Gaussian using a CASA task, IMFIT to a velocity integrated flux intensity map with primary beam correction. The velocity integrated flux intensity is $0.083 \pm 0.006$ Jy km s$^{-1}$ (see also Table 5.2). The $1\sigma$ level of map variance is 0.0064 Jy km s $^{-1}$. Following Solomon & Vanden Bout (2005), the CO J=4-3 luminosity of $L'_{\rm CO_{(4-3)}}$ is $(2.3 \pm 0.2) \times 10^9$ K km s$^{-1}$ pc$^2$ with velocity width of 180 km s$^{-1}$ (Table 5.3). The $3\sigma$ upper limit of CO J=4-3 luminosity is $4.8 \times 10^8$ K km s$^{-1}$ pc$^2$ with velocity width of 180 km s$^{-1}$.

Yang et al. (2014) reported that neither 3.5 mm dust continuum emissions nor CO J=3-2 line emissions are detected with PdBI observation for LAB18. The observation resulted a CO J=3-2 upper limit of 0.27 Jy km s$^{-1}$ ($3\sigma$ ) with velocity width of 400 km s$^{-1}$. This deduced CO J=3-2 luminosity is $L'_{\rm CO_{(3-2)}} = 12 \times 10^9$ K km s$^{-1}$ pc$^2$. We estimate $3\sigma$ upper limit of $L'_{\rm CO_{(4-3)}} < 8.4 \times 10^9$ K km s$^{-1}$ pc$^2$ by assuming $L'_{\rm CO_{(4-3)}}/L'_{\rm CO_{(3-2)}}$ ratio of 0.70 (SMG's value from Carilli & Walter 2013) for LAB18. This is consistent with our CO J=4-3 luminosity of $L'_{\rm CO_{(4-3)}} = (2.3 \pm 0.2) \times 10^9$ K km s$^{-1}$ pc$^2$ value of LAB18.b.

## Velocity offset between Ly$\alpha$ emission and CO J=4-3 emission

Our CO J=4-3 observation reveals the CO redshift is lower than the redshift of $z_{\rm Ly\alpha} = 3.104$ with Ly$\alpha$ spectroscopy (Matsuda et al., 2011b). This corresponds to a high velocity offset ($\Delta$Ly$\alpha$ = +762 $\pm$ 15 km s$^{-1}$) between Ly$\alpha$ emission and CO emission. Small equivalent width (EW) of Ly$\alpha$ emission ($35 \pm 6$ Å) estimated from Subaru/Suprime-Cam $R$-band magnitude and continuum subtracted $NB497$-band magnitude of Ly$\alpha$ (Matsuda et al., 2004) is also consistent with large velocity offset between Ly$\alpha$ emission and systematic CO line emission (Hashimoto et al., 2013). Hashimoto et al. (2015) investigates Ly$\alpha$ profile by using uniform expanding shell model, and indicates $\sim$700 km s$^{-1}$ offset suggests that existence of high atomic hydrogen gas column density of $\log {\rm N_{HI}} > 22$ cm$^{-2}$.

However, the Ly$\alpha$ profile is easily affected by galactic superwinds. Galactic superwind can shift the peak of the Ly$\alpha$ emission by up to few hundred km s$^{-1}$ (Zabl et al., 2015). Thus, the large velocity offset could suggest existence of the galactic superwinds. Indeed, LAB18 consists of four DSFGs and a one X-ray AGN (Geach et al., 2009). In Figure 5.8, we show the position of the X-ray emissions and Ly$\alpha$ peak where the spectroscopic observation is conducted. We note that we assume the Ly$\alpha$ spectroscopic redshift at the Ly$\alpha$ peak is the same for the entire of the LAB18 in this discussion.

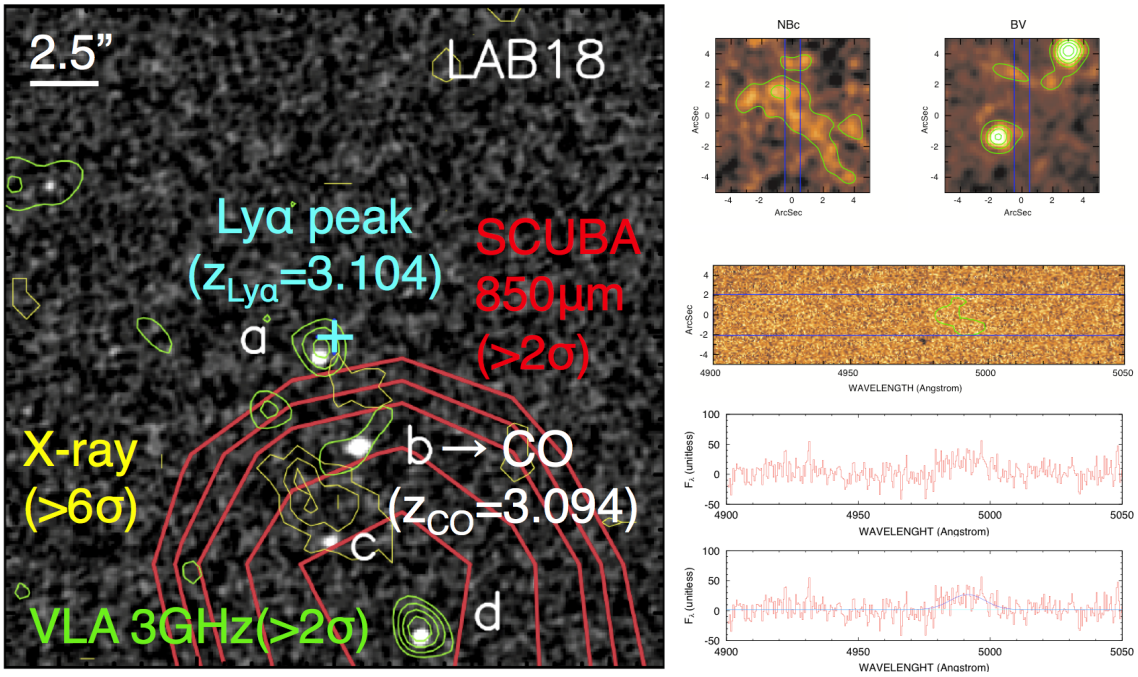


Figure 5.8: (left): The figure adopted from Ao et al. (2018). The positions of X-ray emissions and spectroscopic information of LAB18. We also labeled CO redshift for LAB18.b. (right): Figure from Y. Matsuda's Ph. D thesis. We show the results of Keck/DEIMOS spectroscopic observation for LAB18.

## Molecular gas mass estimation

In the following section, we assume that LAB18.a, LAB18.c and LAB18.d are associated with LAB18 at $z = 3.0936 \pm 0.0002$, since their estimated photometric redshifts imply $z > 2$ with 99% confidence level (see §5.7) and the chance probability is very low from volume density estimation (see §5.4).

Derived CO J=4-3 luminosity is used to estimate gas mass. With the median CO J=4-3 luminosity to CO J=1-0 luminosity ratio of $r_{41} = 0.41$ for 40 luminous SMGs (Bothwell et al., 2013) and the consensus value of CO to $H_2$ conversion factor of $\alpha_{\rm CO} = 0.8$ for local (U)LIRGs and distant SMGs/QSOs (Downes & Solomon, 1998), we derive CO J=1-0 luminosity of $(5.3 \pm 0.2) \times 10^9$ K km s$^{-1}$ pc$^2$ and $M_{\rm gas} = (4.4 \pm 0.3) \times 10^9 M_\odot$ for LAB18.b. We include Helium contribution for gas mass by multiplication of 1.36. The derived gas mass is $M_{\rm gas} = (2.4 \pm 0.3) \times 10^{10} M_\odot$ for LAB18.b if we use galactic conversion factor of $\alpha_{\rm CO} = 4.36$.

For CO non-detected ALMA sources, we derive $3\sigma$ upper limit with same manner as LAB18.b (velocity width of 180 km s$^{-1}$, $r_{41} = 0.41$, $\alpha_{\rm CO} = 0.8 and 4.36$, and $z_{\rm CO} = 3.0936 \pm 0.0002$). The derived $3\sigma$ upper limit gas mass is $< 1.0 \times 10^9\ M_\odot$ ($\alpha_{\rm CO} = 0.8$) and $5.5 \times 10^9 M_\odot$ ($\alpha_{\rm CO} = 4.36$).

## Extended gaseous structures of CO J=4-3

We could not find any obvious ($> 3\sigma$) inflows and/or outflows signatures of CO J=4-3 line emission in the 20 km s$^{-1}$ spectral data cube. In Figure 5.9, we show the 20 km s$^{-1}$ resolution channel maps.

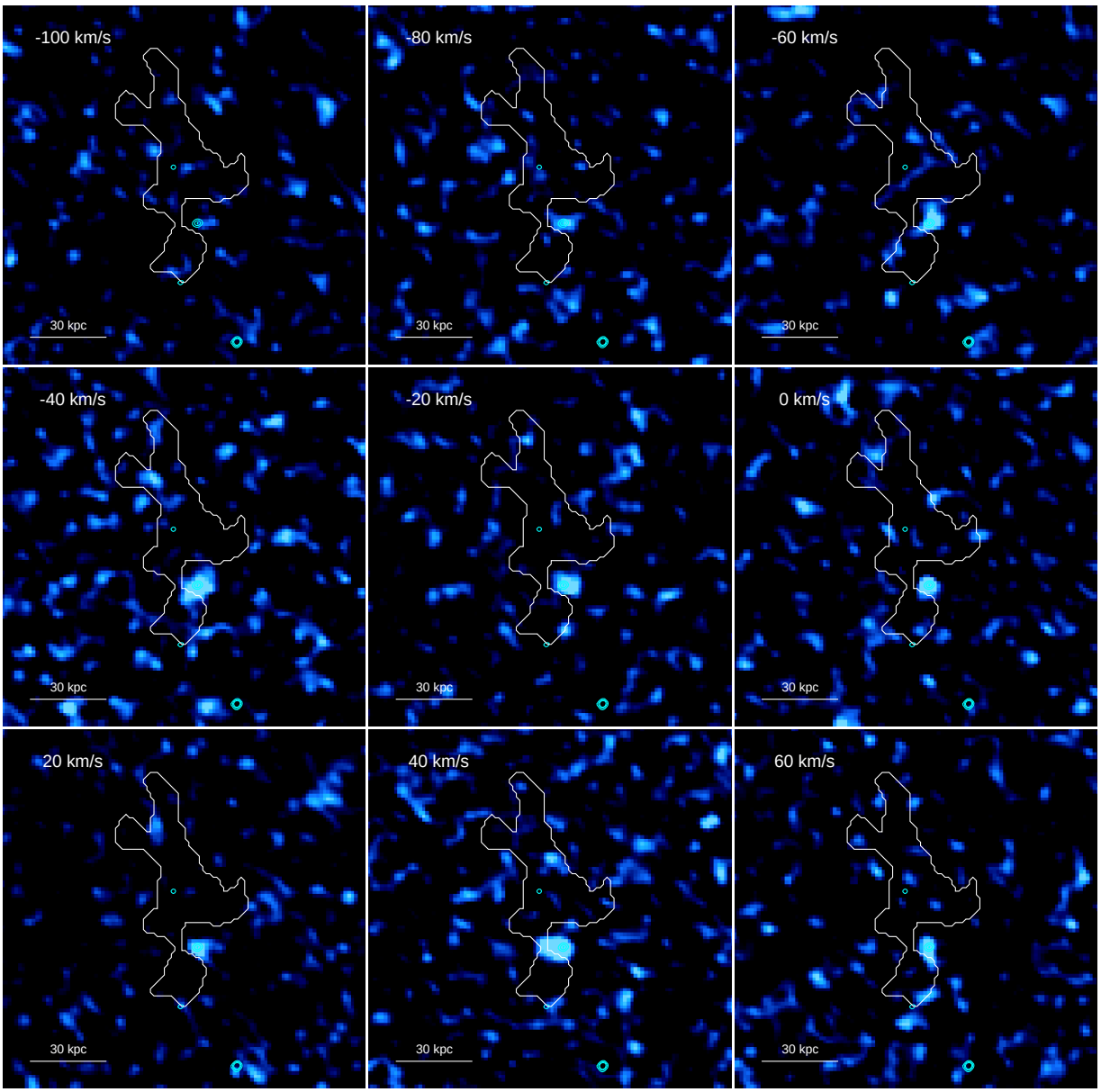


Figure 5.9: The channel maps of CO J=4-3 line emission around the LAB18. The velocity resolution is 20 km $s^{-1}$. The center velocity (relative 0 km $s^{-1}$) corresponds to the frequency of 112.6245 GHz. We show the velocity range of $-110$ to $+70$ km $s^{-1}$. The cyan contours show the 860 $\mu$m emission of 5,10,15$\sigma$ level. The white contour indicates isophotal apertures with a threshold of Ly$\alpha$ emission of $1.4 \times 10^{-18}$ erg $s^{-1}$ $cm^{-2}$ $arcsec^{-2}$. The image size is $21'' \times 21''$ ($160 \times 160$ $kpc^2$). The line at the bottom-left corner represents the 30 kpc scale.

Table 5.2: ALMA Band 3 properties for four DSFGs in the LAB18.

| ID | RA(J2000) (h:m:s) | Dec(J2000) (d:m:s) | $S^a_{\mathrm{CO(4-3)}}dv$ (Jy km s$^{-1}$) | $S^b_{\mathrm{2.85,PBcorr}}$ ($\mu$Jy/beam) |
|---|---|---|---|---|
| LAB18.a | 22:17:29.03 | +00:07:50.2 | $< 0.019$ | $34 \pm 17^c$ |
| LAB18.b | 22:17:28.94 | +00:07:47.0 | $0.083 \pm 0.006$ | $38 \pm 7$ |
| LAB18.c | 22:17:29.01 | +00:07:43.5 | $< 0.019$ | $20 \pm 7$ |
| LAB18.d | 22:17:28.79 | +00:07:40.1 | $< 0.019$ | $51 \pm 6$ |

**Notes**. [a]The $3\sigma$ upper limit is estimated with velocity width of 180 km $s^{-1}$, which corresponds to velocity width of LAB18.b. The $1\sigma$ level is 0.0064 Jy km s $^{-1}$ (map variance). [b]The integrated flux densities measured on the 2.85 mm maps (primary beam corrected). The error comes from 2D Gaussian fitting errors. The $1\sigma$ level is 4.9 $\mu$Jy beam$^{-1}$ (map variance). Our four DSFGs are above $\geq 3\sigma$ at the position of the peak fluxes. [c]For the LAB18.a, we show the flux density of 2.70 mm dust continuum emission (see text in detail).

Table 5.3: Summary of derived properties for LAB18.b.

| ID | | LAB18.b |
|---|---|---|
| $S^a_{\mathrm{CO(4-3)}}dv$ | (Jy km s$^{-1}$) | $0.083 \pm 0.006$ |
| FWHM$^b$ | (km s$^{-1}$) | $123 \pm 27$ |
| $\log L'_{\mathrm{CO(4-3)}}$ | (K km s$^{-1}$ pc$^2$) | $9.36 \pm 0.02$ |
| $\log M^c_{\mathrm{gas,CO}}(\alpha = 0.8)$ | ($M_\odot$) | $9.64 \pm 0.02$ |
| $\log M^c_{\mathrm{gas,CO}}(\alpha = 4.36)$ | ($M_\odot$) | $10.38 \pm 0.02$ |
| Major axis (CO)$^d$ | (kpc) | $5.57 \pm 0.53$ |
| Minor axis (CO)$^d$ | (kpc) | $1.83 \pm 0.99$ |
| Position Angle (CO) | ( $^\circ$) | $120 \pm 9$ |
| Major axis (dust)$^d$ | (kpc) | $1.98 \pm 0.08$ |
| Minor axis (dust)$^d$ | (kpc) | $1.14 \pm 0.08$ |
| Position Angle (dust) | ( $^\circ$) | $98 \pm 3$ |

**Notes**. [a]Velocity and spatially integrated CO flux intensity. [b]Velocity FWHM of red and blue component. [c]CO-based gas mass. We also show the results with different conversion factor of $\alpha$. [d]Beam-deconvolved FWHM source size of the major axis and minor axis derived with IMFIT task.

## 5.6 Results of 2.85 mm Dust Continuum Observations

### Detections of 2.85 mm dust continuum emissions from LAB18

2.85 mm dust continuum emissions (composite of 97-101 GHz bandwidth and 109-113 GHz bandwidth) are detected at the position of LAB18.b, LAB18.c and LAB18.d above $3\sigma$ level (peak flux densities from the map variance of $1\sigma = 4.9\mu$Jy beam$^{-1}$). The flux densities of the detected continuum sources are measured with the IMFIT task of CASA using the map after correction for the primary beam attenuation. We show the thumbnails for 2.85 mm dust continuum emissions for four DSFGs in LAB18 in Figure 5.10 and the flux densities are shown in Table 5.2. We could not resolve 2.85 mm dust continuum emissions with beam size of $1.15'' \times 1.06''$.

The 2.70 and 3.00 mm natural-weighted continuum images are also made by using the same manner as 2.85 mm dust continuum image. The $1\sigma$ noises of 2.70 mm and 3.00 mm dust continuum image is 8.7 and 5.9 $\mu$Jy beam$^{-1}$. The $1\sigma$ noises are measured where the primary beam sensitivity is larger than 90%. The pixel size is set to $0.1''$ for all image. The 2.70 mm natural-weighted dust continuum image is made with CO J=4-3 line free channels. In Figure 5.10, we show the 2.70, 2.85, and 3.00 mm dust continuum images for LAB18.a, LAB18.b, LAB18.c and LAB18.d. For the LAB18.a, we only detected 2.70 mm dust continuum emission at 3.7 $\sigma$ level at the position of the 860 $\mu$m dust continuum emission of LAB18.a. Thus, we use 2.70 mm dust continuum flux densities instead of 2.85mm to deduce a FIR SED for LAB18.a in the latter section.

### FIR SED fitting, FIR luminosity and SFR

The FIR continuum flux densities are used to estimate far-infrared (FIR) SEDs and their luminosity, where $L_{\rm FIR}$ is the integrated luminosity of $8 - 1000$ $\mu$m (see also, equation 3.1). In addition to the ALMA flux densities of 860 $\mu$m and 2.85 mm (and only for LAB18.a, we use 2.70 mm continuum flux density), we also use *Herschel*/SPIRE data (Kato et al., 2016), ASTE/AzTEC 1.1 mm data (Tamura et al., 2013) and PdBI 3.5 mm data (Yang et al., 2014) to constrain FIR SEDs for four DSFGs in the LAB18. Since four DSFGs in the LAB18 are highly blended in the large FWHM of SPIRE and AzTEC camera (see also Figure 5.4 left), we only use the *Herschel*/SPIRE 250 $\mu$m flux densities as a lower limit and an upper limit because of the better resolution and shorter wavelength. The data points in Figure 5.11 and data in Table 5.4 show the ranges of an upper limit and a lower limit of SPIRE and AzTEC camera. We re-measure the flux densities at the precise positions of the peak 860 $\mu$m dust continuum emissions for the SPIRE 250 $\mu$m upper limits. We can see the absolute flux densities and the SPIRE colors are actually changed, although the four DSFGs are actually blended (see also Figure 5.11 and Table 5.4). For the upper limit for AzTEC, we sum up flux densities of LAB18-a and LAB18-b sources in Tamura et al. (2013) to suit upper limit of SPIRE flux densities (i.e., we arrange SPIRE and AzTEC upper limit for blended, total flux densities of all four DSFGs in LAB18). Originally, these two (LAB18-a and LAB18-b) sources are detected within LAB18 with *Spitzer*/IRAC band (Webb et al., 2009), but considering larger beam size of AzTEC camera (FWHM of $34''$) and SPIRE camera, we should think these are highly blended (i.e., the projected offset is less than $10''$). Then, for the lower limits of SPIRE and AzTEC flux densities, we divided these upper limits as normalized

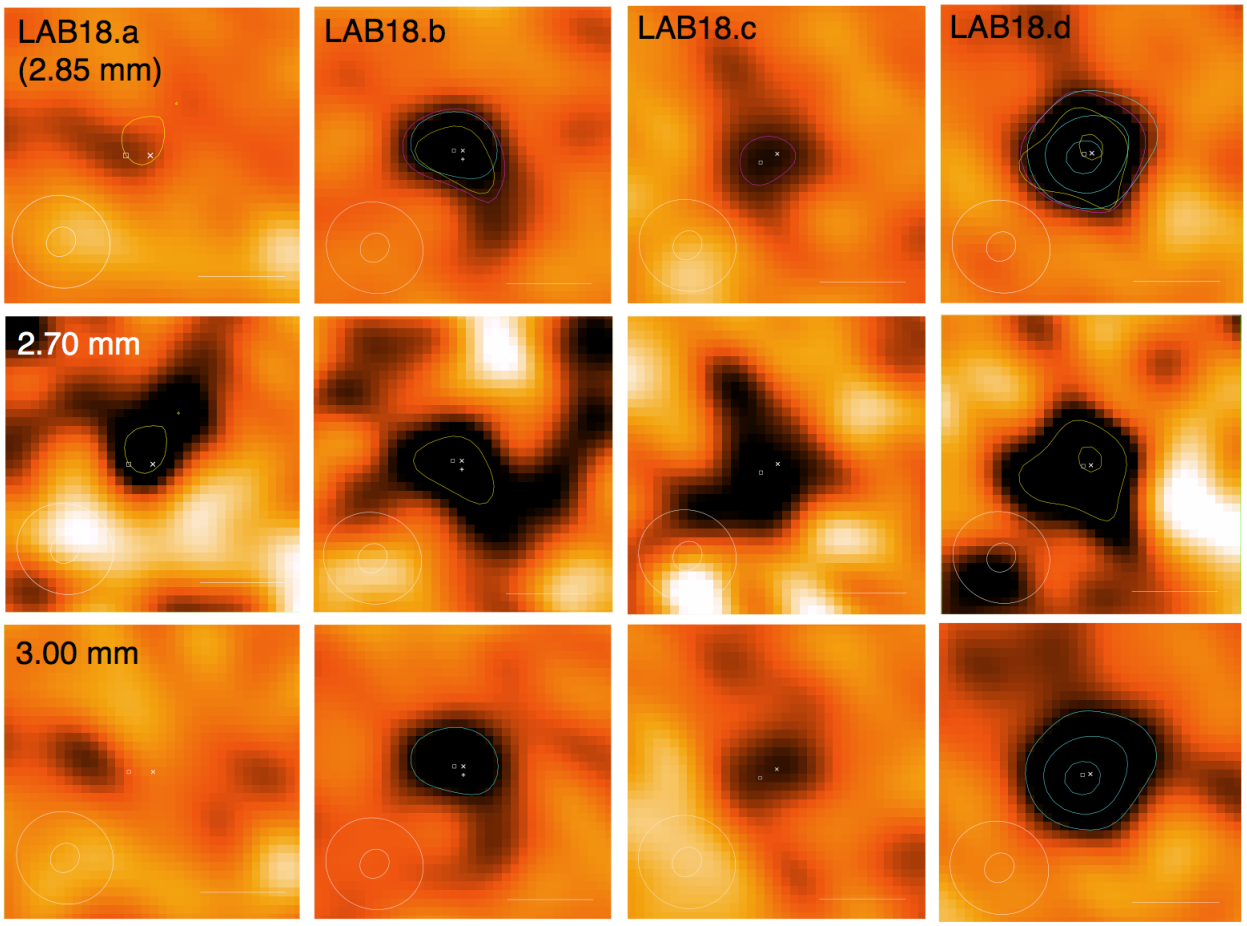


Figure 5.10: From left to right, we show the ALMA Band 3 natural weighted dust continuum images for LAB18.a, LAB18.b, LAB18.c and LAB18.d. The top, middle, and bottom rows show 2.85, 2.70, and 3.00 mm dust continuum images, respectively. Each image has size of $3.5'' \times 3.5''$ ($\sim$27 $\times$27 kpc$^2$). The contours on the 2.85 mm image show 3,5,7$\sigma$ level of 2.70, 2.85, and 3.00 mm dust continuum emissions (yellow, magenta, and cyan, respectively). The white x-cross represents the peak positions of 860 $\mu$m dust continuum emissions. The white boxes represent the peak of 2.85 mm dust continuum emissions. For the LAB18.b, we show the plus-cross which represents the peak of CO J=4-3 line emission. The ellipse at the bottom-left corner represents naturally-weighted beam size of 2.85 mm dust continuum image ($1.15'' \times 1.06''$). The inner ellipse represents the naturally-weighted beam size of 860 $\mu$m dust continuum image ($0.35'' \times 0.33''$). The horizontal bar in the right corner shows $1''$ scale (7.6 kpc). The pixel size is set to $0.1''$.

Table 5.4: FIR flux densities, $T_d$, $\beta$, $L_{\rm FIR}$ and SFR of four DSFGs in LAB18.

| ID | $S^a_{250}$ (mJy) | $S^a_{350}$ (mJy) | $S^a_{500}$ (mJy) | $S^a_{1100}$ (mJy) | $T^b_d$ (K) | $\beta^b$ - | $\log M^c_{\rm dust}$ ($M_\odot$) | $\delta^c_{\rm GDR}$ – | $L^d_{\rm FIR}$ ($10^{12}$ $L_\odot$) | SFR$^d$ ($M_\odot$ yr$^{-1}$) |
|---|---|---|---|---|---|---|---|---|---|---|
| LAB18.a | 1.1–9.4 | 1.7–14.4 | 1.8–15.3 | 0.5–3.9 | 27–51 | 1.6–2.1 | 7.37–7.68 | 21–43 | 0.51–3.11 | 51–311 |
| LAB18.b | 2.6–9.0 | 5.3–18.3 | 5.4–18.1 | 1.1–3.9 | 24–32 | 2.3–2.6 | 7.70–7.85 | 63–90 | 1.24–2.72 | 124–272 |
| LAB18.c | 1.1–9.1 | 1.7–13.8 | 1.8–14.8 | 0.5–3.9 | 26–46 | 1.8–2.3 | 7.26–7.54 | 29–55 | 0.52–2.81 | 52–281 |
| LAB18.d | 8.4–17.2 | 8.9–18.2 | 7.7–15.7 | 1.9–3.9 | 26–30 | 2.6–2.8 | 7.84–7.91 | 12–15 | 3.17–5.17 | 317–517 |

**Notes**. [a]The ranges of flux densities show an upper and lower limit. For the upper limit, we show the raw flux densities measured at the position of the four DSFGs in LAB18. For the lower limit, we show the 860 $\mu$m normalized flux densities of each band. [b]We fitted an optically thin, single temperature, modified black body radiation to the *Herschel*/SPIRE 250 $\mu$m, ALMA Band 7 860 $\mu$m, and ALMA Band 3 2.85 mm flux densities (see Figure 5.10). The ranges come from *Herschel*/SPIRE 250 $\mu$m upper limit and lower limit. [c]We assumed $\kappa_{850} = 3.2$ cm$^2$ g$^{-1}$ for the dust mass estimation. We used molecular gas mass with the conversion factor of $\alpha = 0.8$. [d]The ranges come from *Herschel*/SPIRE 250 $\mu$m upper limits and lower limits. We assumed Chabrier IMF Chabrier (2003).

as ALMA 860 $\mu$m flux densities. Since PdBI 3.5 mm dust continuum emission is not detected, we only use this value as an $3\sigma$ upper limit of 0.13 mJy beam$^{-1}$ (Yang et al., 2014). We assumed the same redshift as LAB18.b ($z = 3.0936 \pm 0.0002$) for the CO non-detected sources of LAB18.a, LAB18.c, and LAB18.d.

In Figure 5.11, we show the fitting results. We fitted a single temperature, optically thin modified black body radiation to the observed *Herschel*/SPIRE 250 $\mu$m, ALMA Band 7 (860 $\mu$m) and ALMA Band 3 (2.85 mm) flux densities. We show the single temperature, optically thin modified black body radiation with $T_d = 25$ K and 75 K and dust emissivity index of $\beta = 1.8$ (green and magenta dotted lines) as Scoville et al. (2016). The observed data does not match. Thus, we changed $T_d$ and $\beta$ to fit the observed *Herschel*/SPIRE 250 $\mu$m, ALMA Band 7 (860 $\mu$m) and ALMA Band 3 (2.85 mm) flux densities. The red and blue solid lines show the best fitted results for the *Herschel*/SPIRE 250 $\mu$m upper and lower limits. We summarize the deduced $T_d$, $\beta$, $M_{\rm dust}$, $L_{\rm FIR}$, and SFR from the SED fitting for FIR wavelength in Table 5.4. We note that we assume the Chabrier IMF Chabrier (2003) in §5, which returns the SFR empirical conversion with SFR/$M_\odot$ yr$^{-1}$ $= 1.0 \times 10^{-10}$ $L_{\rm FIR}/L_\odot$ (Kennicutt, 1998).

## Dust mass estimation

The observed-frame 2.85 mm wavelength corresponds to rest-frame $\sim$ 700 $\mu$m dust continuum emission at $z = 3.0936$. The longer part of far-infrared wavelength ($\lambda_{\rm rests} \gtrsim$ 250$\mu$m) is very useful to estimate dust mass, because the Rayleigh-Jeans (RJ) tail is likely to be optically thin, dust emission is rarely optically thick at this longer part of far-infrared wavelength than the shorter part of far-infrared wavelength. At $z \sim 3$, *Herschel*/SPIRE data is not reliable to estimate dust mass of cold component. Because the SPIRE data will be probing near the rest frame far infrared luminosity peak, SPIRE data does not trace the RJ tail and not necessarily optically thin. The longest 500 $\mu$m band will be probing rest frame 130 $\mu$m for $z \sim 3$. In addition, the SPIRE 500 $\mu$m band has relatively high source confusion on account of the large beam size. Thus, by assuming the dust continuum emission at 700 $\mu$m mainly associates with dust thermal emission and adopting the optically thin approximation as FIR SED fitting in previous subsection, we estimate dust mass of four

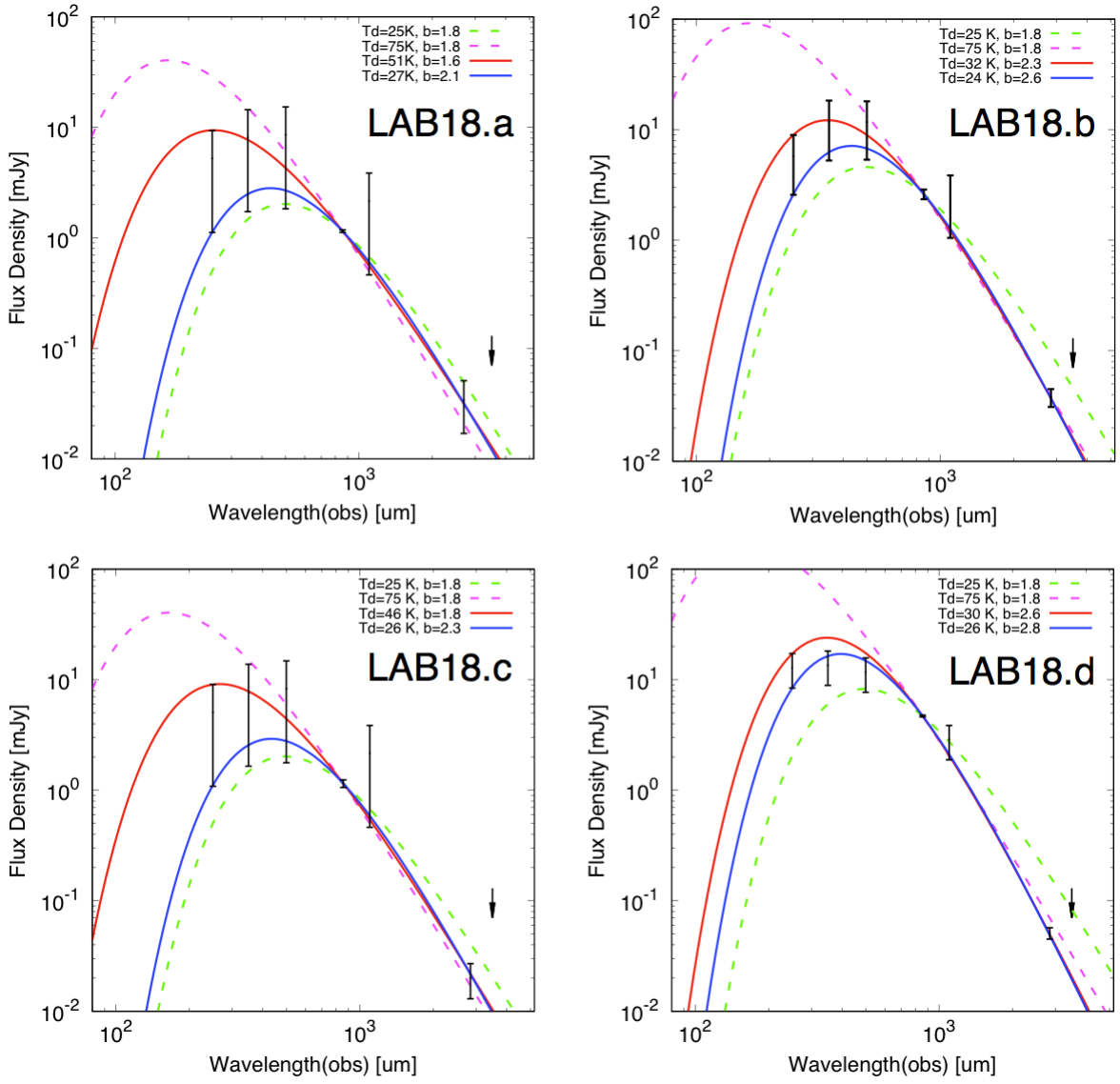


Figure 5.11: The results of FIR SEDs fitting for four DSFGs in LAB18. We fitted a single temperature, optically thin modified black body radiation to the *Herschel*/SPIRE 250 $\mu$m, ALMA Band 7 (860 $\mu$m) and ALMA Band 3 (2.85 mm) flux densities. The red and blue solid lines are best fitted, and used for upper limits and lower limits of far-infrared luminosities. We assumed that all ALMA sources in LAB18 are at the redshift of 3.0936±0.0002. We summarize the results of the SED fitting for FIR wavelength in Table 5.4.

DSFGs in LAB18. We estimated dust mass of $M_{\rm d}$ with 2.85 mm (2.70 mm for LAB18.a) dust continuum flux densities by using the following equation,

$$M_{\rm d} = \frac{S_{\rm obs} D_L^2}{(1+z)\kappa_{\rm d}(\nu_{\rm rest}) B_\nu(\nu_{\rm rest}, T_{\rm dust})} \tag{5.1}$$

$S_{\rm obs}$ is an observed flux density at frequency $\nu_{\rm rest}$, $D_L^2$ is a luminosity distance, $z$ is a redshift, $\kappa_{\rm d}(\nu_{\rm rest})$ is a dust absorption coefficient at frequency $\nu_{\rm rest}$, $B_\nu(\nu_{\rm rest}, T_{\rm dust})$ is the Planck function at temperature $T_{\rm dust}$ and $\nu_{\rm rest}$. The derived dust mass is summarized in Table 5.4. We assumed $\kappa_{850} = 3.2$ cm$^2$ g$^{-1}$ (Demyk et al., 2017) to match large $\beta > 2.0$. Here $\kappa_{\rm d}(\nu_{\rm rest})$ is related in the equation of $\kappa_{\rm d}(\nu_{\rm rest}) = \kappa_{850}(\nu/\nu_{850})^\beta$.

### Dust to gas mass ratio

The derived dust to gas mass ratio of $\delta_{\rm GDR}$ ranges 63–90 with $\kappa_{850} = 3.2$ cm$^2$ g$^{-1}$ (Demyk et al., 2017) with LIRGs/ULIRGs conversion factor of $\alpha = 0.8$ for LAB18.b. The range of $\delta_{\rm GDR}$ come from upper limits and lower limits of $T_d$ and $\beta$ from far-infrared SED fitting (see also, Figure 5.11). This value is broadly consistent with central regions of local LIRG/ULIRGs (Wilson et al., 2008).

For the three CO J=4-3 non-detected DSFGs of LAB18.a, LAB18.c, and LAB18.d, the $\delta_{\rm GDR}$ ranges 12–55 with $\kappa_{850} = 3.2$ cm$^2$ g$^{-1}$ (Demyk et al., 2017) with LIRGs/ULIRGs conversion factor of $\alpha$=0.8 from the $3\sigma$ upper limits of CO J=4-3 line emission. This value is lower than the CO detected DSFGs of LAB18.b, reflecting their smaller gas mass. We summarized $\delta_{\rm GDR}$ in Table 5.4.

## 5.7 Results of Optical to Near-infrared Analysis

### Photometric redshift with EAZY

We did not detect CO J=4-3 line emissions from LAB18.a, LAB18.c, and LAB18.d. To investigate possibilities which these sources are associated with the LAB18 at $z = 3.1$, we estimated photometric redshifts (phot-$z$). We use EAZY code (Brammer, van Dokkum, & Coppi, 2008) and SED templates of Bruzual & Charlot (2003). The photometry conducted as follows as Kubo et al. (2013). We used Palomar/COSMIC $U_n$-band (Steidel et al., 2003), Subaru/Suprime-Cam $B, V, R, i', z'$-band (Hayashino et al., 2004), UKIRT/WFCAM $J$ and $K$-band from WFCAM Science Archive in Deep Extragalactic Survey (Lawrence et al., 2007) and *Spitzer*/IRAC 3.6, 4.5, 5.8, 8.0 $\mu$m band (Webb et al., 2009). The $1\sigma$ AB magnitude of $U_n$, $B, V, R, i', z'$, $J$, $K$, 3.6$\mu$m, 4.5$\mu$m, 5.8$\mu$m and 8.0 $\mu$m are 28.1, 28.2, 28.3, 28.4, 28.1, 27.4, 25.1, 24.7, 25.3, 25.1, 23.6, and 23.3 respectively (Steidel et al., 2003; Matsuda et al., 2004; Hayashino et al., 2004; Lawrence et al., 2007; Webb et al., 2009; Kubo et al., 2013). We measured total magnitudes within 2.0″ diameter apertures from optical to near infrared (NIR) band images. We did not use typical point spread function (PSF) matched images due to highly diffused emissions around the four DSFGs. The PSF of $U_n$ to $K$-band is $\sim 1.0''$. IRAC images were measured within 4.0″ diameter apertures and apertures were corrected for total magnitude. Table 5.5 shows results of optical to NIR wavelengths photometry. Figure 5.12 shows the $\chi^2$ distributions as a function of the redshift estimated by EAZY code (solid blue lines). The best fitted photometric redshifts are shown as a black solid line. The black dotted lines show 99% confidence intervals of the photometric redshift, which

Table 5.5: Optical to near-infrared photometry data for four DSFGs in LAB18.

| ID | $U_n$ ($\mu$Jy) | $B$ ($\mu$Jy) | $V$ ($\mu$Jy) | $R$ ($\mu$Jy) | $i'$ ($\mu$Jy) | $z'$ ($\mu$Jy) |
|---|---|---|---|---|---|---|
| LAB18.a | <0.063 | <0.055 | 0.054 ± 0.017 | 0.089 ± 0.015 | 0.100 ± 0.020 | 0.147 ± 0.038 |
| LAB18.b | <0.063 | <0.055 | <0.050 | <0.046 | <0.06 | <0.114 |
| LAB18.c | <0.063 | <0.055 | <0.050 | <0.046 | <0.06 | <0.114 |
| LAB18.d | <0.063 | 0.058 ± 0.018 | 0.069 ± 0.017 | 0.105 ± 0.015 | 0.130 ± 0.020 | 0.176 ± 0.038 |

| ID | $J$ ($\mu$Jy) | $K$ ($\mu$Jy) | 3.6 $\mu$m ($\mu$Jy) | 4.5 $\mu$m ($\mu$Jy) | 5.8 $\mu$m ($\mu$Jy) | 8.0 $\mu$m ($\mu$Jy) |
|---|---|---|---|---|---|---|
| LAB18.a | <0.982 | 2.464 ± 0.481 | 5.432 ± 0.289 | 6.653 ± 0.336 | 11.013 ± 1.265 | 17.971 ± 1.787 |
| LAB18.b | <0.982 | <1.444 | 2.019 ± 0.289 | 3.183 ± 0.336 | 4.896 ±1.265 | 12.778 ±1.787 |
| LAB18.c | <0.982 | 1.359 ± 0.481 | 3.66 ± 0.289 | 5.779 ± 0.336 | 7.599 ± 1.265 | 17.324 ±1.787 |
| LAB18.d | <0.982 | 1.544 ± 0.481 | 4.276 ± 0.288 | 7.032 ± 0.336 | 8.206 ± 1.265 | 12.412 ± 1.787 |

**Notes**. Upper limits are given by $3\sigma$ fluctiations. We used Palomar/COSMIC $U_n$-band (Steidel et al., 2003), Subaru/Suprime-Cam $B, V, R, i', z'$-band (Hayashino et al., 2004), UKIRT/WFCAM $J$ and $K$-band from WFCAM Science Archive in Deep Extragalactic Survey (Lawrence et al., 2007) and *Spitzer*/IRAC 3.6, 4.5, 5.8, 8.0 $\mu$m band (Webb et al., 2009). Optical to NIR band images are not PSF matched due to highly diffused emissions around the four DSFGs in LAB18. We measured total magnitudes within 2.0″ diameter apertures. The typical PSF of $U_n$ to $K$-band is $\sim 1.0''$. IRAC images are measured within 4.0″ diameter apertures and apertures are corrected for total magnitude.

represents uncertainty of the photometric redshift estimates. Implied phot-$z$ of four DSFGs in LAB18 is $z_{\rm phot} \gtrsim 3$ in 99% confidence intervals.

## Optical to near-infrared SED fitting and inferred stellar mass with FAST

We estimated the stellar masses of four DSFGs in the LAB18 by using SED fitting FAST code (Kriek et al., 2009) which is compatible with EAZY code to derive the stellar masses. In the SED fitting, the templates were taken from the population synthesis model of (Bruzual & Charlot, 2003) with a solar metallicity in accordance with previous research on faint DSFGs (e.g., Tadaki et al., 2015; Yamaguchi et al., 2016). We assumed the Chabrier IMF (Chabrier, 2003), the Calzetti extinction law (Calzetti et al., 2000), and exponentially declining star formation histories. Figure 5.13 shows optical to near infrared SEDs fitting results for four DSFGs in the LAB18. We fixed all of the sources are at the redshift of $z = 3.0936 \pm 0.0002$. The derived stellar mass and visual extinction are listed in Table 5.7.

Figure 5.18 shows SFR derived from FIR SED fitting as a function of stellar mass derived from optical/NIR SED fitting. Our four DSFGs are broadly on the main sequence at $z = 3.1$. The yellow shaded region shows main sequence at $z = 3.1$ within the range of three times higher and lower value of the relation (Speagle et al., 2014). Multi-wavelength thumbnails for four DSFGs in LAB18 are shown in Figure 5.15.

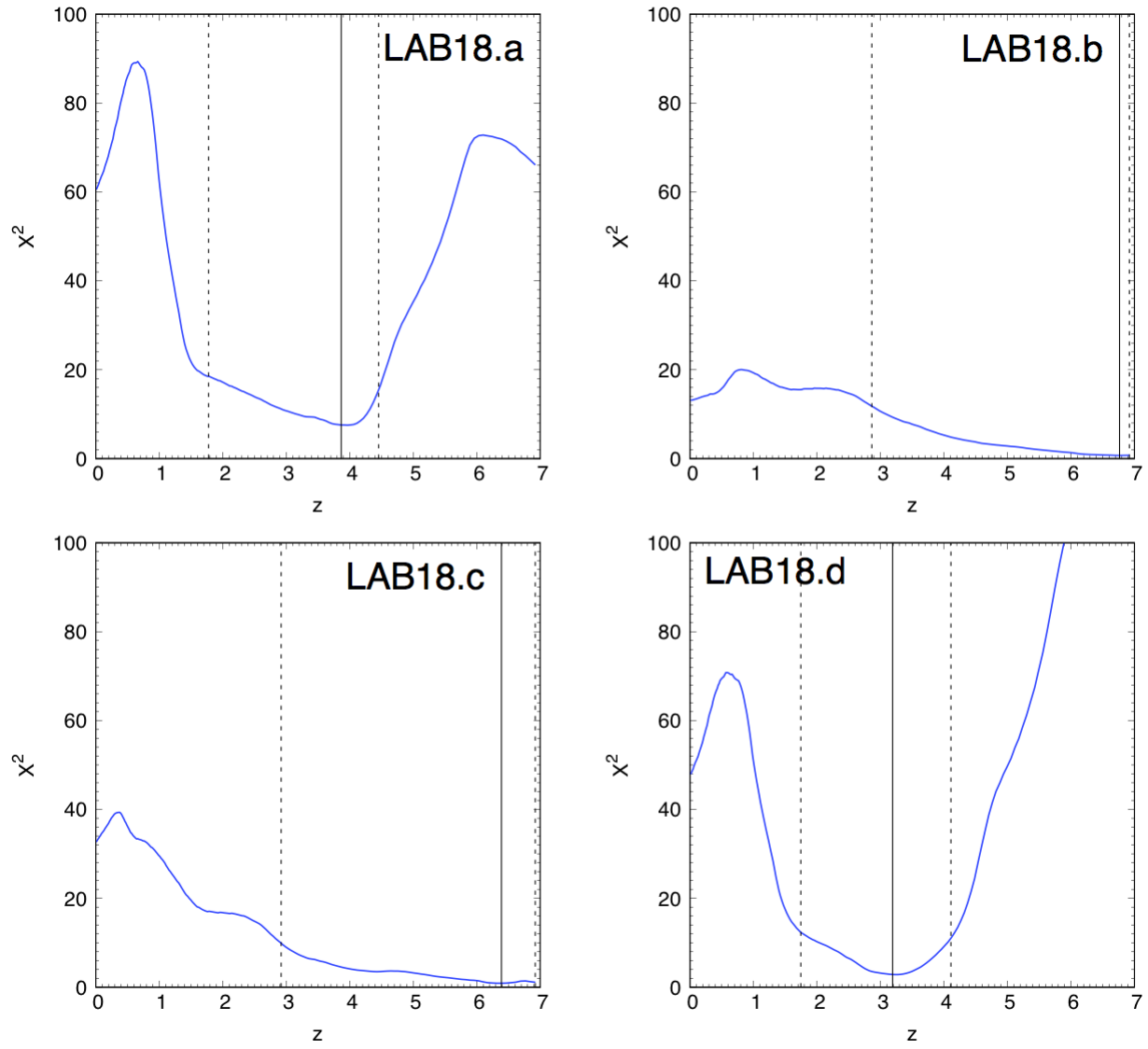


Figure 5.12: The $\chi^2$ distributions as a function of the photometric redshifts estimated by EAZY code (solid blue lines). The best fitted photometric redshifts are shown as a black solid line. The black dotted lines show 99% confidence intervals of the photometric redshift, which represents uncertainty of the photometric redshift estimates. The implied phot-$z$ for four DSFGs in the LAB18 is $z_{\rm phot} \gtrsim 3$ in 99% confidence intervals.

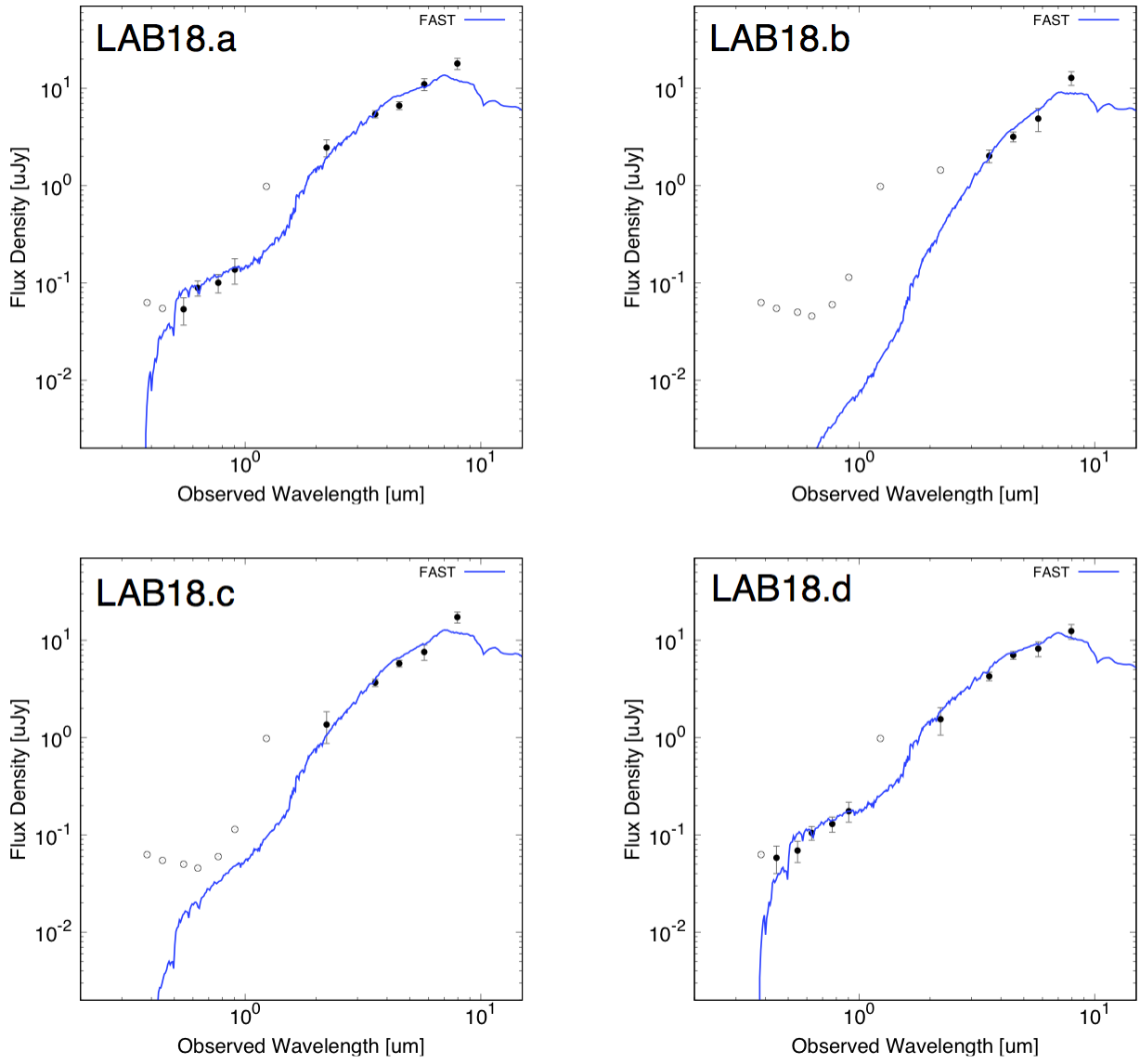


Figure 5.13: The optical to near-infrared SEDs fitting results of four DSFGs in the LAB18. We use FAST code (Kriek et al., 2009). The open circles show 3 $\sigma$ upper limits. We used Palomar/COSMIC $U_n$-band (Steidel et al., 2003), Subaru/Suprime-Cam $B, V, R, i', z'$-band (Hayashino et al., 2004), UKIRT/WFCAM $J$ and $K$-band from WFCAM Science Archive in Deep Extragalactic Survey (Lawrence et al., 2007) and *Spitzer*/IRAC 3.6, 4.5, 5.8, 8.0 $\mu$m band (Webb et al., 2009).

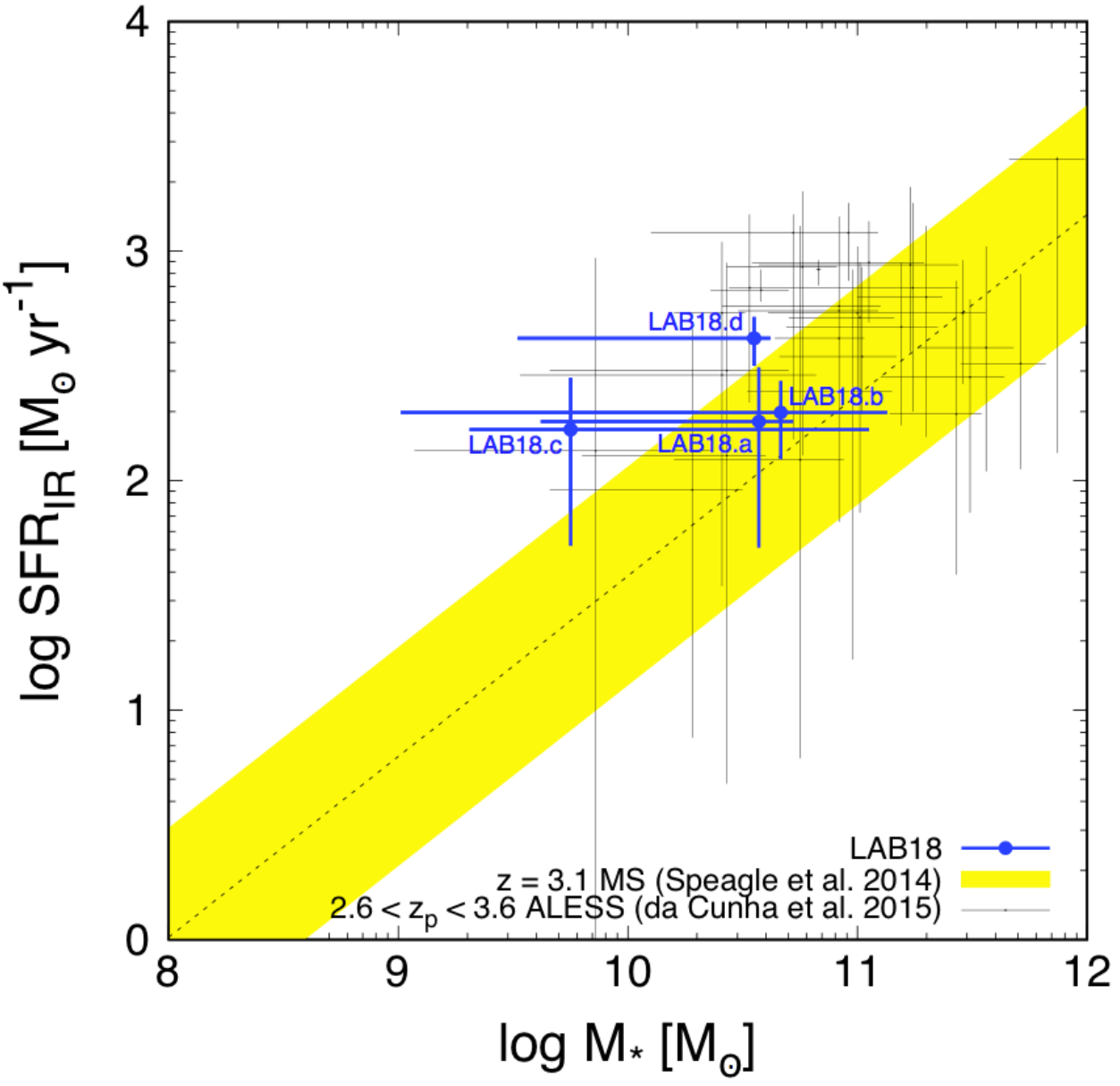


Figure 5.14: SFR vs. stellar mass main sequence plot of four DSFGs in the LAB18. Although there are large stellar mass uncertainties, DSFGs in the LAB18 are likely within the scatter of the star-formation main sequence. We assumed that LAB18.a, LAB18.c, and LAB18.d are located at $z = 3.0936 \pm 0.0002$ as LAB18.b. The relatively large stellar mass uncertainties come from the lack of the detection in the NIR wavelengths (e.g., $J, H, K$-band), which can catch the 4000Å break. Our DSFGs show slightly smaller stellar mass compared with previous ALESS survey with ALMA 870 $\mu$m dust continuum observations (da Cunha et al., 2015).

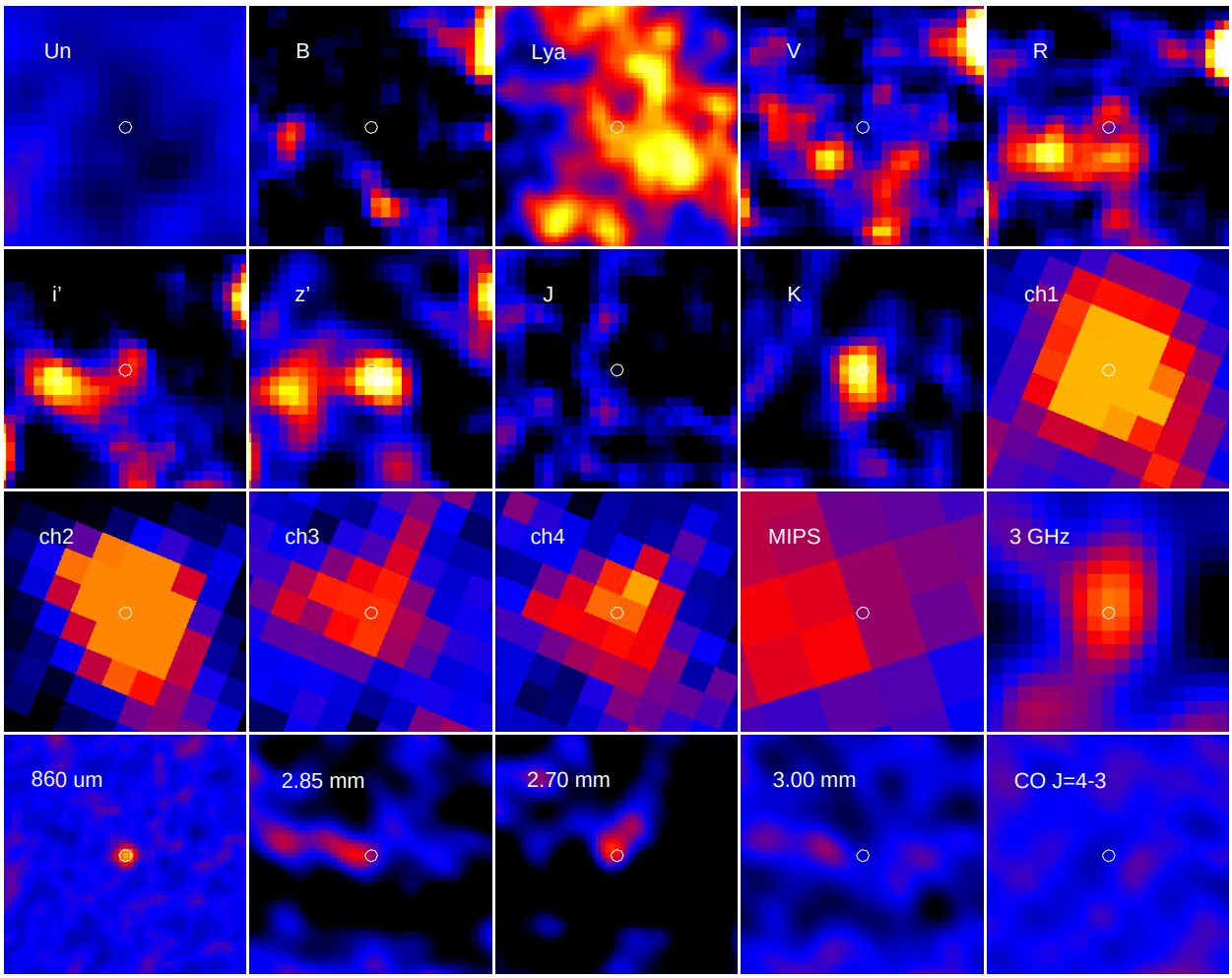


Figure 5.15: (a). Thumbnails of UV to radio wavelength for LAB18.a. The size of each panel is $5'' \times 5''$. From left to right and top to bottom, we show Palomar/COSMIC $U_n$-band (Steidel et al., 2003), Subaru/Suprime-Cam $B, NB497, V, R, i', z'$-band (Hayashino et al., 2004; Matsuda et al., 2004), UKIRT/WFCAM $J, K$-band (Lawrence et al., 2007), *Spitzer*/IRAC and MIPS 3.6 $\mu$m, 4.5 $\mu$m, 5.8 $\mu$m, 8.0 $\mu$m, 24 $\mu$m (Webb et al., 2009), VLA 3 GHz (Ao et al., 2018), ALMA 860 $\mu$m, 2.85 mm, 2.70 mm, 3.00 mm, and CO J=4-3 emission. The white contour shows 5,10,15$\sigma$ level of ALMA 860 $\mu$m. The pixel sizes are $0.1''$ for ALMA 860 $\mu$m, 2.85 mm, 2.70 mm, 3.00 mm, CO J=4-3, and Subaru/Suprime-Cam $NB497$-band, $0.2''$ for Subaru/Suprime-Cam $B, V, R, i', z'$-band and UKIRT/WFCAM $J, K$-band, $0.3''$ for Palomar/COSMIC $U_n$-band and VLA 3 GHz, $0.6''$ for *Spitzer*/IRAC band, and $1.3''$ for *Spitzer*/MIPS band.

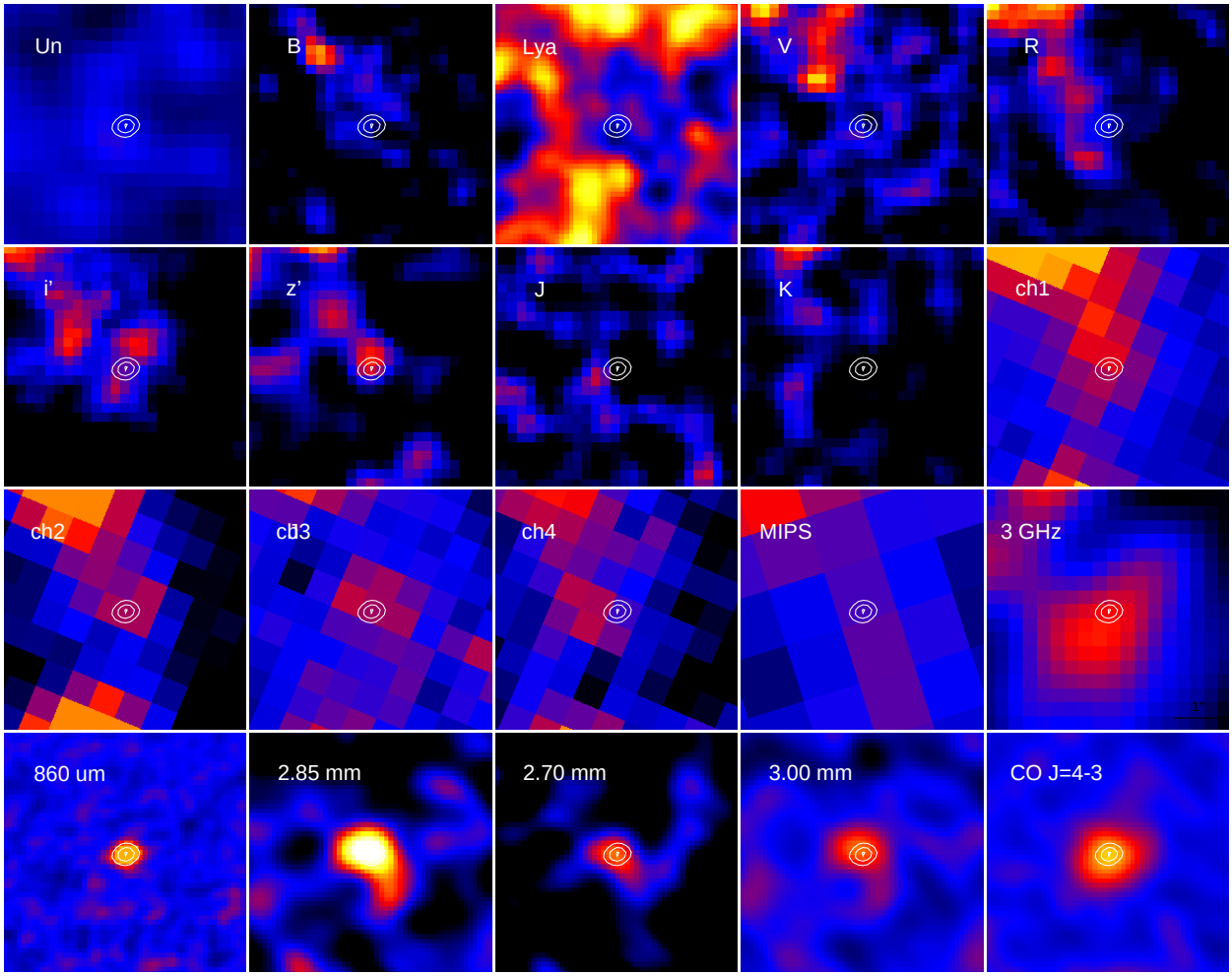


Figure 5.15: (b). Thumbnails of UV to radio wavelength for LAB18.b. The size of each panel is $5'' \times 5''$. From left to right and top to bottom, we show Palomar/COSMIC $U_n$-band (Steidel et al., 2003), Subaru/Suprime-Cam $B, NB497, V, R, i', z'$-band (Hayashino et al., 2004; Matsuda et al., 2004), UKIRT/WFCAM $J, K$-band (Lawrence et al., 2007), *Spitzer*/IRAC and MIPS 3.6 $\mu$m, 4.5 $\mu$m, 5.8 $\mu$m, 8.0 $\mu$m, 24 $\mu$m (Webb et al., 2009), VLA 3 GHz (Ao et al., 2018), ALMA 860 $\mu$m, 2.85 mm, 2.70 mm, 3.00 mm, and CO J=4-3 emission. The white contour shows 5,10,15$\sigma$ level of ALMA 860 $\mu$m. The pixel sizes are $0.1''$ for ALMA 860 $\mu$m, 2.85 mm, 2.70 mm, 3.00 mm, CO J=4-3, and Subaru/Suprime-Cam $NB497$-band, $0.2''$ for Subaru/Suprime-Cam $B, V, R, i', z'$-band and UKIRT/WFCAM $J, K$-band, $0.3''$ for Palomar/COSMIC $U_n$-band and VLA 3 GHz, $0.6''$ for *Spitzer*/IRAC band, and $1.3''$ for *Spitzer*/MIPS band.

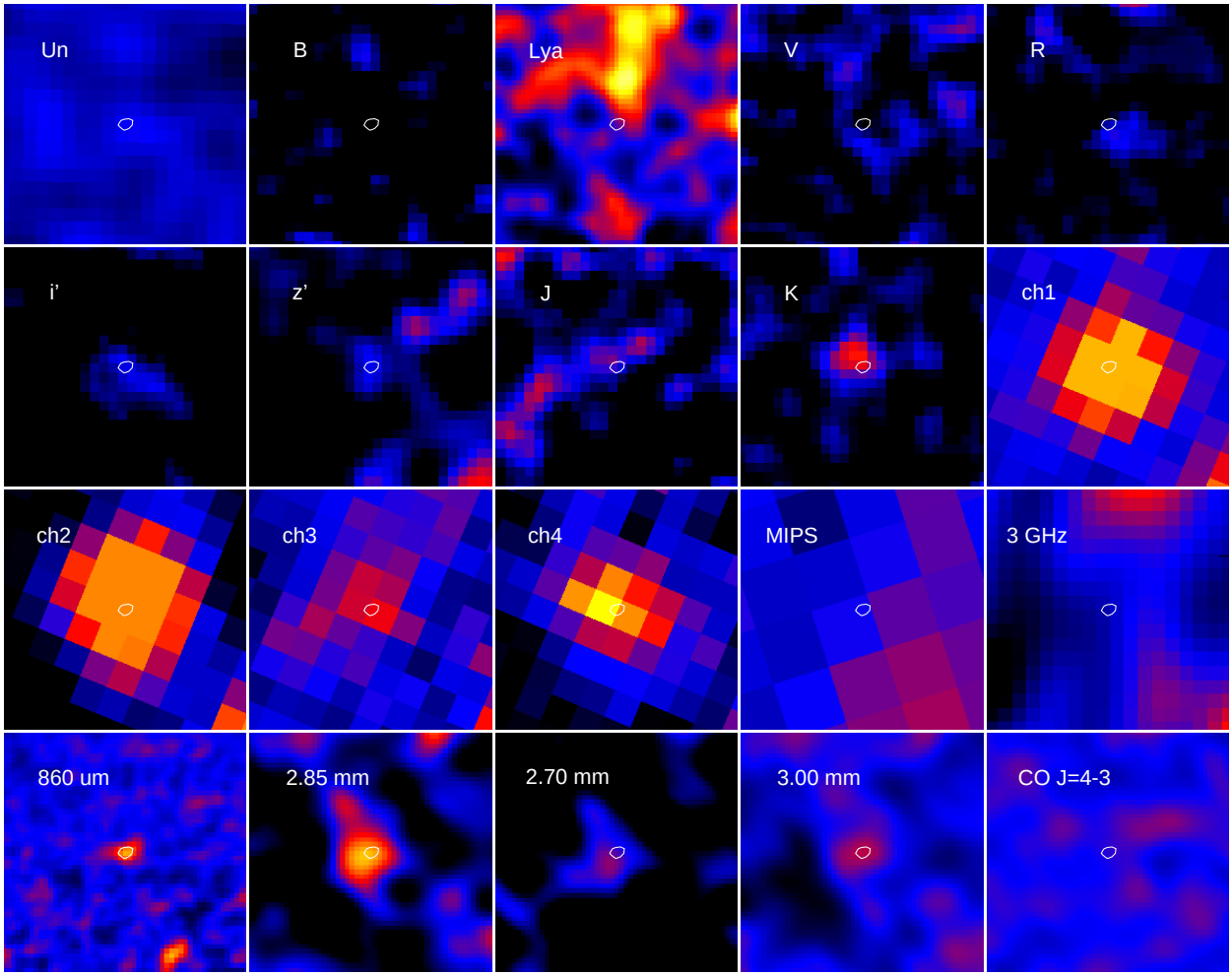


Figure 5.15: (c). Thumbnails of UV to radio wavelength for LAB18.c. The size of each panel is $5'' \times 5''$. From left to right and top to bottom, we show Palomar/COSMIC $U_n$-band (Steidel et al., 2003), Subaru/Suprime-Cam $B, NB497, V, R, i', z'$-band (Hayashino et al., 2004; Matsuda et al., 2004), UKIRT/WFCAM $J, K$-band (Lawrence et al., 2007), *Spitzer*/IRAC and MIPS 3.6 $\mu$m, 4.5 $\mu$m, 5.8 $\mu$m, 8.0 $\mu$m, 24 $\mu$m (Webb et al., 2009), VLA 3 GHz (Ao et al., 2018), ALMA 860 $\mu$m, 2.85 mm, 2.70 mm, 3.00 mm, and CO J=4-3 emission. The white contour shows 5,10,15$\sigma$ level of ALMA 860 $\mu$m. The pixel sizes are $0.1''$ for ALMA 860 $\mu$m, 2.85 mm, 2.70 mm, 3.00 mm, CO J=4-3, and Subaru/Suprime-Cam $NB497$-band, $0.2''$ for Subaru/Suprime-Cam $B, V, R, i', z'$-band and UKIRT/WFCAM $J, K$-band, $0.3''$ for Palomar/COSMIC $U_n$-band and VLA 3 GHz, $0.6''$ for *Spitzer*/IRAC band, and $1.3''$ for *Spitzer*/MIPS band.

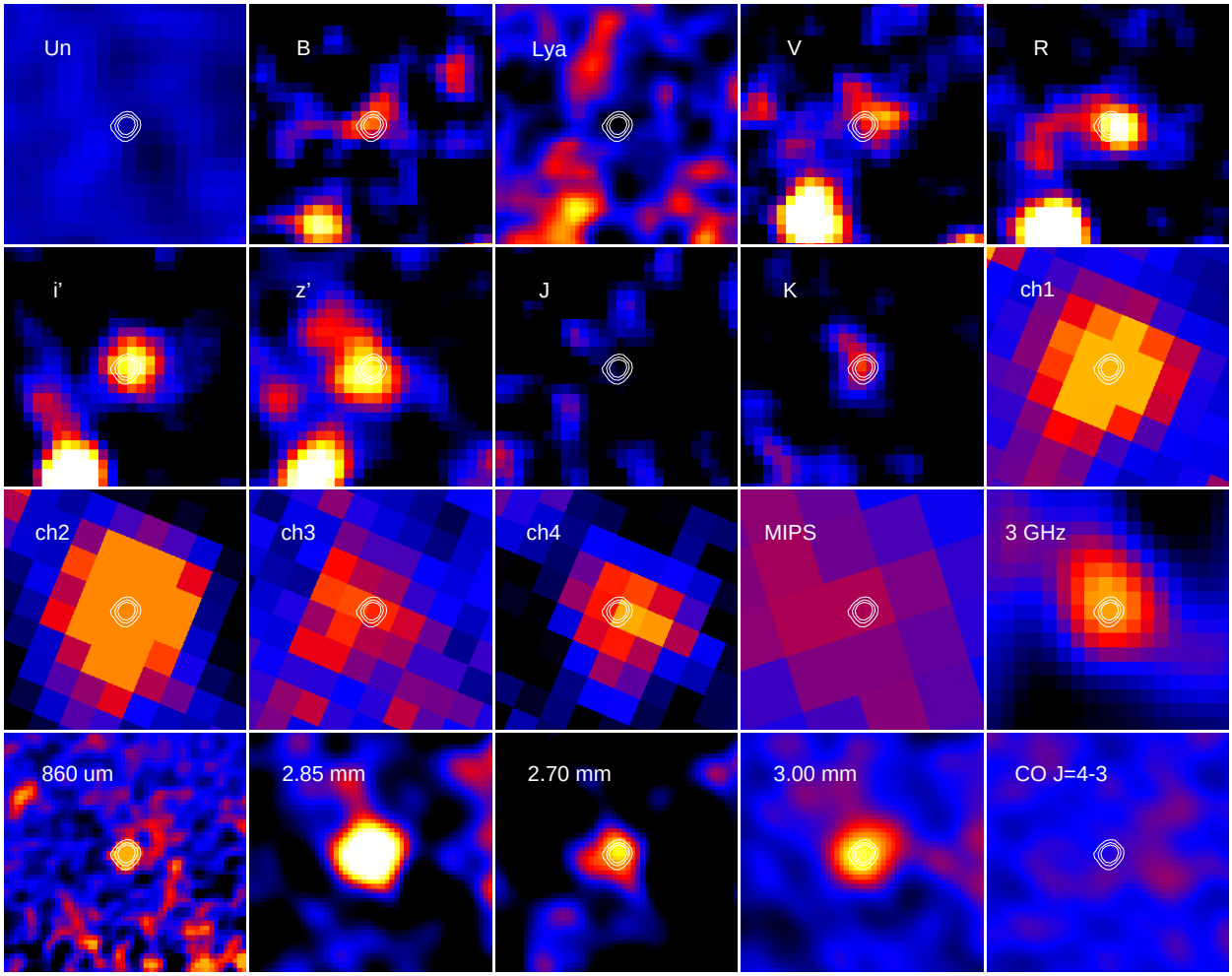


Figure 5.15: (d). Thumbnails of UV to radio wavelength for LAB18.d. The size of each panel is $5'' \times 5''$. From left to right and top to bottom, we show Palomar/COSMIC $U_n$-band (Steidel et al., 2003), Subaru/Suprime-Cam $B, NB497, V, R, i', z'$-band (Hayashino et al., 2004; Matsuda et al., 2004), UKIRT/WFCAM $J, K$-band (Lawrence et al., 2007), *Spitzer*/IRAC and MIPS 3.6 $\mu$m, 4.5 $\mu$m, 5.8 $\mu$m, 8.0 $\mu$m, 24 $\mu$m (Webb et al., 2009), VLA 3 GHz (Ao et al., 2018), ALMA 860 $\mu$m, 2.85 mm, 2.70 mm, 3.00 mm, and CO J=4-3 emission. The white contour shows 5,10,15$\sigma$ level of ALMA 860 $\mu$m. The pixel sizes are $0.1''$ for ALMA 860 $\mu$m, 2.85 mm, 2.70 mm, 3.00 mm, CO J=4-3, and Subaru/Suprime-Cam $NB497$-band, $0.2''$ for Subaru/Suprime-Cam $B, V, R, i', z'$-band and UKIRT/WFCAM $J, K$-band, $0.3''$ for Palomar/COSMIC $U_n$-band and VLA 3 GHz, $0.6''$ for *Spitzer*/IRAC band, and $1.3''$ for *Spitzer*/MIPS band.

Table 5.6: Results of optical to near-infrared SEDs fitting.

| ID | $z^a_{\rm phot}$ (EAZY) | $M^b_*$ ($M_\odot$) | $A^c_{\rm V}$ (mag) | $f^d_{\rm CO}$ (%) |
|---|---|---|---|---|
| LAB18.a | $3.87^{+0.59}_{-2.01}$ | $10.57^{+0.15}_{-0.95}$ | $1.40^{+2.04}_{-1.40}$ | $3^{+17}_{-1}$ |
| LAB18.b | $6.77^{+0.16}_{-3.90}$ | $10.68^{+0.45}_{-1.67}$ | $3.60^{+3.40}_{-3.17}$ | $8^{+73}_{-5}$ |
| LAB18.c | $6.39^{+0.53}_{-3.47}$ | $9.75^{+1.30}_{-0.44}$ | $3.00^{+4.00}_{-2.47}$ | $15^{+18}_{-14}$ |
| LAB18.d | $3.19^{+0.92}_{-1.45}$ | $10.55^{+0.07}_{-1.03}$ | $1.40^{+1.57}_{-0.91}$ | $3^{+20}_{-1}$ |

**Notes**. [a]The error shows 99% confidence intervals calculated with EAZY (Brammer, van Dokkum, & Coppi, 2008). [bc]The error of stellar masses and visual extinction show 99% confidence intervals calculated with Monte Carlo simulations in the SED fitting code FAST (Kriek et al., 2009). [d]The errors come from the stellar mass (column *b*).

### Molecular gas mass fraction

The derived molecular gas mass ($M_{\rm gas}$) and stellar mass ($M_*$) are used to estimate a molecular gas mass fraction, $f_{\rm gas} = M_{\rm gas}/(M_{\rm gas} + M_*)$. We summarize our estimation of $f_{\rm gas}$ in Table 5.7. LAB18.b shows $f_{\rm gas} = 8^{+73}_{-5}$% and CO non-detected sources show $f_{\rm gas} = 3-15$% from $3\sigma$ upper limit of CO J=4-3 luminosity.

We found that our four DSFGs in LAB18 have smaller molecular gas mass fraction compared with other studies of protocluster fields and blank fields. Our average $f_{\rm gas}$ is $7^{+32}_{-5}$% for four DSFGs in the LAB18 at $z = 3.1$. Lee et al. (2017) reported that average $f_{\rm gas}$ for CO J=3-2 line detected H$\alpha$ emitters (HAEs) at $z = 2.5$ protocluster is $55 \pm 7$%. Tacconi et al. (2017) also shows $f_{\rm gas} = 56$% at $z = 3.0936$ ($\log \mu = 0.12 - 3.62(\log(1 + z) - 0.66)^2$, where $\mu = M_{\rm gas}/M_*$). Thus, our four DSFGs in the LAB18 show low molecular gas mass fraction. However, we need deep near-infrared observations to decrease stellar mass uncertainties for sure discussions.

## 5.8 Discussions

Here we discuss (1). CO J=4-3 morphology and kinematics of LAB18.b, (2). $L_{\rm FIR}$ and $L'_{\rm CO(4-3)}$ relation and small gas depletion time of LAB18.b, (3). Large $\beta$ and small $T_d$ of LAB18.b, and (4). possible origins of DSFGs and LAB18, which all of them are related to formation and evolution of DSFGs and LABs.

### 5.8.1 CO J=4-3 morphology and kinematics of LAB18.b

In the galactic superwind model of LABs, the origin is attributed to star-formation induced by galaxy-galaxy mergers/interactions (e.g., Taniguchi & Shioya, 2000; Mori & Umemura, 2006) and/or AGNs. Here we discuss whether LAB18.b has sings of galaxy-galaxy mergers, and/or, rotational disk. We follow the step of Wisnioski et al. (2015).

#### Velocity moment map

First, we investigated a velocity moment map of LAB18.b. Figure 5.7 right shows a CO J=4-3 velocity moment map of LAB18.b. We show the only pixels which have S/N level above $3\sigma$. The velocity gradient

Table 5.7: Kinematic parameters of LAB18.b.

| ID | | LAB18.b |
|---|---|---|
| $v_{\rm circ}^{a}$ | (km s$^{-1}$) | $41^{+3}_{-2}$ |
| $i^{b}$ | (°) | $71 \pm 11$ |
| $\sigma_0^{c}$ | (km s$^{-1}$) | $34 \pm 2$ |
| $v_{\rm circ}/\sigma_0$ | (–) | $1.2 \pm 0.1$ |

**Notes.** $^{a}v_{\rm circ}$ is estimated from $v_{\rm circ} \sin i = (v_{\rm red} - v_{\rm blue})/2$, where $i$ is inclination. $v_{\rm red}$ and $v_{\rm blue}$ is central velocity estimated from Gaussian fitting for each components. $^{b}$Inclination is given by $\cos i = b/a$, where $a$ and $b$ are major and minor axis of CO. $^{d}$We estimated local velocity dispersion by fitting line width of blue component.

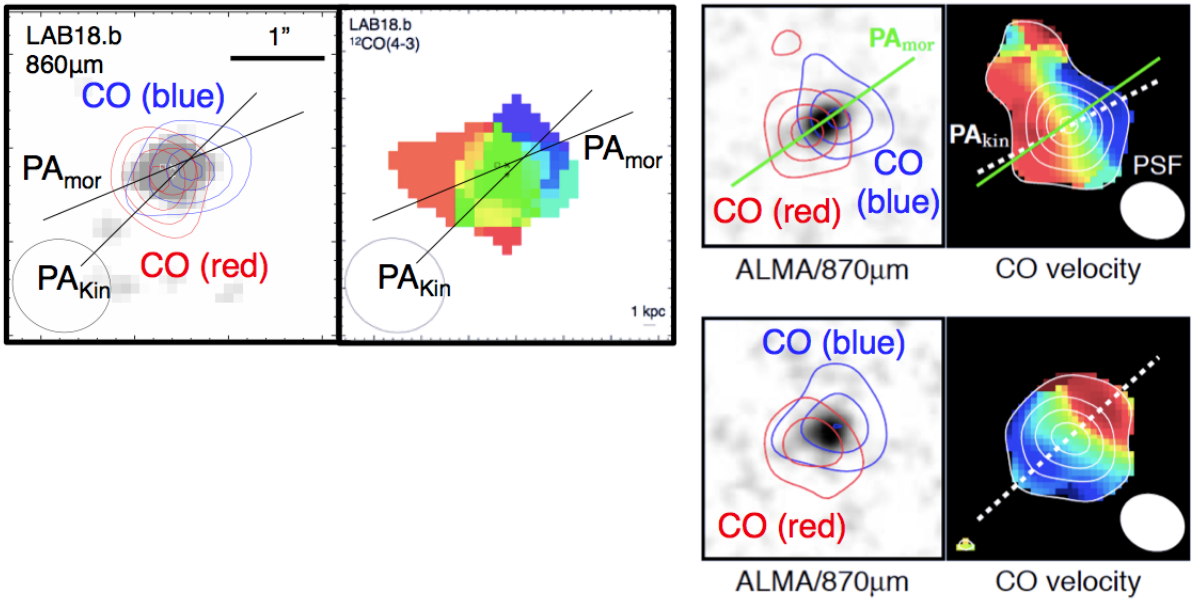


Figure 5.16: (left): We show the contours of red and blue component of CO J=4-3 line emission over the 860 $\mu$m dust continuum emission of LAB18.b at $z = 3.1$. We also show the CO J=4-3 velocity moment map. (right): The ordered rotation of CO J=3-2 molecular disks and dusty starburst bulge is reported in $z = 2.5$ massive ($\log M_*(M_\odot) > 11$) galaxies with $v_{\rm circ}/\sigma_0 = 4 - 7$ (Tadaki et al., 2017). We might see the ancestor of such massive galaxies. LAB18.b becomes large $v_{\rm circ}/\sigma_0$ and stellar mass as redshift, and would evolve massive galaxies in Tadaki et al. (2017). The scale of images are arranged.

seems to be different from the case of rotational disks. The peak locations of maximum positive (red) and negative (blue) velocity component shows asymmetry distribution. We also make velocity map by fitting a Gaussian function to the CO J=4-3 line spectrum in each spatial pixel. However, we couldn't see such monotonic velocity gradient expected from ideal rotation of the molecular gas. We need more spatial resolution to see the kinematics from velocity map.

### Circular velocity to local velocity dispersion ratio

Second, we investigated $v_{\rm circ}/\sigma_0$, where $v_{\rm circ}$ is an inclination corrected circular velocity and $\sigma_0$ is a local velocity dispersion. In Wisnioski et al. (2015), $v_{\rm circ}/\sigma_0 > 1$ suggests rotational disk. $v_{\rm circ}$ is estimated from $v_{\rm circ} \sin i = (v_{\rm red} - v_{\rm blue})/2$, where $i$ is an inclination. We estimated $v_{\rm red}$ and $v_{\rm blue}$ from CO J=4-3 line spectrum (Figure 5.7 left) by assuming Gaussian profile for each components. The Inclination is estimated from $\cos i = b/a$, where $a$ and $b$ are major axis and minor axis of CO J=4-3 emission. The estimated inclination is $i = 70.8 \pm 11.4°$. Thus, the estimated circular velocity is $v_{\rm circ} = 41^{+3}_{-2}$ km s$^{-1}$. $\sigma_0$ is difficult to estimate especially for the case of edge-on galaxy, because of the contribution of the radial rotational velocity. However, by assuming that CO J=4-3 spectrum line width of blue component (larger than the red component) is reflecting $\sigma_0$, we estimated local velocity dispersion of $\sigma_0 = 34 \pm 2$ km s$^{-1}$. Thus, the estimated ratio of circular velocity and local velocity dispersion is $v_{\rm circ}/\sigma_0 = 1.2 \pm 0.1$. This suggests the circular velocity is slightly higher than the local velocity dispersion. Compared with the $z = 2$ samples in Wisnioski et al. (2015), LAB18.b has a much lower $v_{\rm circ}/\sigma_0$ value. This suggests that even if LAB18.b has a rotational disk, the local velocity dispersion is much higher, and a highly unstable disk is expected. This is consistent with the redshift evolution of $v_{\rm circ}/\sigma_0$ in Wisnioski et al. (2015), the galaxies at higher redshift have lower values of $v_{\rm circ}/\sigma_0$.

### Location of the velocity dispersion peak

Third, we checked whether the location of the velocity dispersion peak corresponds to the location of systematic velocity of $v_{\rm sys} = 0$ km s$^{-1}$. We found that the location of the velocity dispersion peak is south-east from the peak position of the CO J=4-3 line emission. This is due to the elongated shape of blue component, whose direction is from north-west to south-east (Figure 5.7, middle right and right planels). We can see this elongated shape in -40 and -60 km s$^{-1}$ component of Figure 5.9. Same trend is seen at the velocity map by fitting a Gaussian function to the CO J=4-3 line spectrum in each spatial pixel. This might suggest the existence of turbulent gas motion and/or inflows/outflows.

### Kinematic major axis and morphological major axis

Finally, we checked whether the kinematic major axis of CO J=4-3 line emission corresponds to the morphological major axis of 860 $\mu$m dust continuum emission. We note that there are no deep and spatially resolved near infrared (NIR) imaging data, we cannot compare the morphology of stellar components for LAB18.b. We found that the difference between $\rm PA_{kin}$ and $\rm PA_{mor}$ is $22 \pm 6$ °, could suggest dust component and CO molecular gas component have ordered rotation. The positions of the flux peak of CO J=4-3 line emission and dust continuum emission are almost same, and CO spatial FWHM ($\sim 6$ kpc) is larger than the dust spatial

FWHM ($\sim$ 2kpc). This situation is very similar to the $z = 2.5$ massive ($\log M_*(M_\odot) > 11$) galaxies with $v_{\rm circ}/\sigma_0 = 4-7$ (Tadaki et al., 2017). We might see an ancestor of such massive galaxies with compact dusty star-forming cores and more extended, highly rotational dominant molecular gas disks. LAB18.b becomes large $v_{\rm circ}/\sigma_0$ as redshift, and would evolve massive galaxies in Tadaki et al. (2017).

### Summary of CO J=4-3 Morphology and Kinematics of LAB18.b

We summarized morphology and kinematics parameters of LAB18.b in Table 5.3 and Table 5.7. Kinematic major axis and morphological major axis and $v_{\rm circ}/\sigma_0 = 1.2 \pm 0.1$ suggests LAB18.b has rotational disks. However, it is far from un ideal case of rotation dominated disks from velocity moment map and location of the velocity dispersion peak. We found elongated shape of blue component, whose direction is from north-west to south-east, could suggest the existence of turbulent gas motion and/or inflows/outflows. We show the comparison of LAB18.b at $z = 3.1$ with massive galaxies at $z = 2.5$ in Tadaki et al. (2017) in Figure 5.16.

It is also possible that LAB18.b is two face-on galaxies due to the very small ($\sim$ 120 km s$^{-1}$) velocity FWHM, although the $b/a$ shows highly edge-on galaxies. For instance, Ueda et al. (2014) reported that late stage mergers and/or merger remnants has also rotational disks. We need more spatial and spectroscopically resolved observations for sure discussion about morphology and kinematics.

## 5.8.2 Small $L'_{\rm CO(4-3)}/L_{\rm FIR}$ ratio and small $\tau_{\rm dep}$ of LAB18.b

$L_{\rm FIR}$ is well correlated with $L'_{\rm CO(4-3)}$. We show $L_{\rm FIR}$ and $L'_{\rm CO(4-3)}$ relation in Figure 5.17. We added $3\sigma$ upper limits of $L'_{\rm CO(4-3)}$ with assuming LAB18.a, LAB18.c and LAB18.d are at $z = 3.0936 \pm 0.0002$. The $L'_{\rm CO(4-3)}$ of four DSFGs in the LAB18 are relatively low compared with $L_{\rm FIR}$, and they are outside of $1\sigma$ scatter of the data points in Greve et al. (2014).

The timescale of dusty star-formation in DSFGs is represented as the molecular gas depletion timescale, $\tau_{\rm dep}$, which is derived from molecular gas mass ($M_{\rm gas}$) over star formation rate (SFR). For LAB18.b, the derived $\tau_{\rm dep}$ is $22^{+14}_{-6}$ Myr with assuming $\alpha$=0.8. The errors come from estimation of far-infrared luminosity (*Herschel*/SPIRE 250 $\mu$m upper limits and lower limits). For the CO non-detected sources of LAB18.a, LAB18.c, and LAB18.d, we derived $\tau_{\rm dep}$ by assuming 3 $\sigma$ CO J=4-3 luminosity with $\alpha$=0.8. We summarized the $\tau_{\rm dep}$ in Table 5.8 and Figure 5.17.

The derived $\tau_{\rm dep} = 22^{+14}_{-6}$ Myr for LAB18.b at $z = 3.0936$ is significantly lower than the average value of 558 Myr from recent work in Tacconi et al. (2017), which gives $\log \tau_{\rm dep} = 0.083 - 0.5 \log 10(1 + z)$ for normal star-forming galaxies. Typically, four different timescales are assumed for DSFGs when the depletion timescale is discussed. For local ULIRGs, it is assumed $\sim$50 Myr Solomon & Sage (1988), for the typical DSFGs and upper limit to QSO lifetimes, it is assumed $\sim$100 Myr (Greve et al., 2005), for some longer lived DSFGs at high-redshift, it is assumed $\sim$150 Myr (Swinbank et al., 2014), and for a DSFG timescale which is on the massive end of the galaxy main sequence, it is assumed $\sim$500 Myr (Elbaz et al., 2011). Derived $\tau_{\rm dep} = 22^{+14}_{-6}$ Myr for LAB18.b at $z = 3.0936$ is lower than the local ULIRGs, and is between early stage mergers ($16^{+6}_{-4}$ Myr) and merging galaxies ($60^{+30}_{-20}$ Myr) (Casey, Narayanan, & Cooray, 2014). Indeed, two LIRGs (NGC7771 and MCG+12-02-001) show similar $L'_{\rm CO(4-3)}/L_{\rm FIR}$ values to the LAB18.b in Figure 5.17, which are initial stage of merging galaxies and systems. Thus, LAB18.b could be a initial stage

Table 5.8: Gas depletion time scale for four DSFGs in the LAB18.

| ID | $\tau^{a}_{\rm dep,\ CO}$ (Myr) |
|---|---|
| LAB18.a | $<20$ |
| LAB18.b | $22^{+14}_{-6}$ |
| LAB18.c | $<19$ |
| LAB18.d | $<3$ |

**Notes**. [a]We use the conversion factor of $\alpha$=0.8. For the CO J=4-3 line non-detected sources of LAB18.a, LAB18.c, and LAB18.d, we show the values from $3\sigma$ upper limit of CO J=4-3 luminosity and SFR lower limit.

of merging galaxies, although there are no significant merger signs (see also §5.8.1). We need more spatially and spectroscopically resolved observation to discuss this.

In protoclusters, simultaneously galaxy-galaxy mergers or much longer molecular gas depletion times are possible explanations to a concentrations of DSFGs. However, we found a very low gas depletion time for LAB18.b. We need further observation and statistical samples to discuss this.

### 5.8.3 Large $\beta$ and small $T_d$ of LAB18.b

The dust emissivity index of $\beta$ has been studied, usually in the range of $\beta = 1.0 - 2.5$, and is not the same in all galaxies and may also vary within galaxies (Hildebrand, 1983; Dunne, Eales, & Edmunds, 2003; Blain, Barnard, & Chapman, 2003; Chapin et al., 2011; Casey, 2012; Smith et al., 2013; Clements et al., 2017). Multi-band flux measurements of dust thermal emission in the Rayleigh-Jeans tail provide the most accurate estimation of $\beta$, as the slope in the long wavelength limit is independent on dust temperature of $T_d$. ALMA observations enable us to measure precise $\beta$ and investigate the differences among the galaxy population and/or optical properties of dust grains for high-$z$ galaxies.

In the situation of the dust grains in extragalactic galaxies, the $\beta$ only depends on optical properties of dust grains. In the typical case of dust grains size ($\lesssim 0.1$ $\mu$m) in interstellar mediums (ISMs), the dust emissivity index of $\beta$ does not change in terms of the dust grains size (i.e., dust size of $a \ll \lambda$). The $\kappa_\nu$ is monotonically decreasing by dust grains size, and thus its frequency dependence of $\beta$ has a constant value (e.g., the galactic ISM value is 1.7 in Ricci et al., 2010). However, the converged $\beta$ of dust grains in ISMs can be changed by dust composition. For instance, the $\beta > 2.0$ is reproduced at the condition of Mg-rich glassy silicates dust with the dust temperature range of 10-30 K (Demyk et al., 2017). The higher $\beta$ corresponds to mass absorption coefficient is higher than that of lower $\beta$. This means the optical properties of dust grains are more emissive. If we use typical interstellar dust value of $\beta = 1.8$ in the Galaxy, the dust mass would be overestimated.

Figure 5.18 shows location of LAB18.b on dust emissivity index $\beta$ vs. $T_d$ space. We note that Yang et al. (2014) also indicates $\beta > 2.0$ for LABd05, and steeper $\beta$ for LAB18. Nonetheless LAB18.b shows $L_{\rm FIR} \gtrsim 10^{12}\ L_\odot$, the location of the $\beta$ vs. $T_d$ space is very similar to the local metal rich, gas poor early type galaxies (Cortese et al., 2014), instead of local ultraluminous infrared galaxies (ULIRGs) (Clements et al., 2017). This situation is similar to our CO J=4-3 observation for LAB18.b, which indicates small molecular

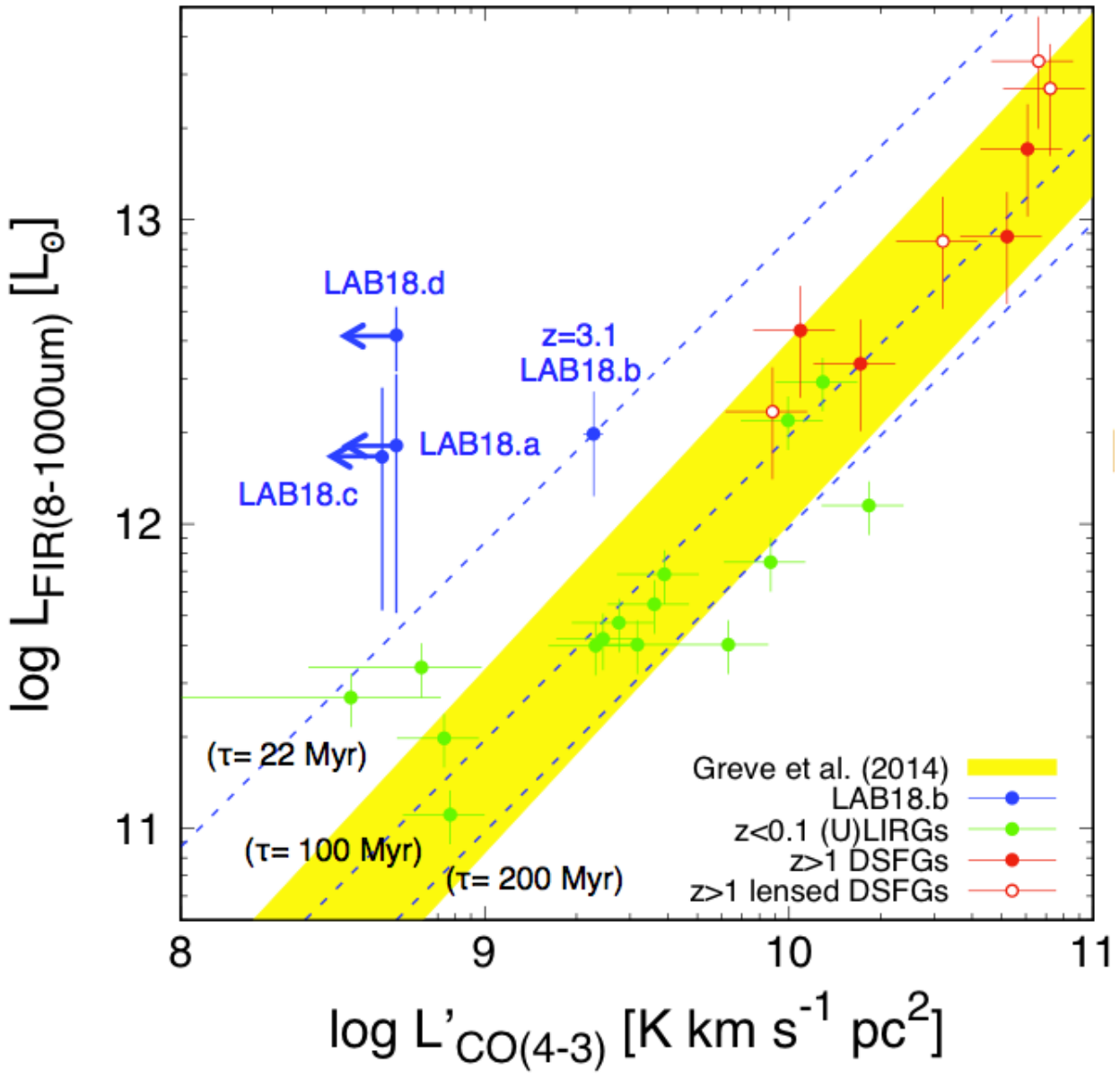


Figure 5.17: $L_{\rm FIR}$ vs. $L'_{\rm CO(4-3)}$ relation for four DSFGs in the LAB18. We assume that LAB18.a, LAB18.c and LAB18.d are at $z = 3.0936$. The yellow shaded region is scatter of the data points in Greve et al. (2014). Our DSFGs in the LAB18 imply significantly lower value of $L'_{\rm CO(4-3)}$ compared to $L_{\rm FIR}$ even for the CO detected source of LAB18.b at $z = 3.0936$. This could suggest $\tau_{\rm dep}$ is very low, although there are systematic uncertainties to estimate gas mass from CO J=4-3 luminosity. The dotted blue lines correspond to labeled gas depletion times. We can see typical gas depletion time of $\tau_{\rm dep} = 100 - 200$ Myr for other DSFGs.

gas fraction of 8%. We may see the evolution from DSFGs to the early type galaxies on the $\beta$ vs. $T_d$ space. ALMA long wavelength multi-band continuum observations will reveal differences of $\beta$ among the various galaxy populations and optical properties of interstellar dust grains.

### 5.8.4 Possible origins of DSFGs and LAB18

Here we discuss possible origins of DSFGs and LAB18.

#### Photoionization

We see the extended star-forming regions and the diffuse hydrogen gas surrounding the galaxies in the photoionization model. Indeed, LAB18 has been reported that there are extended UV continuum emissions (Matsuda et al., 2004; Webb et al., 2009) (see also Figure 5.6). We revealed that the extended UV continuum emissions are along the direction from LAB18.a to LAB18.b with ALMA 860 $\mu$m observation.

Geach et al. (2016) conducted a high resolution cosmological hydrodynamic simulation with radiative transfer to develop a hypothesis about the role of the DSFGs in contributing to the SSA22-LAB1. They successfully reproduce observational properties of LAB1, and suggest the importance of satellite galaxies in the LABs for photoionization model. The *HST*/STIS image of LAB1 shows UV continuum emissions around DSFGs, and they possibly represent a population of low-mass star-forming satellite galaxies surrounding the DSFGs. They concluded that satellite galaxies contribute to growth of DSFGs thorough accretions onto them. Although the CO J=4-3 line emission is not detected around Subaru/$R$-band UV continuum emission and *HST*/ACS F814W continuum emission in the LAB18, these diffuse UV continuum emissions might reflect satellite galaxies accreting onto LAB18.a and LAB18.b.

AGNs are also the possible origin of the ionized photons. Since LAB18 has one X-ray detection (Geach et al., 2009), at least one galaxy could have X-ray AGN. Although the X-ray positional accuracy is not so high, LAB18.b and LAB18.c are the possible counterpart of their X-ray detections. Geach et al. (2009) shows that the UV luminosities of the AGN are easily capable of powering the extended Ly$\alpha$ emission via photoionization. Our one X-ray detection and the larger total SFR of four DSFGs in LAB18 ($\sim$550 $M_\odot$ yr$^{-1}$) compared with LAB1 ($\sim$300 $M_\odot$ yr$^{-1}$), suggesting that photoionization is possible origin of LAB18.

#### Galactic Superwind

We found SFR surface densities of the LAB18.a, LAB18.b, LAB18.c and LAB18.d range 18$-$120 $M_\odot$ yr$^{-1}$ kpc$^{-2}$, which is much higher than the threshold of galactic superwinds for high-$z$ star-forming clumps (1 $M_\odot$ yr$^{-1}$ kpc$^{-2}$; Newman et al., 2012). This suggests that large-scale gas outflows can be induced by four DSFGs, LAB18.a, LAB18.b, LAB18.c and LAB18.d. This is the lower limit of star-formation rate surface density since these are derived from the peak flux density and the synthesized beam area. Thus, the galactic superwind is possible scenario to illuminate LAB18. Our one X-ray detection could also suggest the possibility of the AGN driven galactic superwind.

Recent numerical simulations suggest that galactic superwinds increase the atomic hydrogen gas covering fractions in galaxy halos by carrying gas to larger galactocentric radii (Rahmati et al., 2015; Faucher-Giguère et al., 2015, 2016). The galactic superwinds also could be very useful in promoting the escape of Ly$\alpha$ photons

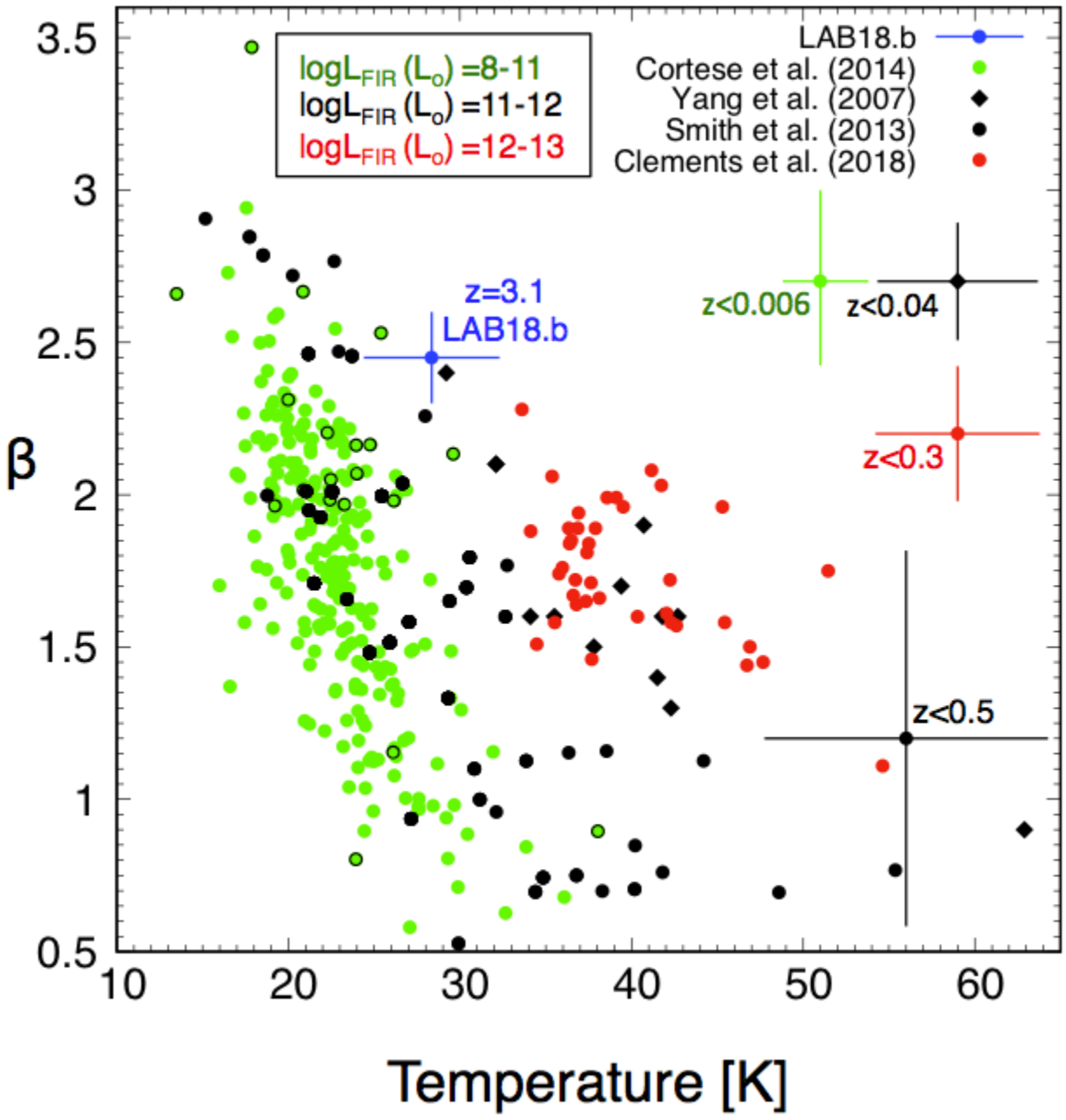


Figure 5.18: Distribution of dust temperature and $\beta$ for various $L_{\rm FIR}$ galaxies. Compilation from Yang & Phillips (2007) for black points, Smith et al. (2013) for black diamonds, Cortese et al. (2014) for green points, and Clements et al. (2017) for red points. The points with black circles for Cortese et al. (2014) show locations of early type galaxies.

from the galaxies, which can then scatter within circumgalactic gas. Our large velocity offset between Ly$\alpha$ line emission and CO J=4-3 emission ($\Delta\ v\ =\ 762$ km $s^{-1}$, see §5.5) also suggests existence of galactic superwinds. The existence of strong galactic superwinds might blow out the large amount of the gas mass, and then might induce relatively low gas mass fraction and gas depletion time of LAB18.b. LAB18 might be reflect a dying nebulae.

### Inflowing gas

It is suggested that the gas circulation between galaxies and the surrounding IGMs are important processes for galaxy formation and evolution across cosmic time (e.g., Kereš et al., 2005; Dekel et al., 2009). Such extended gaseous structures, gas circulation and/or inflowing gas are expected to be seen as LABs around high-$z$ galaxies. Although it is hard to examine the formation mechanisms of LABs only from the Ly$\alpha$ morphologies, the highest filamentarity of LAB18 may relate to inflowing gas from the surrounding IGMs (Matsuda et al., 2011b).

Although the extended gaseous structure of CO J=4-3 line emissions could not been seen, LAB18 has very low gas mass and depletion time (see Figure 5.17 and §5.6). LAB18.b is depleted their gas mass within $22^{+14}_{-6}$ Myr with current SFR, and achieved stellar mass is $5.2\times10^{10}M_{\odot}$ if all of the gas mass is converted to stellar mass. Thus, LAB18.b could not evolve massive galaxies in local clusters with stellar mass above $\sim 10^{11}M_{\odot}$ unless outer gas feeds into the galaxy and/or galaxy mergers are occurred. Although the Ly$\alpha$ emission surrounding four DSFGs could be illuminated by galactic superwinds and photoionization, LAB18.b needs outer gas to evolve more massive galaxies. Although the CO J=4-3 line emission is not detected around $R$-band UV continuum emission whose shape is elongated from LAB18.a and LAB18.b, these might reflect satellite galaxies with inflowing gas accreting onto DSFGs as discussed for SSA22-LAB1 in (Geach et al., 2016).

## 5.9 ALMA Observations Summary

Simultaneously galaxy-galaxy mergers or much longer molecular gas depletion times are possible explanations to concentration of DSFGs in protoclusters. The key observational challenge is to investigate the morphology (i.e., to see whether DSFGs show signatures of galaxy-galaxy merger or not), measure molecular gas mass and molecular gas depletion time, and search for the extended gaseous structure such outflows/inflows for DSFGs in protoclusters.

LABs are ∼100 kpc scale Ly$\alpha$ emitting nebula primarily found at protoclusters. The targeted LAB18 in the $z = 3.1$ SSA22 protocluster is previously known with the highest $S_{850}$ flux density and the filamentary structure of Ly$\alpha$ emission, and diffuse UV emissions. However, the lack of the precise spatial information, spectroscopically redshift information, and kinematic information prevent us to discuss possible origins of DSFGs and LAB18 and relation between DSFGs and protoclusters.

We conducted ALMA Cycle 2 Band 7 and Cycle 4 Band 3 observations for LAB18. LAB18 is one of the *Herschel*/SPIRE sources, SSA22-SPIRE394 in §4. Main results are as follows:

- **Detections of 860 $\mu$m dust continuum emissions from LAB18;**
  In ALMA Cycle 2 Band 7 observations, we found that LAB18 consists of four 860 $\mu$m dust continuum sources, LAB18.a, LAB18.b, LAB18.c, and LAB18.d. They are aligned ∼100 kpc Ly$\alpha$ filamentary structure of LAB18.

- **Detection of CO J=4-3 emission from LAB18.b;**
  In ALMA Cycle 4 Band 3 observations, we detected CO J=4-3 line from one of the DSFGs, LAB18.b. The CO based spectroscopically redshift is $z = 3.0936 \pm 0.0002$, which is blueshifted compared with the Ly$\alpha$ spectroscopy of $z = 3.014$. The large velocity offset between CO line emission and Ly$\alpha$ line emission, and a one X-ray detection suggest possible existence of strong galactic superwind. With the median CO J=4-3 luminosity to CO J=1-0 luminosity ratio of $r_{41} = 0.41$ for SMGs and the consensus value of CO to $H_2$ conversion factor of $\alpha_{\rm CO} = 0.8$ for local (U)LIRGs and distant SMGs/QSOs, we derive $M_{\rm gas} = (4.4 \pm 0.3) \times 10^9 M_\odot$ for LAB18.b. For CO non-detected ALMA sources, we derive $3\sigma$ upper limit with the same manner as LAB18.b, the derived $3\sigma$ upper limit gas mass of $M_{\rm gas} = 1.0 \times 10^9\ M_\odot$.

- **Detection of 2.85 mm dust continuum emissions from LAB18;**
  In ALMA Cycle 4 Band 3 observations, we detected 2.85mm (rest-frame 700 $\mu$m) dust continuum emissions from four DSFGs in LAB18. The longer part of far-infrared wavelength is very useful to estimate dust mass, because the Rayleigh-Jeans tail is likely to be optically thin. We estimated dust mass, and found that our four DSFGs in the LAB18 have $M_{\rm dust} = (1.8-8.1)\times10^7$ $M_\odot$. This corresponds to the usual range of $\delta_{\rm GDR}$, $\delta_{\rm GDR} = 12 - 90$. Combining *Herschel*/SPIRE 250 $\mu$m and ALMA Band7 860 $\mu$m flux densities, we conducted far-infrared SEDs fitting by using optically thin, single temperature modified black body radiation as $\beta$ and $T_d$ free parameters. We assumed that LAB18.a, LAB18.c and LAB18.d are located at $z = 3.0936$. We found that four DSFGs in the LAB18 have ULIRGs class far-infrared luminosities of $L_{\rm FIR} = (1.7 - 4.2) \times 10^{12}$ $L_\odot$.

- **Optical to Near-infrared Analysis**; We estimated photometric redshifts for four DSFGs in the LAB18 by using rest-frame optical to near-infrared data points. The implied phot-$z$ of four DSFGs in

LAB18 is $z_{\rm phot} \gtrsim 3$ in 99% confidence intervals. We also estimated the stellar masses of DSFGs in the LAB18 by using SED fitting code. The SFR derived from FIR SEDs fitting and stellar mass derived from optical/NIR SED fitting suggest that four DSFGs are on the SFR vs. stellar mass main sequence at $z = 3.1$.

Main discussions are as follows:

- **CO J=4-3 morphology and kinematics of LAB18.b;**
  In ALMA Cycle 4 Band 3 observation, we found that LAB18.b has a FWHM of 5.6 kpc extended CO gaseous rotationally disk and a FWHM of 2.0 kpc central 860 $\mu$m dusty star-forming region. Their peak positions are coincident each other, and the kinematical major axis of CO and morphological major axis of dust are also coincident within 22 $^\circ$. This is similar to the massive DSFGs at $z = 2.5$, although LAB18.b shows very low $v_{\rm circ}/\sigma_0 = 1.2 \pm 0.1$. This is due to the blue component of CO J=4-3 line emission, which is extended toward south-east, possibly suggests turbulent motion and/or inflows/outflows. LAB18.b could be an ancestor of massive DSFGs at $z = 2.5$, and evolve $v_{\rm circ}/\sigma_0$ as redshift. However, there are possibilities of face-on late mergers and/or merger remnants. We need more spatial resolution for conservative discussion.

- **Relatively low $L'_{\rm CO(4-3)}/L_{\rm FIR}$ ratio and small $\tau_{\rm dep}$ of LAB18.b;**
  The $L'_{\rm CO(4-3)}$ of four DSFGs in the LAB18 are relatively low compared with $L_{\rm FIR}$, and they are outside of $1\sigma$ scatter of previous studies. For LAB18.b, the derived $\tau_{\rm dep}$ from CO J=4-3 is $22^{+14}_{-6}$ Myr with assuming $\alpha$=0.8, which is significantly lower than the average value of 558 Myr for normal star-forming galaxies at the same redshift. This is also lower than the values of local ULIRGs ($\sim$50 Myr), and is between early stage mergers ($16^{+6}_{-4}$ Myr) and merging galaxies ($60^{+30}_{-20}$ Myr). Thus, LAB18.b could be initial stage of merging galaxies although there are no significant merger signs from their morphology and kinematic information. In protoclusters, simultaneously galaxy-galaxy mergers or much longer molecular gas depletion times are possible explanations to concentration of DSFGs. However, we found very low gas mass and gas depletion time for LAB18.b.

- **Large $\beta$ and small $T_d$ of LAB18.b;**
  In ALMA Cycle 4 Band 3 observations, we detected rest-frame 700 $\mu$m dust continuum emissions from four DSFGs in LAB18. We found that LAB18.b has large $\beta$ and small $T_d$ nonetheless its ULIRGs class far-infrared luminosity. Such large $\beta$ can be reproduced with Mg-rich glassy silicates from recent astronomical experiment. The location of large $\beta$ and small $T_d$ of LAB18.b in $\beta$ vs. $T_d$ plane is similar to the metal rich, gas poor early type galaxies and LIRGs. This situation is similar to our CO J=4-3 line observation for LAB18.b, which indicates small gas fraction of 8%. We may see the evolution from DSFGs to the early type galaxies on the $\beta$ vs. $T_d$ space. ALMA long wavelength multi-band continuum observations will reveal differences of $\beta$ among the various galaxy populations and optical properties of interstellar dust grains.

- **Possible origins of DSFGs and LAB18;**
  For the photoionization model, a one X-ray detection and the large total SFR of four DSFGs in LAB18 compared with LAB1 suggest that photoionization is possible origin of LAB18. Recent high resolution

cosmological hydrodynamic simulation with radiative transfer model suggests the importance of satellite galaxies in the photoionization model. Subaru/Suprime-Cam $R$-band UV continuum emission and *HST*/ACS F814W continuum emission might reflect satellite galaxies accreting onto LAB18.a and LAB18.b, and they potentially contribute to growth of DSFGs, and both of them illuminate LABs via the photoionization.

For the galactic superwind model, the ΣSFR derived from 860 $\mu$m dust continuum emissions suggests all of four DSFGs in LAB18 can drive galactic superwinds. Large velocity offset between CO J=4-3 line emission and Ly$\alpha$ line emission, and a one X-ray detection support existence of strong outflows. The blue component of CO J=4-3 of LAB18.b, which is extended toward south-east, possibly suggests turbulent motion and/or inflows/outflows.

For the inflowing gas model, although the extended gaseous structure of CO J=4-3 line emissions could not been seen, LAB18 has very low gas mass and depletion time. LAB18.b is depleted their gas mass within $22^{+14}_{-6}$ Myr with current SFR, and achieved stellar mass is $5.2\times10^{10}M_{\odot}$ if all of the gas mass is converted to stellar mass. Thus, LAB18.b could not evolve massive galaxies in local clusters with stellar mass above $\sim 10^{11}M_{\odot}$ unless outer gas feeds into the galaxy and/or galaxy mergers are induced. Although the LAB18 surrounding four DSFGs could be illuminated by galactic superwinds and photoionization, LAB18.b needs additional gas from IGMs to evolve more massive galaxies. $R$-band UV continuum emission whose shape is elongated from LAB18.a and LAB18.b might reflect satellite galaxies with inflowing gas accreting onto them.

# Chapter 6

# Summary

Protocluster is a few tens of proper Mpc galaxy overdensity seen in the $z > 2$ Universe, which is thought to be a progenitor of local galaxy clusters. Although the formation of elliptical galaxies in local clusters are thought to be occurred at the $z > 2$ Universe, the lack of far-infrared observation prevent us to search for their precursors, massive dusty star-forming galaxies (DSFGs). In protoclusters, simultaneous dusty star-formations through DSFGs are expected due to a frequent galaxy-galaxy merger induced by a rapid collapse of dark matter halos and/or a high potential of gas supply from the large scale structure.

We conducted *Herschel*/SPIRE surveys to search for DSFGs in three protoclusters, 2QZCluster ($z = 2.23$), HS1700 ($z = 2.30$) and SSA22 ($z = 3.09$). We targeted these protoclusters with a few tens of proper Mpc filamentary, large scale structures and evidence for enhancement of AGNs fractions. In addition, all of the three protoclusters have Ly$\alpha$ blobs (LABs) or H$\alpha$ blobs (HABs), which are the site of massive galaxy formation. Based on the SPIRE colors of $S_{350}/S_{250}$ and $S_{500}/S_{350}$, we selected DSFGs potentially associated with the protoclusters. Main findings are following;

1. By using 6 comoving Mpc radius apertures, we found a $4\sigma$ overdensity of six SPIRE sources $4.5'$ ($\sim 2$ proper Mpc) west to a density peak of HAEs at $z = 2.23$ in the 2QZCluster field. In the HS1700 field, we found a $5\sigma$ overdensity of eight SPIRE sources $2.1'$ ($\sim 1$ proper Mpc) north to a density peak of LBGs at $z = 2.30$. We found three 500 $\mu$m sources are concentrated $3'$ ($\sim$1.5 proper Mpc) east to a density peak of LAEs at $z = 3.09$ in the SSA22 field.

2. If all of the SPIRE sources in these three overdensities are associated with protoclusters, the inferred star-formation rate densities are possibly $\sim$100-1000 times higher than the average value at the same redshifts. This suggests that simultaneously, intensive dusty star-formation of DSFGs are possibly occurred in the $z \sim 2 - 3$ protoclusters. We see the formation scene of local elliptical galaxies as concentration of DSFGs in the protoclusters.

3. Simultaneously galaxy-galaxy mergers or much longer molecular gas depletion times are possible explanations to concentration of DSFGs in protoclusters. The key observational challenge is to investigate the morphology, measure molecular gas mass and molecular gas depletion time, and search for the extended gaseous structure such outflows and/or inflows for DSFGs in protoclusters.

We conducted ALMA Band 7 and Band 3 observations for one of spectroscopically confirmed *Herschel*/SPIRE source SSA22-SPIRE394, which corresponds to SSA22-LAB18 (LAB18) at $z = 3.1$ SSA22 protocluster. LAB18 is known to the highest FIR, Millimeter/Sub-millimeter wavelengths flux densities and its filamentary structure of Ly$\alpha$ emission. Main findings are following;

1. In ALMA Cycle 2 Band 7 observation, we found that LAB18 consists of four 860 $\mu$m dust continuum sources, LAB18.a, LAB18.b, LAB18.c, and LAB18.d. They are aligned $\sim$100 kpc Ly$\alpha$ filamentary structure of LAB18.

2. In ALMA Cycle 4 Band 3 observations, we detected CO J=4-3 line from one of the DSFGs, LAB18.b. The CO based spectroscopically redshift is $z = 3.0936 \pm 0.0002$, which is blueshifted compared with the Ly$\alpha$ spectroscopy of $z = 3.014$. The large velocity offset between CO line emission and Ly$\alpha$ line emission and a one X-ray detection suggest possible existence of strong galactic superwinds.

3. We estimated photometric redshifts, and the implied phot-$z$ of four DSFGs in LAB18 are $z_{\rm phot} \gtrsim 3$ in 99% confidence intervals. We also estimated the stellar masses of four DSFGs in the LAB18 from SED fitting to optical/NIR data points. SFR derived from far-infrared SED fitting and stellar mass derived from optical/NIR SED fitting suggest four DSFGs in LAB18 are on the SFR-stellar mass main sequence at $z = 3.1$.

4. In ALMA Cycle 4 Band 3 observation, we found that LAB18.b has a FWHM of 5.6 kpc extended CO gaseous rotationally disk and a FWHM of 2.0 kpc central 860 $\mu$m dusty star-forming region. This situation is similar to the massive ($M_* > 10^{11}$ $M_\odot$) DSFGs at $z = 2.5$, although LAB18.b shows very low $v_{\rm circ}/\sigma_0 = 1.2 \pm 0.1$. This is due to the blue component of CO J=4-3 line emission, which is extended toward south-east, possibly suggesting turbulent motion and/or inflows/outflows. However, there are possibilities of face-on mergers, and/or merger remnant.

5. In ALMA Cycle 4 Band 3 observations, we derived $M_{\rm gas} = (4.4 \pm 0.3) \times 10^9 M_\odot$ for LAB18.b. For CO non-detected DSFGs in LAB18, we derived $3\sigma$ upper limit of $M_{\rm gas} = 1.0 \times 10^9$ $M_\odot$ as the same manner as LAB18.b.

6. In ALMA Cycle 4 Band 3 observations, with combining *Herschel*/SPIRE 250 $\mu$m and ALMA Band 7 860 $\mu$m flux densities, we conducted far-infrared SED fitting by using optically thin, single temperature modified black body radiation as $\beta$ and $T_d$ free parameters. We found that four DSFGs in the LAB18 have ULIRGs class far-infrared luminosities of $L_{\rm FIR} = (1.7 - 4.2) \times 10^{12}$ L$_\odot$.

7. In ALMA Cycle 4 Band 3 observations, the $L'_{\rm CO(4-3)}$ of four DSFGs in the LAB18 are relatively low compared with $L_{\rm FIR}$, and they are outside of $1\sigma$ scatter of previous studies. For LAB18.b, the derived $\tau_{\rm dep}$ is $22^{+14}_{-6}$ Myr with assuming $\alpha$=0.8, which is significantly lower than the average value of 558 Myr for normal star-forming galaxies at the same redshift. This is also lower than the values of local ULIRGs ($\sim$50 Myr), and is between early stage mergers ($16^{+6}_{-4}$ Myr) and merging galaxies ($60^{+30}_{-20}$ Myr). Thus, LAB18.b could be initial stage of merging galaxies although there are no signs of galaxy-galaxy mergers from their morphological and kinematic information.

8. In ALMA Cycle 4 Band 3 observation, we detected 2.85mm (rest-frame 700 $\mu$m) dust continuum emission from four DSFGs in LAB18. We estimated dust mass, and found that four DSFGs in LAB18 have $M_{\rm dust} = (1.8 - 8.1) \times 10^7$ M$_\odot$. This corresponds to the usual range of gas to dust mass ratio of $\delta_{\rm GDR} = 12 - 90$.

9. In ALMA Cycle 4 Band 3 observations, we found that LAB18.b has large $\beta$ and small $T_d$ nonetheless it has ULIRGs class far-infrared luminosity. Such large $\beta$ can be reproduced with Mg-rich glassy silicates from a recent astronomical experiment. The location of large $\beta$ and small $T_d$ of LAB18.b in $\beta$ vs. $T_d$ plane is similar to the metal rich, gas poor early type galaxies and local LIRGs. This situation is similar to CO J=4-3 line observation for LAB18.b, which indicates small gas fraction of 8%. We may see the evolution from DSFGs to the early type galaxies on the $\beta$ vs. $T_d$ space. ALMA long wavelength multi-band continuum observations will reveal differences of $\beta$ among the various galaxy populations and optical properties of interstellar dust grains.

10. Combining these results, we discuss possible origins of LAB18. For the photoionization model, a one X-ray detection and large total SFR of four DSFGs in LAB18 suggest photoionization is possible origin of LAB18. Subaru/Suprime-Cam $R$-band UV continuum emission and $HST$/ACS F814W continuum emission might reflect satellite galaxies accreting onto LAB18.a and LAB18.b, and they potentially contribute to growth of DSFGs, and illuminate LABs via the photoionization. For the galactic superwind model, the $\Sigma$SFR derived from 860 $\mu$m dust continuum emissions suggests all of four DSFGs in LAB18 can drive galactic superwinds. Large velocity offset between CO J=4-3 line emission and Ly$\alpha$ line emission and a one X-ray detection suggest possible existence of strong galactic superwinds. The blue component of CO J=4-3 line emission of LAB18.b, which is extended toward south-east, possibly suggests turbulent motion and/or inflows/outflows. For the inflowing gas model, LAB18.b needs additional gas from IGMs to evolve more massive galaxies. LAB18.b is depleted their gas mass within $22^{+14}_{-6}$ Myr with current SFR, and achieved stellar mass is $5.2\times10^{10} M_\odot$ if all of the gas mass is converted to stellar mass. Thus, LAB18.b could not be evolved massive galaxies in local clusters with stellar mass above $\sim 10^{11} M_\odot$ unless outer gas feeds into the galaxy and/or galaxy mergers are induced. Subaru/Suprime-Cam $R$-band UV continuum emission whose shape is elongated from LAB18.a and LAB18.b might reflect satellite galaxies with inflowing gas accreting onto them.

In protoclusters, simultaneously galaxy-galaxy mergers or much longer molecular gas depletion times are possible explanations to concentration of DSFGs. However, we found very low gas mass and gas depletion time for LAB18. Further statistical samples are needed to discuss this.

# Appendix

## A.1 Additional Candidate Sources in LAB18

We show the additional candidate sources which possibly associated with LAB18 in Figure A.1 and A.2. Both candidates are found from JVLA 3 GHz continuum observations. Figure A.1 shows possible source, LAB18.e. This source has possible emission in ALMA 860 $\mu$m image. Figure A.2 shows possible source, LAB18.f. This source has possible emission in Subaru/Suprime-Cam $NB497$ band (continuum subtracted Ly$\alpha$). If these sources are really associated with LAB18, these are the additional Ly$\alpha$ powering sources.

## A.2 Herschel Matching Catalogue for 2QZCluster & HS1700

Table A.1: Results of LBGs counterpart matching with SPIRE sources in HS1700 field.

| ID[1] (SPIRE) | R.A.[2] (J2000) | Dec.[3] (J2000) | ID[4] (Count.) | R.A.[5] (J2000) | Dec.[6] (J2000) | $z$[7] (Ly$\alpha$) | $z$[8] (abs) | $z$[9] (neb) | Sepa.[10] (arcsec) | $p$-value[11] | Member[12] |
|---|---|---|---|---|---|---|---|---|---|---|---|
| HS1700-SPIRE5 | 254.994379 | 64.264104 | MD162 | 254.994280 | 64.264200 | -1.000 | -1.000 | -1.000 | 0.38 | 0.00 | Secure |
| HS1700-SPIRE108 | 255.435603 | 64.192152 | C32 | 255.435090 | 64.192190 | -1.000 | -1.000 | -1.000 | 0.82 | 0.01 | Secure |
| HS1700-SPIRE134 | 255.394305 | 64.214057 | MD123 | 255.394350 | 64.214600 | -1.000 | -1.000 | -2.000 | 1.96 | 0.04 | Secure |
| HS1700-SPIRE166 | 255.302623 | 64.125673 | BM262 | 255.302360 | 64.125240 | -1.000 | -1.000 | -1.000 | 1.61 | 0.03 | Secure |
| HS1700-SPIRE214 | 255.117542 | 64.225962 | RK103 | 255.118480 | 64.225880 | -1.000 | -1.000 | -1.000 | 1.50 | 0.02 | Secure |
| HS1700-SPIRE222 | 255.143784 | 64.079331 | BX83 | 255.143360 | 64.078990 | -1.000 | -1.000 | -1.000 | 1.40 | 0.02 | Secure |
| HS1700-SPIRE281 | 255.068249 | 64.184090 | BM494 | 255.068240 | 64.183800 | -1.000 | -1.000 | -1.000 | 1.04 | 0.01 | Secure |
| HS1700-SPIRE300 | 254.925594 | 64.246454 | BX958 | 254.926000 | 64.246100 | -1.000 | -1.000 | -1.000 | 1.42 | 0.02 | Secure |
| HS1700-SPIRE321 | 255.273221 | 64.204569 | BM576 | 255.273070 | 64.205150 | -1.000 | -1.000 | -1.000 | 2.11 | 0.04 | Secure |
| HS1700-SPIRE372 | 255.313854 | 64.189019 | RK123 | 255.314200 | 64.188810 | -1.000 | -1.000 | 2.289 | 0.93 | 0.01 | Secure |
| HS1700-SPIRE61 | 255.446660 | 64.247148 | BM768 | 255.446830 | 64.247880 | -1.000 | -1.000 | -1.000 | 2.65 | 0.07 | Tentative |
| HS1700-SPIRE86 | 255.481127 | 64.176486 | BX551 | 255.479880 | 64.176940 | -1.000 | -1.000 | -1.000 | 2.55 | 0.06 | Tentative |
| HS1700-SPIRE102 | 255.367833 | 64.218005 | D46 | 255.367280 | 64.217220 | -2.000 | 3.466 | 3.476 | 2.96 | 0.08 | Tentative |
| HS1700-SPIRE105 | 255.258613 | 64.095831 | BX142 | 255.257150 | 64.095680 | -1.000 | -1.000 | -1.000 | 2.36 | 0.05 | Tentative |
| HS1700-SPIRE130 | 255.042780 | 64.124007 | C12 | 255.041170 | 64.123870 | 2.316 | 2.307 | -1.000 | 2.58 | 0.07 | Tentative |
| HS1700-SPIRE142 | 255.266783 | 64.246938 | BM759 | 255.266260 | 64.246140 | -1.000 | -1.000 | -1.000 | 2.99 | 0.09 | Tentative |
| HS1700-SPIRE162 | 255.445864 | 64.313208 | MD229 | 255.444060 | 64.313390 | -1.000 | -1.000 | -1.000 | 2.89 | 0.08 | Tentative |
| HS1700-SPIRE172 | 255.489407 | 64.084077 | BM81 | 255.489650 | 64.083320 | -1.000 | -1.000 | -1.000 | 2.75 | 0.07 | Tentative |
| HS1700-SPIRE179 | 255.376787 | 64.198781 | BX713 | 255.375770 | 64.198070 | -1.000 | -1.000 | 2.138 | 3.02 | 0.09 | Tentative |
| HS1700-SPIRE203 | 255.073449 | 64.115186 | BX246 | 255.073530 | 64.115940 | -1.000 | -1.000 | -1.000 | 2.72 | 0.07 | Tentative |
| HS1700-SPIRE220 | 255.328321 | 64.208090 | BM593 | 255.327080 | 64.208760 | -1.000 | -1.000 | -2.000 | 3.10 | 0.09 | Tentative |
| HS1700-SPIRE225 | 255.109150 | 64.316371 | MD237 | 255.107190 | 64.316600 | -1.000 | -1.000 | -1.000 | 3.17 | 0.10 | Tentative |
| HS1700-SPIRE290 | 255.403724 | 64.145417 | BX420 | 255.402150 | 64.145850 | 1.923 | 1.923 | -1.000 | 2.92 | 0.08 | Tentative |
| HS1700-SPIRE354 | 255.381511 | 64.317082 | BM1065 | 255.382760 | 64.317560 | -1.000 | -1.000 | -1.000 | 2.60 | 0.07 | Tentative |
| HS1700-SPIRE360 | 255.005747 | 64.239963 | MD146 | 255.004440 | 64.240650 | -1.000 | -1.000 | -1.000 | 3.21 | 0.10 | Tentative |

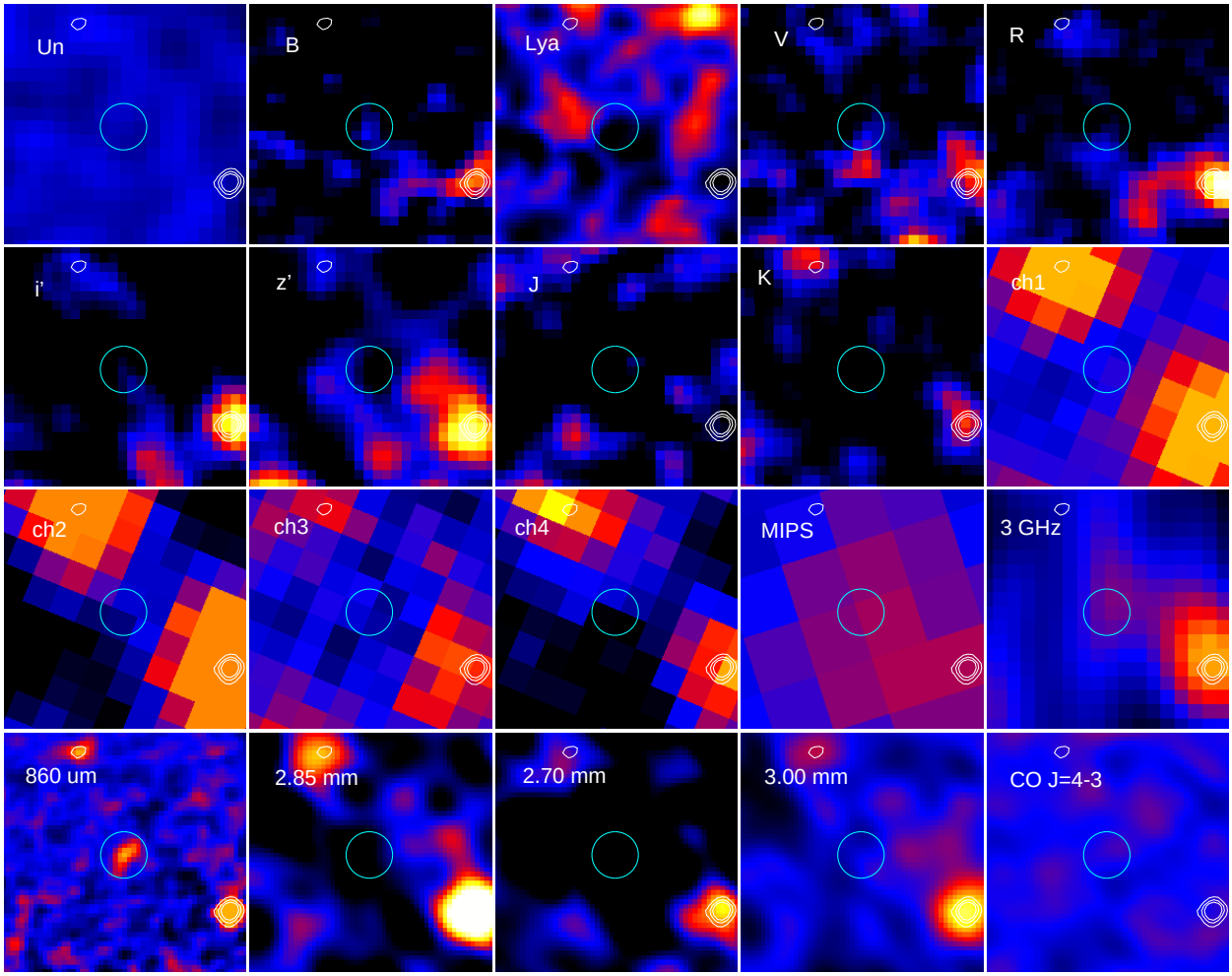


Figure A.1: Thumbnails of UV to radio wavelength for LAB18.e. The size of each panel is $5'' \times 5''$. From left to right and top to bottom, we show Palomar/COSMIC $U_n$-band (Steidel et al., 2003), Subaru/Suprime-Cam $B, NB497, V, R, i', z'$-band (Hayashino et al., 2004; Matsuda et al., 2004), UKIRT/WFCAM $J, K$-band (Lawrence et al., 2007), *Spitzer*/IRAC and MIPS 3.6 $\mu$m, 4.5 $\mu$m, 5.8 $\mu$m, 8.0 $\mu$m, 24 $\mu$m (Webb et al., 2009), JVLA 3 GHz (Ao et al., 2018), ALMA 860 $\mu$m, 2.85 mm, 2.70 mm, 3.00 mm, and CO J=4-3 emission. The white contour shows 5,10,15$\sigma$ level of ALMA 860 $\mu$m. The pixel sizes are $0.1''$ for ALMA 860 $\mu$m, 2.85 mm, 2.70 mm, 3.00 mm, CO J=4-3, and Subaru/Suprime-Cam $NB497$-band, $0.2''$ for Subaru/Suprime-Cam $B, V, R, i', z'$-band and UKIRT/WFCAM $J, K$-band, $0.3''$ for Palomar/COSMIC $U_n$-band and JVLA 3 GHz, $0.6''$ for *Spitzer*/IRAC band, and $1.3''$ for *Spitzer*/MIPS band. The position of the LAB18.e is marked as a cyan circle with radius of $0.5''$. It is bright in 24 $\mu$m, 3 GHz continuum and 860 $\mu$m continuum.

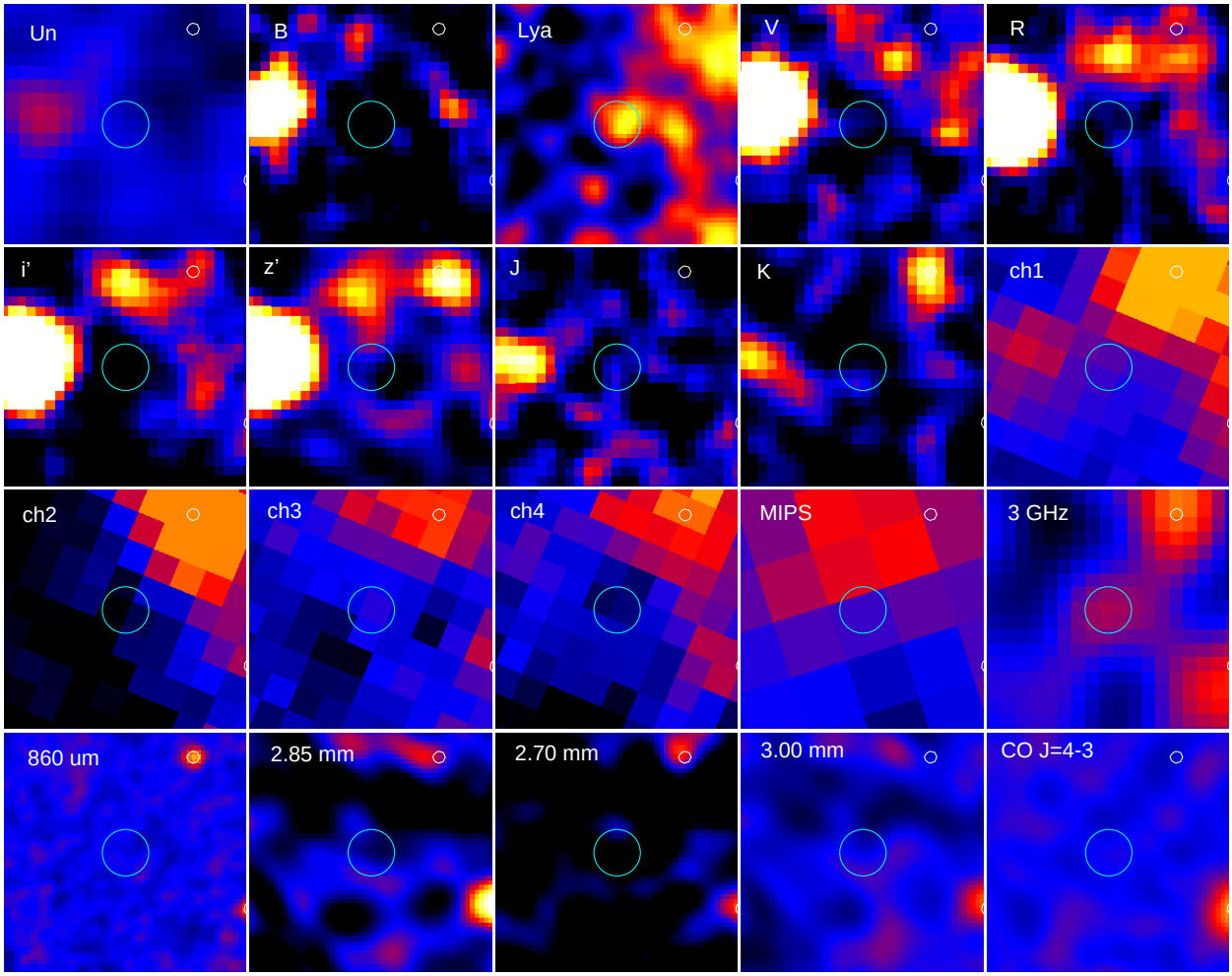


Figure A.2: Thumbnails of UV to radio wavelength for LAB18.f. The size of each panel is $5'' \times 5''$. From left to right and top to bottom, we show Palomar/COSMIC $U_n$-band (Steidel et al., 2003), Subaru/Suprime-Cam $B, NB497, V, R, i', z'$-band (Hayashino et al., 2004; Matsuda et al., 2004), UKIRT/WFCAM $J, K$-band (Lawrence et al., 2007), *Spitzer*/IRAC and MIPS 3.6 $\mu$m, 4.5 $\mu$m, 5.8 $\mu$m, 8.0 $\mu$m, 24 $\mu$m (Webb et al., 2009), JVLA 3 GHz (Ao et al., 2018), ALMA 860 $\mu$m, 2.85 mm, 2.70 mm, 3.00 mm, and CO J=4-3 emission. The white contour shows 5,10,15$\sigma$ level of ALMA 860 $\mu$m. The pixel sizes are $0.1''$ for ALMA 860 $\mu$m, 2.85 mm, 2.70 mm, 3.00 mm, CO J=4-3, and Subaru/Suprime-Cam $NB497$-band, $0.2''$ for Subaru/Suprime-Cam $B, V, R, i', z'$-band and UKIRT/WFCAM $J, K$-band, $0.3''$ for Palomar/COSMIC $U_n$-band and JVLA 3 GHz, $0.6''$ for *Spitzer*/IRAC band, and $1.3''$ for *Spitzer*/MIPS band. The position of the LAB18.f is marked as a cyan circle with radius of $0.5''$. It is bright in Ly$\alpha$ and 3 GHz continuum.

Table A.2: Results of DRGs counterpart matching with SPIRE sources in HS1700 field.

| ID[1] (SPIRE) | R.A.[2] (J2000) | Dec.[3] (J2000) | ID[4] (Count.) | R.A.[5] (J2000) | Dec.[6] (J2000) | $z$[7] (Ly$\alpha$) | $z$[8] (abs) | Sepa.[9] (neb) | $p$-value[10] (arcsec) | Note[11] | Member[12] |
|---|---|---|---|---|---|---|---|---|---|---|---|
| HS1700-SPIRE24 | 255.334861 | 64.240306 | DRG53 | 255.33776 | 64.239514 | -1.000 | -1.00 | 5.36 | 0.03 | - | Secure |
| HS1700-SPIRE42 | 255.242783 | 64.219633 | DRG46 | 255.24194 | 64.219532 | -1.000 | -1.00 | 1.37 | 0.00 | NB35 | Secure |
| HS1700-SPIRE84 | 255.372104 | 64.145975 | DRG9 | 255.37351 | 64.145634 | -1.000 | -1.00 | 2.53 | 0.01 | - | Secure |
| HS1700-SPIRE134 | 255.394305 | 64.214057 | DRG41 | 255.39631 | 64.213418 | -1.000 | -1.00 | 3.89 | 0.01 | - | Secure |
| HS1700-SPIRE186 | 255.187683 | 64.195121 | DRG36 | 255.18515 | 64.195805 | -1.000 | -1.00 | 4.67 | 0.02 | - | Secure |
| HS1700-SPIRE231 | 255.308249 | 64.269297 | DRG66 | 255.31133 | 64.268951 | -1.000 | -1.00 | 4.97 | 0.02 | - | Secure |
| HS1700-SPIRE242 | 255.199999 | 64.223791 | DRG48 | 255.20161 | 64.223904 | -1.000 | -1.00 | 2.55 | 0.01 | - | Secure |
| HS1700-SPIRE290 | 255.403724 | 64.145417 | DRG8 | 255.40259 | 64.144932 | -1.000 | -1.00 | 2.49 | 0.01 | - | Secure |
| HS1700-SPIRE299 | 255.312643 | 64.137046 | DRG5 | 255.31408 | 64.138577 | -1.000 | -1.00 | 5.96 | 0.03 | - | Secure |
| HS1700-SPIRE358 | 255.183013 | 64.138250 | DRG2 | 255.1859 | 64.137414 | -1.000 | -1.00 | 5.44 | 0.03 | BX370 | Secure |
| HS1700-SPIRE178 | 255.130287 | 64.245326 | DRG60 | 255.129 | 64.247356 | -1.000 | -1.00 | 7.58 | 0.05 | - | Tentative |
| HS1700-SPIRE253 | 255.382640 | 64.177543 | DRG28 | 255.38916 | 64.178463 | -1.000 | -1.00 | 10.75 | 0.10 | - | Tentative |
| HS1700-SPIRE366 | 255.391738 | 64.189252 | DRG32 | 255.39313 | 64.186701 | -1.000 | -1.00 | 9.44 | 0.08 | - | Tentative |
| HS1700-SPIRE321 | 255.273221 | 64.204569 | DRG38 | 255.2669 | 64.203249 | 2.286 | -2.00 | 10.98 | 0.10 | NB30 | Not |

Table A.3: Results of LAEs counterparts matching with SPIRE sources in HS1700 field.

| ID[1] (SPIRE) | R.A.[2] (J2000) | Dec.[3] (J2000) | ID[4] (Count.) | R.A.[5] (J2000) | Dec.[6] (J2000) | $z$[7] (Ly$\alpha$) | $z$[8] (abs) | Sepa.[9] (neb) | $p$-value[10] (arcsec) | Member[12] |
|---|---|---|---|---|---|---|---|---|---|---|
| HS1700-SPIRE21 | 255.395064 | 64.248379 | BNB1 | 255.395271 | 64.247934 | -1.000 | -1.000 | 1.63 | 0.00 | Secure |
| HS1700-SPIRE70 | 255.282673 | 64.258605 | BNB155 | 255.281054 | 64.257366 | 2.290 | -2.000 | 5.13 | 0.01 | Secure |
| HS1700-SPIRE78 | 255.435784 | 64.260703 | BNB139 | 255.433054 | 64.262192 | -1.000 | -1.000 | 6.85 | 0.02 | Secure |
| HS1700-SPIRE260 | 255.063932 | 64.291203 | BNB158 | 255.062617 | 64.289161 | -1.000 | -1.000 | 7.63 | 0.03 | Secure |
| HS1700-SPIRE289 | 255.211324 | 64.237171 | BNB75 | 255.210779 | 64.238590 | 2.308 | -2.000 | 5.18 | 0.01 | Secure |
| HS1700-SPIRE321 | 255.273221 | 64.204569 | BNB41 | 255.268800 | 64.202705 | -2.000 | 2.287 | 9.64 | 0.04 | Secure |
| HS1700-SPIRE335 | 255.398882 | 64.155265 | BNB61 | 255.401846 | 64.153610 | 2.340 | -2.000 | 7.56 | 0.03 | Secure |
| HS1700-SPIRE5 | 254.994379 | 64.264104 | BNB170 | 254.991433 | 64.266833 | -1.000 | -1.000 | 10.85 | 0.06 | Tentative |
| HS1700-SPIRE321 | 255.273221 | 64.204569 | BLOB536 | 255.267333 | 64.203275 | 2.290 | 2.260 | 10.33 | 0.05 | Tentative |

Table A.4: Results of HAEs counterparts matching with SPIRE sources in HS1700 field.

| ID[1] (SPIRE) | R.A.[2] (J2000) | Dec.[3] (J2000) | ID[4] (Count.) | R.A.[5] (J2000) | Dec.[6] (J2000) | $z$[7] (Ly$\alpha$) | $z$[8] (abs) | Sepa.[9] (neb) | $p$-value[10] (arcsec) | Member[12] |
|---|---|---|---|---|---|---|---|---|---|---|
| HS1700-SPIRE42 | 255.242783 | 64.219633 | HaNB2 | 255.241667 | 64.219639 | -1.000 | -1.000 | 1.75 | 0.00 | Secure |
| HS1700-SPIRE98 | 255.242058 | 64.152534 | HaNB47 | 255.238542 | 64.153361 | -1.000 | -1.000 | 6.27 | 0.04 | Secure |
| HS1700-SPIRE142 | 255.266783 | 64.246938 | HaNB83 | 255.265250 | 64.248667 | -1.000 | -1.000 | 6.67 | 0.04 | Secure |
| HS1700-SPIRE142 | 255.266783 | 64.246938 | HaNB76 | 255.266125 | 64.246139 | -1.000 | -1.000 | 3.06 | 0.01 | Secure |
| HS1700-SPIRE179 | 255.376787 | 64.198781 | HaNB45 | 255.379625 | 64.199639 | -1.000 | -1.000 | 5.41 | 0.03 | Secure |
| HS1700-SPIRE303 | 255.244930 | 64.190623 | HaNB43 | 255.243542 | 64.189833 | -1.000 | -1.000 | 3.58 | 0.01 | Secure |
| HS1700-SPIRE372 | 255.313854 | 64.189019 | HaNB22 | 255.314042 | 64.188889 | -1.000 | -1.000 | 0.55 | 0.00 | Secure |
| HS1700-SPIRE70 | 255.282673 | 64.258605 | HaNB27 | 255.287292 | 64.257778 | -1.000 | -1.000 | 7.81 | 0.06 | Tentative |
| HS1700-SPIRE77 | 255.273241 | 64.196266 | HaNB21 | 255.279000 | 64.197250 | -1.000 | -1.000 | 9.70 | 0.09 | Tentative |
| HS1700-SPIRE24 | 255.334861 | 64.240306 | HaNB10 | 255.339917 | 64.238417 | -2.000 | 2.289 | 10.43 | 0.10 | Tentative |

Table A.5: Results of HAEs counterpart matching with SPIRE sources in 2QZCluster.

| ID[1] (SPIRE) | R.A.[2] (J2000) | Dec.[3] (J2000) | ID[4] (Count.) | R.A.[5] (J2000) | Dec.[6] (J2000) | Sepa.[7] (arcsec) | $p$-value[8] | Member[9] |
|---|---|---|---|---|---|---|---|---|
| 2QZCluster-SPIRE10 | 150.916320 | 0.352456 | QZC-C1-HAE02Q | 150.915790 | 0.353000 | 2.73 | <0.01 | Secure |
| 2QZCluster-SPIRE124 | 150.965998 | 0.249463 | QZC-C1-HAE03Q | 150.964920 | 0.250583 | 5.60 | <0.01 | Secure |
| 2QZCluster-SPIRE239 | 151.069470 | 0.310488 | QZC-C1-HAE20 | 151.069750 | 0.309167 | 4.86 | <0.01 | Secure |
| 2QZCluster-SPIRE251 | 150.885551 | 0.168325 | QZC-C1-HAE09 | 150.887370 | 0.167917 | 6.71 | <0.01 | Secure |
| 2QZCluster-SPIRE261 | 150.852526 | 0.155903 | QZC-C1-HAE05 | 150.854380 | 0.155694 | 6.72 | <0.01 | Secure |
| 2QZCluster-SPIRE353 | 150.916183 | 0.187292 | QZC-C1-HAE16 | 150.915750 | 0.187722 | 2.20 | <0.01 | Secure |
| 2QZCluster-SPIRE372 | 150.935267 | 0.238716 | QZC-C1-HAE15 | 150.932670 | 0.238944 | 9.39 | 0.01 | Secure |

## A.3 *Herschel*/SPIRE catalogues in 2QZCluster, HS1700 and SSA22

Table A.6: SPIRE sources catalogue of 2QZCluster field.

| ID[1] | R.A.[2] (J2000) | Dec.[3] (J2000) | $S_{250}$[4] (mJy) | $S_{350}$[5] (mJy) | $S_{500}$[6] (mJy) |
|---|---|---|---|---|---|
| 2QZCluster-SPIRE1 | 150.81846968368112 | 0.029424092103377656 | 127.0 ± 2.1 | 54.2 ± 1.9 | 24.6 ± 2.2 |
| 2QZCluster-SPIRE2 | 150.76480950482065 | 0.22501254698200338 | 139.1 ± 2.4 | 117.9 ± 1.8 | 71.4 ± 2.3 |
| 2QZCluster-SPIRE3 | 150.91517959664077 | 0.3909833462929028 | 111.4 ± 2.4 | 55.2 ± 1.8 | 21.2 ± 2.4 |
| 2QZCluster-SPIRE4 | 151.02463506680982 | 0.1206541823404277 | 97.4 ± 2.2 | 54.2 ± 1.8 | 26.5 ± 2.4 |
| 2QZCluster-SPIRE5 | 151.04455762206453 | 0.4047339937359634 | 93.6 ± 2.3 | 61.3 ± 1.8 | 24.2 ± 2.2 |
| 2QZCluster-SPIRE6 | 151.07930718745527 | 0.12006911913976963 | 84.1 ± 2.3 | 58.9 ± 1.8 | 31.3 ± 2.3 |
| 2QZCluster-SPIRE7 | 151.11225122198036 | 0.17674219593981788 | 66.1 ± 2.2 | 36.2 ± 2.1 | 13.2 ± 2.1 |
| 2QZCluster-SPIRE8 | 150.7066091154151 | 0.2830585502030584 | 67.4 ± 2.3 | 54.5 ± 1.8 | 18.4 ± 2.2 |

Table A.6: SPIRE sources catalogue of 2QZCluster field.

| ID[1] | R.A.[2] (J2000) | Dec.[3] (J2000) | $S_{250}$[4] (mJy) | $S_{350}$[5] (mJy) | $S_{500}$[6] (mJy) |
|---|---|---|---|---|---|
| 2QZCluster-SPIRE9 | 150.94968775985714 | 0.33116978814976 | 64.4 ± 2.2 | 22.2 ± 1.9 | 0.0 ± 2.1 |
| 2QZCluster-SPIRE10 | 150.91631977926835 | 0.3524558479517708 | 60.1 ± 2.1 | 64.7 ± 1.8 | 45.6 ± 2.0 |
| 2QZCluster-SPIRE11 | 150.98918513949715 | 0.46678765869277206 | 79.2 ± 2.9 | 39.1 ± 2.4 | 20.6 ± 3.3 |
| 2QZCluster-SPIRE12 | 150.8542823160533 | 0.386238270952972 | 64.3 ± 2.5 | 33.6 ± 1.7 | 10.6 ± 2.3 |
| 2QZCluster-SPIRE13 | 150.9871739349042 | 0.24943624176646492 | 55.8 ± 2.2 | 27.2 ± 1.7 | 10.7 ± 2.3 |
| 2QZCluster-SPIRE14 | 150.83461322694697 | 0.17215116597481522 | 65.5 ± 2.6 | 41.3 ± 1.8 | 8.0 ± 2.3 |
| 2QZCluster-SPIRE15 | 150.94559026691908 | 0.35503691775490037 | 50.5 ± 2.1 | 17.4 ± 1.7 | 9.0 ± 2.1 |
| 2QZCluster-SPIRE16 | 151.03733112704157 | 0.3727825028276875 | 48.5 ± 2.1 | 24.4 ± 1.7 | 16.2 ± 2.1 |
| 2QZCluster-SPIRE17 | 151.00317615320708 | 0.39286141210328035 | 51.1 ± 2.2 | 33.7 ± 1.8 | 18.4 ± 2.2 |
| 2QZCluster-SPIRE18 | 151.05898714479937 | 0.26211367289930665 | 47.7 ± 2.1 | 21.8 ± 1.9 | 8.0 ± 2.2 |
| 2QZCluster-SPIRE19 | 150.75317971832106 | 0.15625454019918225 | 57.7 ± 2.5 | 59.2 ± 1.8 | 26.3 ± 2.4 |
| 2QZCluster-SPIRE20 | 150.83020603490908 | 0.3034098480747363 | 47.8 ± 2.2 | 40.6 ± 1.8 | 21.6 ± 2.1 |
| 2QZCluster-SPIRE21 | 151.01371879891934 | 0.2891292322392597 | 48.8 ± 2.2 | 22.5 ± 1.7 | 8.3 ± 2.4 |
| 2QZCluster-SPIRE22 | 150.75870642897954 | 0.2095141108715229 | 46.9 ± 2.2 | 56.0 ± 1.9 | 36.2 ± 2.2 |
| 2QZCluster-SPIRE23 | 151.0020734160798 | 0.2400445692431416 | 49.5 ± 2.5 | 26.5 ± 1.7 | 12.6 ± 2.1 |
| 2QZCluster-SPIRE24 | 150.77965977660924 | 0.16337391723345335 | 43.7 ± 2.2 | 45.0 ± 1.8 | 27.3 ± 2.0 |
| 2QZCluster-SPIRE25 | 150.81505867490284 | 0.15297938814123752 | 47.0 ± 2.4 | 51.5 ± 2.0 | 37.3 ± 2.2 |
| 2QZCluster-SPIRE26 | 150.79870763962836 | 0.13692969988686893 | 45.1 ± 2.3 | 36.0 ± 1.9 | 13.0 ± 2.3 |
| 2QZCluster-SPIRE27 | 151.01202468040105 | 0.25230822618027765 | 43.6 ± 2.3 | 11.3 ± 1.8 | 3.7 ± 2.3 |
| 2QZCluster-SPIRE28 | 150.9404444832334 | 0.3486043844831334 | 40.3 ± 2.1 | 24.9 ± 1.8 | 23.3 ± 2.1 |
| 2QZCluster-SPIRE29 | 151.05025662831832 | 0.23355374530924283 | 39.9 ± 2.2 | 37.8 ± 1.8 | 28.8 ± 2.1 |
| 2QZCluster-SPIRE30 | 150.7935602231388 | 0.12668543113715836 | 38.2 ± 2.2 | 20.7 ± 1.8 | 5.5 ± 2.2 |
| 2QZCluster-SPIRE31 | 150.74349416918454 | 0.24816674165406505 | 37.7 ± 2.2 | 24.5 ± 1.9 | 10.1 ± 2.1 |
| 2QZCluster-SPIRE32 | 150.8935275578894 | 0.07536939729988636 | 37.7 ± 2.2 | 26.0 ± 1.8 | 8.0 ± 2.1 |
| 2QZCluster-SPIRE33 | 150.8370714829737 | 0.051938665060744 | 37.6 ± 2.3 | 29.8 ± 1.9 | 19.4 ± 2.4 |
| 2QZCluster-SPIRE34 | 150.79456280720885 | 0.0613366934331795 | 41.4 ± 2.5 | 46.8 ± 2.0 | 44.7 ± 2.3 |
| 2QZCluster-SPIRE35 | 150.79642665093783 | 0.34546174162810006 | 35.7 ± 2.1 | 37.0 ± 1.8 | 22.0 ± 2.1 |
| 2QZCluster-SPIRE36 | 150.87595310655286 | 0.1956079846832166 | 36.7 ± 2.2 | 27.6 ± 1.9 | 6.1 ± 2.4 |
| 2QZCluster-SPIRE37 | 150.78382091421508 | 0.3031235246956488 | 39.8 ± 2.4 | 25.7 ± 1.6 | 9.9 ± 2.1 |
| 2QZCluster-SPIRE38 | 150.87992957264163 | 0.3266955213673425 | 38.4 ± 2.4 | 47.9 ± 1.7 | 29.6 ± 2.1 |
| 2QZCluster-SPIRE39 | 150.90395049825588 | 0.3743369126846863 | 35.1 ± 2.2 | 17.2 ± 1.9 | 15.9 ± 2.2 |
| 2QZCluster-SPIRE40 | 150.79109143769648 | 0.14905387615295915 | 38.0 ± 2.4 | 14.4 ± 2.0 | 1.2 ± 2.3 |
| 2QZCluster-SPIRE41 | 150.9635729720083 | 0.29864731945897 | 38.7 ± 2.4 | 22.4 ± 1.9 | 15.7 ± 2.1 |
| 2QZCluster-SPIRE42 | 151.01098456995092 | 0.2038216264564903 | 34.8 ± 2.2 | 22.9 ± 1.9 | 11.5 ± 2.2 |
| 2QZCluster-SPIRE43 | 150.7535270671499 | 0.18044123466639317 | 36.1 ± 2.3 | 23.9 ± 1.9 | 8.6 ± 2.3 |
| 2QZCluster-SPIRE44 | 150.85045604075407 | 0.206103909868175 | 33.2 ± 2.1 | 31.1 ± 1.7 | 13.8 ± 2.0 |
| 2QZCluster-SPIRE45 | 150.7961618437887 | 0.27177676435203896 | 41.3 ± 2.6 | 36.3 ± 1.7 | 20.3 ± 2.3 |
| 2QZCluster-SPIRE46 | 151.05094496837575 | 0.2872549917703474 | 34.0 ± 2.2 | 24.9 ± 1.8 | 21.8 ± 2.2 |
| 2QZCluster-SPIRE47 | 151.0328520742358 | 0.2956370890970118 | 31.6 ± 2.0 | 15.3 ± 1.8 | 5.4 ± 2.2 |
| 2QZCluster-SPIRE48 | 150.8156246379502 | 0.1898493942591047 | 36.1 ± 2.3 | 49.0 ± 1.8 | 46.2 ± 2.0 |
| 2QZCluster-SPIRE49 | 151.0708679975335 | 0.3439286719779001 | 36.9 ± 2.4 | 23.1 ± 1.9 | 8.5 ± 2.1 |
| 2QZCluster-SPIRE50 | 151.06291850115406 | 0.30768307402967426 | 34.3 ± 2.2 | 9.2 ± 1.9 | 2.8 ± 2.3 |
| 2QZCluster-SPIRE51 | 150.83642422748912 | 0.01002096071802058 | 37.9 ± 2.5 | 16.2 ± 2.0 | 9.1 ± 2.4 |
| 2QZCluster-SPIRE52 | 150.82636414215403 | 0.3866268720691538 | 38.2 ± 2.5 | 30.0 ± 1.8 | 15.7 ± 2.5 |
| 2QZCluster-SPIRE53 | 150.84146082213343 | 0.11362146948140173 | 33.4 ± 2.2 | 11.5 ± 1.8 | 0.7 ± 2.1 |
| 2QZCluster-SPIRE54 | 150.87008780796128 | 0.3779344807149017 | 39.5 ± 2.6 | 20.2 ± 1.8 | 9.4 ± 2.2 |
| 2QZCluster-SPIRE55 | 150.9076739853764 | 0.3204702686864118 | 30.1 ± 2.0 | 16.3 ± 1.7 | 5.7 ± 2.1 |
| 2QZCluster-SPIRE56 | 150.87462146366883 | 0.28099262065920955 | 33.2 ± 2.3 | 30.5 ± 1.9 | 22.0 ± 2.3 |
| 2QZCluster-SPIRE57 | 151.0496846668223 | 0.41495536501785607 | 36.0 ± 2.5 | 28.1 ± 1.9 | 22.9 ± 2.3 |
| 2QZCluster-SPIRE58 | 150.91039349136025 | 0.1662302486412554 | 32.7 ± 2.2 | 28.8 ± 1.9 | 9.1 ± 2.2 |
| 2QZCluster-SPIRE59 | 150.93840625364638 | 0.15125520172813897 | 32.1 ± 2.2 | 23.4 ± 1.7 | 8.4 ± 2.0 |
| 2QZCluster-SPIRE60 | 150.84232715532812 | 0.26072674528374334 | 31.6 ± 2.2 | 22.8 ± 2.0 | 13.8 ± 2.0 |
| 2QZCluster-SPIRE61 | 151.07042903450477 | 0.22586603662185514 | 31.9 ± 2.2 | 24.2 ± 2.0 | 13.4 ± 2.2 |
| 2QZCluster-SPIRE62 | 150.71559963102655 | 0.24939944603130743 | 38.6 ± 2.7 | 24.1 ± 2.1 | 12.0 ± 3.0 |
| 2QZCluster-SPIRE63 | 151.0387107407021 | 0.4244276968330758 | 37.1 ± 2.7 | 25.0 ± 1.8 | 7.5 ± 2.4 |
| 2QZCluster-SPIRE64 | 150.82766864970753 | 0.3118663822416966 | 30.3 ± 2.2 | 26.8 ± 1.8 | 17.6 ± 2.0 |
| 2QZCluster-SPIRE65 | 150.85631805403625 | 0.26752966069640743 | 32.2 ± 2.3 | 29.8 ± 1.8 | 21.9 ± 2.2 |
| 2QZCluster-SPIRE66 | 150.72300433920725 | 0.36229949987081556 | 34.3 ± 2.5 | 24.4 ± 2.0 | 11.5 ± 2.6 |
| 2QZCluster-SPIRE67 | 150.8781630333377 | 0.12461084795456631 | 28.6 ± 2.1 | 33.5 ± 1.7 | 27.2 ± 2.0 |
| 2QZCluster-SPIRE68 | 150.8877893905804 | 0.243100317033642 | 30.0 ± 2.2 | 38.8 ± 1.7 | 23.9 ± 2.2 |
| 2QZCluster-SPIRE69 | 150.84940561519392 | 0.16536008346243636 | 33.3 ± 2.4 | 20.6 ± 1.8 | 10.0 ± 2.2 |
| 2QZCluster-SPIRE70 | 150.93487047471783 | 0.41756893225468283 | 34.2 ± 2.5 | 34.3 ± 1.8 | 21.6 ± 2.4 |
| 2QZCluster-SPIRE71 | 150.94699449283507 | 0.33957924590829924 | 28.7 ± 2.1 | 5.1 ± 1.8 | 5.0 ± 2.2 |
| 2QZCluster-SPIRE72 | 150.95887387013806 | 0.4369686236737234 | 33.4 ± 2.5 | 25.9 ± 2.0 | 14.2 ± 2.5 |
| 2QZCluster-SPIRE73 | 150.73804486314714 | 0.34564001644451164 | 30.4 ± 2.3 | 17.3 ± 1.9 | 5.1 ± 2.2 |
| 2QZCluster-SPIRE74 | 151.0349515307015 | 0.31786349064994723 | 31.5 ± 2.4 | 21.0 ± 1.9 | 6.6 ± 2.1 |
| 2QZCluster-SPIRE75 | 150.92043877571075 | 0.2538881221148497 | 29.1 ± 2.2 | 24.3 ± 1.8 | 10.7 ± 2.2 |
| 2QZCluster-SPIRE76 | 150.8032721102473 | 0.3391216241102625 | 28.0 ± 2.1 | 6.6 ± 1.8 | 0.0 ± 2.0 |
| 2QZCluster-SPIRE77 | 150.89586999060586 | 0.3421115186996857 | 28.4 ± 2.2 | 33.1 ± 1.7 | 21.1 ± 2.1 |
| 2QZCluster-SPIRE78 | 150.99759333531358 | 0.12687215290658993 | 29.2 ± 2.3 | 31.7 ± 1.7 | 26.4 ± 2.0 |
| 2QZCluster-SPIRE79 | 150.87634828335393 | 0.26317420506382705 | 30.3 ± 2.3 | 16.1 ± 1.9 | 1.3 ± 2.1 |
| 2QZCluster-SPIRE80 | 150.83439706467567 | 0.02957832330296228 | 27.9 ± 2.2 | 22.9 ± 1.9 | 0.0 ± 2.3 |
| 2QZCluster-SPIRE81 | 150.81478220892367 | 0.041904735838698234 | 29.4 ± 2.3 | 20.9 ± 2.0 | 25.5 ± 2.1 |
| 2QZCluster-SPIRE82 | 151.14026315164585 | 0.16271339253146577 | 30.2 ± 2.4 | 34.3 ± 1.9 | 25.7 ± 2.3 |
| 2QZCluster-SPIRE83 | 151.0070667356181 | 0.11817415247579867 | 30.9 ± 2.5 | 12.8 ± 1.8 | 0.0 ± 2.1 |
| 2QZCluster-SPIRE84 | 150.7912710835411 | 0.10905215969580524 | 25.9 ± 2.1 | 22.1 ± 1.8 | 11.2 ± 2.1 |

Table A.6: SPIRE sources catalogue of 2QZCluster field.

| ID[1] | R.A.[2] (J2000) | Dec.[3] (J2000) | $S_{250}$[4] (mJy) | $S_{350}$[5] (mJy) | $S_{500}$[6] (mJy) |
|---|---|---|---|---|---|
| 2QZCluster-SPIRE85 | 150.79491475084842 | 0.329075459414398 | 27.9 ± 2.2 | 27.3 ± 1.7 | 13.6 ± 2.2 |
| 2QZCluster-SPIRE86 | 150.95660795446184 | 0.3770465976681214 | 29.5 ± 2.4 | 12.6 ± 1.7 | 0.6 ± 2.2 |
| 2QZCluster-SPIRE87 | 150.95742753496606 | 0.1323130617035027 | 27.1 ± 2.2 | 31.5 ± 1.9 | 13.5 ± 2.3 |
| 2QZCluster-SPIRE88 | 150.8828063844225 | 0.2888590381852744 | 28.4 ± 2.3 | 26.9 ± 1.7 | 22.0 ± 2.0 |
| 2QZCluster-SPIRE89 | 150.9610310904905 | 0.32747846563400673 | 30.1 ± 2.5 | 20.5 ± 1.7 | 4.9 ± 2.3 |
| 2QZCluster-SPIRE90 | 150.95043165964037 | 0.21311716442043596 | 26.3 ± 2.2 | 11.0 ± 1.7 | 3.0 ± 2.1 |
| 2QZCluster-SPIRE91 | 151.04292236834868 | 0.3828209995549043 | 26.7 ± 2.2 | 20.0 ± 1.7 | 2.9 ± 2.1 |
| 2QZCluster-SPIRE92 | 151.0382272098183 | 0.12728108561462734 | 28.7 ± 2.4 | 20.4 ± 1.8 | 8.9 ± 2.3 |
| 2QZCluster-SPIRE93 | 150.80833279976918 | 0.2052146811644575 | 27.2 ± 2.3 | 12.3 ± 1.7 | 2.7 ± 2.0 |
| 2QZCluster-SPIRE94 | 151.09352234251193 | 0.2311933814096099 | 28.1 ± 2.4 | 17.7 ± 1.9 | 7.5 ± 2.1 |
| 2QZCluster-SPIRE95 | 150.8416385733023 | 0.3490634429484569 | 27.2 ± 2.3 | 19.2 ± 1.9 | 10.3 ± 2.1 |
| 2QZCluster-SPIRE96 | 150.80170375452644 | 0.36365413757607656 | 26.9 ± 2.3 | 15.6 ± 1.8 | 10.5 ± 2.1 |
| 2QZCluster-SPIRE97 | 150.790148972863 | 0.2196138762658005 | 25.1 ± 2.2 | 28.8 ± 1.8 | 24.9 ± 2.2 |
| 2QZCluster-SPIRE98 | 150.98801415667228 | 0.2979731298796211 | 28.3 ± 2.5 | 27.2 ± 1.8 | 18.1 ± 2.2 |
| 2QZCluster-SPIRE99 | 151.09618249647005 | 0.2782104555429363 | 26.9 ± 2.4 | 21.9 ± 1.8 | 11.3 ± 2.3 |
| 2QZCluster-SPIRE100 | 150.95485696063005 | 0.1791155426031014 | 24.7 ± 2.2 | 16.5 ± 1.7 | 14.6 ± 2.2 |
| 2QZCluster-SPIRE101 | 151.07936715308162 | 0.10912957717167902 | 25.1 ± 2.2 | 3.1 ± 1.8 | 6.7 ± 2.3 |
| 2QZCluster-SPIRE102 | 150.7466621032041 | 0.31409514285118567 | 23.7 ± 2.1 | 13.6 ± 1.9 | 5.4 ± 2.3 |
| 2QZCluster-SPIRE103 | 151.00082016722524 | 0.37573800891505144 | 22.3 ± 2.0 | 24.0 ± 1.7 | 15.7 ± 2.1 |
| 2QZCluster-SPIRE104 | 150.94813675695443 | 0.31811683038253846 | 23.9 ± 2.2 | 25.4 ± 1.8 | 23.0 ± 2.5 |
| 2QZCluster-SPIRE105 | 150.93220328416564 | 0.20001642273342626 | 26.5 ± 2.4 | 20.3 ± 1.8 | 9.6 ± 2.2 |
| 2QZCluster-SPIRE106 | 150.73112023575214 | 0.20286614129738817 | 27.7 ± 2.5 | 22.2 ± 2.0 | 9.7 ± 2.4 |
| 2QZCluster-SPIRE107 | 151.03929573338078 | 0.35164448548937527 | 24.3 ± 2.2 | 14.1 ± 1.8 | 8.3 ± 2.2 |
| 2QZCluster-SPIRE108 | 150.7851557690807 | 0.31603011989231766 | 24.2 ± 2.2 | 22.1 ± 1.8 | 6.2 ± 2.2 |
| 2QZCluster-SPIRE109 | 150.96625948974386 | 0.3891485397082526 | 24.7 ± 2.3 | 12.8 ± 1.9 | 7.5 ± 2.1 |
| 2QZCluster-SPIRE110 | 150.94593312788828 | 0.06078183459446307 | 22.4 ± 2.1 | 11.6 ± 1.9 | 0.2 ± 2.3 |
| 2QZCluster-SPIRE111 | 150.708450363845 | 0.3454364589197822 | 22.7 ± 2.1 | 13.5 ± 1.8 | 10.4 ± 2.3 |
| 2QZCluster-SPIRE112 | 150.7309929685114 | 0.23177841638509183 | 25.4 ± 2.4 | 15.9 ± 2.1 | 10.5 ± 2.3 |
| 2QZCluster-SPIRE113 | 150.94083458892248 | 0.1406156345027501 | 23.2 ± 2.2 | 14.5 ± 1.8 | 12.0 ± 2.1 |
| 2QZCluster-SPIRE114 | 151.12859509531748 | 0.1384343936516573 | 22.8 ± 2.2 | 7.8 ± 2.0 | 9.3 ± 2.2 |
| 2QZCluster-SPIRE115 | 150.9850353010843 | 0.3452751947344621 | 23.2 ± 2.2 | 28.4 ± 1.8 | 20.0 ± 2.2 |
| 2QZCluster-SPIRE116 | 151.0324472308443 | 0.16632586120490717 | 23.1 ± 2.2 | 17.0 ± 1.7 | 16.9 ± 2.0 |
| 2QZCluster-SPIRE117 | 150.82848622188703 | 0.3402561429809171 | 23.3 ± 2.2 | 9.4 ± 1.8 | 0.3 ± 2.4 |
| 2QZCluster-SPIRE118 | 150.92490333428475 | 0.19275152246974223 | 27.2 ± 2.6 | 25.9 ± 1.8 | 22.8 ± 2.3 |
| 2QZCluster-SPIRE119 | 150.71578652080586 | 0.30894842374162496 | 21.4 ± 2.1 | 12.1 ± 1.9 | 0.5 ± 2.3 |
| 2QZCluster-SPIRE120 | 150.95131342794107 | 0.43288623723569586 | 28.5 ± 2.8 | 14.7 ± 1.9 | 10.0 ± 2.3 |
| 2QZCluster-SPIRE121 | 150.8354772426735 | 0.3535397008614285 | 23.1 ± 2.3 | 17.3 ± 2.0 | 8.5 ± 2.2 |
| 2QZCluster-SPIRE122 | 151.06980649169782 | 0.33240801041802415 | 29.5 ± 2.9 | 18.5 ± 1.8 | 6.9 ± 2.3 |
| 2QZCluster-SPIRE123 | 150.79397326861087 | 0.2370199166897544 | 23.5 ± 2.3 | 12.1 ± 1.9 | 0.6 ± 2.1 |
| 2QZCluster-SPIRE124 | 150.96599810429714 | 0.24946314693710775 | 21.9 ± 2.2 | 14.2 ± 1.8 | 9.7 ± 2.2 |
| 2QZCluster-SPIRE125 | 150.75948367585104 | 0.23468384706960108 | 22.4 ± 2.2 | 6.9 ± 2.0 | 0.0 ± 2.3 |
| 2QZCluster-SPIRE126 | 150.9421960432471 | 0.43118677606364963 | 29.3 ± 2.9 | 15.7 ± 1.9 | 4.3 ± 2.5 |
| 2QZCluster-SPIRE127 | 151.09374632745926 | 0.2537686439914208 | 22.7 ± 2.3 | 14.0 ± 1.8 | 7.3 ± 2.2 |
| 2QZCluster-SPIRE128 | 150.77270162361165 | 0.3134219408820535 | 23.8 ± 2.4 | 11.9 ± 1.8 | 0.0 ± 2.0 |
| 2QZCluster-SPIRE129 | 150.84597708888785 | 0.022768583849124356 | 22.2 ± 2.3 | 22.6 ± 1.8 | 11.1 ± 2.2 |
| 2QZCluster-SPIRE130 | 150.79762638521575 | 0.2259945743460828 | 21.6 ± 2.2 | 8.5 ± 1.8 | 0.8 ± 2.2 |
| 2QZCluster-SPIRE131 | 150.95739836919145 | 0.38102583284363717 | 22.2 ± 2.3 | 11.7 ± 1.8 | 6.3 ± 2.2 |
| 2QZCluster-SPIRE132 | 150.80659054604118 | 0.30449781904110695 | 21.5 ± 2.2 | 19.3 ± 1.8 | 11.5 ± 2.0 |
| 2QZCluster-SPIRE133 | 151.02923523993036 | 0.4300167053446881 | 22.6 ± 2.3 | 10.6 ± 1.9 | 3.1 ± 2.1 |
| 2QZCluster-SPIRE134 | 151.06939046173792 | 0.2848885455856504 | 20.6 ± 2.1 | 23.5 ± 1.7 | 14.1 ± 2.1 |
| 2QZCluster-SPIRE135 | 151.0198522050932 | 0.4290445459840974 | 21.9 ± 2.3 | 19.8 ± 1.9 | 8.9 ± 2.2 |
| 2QZCluster-SPIRE136 | 150.89133428307423 | 0.3184054052466527 | 22.0 ± 2.3 | 19.4 ± 1.8 | 8.2 ± 2.2 |
| 2QZCluster-SPIRE137 | 150.79161673369717 | 0.17171284274067253 | 22.5 ± 2.3 | 24.9 ± 1.8 | 5.5 ± 2.3 |
| 2QZCluster-SPIRE138 | 150.82614847723679 | 0.2070271650682105 | 21.6 ± 2.3 | 7.9 ± 1.8 | 0.0 ± 2.2 |
| 2QZCluster-SPIRE139 | 150.77267582821685 | 0.21534494133738913 | 20.0 ± 2.1 | 0.0 ± 1.8 | 8.3 ± 2.3 |
| 2QZCluster-SPIRE140 | 150.91115331372671 | 0.21144451342831425 | 23.6 ± 2.5 | 26.4 ± 1.7 | 17.6 ± 2.2 |
| 2QZCluster-SPIRE141 | 150.8544911025831 | 0.3404533971243268 | 19.9 ± 2.1 | 20.4 ± 1.8 | 9.3 ± 2.1 |
| 2QZCluster-SPIRE142 | 151.0470605726284 | 0.1579099884772861 | 23.1 ± 2.5 | 7.9 ± 1.8 | 2.5 ± 2.1 |
| 2QZCluster-SPIRE143 | 150.9000735545713 | 0.4090658700323208 | 22.0 ± 2.3 | 26.5 ± 1.8 | 22.3 ± 2.6 |
| 2QZCluster-SPIRE144 | 151.00086896793493 | 0.0934236620671375 | 19.8 ± 2.1 | 17.7 ± 1.8 | 15.6 ± 2.0 |
| 2QZCluster-SPIRE145 | 151.01728475920785 | 0.1496499540501932 | 20.4 ± 2.2 | 12.0 ± 2.0 | 4.8 ± 2.1 |
| 2QZCluster-SPIRE146 | 151.09804958657602 | 0.12255475373819139 | 20.0 ± 2.2 | 11.6 ± 1.9 | 3.9 ± 2.1 |
| 2QZCluster-SPIRE147 | 150.9976122497206 | 0.31212564637462237 | 23.6 ± 2.5 | 15.1 ± 1.8 | 0.3 ± 2.2 |
| 2QZCluster-SPIRE148 | 150.84329195052132 | 0.3652311980929477 | 22.3 ± 2.4 | 12.8 ± 1.8 | 4.0 ± 2.2 |
| 2QZCluster-SPIRE149 | 150.7370994222113 | 0.2661749738607812 | 20.9 ± 2.3 | 24.2 ± 1.9 | 13.4 ± 2.0 |
| 2QZCluster-SPIRE150 | 151.07575968760443 | 0.15786064990255746 | 20.6 ± 2.2 | 30.6 ± 1.6 | 31.7 ± 2.0 |
| 2QZCluster-SPIRE151 | 150.75719367966857 | 0.312588760301311 | 18.9 ± 2.1 | 13.4 ± 1.8 | 5.9 ± 2.4 |
| 2QZCluster-SPIRE152 | 150.82686696395632 | 0.1729468033747285 | 22.8 ± 2.5 | 0.0 ± 1.8 | 11.7 ± 2.0 |
| 2QZCluster-SPIRE153 | 150.82196698706355 | 0.3955515514470401 | 22.1 ± 2.4 | 6.2 ± 2.2 | 4.0 ± 2.5 |
| 2QZCluster-SPIRE154 | 150.8169144184704 | 0.10356305706610976 | 19.3 ± 2.1 | 7.2 ± 1.7 | 0.0 ± 2.3 |
| 2QZCluster-SPIRE155 | 150.81497278799839 | 0.35508686183899874 | 19.2 ± 2.1 | 19.5 ± 1.9 | 20.7 ± 2.2 |
| 2QZCluster-SPIRE156 | 150.8789777308746 | 0.3046776525124736 | 22.0 ± 2.5 | 13.8 ± 1.7 | 2.9 ± 2.1 |
| 2QZCluster-SPIRE157 | 151.0816129124121 | 0.09988062856889866 | 20.5 ± 2.3 | 16.4 ± 1.7 | 2.7 ± 2.2 |
| 2QZCluster-SPIRE158 | 150.79924466934335 | 0.17677702486385688 | 19.4 ± 2.2 | 8.1 ± 1.8 | 8.4 ± 2.3 |
| 2QZCluster-SPIRE159 | 150.99107036010784 | 0.32663854294069183 | 20.6 ± 2.3 | 25.1 ± 1.8 | 17.2 ± 2.2 |
| 2QZCluster-SPIRE160 | 150.89607930366225 | 0.13738252378570437 | 18.9 ± 2.1 | 16.8 ± 1.8 | 8.6 ± 2.0 |

Table A.6: SPIRE sources catalogue of 2QZCluster field.

| ID[1] | R.A.[2] (J2000) | Dec.[3] (J2000) | $S_{250}$[4] (mJy) | $S_{350}$[5] (mJy) | $S_{500}$[6] (mJy) |
|---|---|---|---|---|---|
| 2QZCluster-SPIRE161 | 150.92184005214472 | 0.2333659471688594 | 20.0 ± 2.3 | 16.0 ± 1.8 | 5.6 ± 2.1 |
| 2QZCluster-SPIRE162 | 150.78811436355892 | 0.08642608096453316 | 20.9 ± 2.4 | 15.5 ± 2.0 | 0.1 ± 2.2 |
| 2QZCluster-SPIRE163 | 150.72712684110007 | 0.31229360745902357 | 18.6 ± 2.1 | 13.9 ± 1.9 | 8.4 ± 2.3 |
| 2QZCluster-SPIRE164 | 151.06449441811014 | 0.13664705797449955 | 19.8 ± 2.3 | 9.2 ± 1.8 | 4.9 ± 2.1 |
| 2QZCluster-SPIRE165 | 150.8076637827496 | 0.2339653853603514 | 19.3 ± 2.2 | 12.4 ± 1.8 | 4.3 ± 2.1 |
| 2QZCluster-SPIRE166 | 150.94685160462146 | 0.20307547519310248 | 21.6 ± 2.5 | 9.0 ± 1.8 | 5.6 ± 2.3 |
| 2QZCluster-SPIRE167 | 150.96994723668874 | 0.4203162374654388 | 19.2 ± 2.2 | 16.9 ± 1.7 | 9.2 ± 2.3 |
| 2QZCluster-SPIRE168 | 151.0330601292465 | 0.23900721906100214 | 19.6 ± 2.3 | 20.2 ± 1.7 | 2.3 ± 2.3 |
| 2QZCluster-SPIRE169 | 150.8050908149595 | 0.27875588092482523 | 19.3 ± 2.3 | 10.7 ± 1.6 | 7.3 ± 2.2 |
| 2QZCluster-SPIRE170 | 150.69591278428408 | 0.2962429811434034 | 19.9 ± 2.3 | 18.4 ± 2.0 | 6.3 ± 2.7 |
| 2QZCluster-SPIRE171 | 151.0112601286365 | 0.43860905985529086 | 20.3 ± 2.4 | 21.0 ± 2.0 | 3.9 ± 2.4 |
| 2QZCluster-SPIRE172 | 151.08799954230372 | 0.2042040910320149 | 17.8 ± 2.1 | 4.2 ± 1.8 | 2.9 ± 2.3 |
| 2QZCluster-SPIRE173 | 150.83848194129706 | 0.2151793799889627 | 18.9 ± 2.3 | 16.8 ± 1.7 | 0.0 ± 2.1 |
| 2QZCluster-SPIRE174 | 151.08498726532673 | 0.32223908241586013 | 21.6 ± 2.6 | 9.0 ± 2.0 | 7.1 ± 2.2 |
| 2QZCluster-SPIRE175 | 150.76316261930995 | 0.294989350101309 | 17.9 ± 2.1 | 8.1 ± 1.7 | 0.5 ± 2.2 |
| 2QZCluster-SPIRE176 | 150.89889512527571 | 0.35485445947271493 | 17.3 ± 2.1 | 11.9 ± 1.7 | 0.0 ± 2.1 |
| 2QZCluster-SPIRE177 | 150.98059323211908 | 0.2411036647043666 | 18.0 ± 2.2 | 18.9 ± 1.9 | 12.0 ± 2.2 |
| 2QZCluster-SPIRE178 | 151.01721799594645 | 0.3292785636090037 | 18.4 ± 2.2 | 23.9 ± 1.8 | 25.5 ± 2.0 |
| 2QZCluster-SPIRE179 | 150.82319992546883 | 0.061415584375988375 | 21.7 ± 2.6 | 7.4 ± 1.9 | 0.0 ± 2.2 |
| 2QZCluster-SPIRE180 | 150.97451053044904 | 0.1374712051188647 | 18.0 ± 2.2 | 14.9 ± 1.9 | 11.9 ± 2.1 |
| 2QZCluster-SPIRE181 | 150.93392287721775 | 0.39459835596883475 | 21.6 ± 2.6 | 17.0 ± 1.8 | 4.7 ± 2.4 |
| 2QZCluster-SPIRE182 | 150.99776929529597 | 0.28642721165728957 | 18.6 ± 2.3 | 16.9 ± 1.7 | 1.2 ± 2.3 |
| 2QZCluster-SPIRE183 | 150.73060734971105 | 0.2618630398342802 | 19.3 ± 2.3 | 2.0 ± 1.7 | 2.2 ± 2.2 |
| 2QZCluster-SPIRE184 | 150.7466299081645 | 0.333268511994775236 | 18.3 ± 2.2 | 17.8 ± 2.0 | 8.3 ± 2.3 |
| 2QZCluster-SPIRE185 | 150.85862502706198 | 0.32513373769780396 | 17.7 ± 2.2 | 14.0 ± 1.8 | 4.6 ± 2.1 |
| 2QZCluster-SPIRE186 | 150.83336031596224 | 0.40500563384596705 | 23.6 ± 2.9 | 7.3 ± 2.1 | 0.0 ± 2.7 |
| 2QZCluster-SPIRE187 | 151.00115022575105 | 0.20740385904358505 | 18.9 ± 2.3 | 6.4 ± 1.8 | 0.0 ± 2.2 |
| 2QZCluster-SPIRE188 | 150.80869789036382 | 0.05823826532563154 | 20.7 ± 2.5 | 13.6 ± 1.9 | 6.8 ± 2.2 |
| 2QZCluster-SPIRE189 | 150.8893553407071 | 0.39856748109697837 | 17.2 ± 2.1 | 9.2 ± 1.8 | 3.9 ± 2.2 |
| 2QZCluster-SPIRE190 | 150.97032640983176 | 0.15407904948469628 | 17.1 ± 2.1 | 6.9 ± 1.6 | 1.0 ± 2.0 |
| 2QZCluster-SPIRE191 | 150.95509724003546 | 0.16937720144656998 | 17.9 ± 2.2 | 10.4 ± 1.8 | 9.0 ± 2.3 |
| 2QZCluster-SPIRE192 | 150.87139160638935 | 0.06334744855548674 | 19.7 ± 2.4 | 16.4 ± 1.8 | 12.6 ± 2.2 |
| 2QZCluster-SPIRE193 | 151.0159925277392 | 0.38679846895232006 | 17.3 ± 2.2 | 15.2 ± 1.8 | 3.3 ± 2.4 |
| 2QZCluster-SPIRE194 | 150.84933607127113 | 0.2415484996142407 | 17.3 ± 2.2 | 11.9 ± 1.8 | 2.7 ± 2.1 |
| 2QZCluster-SPIRE195 | 150.8703288398162 | 0.39079904897246276 | 18.6 ± 2.4 | 20.4 ± 1.7 | 10.0 ± 2.4 |
| 2QZCluster-SPIRE196 | 150.7830676914411 | 0.11608586092036102 | 17.8 ± 2.3 | 16.0 ± 1.9 | 6.1 ± 2.1 |
| 2QZCluster-SPIRE197 | 150.73593232555282 | 0.3620753434540134 | 18.4 ± 2.3 | 10.0 ± 1.8 | 0.3 ± 2.6 |
| 2QZCluster-SPIRE198 | 150.8961315177207 | 0.2893837804622898 | 18.9 ± 2.4 | 9.3 ± 1.7 | 0.0 ± 2.3 |
| 2QZCluster-SPIRE199 | 151.0234138191973 | 0.09633307458407779 | 18.2 ± 2.3 | 17.5 ± 1.8 | 0.0 ± 2.4 |
| 2QZCluster-SPIRE200 | 150.7373505217809 | 0.22814834822185168 | 17.6 ± 2.3 | 25.0 ± 2.0 | 9.3 ± 2.3 |
| 2QZCluster-SPIRE201 | 150.92658075887815 | 0.1537615176935511 | 17.4 ± 2.2 | 22.6 ± 1.8 | 16.7 ± 2.1 |
| 2QZCluster-SPIRE202 | 151.01900233203224 | 0.36557815354630646 | 15.2 ± 2.0 | 15.0 ± 1.8 | 12.3 ± 2.2 |
| 2QZCluster-SPIRE203 | 151.01766824260724 | 0.4646465147016753 | 23.2 ± 3.0 | 13.0 ± 2.2 | 1.4 ± 2.6 |
| 2QZCluster-SPIRE204 | 151.04127572981707 | 0.3665145315070501 | 17.2 ± 2.2 | 9.6 ± 1.7 | 14.6 ± 2.2 |
| 2QZCluster-SPIRE205 | 150.73344297795558 | 0.32401237604206556 | 17.4 ± 2.2 | 30.2 ± 1.9 | 23.3 ± 2.3 |
| 2QZCluster-SPIRE206 | 150.96528413553904 | 0.31115835518038854 | 17.3 ± 2.2 | 8.5 ± 1.9 | 7.6 ± 2.2 |
| 2QZCluster-SPIRE207 | 150.9303719133462 | 0.09150032386403817 | 21.6 ± 2.8 | 12.0 ± 1.9 | 5.6 ± 2.5 |
| 2QZCluster-SPIRE208 | 150.90786764124095 | 0.126851045237643 | 17.2 ± 2.3 | 17.9 ± 1.7 | 7.2 ± 2.4 |
| 2QZCluster-SPIRE209 | 150.80845676073767 | 0.009145561022462224 | 19.7 ± 2.6 | 14.4 ± 2.0 | 4.2 ± 2.6 |
| 2QZCluster-SPIRE210 | 151.07840650914886 | 0.17137848551617493 | 16.9 ± 2.2 | 23.9 ± 1.9 | 10.7 ± 2.3 |
| 2QZCluster-SPIRE211 | 150.95251210900122 | 0.2333298018274624 | 15.7 ± 2.1 | 9.9 ± 1.9 | 2.9 ± 2.1 |
| 2QZCluster-SPIRE212 | 150.84040458497407 | 0.06574283341587099 | 19.4 ± 2.5 | 15.5 ± 1.8 | 9.3 ± 2.4 |
| 2QZCluster-SPIRE213 | 150.8151685941877 | 0.06898854318570419 | 16.0 ± 2.1 | 6.1 ± 1.9 | 0.6 ± 2.1 |
| 2QZCluster-SPIRE214 | 150.87974394645926 | 0.16222263623026464 | 16.6 ± 2.2 | 13.6 ± 1.9 | 6.0 ± 2.0 |
| 2QZCluster-SPIRE215 | 150.82393831942784 | 0.40613994436544915 | 20.5 ± 2.7 | 13.6 ± 2.1 | 8.5 ± 2.8 |
| 2QZCluster-SPIRE216 | 150.9010941641005 | 0.06221619393225701 | 16.5 ± 2.2 | 13.1 ± 1.8 | 9.8 ± 2.1 |
| 2QZCluster-SPIRE217 | 150.97643288490954 | 0.12954113609020557 | 18.3 ± 2.4 | 6.3 ± 1.6 | 0.3 ± 2.2 |
| 2QZCluster-SPIRE218 | 151.1323169999353 | 0.15083378889286236 | 17.9 ± 2.4 | 3.6 ± 1.8 | 0.0 ± 2.4 |
| 2QZCluster-SPIRE219 | 150.7518402452608 | 0.3059122095193959 | 16.3 ± 2.2 | 18.0 ± 1.9 | 7.3 ± 2.2 |
| 2QZCluster-SPIRE220 | 150.9183884841128 | 0.28617156046303294 | 18.2 ± 2.4 | 24.8 ± 1.8 | 18.4 ± 2.1 |
| 2QZCluster-SPIRE221 | 150.7263074723792 | 0.33598610532501494 | 18.5 ± 2.5 | 3.8 ± 1.8 | 0.0 ± 2.4 |
| 2QZCluster-SPIRE222 | 150.7687583484075 | 0.20596306579714738 | 15.8 ± 2.1 | 11.1 ± 1.8 | 4.9 ± 2.2 |
| 2QZCluster-SPIRE223 | 150.85601925048343 | 0.3061033028320979 | 16.1 ± 2.2 | 16.3 ± 2.0 | 13.2 ± 2.1 |
| 2QZCluster-SPIRE224 | 150.81924418002566 | 0.26506657165325176 | 17.4 ± 2.4 | 15.1 ± 1.7 | 11.1 ± 2.1 |
| 2QZCluster-SPIRE225 | 150.8731103670741 | 0.034011378692691 | 17.5 ± 2.4 | 8.6 ± 1.8 | 11.3 ± 2.1 |
| 2QZCluster-SPIRE226 | 150.77007870217977 | 0.34959558544281555 | 18.9 ± 2.6 | 16.6 ± 1.8 | 11.0 ± 2.4 |
| 2QZCluster-SPIRE227 | 150.87918864949435 | 0.3385503474254718 | 16.8 ± 2.3 | 8.5 ± 1.8 | 3.3 ± 2.2 |
| 2QZCluster-SPIRE228 | 151.07121981814606 | 0.1904928260646215 | 14.8 ± 2.1 | 22.9 ± 1.8 | 20.3 ± 2.1 |
| 2QZCluster-SPIRE229 | 150.9305656546674 | 0.3167370388948136 | 16.8 ± 2.3 | 26.3 ± 1.6 | 21.7 ± 2.2 |
| 2QZCluster-SPIRE230 | 150.89368643445698 | 0.2571852202920889 | 14.8 ± 2.1 | 16.5 ± 1.8 | 8.3 ± 2.2 |
| 2QZCluster-SPIRE231 | 150.90199148896951 | 0.18508329003004922 | 17.8 ± 2.5 | 16.3 ± 2.0 | 13.9 ± 2.2 |
| 2QZCluster-SPIRE232 | 150.84246607549682 | 0.191258002565328 | 16.8 ± 2.3 | 11.5 ± 1.6 | 8.2 ± 2.4 |
| 2QZCluster-SPIRE233 | 151.0319971929263 | 0.2172402643167666 | 15.9 ± 2.2 | 8.5 ± 1.8 | 9.3 ± 2.1 |
| 2QZCluster-SPIRE234 | 150.99737456582065 | 0.25841704759385464 | 15.6 ± 2.2 | 8.4 ± 1.8 | 0.0 ± 2.1 |
| 2QZCluster-SPIRE235 | 150.92659706489064 | 0.2713817420976716 | 16.7 ± 2.3 | 12.1 ± 1.7 | 1.5 ± 2.1 |
| 2QZCluster-SPIRE236 | 150.9127993399629 | 0.1283677294865458 | 15.5 ± 2.2 | 17.9 ± 1.7 | 0.1 ± 2.3 |

Table A.6: SPIRE sources catalogue of 2QZCluster field.

| ID[1] | R.A.[2] (J2000) | Dec.[3] (J2000) | $S_{250}$[4] (mJy) | $S_{350}$[5] (mJy) | $S_{500}$[6] (mJy) |
|---|---|---|---|---|---|
| 2QZCluster-SPIRE237 | 151.02481860849156 | 0.1978053703313899 | 17.2 ± 2.4 | 9.6 ± 1.8 | 2.6 ± 2.1 |
| 2QZCluster-SPIRE238 | 151.03715064832429 | 0.1372771786199001 | 15.2 ± 2.1 | 6.6 ± 1.8 | 0.0 ± 2.1 |
| 2QZCluster-SPIRE239 | 151.06947030615623 | 0.31048814521946677 | 15.4 ± 2.2 | 4.1 ± 1.8 | 6.9 ± 2.3 |
| 2QZCluster-SPIRE240 | 150.99118649485564 | 0.19178683070873834 | 16.5 ± 2.3 | 7.2 ± 1.8 | 4.1 ± 2.2 |
| 2QZCluster-SPIRE241 | 150.71327876950687 | 0.33273141128934475 | 17.6 ± 2.5 | 10.9 ± 1.9 | 6.8 ± 2.2 |
| 2QZCluster-SPIRE242 | 150.90117197438556 | 0.31355892977914 | 17.2 ± 2.4 | 8.2 ± 1.8 | 1.3 ± 2.1 |
| 2QZCluster-SPIRE243 | 151.05107775502924 | 0.16627404384343342 | 15.3 ± 2.2 | 24.4 ± 1.7 | 26.6 ± 2.3 |
| 2QZCluster-SPIRE244 | 151.0197132580291 | 0.24142605566844974 | 17.2 ± 2.4 | 11.7 ± 1.6 | 8.7 ± 2.4 |
| 2QZCluster-SPIRE245 | 151.0007956693026 | 0.3503225583078614 | 15.4 ± 2.2 | 19.7 ± 1.7 | 7.6 ± 2.1 |
| 2QZCluster-SPIRE246 | 150.91907234406978 | 0.20770440115520472 | 18.3 ± 2.6 | 0.0 ± 1.8 | 0.0 ± 2.3 |
| 2QZCluster-SPIRE247 | 151.06738633592346 | 0.21230827487105586 | 15.4 ± 2.2 | 9.8 ± 1.8 | 10.7 ± 2.0 |
| 2QZCluster-SPIRE248 | 151.01913376324993 | 0.45150471447404755 | 18.1 ± 2.6 | 20.7 ± 2.2 | 10.0 ± 2.5 |
| 2QZCluster-SPIRE249 | 150.82788501023575 | 0.21590694703565833 | 15.7 ± 2.2 | 9.2 ± 1.6 | 3.6 ± 2.1 |
| 2QZCluster-SPIRE250 | 150.92991884367194 | 0.11284719654323062 | 16.0 ± 2.3 | 16.3 ± 1.8 | 11.1 ± 2.3 |
| 2QZCluster-SPIRE251 | 150.8855513827945 | 0.16832471355289963 | 15.5 ± 2.2 | 6.8 ± 2.0 | 3.7 ± 2.3 |
| 2QZCluster-SPIRE252 | 150.79373443997085 | 0.19428866642869352 | 14.8 ± 2.1 | 7.1 ± 1.8 | 2.6 ± 2.3 |
| 2QZCluster-SPIRE253 | 150.94878928291584 | 0.04938326837661398 | 15.4 ± 2.2 | 12.0 ± 1.9 | 9.7 ± 2.3 |
| 2QZCluster-SPIRE254 | 151.06202206740994 | 0.15574290434648616 | 17.1 ± 2.5 | 12.0 ± 1.7 | 0.0 ± 2.2 |
| 2QZCluster-SPIRE255 | 150.75638888104044 | 0.2783739643837899 | 15.1 ± 2.2 | 16.7 ± 1.8 | 6.0 ± 2.3 |
| 2QZCluster-SPIRE256 | 150.93582517847366 | 0.3842615847753579 | 14.5 ± 2.1 | 13.0 ± 1.9 | 2.0 ± 2.3 |
| 2QZCluster-SPIRE257 | 150.88305995617017 | 0.08746071761330128 | 15.9 ± 2.3 | 9.6 ± 1.8 | 2.5 ± 2.3 |
| 2QZCluster-SPIRE258 | 150.87676705903783 | 0.07957104405665957 | 16.3 ± 2.4 | 3.9 ± 1.9 | 0.0 ± 2.2 |
| 2QZCluster-SPIRE259 | 151.0883115061805 | 0.1782504823523088 | 15.1 ± 2.2 | 13.3 ± 1.7 | 20.3 ± 2.3 |
| 2QZCluster-SPIRE260 | 150.74061189354717 | 0.373758657165491 | 17.1 ± 2.5 | 23.9 ± 2.1 | 8.7 ± 2.5 |
| 2QZCluster-SPIRE261 | 150.8525261558121 | 0.15590283616430975 | 15.8 ± 2.3 | 13.8 ± 1.8 | 12.1 ± 2.2 |
| 2QZCluster-SPIRE262 | 150.98268688438267 | 0.1895260782253963 | 14.8 ± 2.2 | 14.8 ± 1.9 | 2.9 ± 2.2 |
| 2QZCluster-SPIRE263 | 150.9571001963364 | 0.08263918229581807 | 15.4 ± 2.3 | 20.6 ± 1.9 | 12.5 ± 2.1 |
| 2QZCluster-SPIRE264 | 150.79681971461986 | 0.1998907869012189 | 15.8 ± 2.4 | 4.9 ± 1.8 | 1.6 ± 2.2 |
| 2QZCluster-SPIRE265 | 151.06160364212735 | 0.11720407687993407 | 15.3 ± 2.3 | 14.6 ± 1.8 | 12.1 ± 2.2 |
| 2QZCluster-SPIRE266 | 150.95007848935666 | 0.38009572409916864 | 15.0 ± 2.3 | 20.7 ± 1.8 | 21.8 ± 2.1 |
| 2QZCluster-SPIRE267 | 151.06559082334945 | 0.20000449174308702 | 14.3 ± 2.2 | 7.9 ± 1.9 | 0.0 ± 2.1 |
| 2QZCluster-SPIRE268 | 151.109474575594 | 0.22379863862343605 | 15.4 ± 2.3 | 13.1 ± 1.8 | 9.4 ± 2.1 |
| 2QZCluster-SPIRE269 | 150.915030398503 | 0.0617154240874663 | 13.6 ± 2.1 | 8.0 ± 1.8 | 0.0 ± 2.2 |
| 2QZCluster-SPIRE270 | 150.83611096177958 | 0.1994453284884657 | 15.0 ± 2.3 | 9.1 ± 1.9 | 2.5 ± 2.1 |
| 2QZCluster-SPIRE271 | 150.81882661035726 | 0.3263777112655883 | 14.0 ± 2.1 | 3.5 ± 1.8 | 0.5 ± 2.0 |
| 2QZCluster-SPIRE272 | 150.95793299964717 | 0.28697872465972873 | 14.9 ± 2.3 | 9.0 ± 1.9 | 1.5 ± 2.2 |
| 2QZCluster-SPIRE273 | 151.07299000414696 | 0.29972800232853736 | 14.4 ± 2.2 | 13.4 ± 1.8 | 14.0 ± 2.3 |
| 2QZCluster-SPIRE274 | 150.98768777741066 | 0.3921316303590258 | 13.7 ± 2.1 | 6.7 ± 1.7 | 2.0 ± 2.0 |
| 2QZCluster-SPIRE275 | 150.9477543610148 | 0.22147820848885458 | 14.8 ± 2.3 | 12.5 ± 1.6 | 5.9 ± 2.1 |
| 2QZCluster-SPIRE276 | 150.78724183904114 | 0.14120755123526704 | 13.4 ± 2.1 | 9.9 ± 1.9 | 0.0 ± 2.2 |
| 2QZCluster-SPIRE277 | 150.94443235167824 | 0.264584525065859 | 14.2 ± 2.2 | 20.1 ± 1.8 | 25.6 ± 2.2 |
| 2QZCluster-SPIRE278 | 151.1210073515418 | 0.21200045775749554 | 14.7 ± 2.3 | 10.8 ± 1.8 | 2.7 ± 2.3 |
| 2QZCluster-SPIRE279 | 150.8933176830212 | 0.04711960232200302 | 13.9 ± 2.2 | 3.0 ± 1.8 | 2.7 ± 2.1 |
| 2QZCluster-SPIRE280 | 150.82017176006417 | 0.25504350197990133 | 14.7 ± 2.3 | 20.7 ± 1.7 | 18.7 ± 2.2 |
| 2QZCluster-SPIRE281 | 150.99712597069467 | 0.15060343853558522 | 13.7 ± 2.1 | 7.5 ± 1.8 | 6.3 ± 2.3 |
| 2QZCluster-SPIRE282 | 151.06347534840924 | 0.22176515201093322 | 15.0 ± 2.3 | 12.2 ± 2.0 | 14.3 ± 2.2 |
| 2QZCluster-SPIRE283 | 150.78625238324628 | 0.32850195834971263 | 14.4 ± 2.3 | 7.9 ± 1.7 | 0.0 ± 2.2 |
| 2QZCluster-SPIRE284 | 150.97980902901836 | 0.20562281089769674 | 16.4 ± 2.6 | 5.0 ± 1.9 | 1.0 ± 2.3 |
| 2QZCluster-SPIRE285 | 150.97704654176894 | 0.43869649611588035 | 16.0 ± 2.5 | 10.8 ± 2.0 | 8.4 ± 2.5 |
| 2QZCluster-SPIRE286 | 150.93749169166 | 0.18819343121859797 | 14.3 ± 2.3 | 11.2 ± 1.9 | 2.4 ± 2.1 |
| 2QZCluster-SPIRE287 | 150.91435543947918 | 0.3371712921965592 | 13.2 ± 2.1 | 12.1 ± 1.7 | 5.2 ± 2.0 |
| 2QZCluster-SPIRE288 | 150.7831956614849 | 0.29094504615215805 | 15.2 ± 2.4 | 8.9 ± 1.7 | 4.1 ± 2.3 |
| 2QZCluster-SPIRE289 | 150.91318018215725 | 0.17678220359981156 | 13.9 ± 2.2 | 4.0 ± 1.9 | 0.9 ± 2.3 |
| 2QZCluster-SPIRE290 | 151.0088417145264 | 0.1277531724502722 | 13.8 ± 2.2 | 2.2 ± 1.8 | 0.0 ± 2.2 |
| 2QZCluster-SPIRE291 | 150.77592358188832 | 0.24230090234787824 | 13.0 ± 2.1 | 7.8 ± 2.0 | 0.0 ± 2.2 |
| 2QZCluster-SPIRE292 | 150.81054426652668 | 0.16785956309309027 | 13.9 ± 2.2 | 16.6 ± 1.9 | 1.8 ± 2.2 |
| 2QZCluster-SPIRE293 | 150.86598298332842 | 0.3301212160244767 | 12.9 ± 2.1 | 9.9 ± 1.7 | 2.6 ± 1.9 |
| 2QZCluster-SPIRE294 | 150.9345658556179 | 0.4486497061830582 | 21.9 ± 3.6 | 17.6 ± 2.2 | 7.0 ± 3.0 |
| 2QZCluster-SPIRE295 | 150.9016434586326 | 0.046496358469518065 | 13.3 ± 2.2 | 8.4 ± 1.7 | 3.2 ± 2.5 |
| 2QZCluster-SPIRE296 | 150.8200442758231 | 0.36000632497558266 | 15.3 ± 2.5 | 21.0 ± 1.8 | 27.9 ± 2.3 |
| 2QZCluster-SPIRE297 | 150.95431906973812 | 0.28024728069412047 | 13.6 ± 2.2 | 6.5 ± 1.8 | 1.5 ± 2.3 |
| 2QZCluster-SPIRE298 | 150.86335949812778 | 0.2483909867572047 | 12.9 ± 2.1 | 10.9 ± 1.8 | 6.3 ± 2.4 |
| 2QZCluster-SPIRE299 | 150.97523336504526 | 0.3551117462807689 | 14.2 ± 2.3 | 12.0 ± 1.7 | 5.5 ± 2.2 |
| 2QZCluster-SPIRE300 | 150.8141932592971 | 0.27099859563083323 | 13.6 ± 2.2 | 10.8 ± 1.7 | 3.3 ± 2.1 |
| 2QZCluster-SPIRE301 | 150.91806499440895 | 0.36142602401198176 | 13.1 ± 2.1 | 8.2 ± 1.8 | 20.9 ± 2.4 |
| 2QZCluster-SPIRE302 | 151.00546814696534 | 0.3142763284515066 | 15.6 ± 2.6 | 6.8 ± 1.7 | 2.6 ± 2.3 |
| 2QZCluster-SPIRE303 | 150.90337702472888 | 0.17611115763017324 | 13.3 ± 2.2 | 12.8 ± 2.0 | 14.1 ± 2.3 |
| 2QZCluster-SPIRE304 | 151.01530663375632 | 0.09316135918979683 | 13.1 ± 2.2 | 3.7 ± 1.8 | 1.5 ± 2.2 |
| 2QZCluster-SPIRE305 | 151.03035997150766 | 0.45615702079927534 | 17.7 ± 2.9 | 6.4 ± 2.0 | 0.0 ± 2.6 |
| 2QZCluster-SPIRE306 | 150.94355809364302 | 0.08948910836084548 | 14.2 ± 2.3 | 8.4 ± 1.9 | 3.1 ± 2.2 |
| 2QZCluster-SPIRE307 | 150.90634336050812 | 0.3366020122791925 | 12.3 ± 2.0 | 16.4 ± 1.6 | 12.0 ± 2.0 |
| 2QZCluster-SPIRE308 | 150.85671283006766 | 0.0911786042608974 | 14.3 ± 2.4 | 16.2 ± 1.7 | 15.3 ± 2.2 |
| 2QZCluster-SPIRE309 | 150.72715855056344 | 0.2677902137337443 | 13.4 ± 2.2 | 8.2 ± 2.0 | 6.2 ± 2.1 |
| 2QZCluster-SPIRE310 | 150.92067733752313 | 0.4120368138859689 | 14.5 ± 2.4 | 1.8 ± 1.9 | 0.0 ± 2.4 |
| 2QZCluster-SPIRE311 | 150.80823411097433 | 0.38868490750128604 | 16.0 ± 2.7 | 14.7 ± 2.0 | 6.4 ± 2.6 |
| 2QZCluster-SPIRE312 | 150.75265052272073 | 0.35987375620393985 | 14.7 ± 2.5 | 18.0 ± 1.8 | 19.0 ± 2.2 |

Table A.6: SPIRE sources catalogue of 2QZCluster field.

| ID[1] | R.A.[2] (J2000) | Dec.[3] (J2000) | $S_{250}$[4] (mJy) | $S_{350}$[5] (mJy) | $S_{500}$[6] (mJy) |
|---|---|---|---|---|---|
| 2QZCluster-SPIRE313 | 150.87496349445445 | 0.36386409166982986 | 13.6 ± 2.3 | 14.0 ± 1.8 | 10.7 ± 2.2 |
| 2QZCluster-SPIRE314 | 151.1439725599331 | 0.13457135158132646 | 13.4 ± 2.3 | 7.1 ± 1.9 | 3.5 ± 2.1 |
| 2QZCluster-SPIRE315 | 150.8227778447938 | 0.009261805123606826 | 13.8 ± 2.3 | 8.3 ± 1.9 | 0.0 ± 2.3 |
| 2QZCluster-SPIRE316 | 151.03587189289814 | 0.2771816984055311 | 12.0 ± 2.0 | 6.8 ± 1.7 | 0.0 ± 2.0 |
| 2QZCluster-SPIRE317 | 150.76762919926372 | 0.2840073827722543 | 12.2 ± 2.1 | 4.0 ± 1.8 | 0.0 ± 2.5 |
| 2QZCluster-SPIRE318 | 150.98054288003888 | 0.09735817065411943 | 13.3 ± 2.3 | 3.1 ± 1.9 | 2.2 ± 2.4 |
| 2QZCluster-SPIRE319 | 150.89834273240308 | 0.24386637402320577 | 13.0 ± 2.2 | 17.1 ± 1.7 | 10.7 ± 2.0 |
| 2QZCluster-SPIRE320 | 150.8435856742194 | 0.24956774445677105 | 13.1 ± 2.2 | 6.2 ± 1.9 | 4.2 ± 2.1 |
| 2QZCluster-SPIRE321 | 150.88417088903296 | 0.031584754719909645 | 13.1 ± 2.2 | 8.8 ± 1.8 | 7.6 ± 2.1 |
| 2QZCluster-SPIRE322 | 151.0685142869196 | 0.2954659636575827 | 13.4 ± 2.3 | 12.6 ± 1.8 | 11.7 ± 2.1 |
| 2QZCluster-SPIRE323 | 150.99884888130956 | 0.4487672337337461 | 15.2 ± 2.6 | 28.3 ± 2.1 | 21.0 ± 2.8 |
| 2QZCluster-SPIRE324 | 150.92721002068595 | 0.2979868199310082 | 12.6 ± 2.2 | 17.1 ± 1.8 | 11.3 ± 2.1 |
| 2QZCluster-SPIRE325 | 151.04447141402468 | 0.17572722877914979 | 12.8 ± 2.2 | 5.0 ± 1.6 | 0.0 ± 2.1 |
| 2QZCluster-SPIRE326 | 150.95800354641955 | 0.4116310919266733 | 13.8 ± 2.4 | 6.5 ± 1.8 | 2.1 ± 2.2 |
| 2QZCluster-SPIRE327 | 150.777250028704 | 0.25938440106718397 | 13.0 ± 2.3 | 4.1 ± 1.8 | 0.0 ± 2.2 |
| 2QZCluster-SPIRE328 | 150.95800640010322 | 0.14548777345398073 | 12.6 ± 2.2 | 12.6 ± 1.8 | 0.0 ± 2.0 |
| 2QZCluster-SPIRE329 | 150.9138204990902 | 0.20121386043743983 | 14.1 ± 2.5 | 1.5 ± 1.8 | 0.0 ± 2.1 |
| 2QZCluster-SPIRE330 | 150.98318033406326 | 0.08602373281433771 | 13.1 ± 2.3 | 12.3 ± 1.7 | 6.0 ± 2.1 |
| 2QZCluster-SPIRE331 | 151.05692104113368 | 0.18903488712293293 | 13.4 ± 2.3 | 7.0 ± 1.7 | 0.0 ± 2.0 |
| 2QZCluster-SPIRE332 | 150.97457737824448 | 0.06815914539647322 | 12.5 ± 2.2 | 8.0 ± 1.8 | 0.0 ± 2.1 |
| 2QZCluster-SPIRE333 | 150.8499659349547 | 0.060228813041207016 | 13.6 ± 2.4 | 3.2 ± 2.0 | 0.0 ± 2.2 |
| 2QZCluster-SPIRE334 | 150.87032660917342 | 0.4194134565617384 | 15.5 ± 2.7 | 9.3 ± 2.0 | 7.4 ± 2.8 |
| 2QZCluster-SPIRE335 | 150.76001934536527 | 0.33612541180976047 | 12.8 ± 2.3 | 7.9 ± 1.8 | 4.3 ± 2.1 |
| 2QZCluster-SPIRE336 | 150.77766328220963 | 0.19709120337627897 | 12.1 ± 2.2 | 12.8 ± 1.8 | 1.3 ± 2.2 |
| 2QZCluster-SPIRE337 | 150.8934715975371 | 0.4340695850865331 | 17.3 ± 3.1 | 19.9 ± 2.2 | 10.2 ± 3.1 |
| 2QZCluster-SPIRE338 | 150.84765896483194 | 0.17594998822063868 | 13.3 ± 2.4 | 11.9 ± 1.7 | 4.5 ± 2.3 |
| 2QZCluster-SPIRE339 | 151.0604476193186 | 0.36135416230379863 | 13.2 ± 2.4 | 15.1 ± 1.9 | 11.9 ± 2.1 |
| 2QZCluster-SPIRE340 | 150.9721884135593 | 0.2003319550162692 | 12.0 ± 2.2 | 8.3 ± 1.8 | 2.5 ± 2.1 |
| 2QZCluster-SPIRE341 | 150.99108479914787 | 0.4085779805521634 | 14.3 ± 2.6 | 3.8 ± 1.9 | 0.4 ± 2.2 |
| 2QZCluster-SPIRE342 | 150.80879039316568 | 0.2521677172270751 | 12.9 ± 2.3 | 13.3 ± 1.8 | 3.0 ± 2.3 |
| 2QZCluster-SPIRE343 | 150.86359478265123 | 0.1072813967500251 | 12.2 ± 2.2 | 2.9 ± 1.7 | 0.4 ± 2.2 |
| 2QZCluster-SPIRE344 | 150.6916094343718 | 0.3518431656571255 | 14.7 ± 2.7 | 32.6 ± 2.1 | 32.3 ± 2.7 |
| 2QZCluster-SPIRE345 | 150.99140014128434 | 0.2733292285949821 | 12.0 ± 2.2 | 9.0 ± 1.7 | 4.1 ± 2.0 |
| 2QZCluster-SPIRE346 | 150.8632833179058 | 0.06433074730072826 | 12.8 ± 2.3 | 11.1 ± 1.9 | 11.6 ± 2.1 |
| 2QZCluster-SPIRE347 | 151.011965051167 | 0.10097887536762586 | 11.9 ± 2.2 | 27.1 ± 1.9 | 25.3 ± 2.1 |
| 2QZCluster-SPIRE348 | 150.88800689608277 | 0.21271333844002183 | 12.4 ± 2.3 | 12.3 ± 2.0 | 1.1 ± 2.1 |
| 2QZCluster-SPIRE349 | 150.86045655660786 | 0.3567835945346636 | 13.0 ± 2.4 | 0.0 ± 1.8 | 6.7 ± 2.1 |
| 2QZCluster-SPIRE350 | 150.851561267553 | 0.27532738887273456 | 13.2 ± 2.5 | 0.0 ± 1.8 | 2.6 ± 2.3 |
| 2QZCluster-SPIRE351 | 150.82673806658374 | 0.09031618427960127 | 12.3 ± 2.3 | 5.6 ± 1.8 | 0.0 ± 2.2 |
| 2QZCluster-SPIRE352 | 150.78097683314218 | 0.20789440322590005 | 12.0 ± 2.3 | 2.2 ± 1.7 | 0.0 ± 2.1 |
| 2QZCluster-SPIRE353 | 150.91618318915945 | 0.1872915426760585 | 14.4 ± 2.7 | 12.1 ± 1.8 | 3.0 ± 2.1 |
| 2QZCluster-SPIRE354 | 150.7167871770831 | 0.29166621067363946 | 12.0 ± 2.3 | 13.0 ± 1.8 | 8.1 ± 2.1 |
| 2QZCluster-SPIRE355 | 150.81958892949584 | 0.19766950864558316 | 12.9 ± 2.4 | 0.0 ± 1.7 | 16.1 ± 2.3 |
| 2QZCluster-SPIRE356 | 150.7068226828234 | 0.297982533861947 | 12.4 ± 2.3 | 8.7 ± 1.9 | 1.6 ± 2.3 |
| 2QZCluster-SPIRE357 | 151.01916378939683 | 0.2326737188133764 | 13.0 ± 2.5 | 9.0 ± 1.7 | 8.4 ± 2.3 |
| 2QZCluster-SPIRE358 | 151.06932231785038 | 0.26765557820294006 | 11.6 ± 2.2 | 21.5 ± 1.9 | 17.4 ± 2.3 |
| 2QZCluster-SPIRE359 | 151.06376056620957 | 0.10266820460871635 | 12.1 ± 2.3 | 13.1 ± 1.7 | 6.8 ± 2.2 |
| 2QZCluster-SPIRE360 | 151.1401707712136 | 0.15050560718966643 | 14.5 ± 2.8 | 8.7 ± 1.8 | 0.0 ± 2.2 |
| 2QZCluster-SPIRE361 | 150.98125454443203 | 0.1083870564661207 | 12.6 ± 2.5 | 11.0 ± 1.7 | 0.0 ± 2.3 |
| 2QZCluster-SPIRE362 | 151.05017516029187 | 0.14616209462621613 | 12.0 ± 2.4 | 14.1 ± 1.7 | 11.3 ± 2.4 |
| 2QZCluster-SPIRE363 | 150.9664520779312 | 0.2244091699731535 | 10.8 ± 2.2 | 13.9 ± 1.8 | 6.1 ± 2.2 |
| 2QZCluster-SPIRE364 | 150.91139997071042 | 0.4030573085421576 | 11.7 ± 2.4 | 10.2 ± 1.8 | 15.3 ± 2.4 |
| 2QZCluster-SPIRE365 | 150.97446829271195 | 0.4066178923575616 | 12.5 ± 2.5 | 6.0 ± 1.8 | 7.4 ± 2.1 |
| 2QZCluster-SPIRE366 | 150.74537728843165 | 0.3400149306024909 | 13.3 ± 2.7 | 12.4 ± 1.8 | 3.2 ± 2.3 |
| 2QZCluster-SPIRE367 | 150.84977965688097 | 0.0782345492130146 | 11.4 ± 2.3 | 14.2 ± 1.9 | 6.4 ± 2.1 |
| 2QZCluster-SPIRE368 | 150.96183617871552 | 0.3632305540976805 | 11.6 ± 2.4 | 15.2 ± 1.7 | 20.9 ± 2.2 |
| 2QZCluster-SPIRE369 | 150.81040101980926 | 0.3583378023775709 | 13.5 ± 2.8 | 8.8 ± 1.9 | 2.3 ± 2.2 |
| 2QZCluster-SPIRE370 | 150.76477916706133 | 0.14164368256710455 | 12.5 ± 2.6 | 10.9 ± 2.0 | 6.4 ± 2.3 |
| 2QZCluster-SPIRE371 | 150.87554206880242 | 0.40604285698397263 | 12.1 ± 2.6 | 0.4 ± 1.7 | 0.0 ± 2.3 |
| 2QZCluster-SPIRE372 | 150.93526728585985 | 0.238716121827333 | 10.2 ± 2.2 | 16.2 ± 1.8 | 14.0 ± 2.1 |
| 2QZCluster-SPIRE373 | 150.94753920357326 | 0.11070175893193998 | 12.2 ± 2.6 | 10.6 ± 1.8 | 7.4 ± 2.1 |
| 2QZCluster-SPIRE374 | 151.01737179331005 | 0.35340163331311736 | 9.8 ± 2.1 | 12.7 ± 1.9 | 7.4 ± 2.1 |
| 2QZCluster-SPIRE375 | 150.81342327255965 | 0.3189220469332396 | 10.2 ± 2.2 | 12.7 ± 1.8 | 4.4 ± 2.1 |
| 2QZCluster-SPIRE376 | 151.1107738611311 | 0.21615707645072846 | 10.0 ± 2.2 | 13.5 ± 1.8 | 2.8 ± 2.3 |
| 2QZCluster-SPIRE377 | 150.80504528346088 | 0.1011479304312866 | 10.2 ± 2.2 | 16.3 ± 1.8 | 11.2 ± 2.1 |
| 2QZCluster-SPIRE378 | 150.80476579062824 | 0.08373821361719407 | 10.3 ± 2.2 | 15.1 ± 1.9 | 8.9 ± 2.2 |
| 2QZCluster-SPIRE379 | 151.0230446233666 | 0.35942995098014996 | 10.4 ± 2.3 | 15.2 ± 1.8 | 16.0 ± 2.4 |
| 2QZCluster-SPIRE380 | 150.80147320345225 | 0.18522773528375414 | 10.9 ± 2.4 | 18.2 ± 1.9 | 15.1 ± 2.1 |
| 2QZCluster-SPIRE381 | 150.92531210040184 | 0.13018866871982165 | 10.8 ± 2.4 | 23.4 ± 1.8 | 19.4 ± 2.3 |
| 2QZCluster-SPIRE382 | 150.9617009481577 | 0.4493959480833938 | 12.0 ± 2.7 | 12.8 ± 2.1 | 3.1 ± 2.4 |
| 2QZCluster-SPIRE383 | 151.0183647967348 | 0.22095008049014114 | 11.4 ± 2.6 | 12.2 ± 1.8 | 10.8 ± 2.3 |
| 2QZCluster-SPIRE384 | 150.98975549952246 | 0.11244864004528837 | 10.0 ± 2.3 | 12.1 ± 1.7 | 10.1 ± 2.1 |
| 2QZCluster-SPIRE385 | 150.94418910264537 | 0.2473573829107605 | 9.2 ± 2.1 | 9.6 ± 1.7 | 14.0 ± 2.0 |
| 2QZCluster-SPIRE386 | 151.0525786107535 | 0.317869066173317 | 9.0 ± 2.2 | 13.8 ± 1.9 | 3.5 ± 2.4 |
| 2QZCluster-SPIRE387 | 150.89612046742505 | 0.19316854580655582 | 9.6 ± 2.4 | 17.1 ± 1.9 | 19.7 ± 2.2 |
| 2QZCluster-SPIRE388 | 151.12429418594692 | 0.20260506312159454 | 9.3 ± 2.3 | 19.2 ± 1.8 | 18.8 ± 2.2 |

Table A.6: SPIRE sources catalogue of 2QZCluster field.

| ID[1] | R.A.[2] (J2000) | Dec.[3] (J2000) | $S_{250}$[4] (mJy) | $S_{350}$[5] (mJy) | $S_{500}$[6] (mJy) |
|---|---|---|---|---|---|
| 2QZCluster-SPIRE389 | 150.8986153543054 | 0.10008762822995709 | 8.9 ± 2.2 | 16.9 ± 1.9 | 20.9 ± 2.2 |
| 2QZCluster-SPIRE390 | 150.84474184790858 | 0.3971260261987385 | 11.4 ± 2.9 | 17.2 ± 1.8 | 7.2 ± 2.5 |
| 2QZCluster-SPIRE391 | 150.81293701577903 | 0.08584991283412813 | 9.6 ± 2.5 | 12.1 ± 1.7 | 15.2 ± 2.2 |
| 2QZCluster-SPIRE392 | 150.81293683200676 | 0.20824934224628783 | 8.3 ± 2.3 | 12.2 ± 1.6 | 3.9 ± 2.1 |
| 2QZCluster-SPIRE393 | 151.0388203840176 | 0.22010631422265026 | 8.6 ± 2.5 | 23.1 ± 1.8 | 24.4 ± 2.3 |
| 2QZCluster-SPIRE394 | 150.9024111093267 | 0.07837574558349986 | 6.8 ± 2.0 | 6.1 ± 1.8 | 17.3 ± 2.1 |
| 2QZCluster-SPIRE395 | 151.02881586019254 | 0.4054128017082181 | 7.2 ± 2.2 | 16.1 ± 1.9 | 22.2 ± 2.1 |
| 2QZCluster-SPIRE396 | 150.87135302509427 | 0.2069419503437577 | 7.0 ± 2.3 | 16.4 ± 1.9 | 12.4 ± 2.1 |
| 2QZCluster-SPIRE397 | 150.77011968967244 | 0.38462443290543025 | 8.0 ± 2.7 | 13.4 ± 2.0 | 0.7 ± 2.8 |
| 2QZCluster-SPIRE398 | 151.02952805913094 | 0.18933686131302777 | 5.7 ± 2.3 | 9.9 ± 1.7 | 12.5 ± 2.2 |
| 2QZCluster-SPIRE399 | 150.96921038571656 | 0.12212106347275974 | 5.2 ± 2.4 | 16.2 ± 1.7 | 12.2 ± 2.3 |

Table A.7: SPIRE sources catalogue of HS1700 field.

| ID[1] | R.A.[2] (J2000) | Dec.[3] (J2000) | $S_{250}$[4] (mJy) | $S_{350}$[5] (mJy) | $S_{500}$[6] (mJy) |
|---|---|---|---|---|---|
| HS1700-SPIRE1 | 255.53646683056928 | 64.2060083253161 | 422.6 ± 3.1 | 181.4 ± 1.9 | 67.3 ± 2.4 |
| HS1700-SPIRE2 | 255.07094202680116 | 64.36337246187729 | 112.4 ± 2.2 | 49.0 ± 1.9 | 19.5 ± 2.2 |
| HS1700-SPIRE3 | 255.10511462429938 | 64.14686204692669 | 86.2 ± 2.4 | 51.5 ± 2.0 | 21.4 ± 2.1 |
| HS1700-SPIRE4 | 255.15806474143926 | 64.22916135482777 | 85.8 ± 2.5 | 60.5 ± 1.8 | 27.9 ± 2.2 |
| HS1700-SPIRE5 | 254.99437853070503 | 64.26410380634614 | 70.8 ± 2.1 | 76.4 ± 1.7 | 51.2 ± 2.2 |
| HS1700-SPIRE6 | 254.91863041158092 | 64.21174308418698 | 76.7 ± 2.4 | 44.4 ± 1.7 | 17.6 ± 2.3 |
| HS1700-SPIRE7 | 255.22359843297363 | 64.38646521955137 | 65.7 ± 2.2 | 21.3 ± 1.9 | 13.0 ± 2.3 |
| HS1700-SPIRE8 | 254.82938021291324 | 64.17873107989598 | 68.7 ± 2.3 | 59.4 ± 1.7 | 27.6 ± 2.2 |
| HS1700-SPIRE9 | 255.20168755944053 | 64.25859055126669 | 66.3 ± 2.2 | 35.3 ± 2.1 | 16.2 ± 2.2 |
| HS1700-SPIRE10 | 255.1823543841818 | 64.03153372522755 | 64.7 ± 2.2 | 64.8 ± 1.9 | 31.2 ± 2.1 |
| HS1700-SPIRE11 | 255.03758364130223 | 64.05101016017498 | 72.3 ± 2.5 | 62.1 ± 1.9 | 40.4 ± 2.4 |
| HS1700-SPIRE12 | 255.51559224970458 | 64.13696977291751 | 60.2 ± 2.1 | 30.5 ± 1.8 | 7.1 ± 2.3 |
| HS1700-SPIRE13 | 255.25438495672074 | 64.20336084637933 | 63.5 ± 2.2 | 46.1 ± 1.8 | 21.0 ± 2.1 |
| HS1700-SPIRE14 | 255.49809875418003 | 64.21319312751477 | 67.9 ± 2.5 | 27.9 ± 1.8 | 0.8 ± 2.2 |
| HS1700-SPIRE15 | 255.64705519915066 | 64.16411905353483 | 61.7 ± 2.3 | 37.3 ± 1.8 | 24.3 ± 2.3 |
| HS1700-SPIRE16 | 255.20902792140345 | 64.31308671851771 | 54.8 ± 2.1 | 56.7 ± 1.7 | 41.0 ± 2.1 |
| HS1700-SPIRE17 | 255.0347138501116 | 64.07206255580076 | 55.9 ± 2.2 | 22.6 ± 1.9 | 15.1 ± 2.2 |
| HS1700-SPIRE18 | 255.24091534844214 | 64.02120538942992 | 53.0 ± 2.1 | 32.9 ± 1.8 | 13.8 ± 2.1 |
| HS1700-SPIRE19 | 255.32866436190417 | 64.22934603621631 | 52.7 ± 2.1 | 21.7 ± 1.9 | 10.4 ± 2.3 |
| HS1700-SPIRE20 | 255.52671081584836 | 64.16207068386463 | 48.2 ± 2.0 | 58.5 ± 1.7 | 44.7 ± 2.1 |
| HS1700-SPIRE21 | 255.39506358659588 | 64.24837875442265 | 52.5 ± 2.2 | 41.2 ± 1.7 | 21.1 ± 2.2 |
| HS1700-SPIRE22 | 255.15351999228764 | 64.27682013237077 | 48.0 ± 2.0 | 26.1 ± 1.9 | 11.1 ± 2.1 |
| HS1700-SPIRE23 | 255.33281402361462 | 64.30499899042118 | 53.4 ± 2.4 | 40.7 ± 1.9 | 19.6 ± 2.1 |
| HS1700-SPIRE24 | 255.33486084261492 | 64.2403063607893 | 51.5 ± 2.3 | 63.0 ± 2.0 | 49.3 ± 2.2 |
| HS1700-SPIRE25 | 255.4031829363954 | 64.25605265727678 | 48.6 ± 2.2 | 24.6 ± 1.8 | 10.7 ± 2.2 |
| HS1700-SPIRE26 | 254.9240684495922 | 64.28608435616314 | 44.2 ± 2.1 | 40.4 ± 1.9 | 18.8 ± 2.1 |
| HS1700-SPIRE27 | 255.15047422383756 | 64.3868052315981 | 46.5 ± 2.2 | 40.5 ± 1.8 | 21.5 ± 2.2 |
| HS1700-SPIRE28 | 255.2796103161224 | 64.10352660074243 | 45.1 ± 2.1 | 17.7 ± 1.9 | 10.0 ± 2.2 |
| HS1700-SPIRE29 | 255.40442144606956 | 64.06170985861061 | 55.8 ± 2.7 | 61.6 ± 1.9 | 29.8 ± 2.4 |
| HS1700-SPIRE30 | 255.27555198634917 | 64.23509318646805 | 46.7 ± 2.3 | 35.8 ± 1.7 | 20.2 ± 2.3 |
| HS1700-SPIRE31 | 255.1113151015799 | 64.41215685334612 | 61.3 ± 3.1 | 29.2 ± 2.2 | 13.1 ± 2.6 |
| HS1700-SPIRE32 | 255.23439808556083 | 64.27486226085705 | 44.8 ± 2.3 | 44.5 ± 1.9 | 35.0 ± 2.1 |
| HS1700-SPIRE33 | 255.03444206094 | 64.24524335839524 | 40.3 ± 2.1 | 36.1 ± 1.8 | 14.3 ± 2.0 |
| HS1700-SPIRE34 | 255.23472630854002 | 64.32303294066622 | 41.8 ± 2.2 | 28.5 ± 1.7 | 8.2 ± 2.2 |
| HS1700-SPIRE35 | 255.01454092896174 | 64.37270966688595 | 44.8 ± 2.4 | 37.6 ± 2.0 | 20.1 ± 2.4 |
| HS1700-SPIRE36 | 255.36880953817646 | 64.03760221232672 | 41.9 ± 2.2 | 42.5 ± 1.8 | 25.0 ± 2.3 |
| HS1700-SPIRE37 | 255.02393137770747 | 64.1918672824805 | 44.6 ± 2.5 | 35.4 ± 1.9 | 24.2 ± 2.3 |
| HS1700-SPIRE38 | 255.68395120804098 | 64.22539347654842 | 38.7 ± 2.1 | 30.5 ± 2.0 | 13.8 ± 2.2 |
| HS1700-SPIRE39 | 255.4746467568773 | 64.28223595417336 | 38.0 ± 2.1 | 35.6 ± 1.8 | 21.5 ± 2.3 |
| HS1700-SPIRE40 | 255.4697538078033 | 64.24726056669022 | 39.4 ± 2.2 | 28.6 ± 1.8 | 14.7 ± 2.2 |
| HS1700-SPIRE41 | 255.4312665420055 | 64.14282409012444 | 39.4 ± 2.2 | 38.4 ± 1.8 | 16.9 ± 2.3 |
| HS1700-SPIRE42 | 255.24278273308224 | 64.21963311146037 | 40.0 ± 2.3 | 46.4 ± 1.8 | 34.3 ± 2.1 |
| HS1700-SPIRE43 | 255.0327866178943 | 64.08713966850861 | 39.8 ± 2.3 | 22.6 ± 1.9 | 11.3 ± 2.3 |
| HS1700-SPIRE44 | 255.61089630627202 | 64.21419909384203 | 37.8 ± 2.2 | 48.4 ± 2.0 | 34.8 ± 2.3 |
| HS1700-SPIRE45 | 255.45369835791007 | 64.21734505394862 | 38.2 ± 2.2 | 52.5 ± 1.8 | 45.0 ± 2.3 |
| HS1700-SPIRE46 | 255.56422570115723 | 64.16600701010962 | 39.0 ± 2.3 | 25.5 ± 1.8 | 12.0 ± 2.2 |
| HS1700-SPIRE47 | 254.9686139009027 | 64.33729883491866 | 42.6 ± 2.5 | 48.7 ± 1.9 | 36.6 ± 2.3 |
| HS1700-SPIRE48 | 255.27729187442546 | 64.29889868234208 | 37.6 ± 2.2 | 26.3 ± 1.8 | 17.6 ± 2.5 |
| HS1700-SPIRE49 | 255.23216136867404 | 64.20229603140722 | 44.6 ± 2.7 | 17.8 ± 1.8 | 4.8 ± 2.3 |
| HS1700-SPIRE50 | 255.12258223020348 | 64.2119133047661 | 42.4 ± 2.5 | 46.2 ± 1.7 | 26.1 ± 2.1 |
| HS1700-SPIRE51 | 255.43612553029516 | 64.29477124539959 | 36.7 ± 2.2 | 21.7 ± 1.7 | 16.9 ± 2.4 |
| HS1700-SPIRE52 | 254.9172597452437 | 64.07809096638823 | 35.9 ± 2.2 | 13.6 ± 1.9 | 3.1 ± 2.2 |
| HS1700-SPIRE53 | 255.18753240270385 | 64.40761476233186 | 33.9 ± 2.1 | 21.0 ± 1.8 | 7.4 ± 2.5 |

Table A.7: SPIRE sources catalogue of HS1700 field.

| ID[1] | R.A.[2] (J2000) | Dec.[3] (J2000) | $S_{250}$[4] (mJy) | $S_{350}$[5] (mJy) | $S_{500}$[6] (mJy) |
|---|---|---|---|---|---|
| HS1700-SPIRE54 | 254.99773183921928 | 64.33665525895374 | 36.2 ± 2.2 | 18.7 ± 1.9 | 16.4 ± 2.4 |
| HS1700-SPIRE55 | 255.4471084791806 | 64.3254096369478 | 39.5 ± 2.5 | 22.4 ± 1.9 | 4.7 ± 2.3 |
| HS1700-SPIRE56 | 255.5407202400225 | 64.2754182123465 | 33.5 ± 2.1 | 14.6 ± 1.9 | 12.6 ± 2.4 |
| HS1700-SPIRE57 | 255.40037088507952 | 64.28267530149303 | 36.5 ± 2.3 | 15.4 ± 1.8 | 10.7 ± 2.3 |
| HS1700-SPIRE58 | 255.06568400202337 | 64.20641096260186 | 34.2 ± 2.2 | 30.4 ± 2.0 | 15.2 ± 2.4 |
| HS1700-SPIRE59 | 254.7469847848302 | 64.16745857367826 | 36.7 ± 2.3 | 31.3 ± 1.8 | 11.6 ± 2.3 |
| HS1700-SPIRE60 | 255.34013321265527 | 64.2515732996532 | 32.5 ± 2.1 | 25.3 ± 1.7 | 0.0 ± 2.0 |
| HS1700-SPIRE61 | 255.4466603811549 | 64.24714789080174 | 35.6 ± 2.3 | 22.6 ± 1.8 | 12.0 ± 2.1 |
| HS1700-SPIRE62 | 254.92838845432908 | 64.14904249969956 | 33.1 ± 2.2 | 44.7 ± 2.0 | 33.4 ± 2.1 |
| HS1700-SPIRE63 | 255.30321354804747 | 64.34965630519547 | 31.2 ± 2.1 | 29.7 ± 1.8 | 21.4 ± 2.3 |
| HS1700-SPIRE64 | 255.53848280803075 | 64.09582869183762 | 35.3 ± 2.4 | 35.0 ± 1.9 | 22.2 ± 2.4 |
| HS1700-SPIRE65 | 255.65057122870448 | 64.18122553734624 | 31.7 ± 2.1 | 34.3 ± 1.8 | 14.2 ± 2.3 |
| HS1700-SPIRE66 | 255.33683695085716 | 64.10418201756993 | 31.9 ± 2.2 | 22.4 ± 1.9 | 11.5 ± 2.1 |
| HS1700-SPIRE67 | 255.45756573044304 | 64.07860940243295 | 35.8 ± 2.4 | 41.9 ± 1.8 | 27.7 ± 2.5 |
| HS1700-SPIRE68 | 255.42877728976194 | 64.20652935472319 | 32.1 ± 2.2 | 17.5 ± 1.9 | 0.0 ± 2.2 |
| HS1700-SPIRE69 | 255.31629147879914 | 64.06030234285014 | 29.7 ± 2.1 | 6.8 ± 1.8 | 0.0 ± 2.5 |
| HS1700-SPIRE70 | 255.28267330564802 | 64.25860511075904 | 31.1 ± 2.2 | 21.4 ± 1.9 | 11.0 ± 2.0 |
| HS1700-SPIRE71 | 254.9549702461632 | 64.1373046620896 | 30.8 ± 2.1 | 27.8 ± 1.9 | 13.5 ± 2.1 |
| HS1700-SPIRE72 | 255.33633632235254 | 64.14950665882763 | 34.5 ± 2.4 | 20.0 ± 1.9 | 14.6 ± 2.2 |
| HS1700-SPIRE73 | 255.59560664397003 | 64.22843708889755 | 30.9 ± 2.2 | 35.5 ± 1.9 | 17.6 ± 2.8 |
| HS1700-SPIRE74 | 255.251710205515 | 64.11718760500916 | 30.8 ± 2.2 | 34.4 ± 1.9 | 17.8 ± 2.3 |
| HS1700-SPIRE75 | 255.0917998875053 | 64.29587751297157 | 30.9 ± 2.2 | 24.6 ± 1.7 | 8.9 ± 2.5 |
| HS1700-SPIRE76 | 254.99217785581988 | 64.04442031918214 | 32.8 ± 2.3 | 19.8 ± 1.9 | 0.0 ± 2.2 |
| HS1700-SPIRE77 | 255.27324078752304 | 64.1962659304789 | 29.5 ± 2.1 | 20.0 ± 1.7 | 5.9 ± 2.0 |
| HS1700-SPIRE78 | 255.43578417756086 | 64.2607028611101 | 30.3 ± 2.2 | 16.9 ± 1.7 | 6.0 ± 2.1 |
| HS1700-SPIRE79 | 255.49112415542598 | 64.19048792701972 | 30.1 ± 2.2 | 1.8 ± 1.7 | 15.0 ± 2.2 |
| HS1700-SPIRE80 | 255.3610244300413 | 64.10017408965868 | 29.5 ± 2.1 | 19.6 ± 1.8 | 9.7 ± 2.1 |
| HS1700-SPIRE81 | 255.30381502358722 | 64.20132565499385 | 30.0 ± 2.2 | 30.3 ± 1.8 | 21.6 ± 2.3 |
| HS1700-SPIRE82 | 255.54135419168915 | 64.28474799738412 | 29.7 ± 2.2 | 18.1 ± 1.9 | 7.1 ± 2.1 |
| HS1700-SPIRE83 | 255.1783092457949 | 64.31189655133583 | 27.3 ± 2.0 | 22.5 ± 1.8 | 3.4 ± 2.2 |
| HS1700-SPIRE84 | 255.37210407232843 | 64.14597537435512 | 30.3 ± 2.3 | 20.9 ± 1.7 | 10.4 ± 2.3 |
| HS1700-SPIRE85 | 255.707149920591 | 64.18471573252242 | 31.6 ± 2.4 | 32.0 ± 1.9 | 15.1 ± 2.5 |
| HS1700-SPIRE86 | 255.48112737261647 | 64.17648551415459 | 29.7 ± 2.2 | 21.7 ± 2.0 | 10.5 ± 2.0 |
| HS1700-SPIRE87 | 254.89331144371315 | 64.22742381561099 | 30.5 ± 2.3 | 24.9 ± 1.8 | 15.9 ± 2.2 |
| HS1700-SPIRE88 | 255.41816686362432 | 64.12261857248345 | 28.8 ± 2.2 | 47.3 ± 1.8 | 40.7 ± 2.0 |
| HS1700-SPIRE89 | 255.15834464778592 | 64.24994987833128 | 28.9 ± 2.2 | 41.7 ± 1.7 | 38.8 ± 2.1 |
| HS1700-SPIRE90 | 255.71307357035528 | 64.21188803228306 | 28.4 ± 2.2 | 17.3 ± 2.0 | 8.0 ± 2.3 |
| HS1700-SPIRE91 | 255.02354546211896 | 64.14203381150895 | 32.1 ± 2.5 | 14.6 ± 1.6 | 6.3 ± 2.1 |
| HS1700-SPIRE92 | 255.38149604721252 | 64.13247539076093 | 29.4 ± 2.3 | 25.2 ± 1.8 | 7.8 ± 2.4 |
| HS1700-SPIRE93 | 254.82961595081719 | 64.14717318303005 | 29.9 ± 2.3 | 39.9 ± 1.9 | 34.7 ± 2.3 |
| HS1700-SPIRE94 | 255.64090743211347 | 64.2141691744354 | 28.7 ± 2.2 | 23.9 ± 1.8 | 8.8 ± 2.2 |
| HS1700-SPIRE95 | 255.34366161127102 | 64.32170829170818 | 26.8 ± 2.1 | 30.1 ± 1.8 | 31.9 ± 2.5 |
| HS1700-SPIRE96 | 255.4306372481341 | 64.24876031530366 | 29.4 ± 2.3 | 14.4 ± 1.6 | 12.7 ± 2.2 |
| HS1700-SPIRE97 | 255.62177794207955 | 64.24298380619103 | 33.1 ± 2.6 | 23.1 ± 2.0 | 6.9 ± 2.3 |
| HS1700-SPIRE98 | 255.2420579262042 | 64.15253376314604 | 29.3 ± 2.3 | 16.5 ± 1.9 | 5.8 ± 2.1 |
| HS1700-SPIRE99 | 255.28152087549546 | 64.09458503866358 | 28.1 ± 2.2 | 20.6 ± 1.8 | 16.0 ± 2.4 |
| HS1700-SPIRE100 | 255.50114014597145 | 64.20026918899313 | 28.6 ± 2.3 | 26.5 ± 1.7 | 7.0 ± 2.4 |
| HS1700-SPIRE101 | 255.56273548529833 | 64.14290705153027 | 26.4 ± 2.2 | 21.5 ± 1.8 | 16.8 ± 2.1 |
| HS1700-SPIRE102 | 255.36783299306614 | 64.2180054979805 | 26.2 ± 2.2 | 15.8 ± 1.8 | 1.0 ± 2.1 |
| HS1700-SPIRE103 | 255.1084701368058 | 64.04376820919043 | 27.0 ± 2.2 | 27.2 ± 1.8 | 11.0 ± 2.2 |
| HS1700-SPIRE104 | 255.59233815517106 | 64.19556805755866 | 26.2 ± 2.2 | 30.4 ± 1.8 | 16.9 ± 2.1 |
| HS1700-SPIRE105 | 255.25861294173654 | 64.09583107371934 | 26.4 ± 2.2 | 25.8 ± 2.0 | 14.7 ± 2.1 |
| HS1700-SPIRE106 | 254.9179703658503 | 64.09282834979511 | 26.0 ± 2.2 | 26.9 ± 1.9 | 24.2 ± 2.2 |
| HS1700-SPIRE107 | 254.8807390258318 | 64.08414984681615 | 29.1 ± 2.5 | 19.6 ± 1.9 | 5.3 ± 2.1 |
| HS1700-SPIRE108 | 255.43560297997638 | 64.19215219506786 | 26.9 ± 2.3 | 16.1 ± 1.8 | 11.1 ± 2.1 |
| HS1700-SPIRE109 | 255.34394607959345 | 64.16868581649486 | 28.1 ± 2.4 | 15.4 ± 1.7 | 6.2 ± 2.1 |
| HS1700-SPIRE110 | 254.81361694551737 | 64.20521624839138 | 26.4 ± 2.3 | 19.3 ± 1.7 | 16.6 ± 2.1 |
| HS1700-SPIRE111 | 255.5307264437436 | 64.22574207852232 | 29.1 ± 2.5 | 25.5 ± 1.7 | 10.2 ± 2.2 |
| HS1700-SPIRE112 | 255.16662654086574 | 64.09318015940926 | 31.7 ± 2.7 | 28.5 ± 1.7 | 16.8 ± 2.3 |
| HS1700-SPIRE113 | 255.0023524955616 | 64.30544078421718 | 25.6 ± 2.2 | 12.8 ± 1.9 | 0.4 ± 2.4 |
| HS1700-SPIRE114 | 255.54990447499637 | 64.15334678144421 | 24.2 ± 2.1 | 17.7 ± 1.8 | 0.0 ± 2.2 |
| HS1700-SPIRE115 | 254.9089216726454 | 64.16651285046049 | 23.8 ± 2.1 | 18.4 ± 1.7 | 5.0 ± 2.1 |
| HS1700-SPIRE116 | 255.17080646757094 | 64.29484592655928 | 24.7 ± 2.2 | 14.9 ± 1.8 | 1.5 ± 2.2 |
| HS1700-SPIRE117 | 255.01119117698195 | 64.31286094262562 | 26.3 ± 2.3 | 29.7 ± 1.8 | 20.1 ± 2.3 |
| HS1700-SPIRE118 | 255.4467354923271 | 64.27426433940775 | 24.3 ± 2.2 | 10.7 ± 1.8 | 4.4 ± 2.4 |
| HS1700-SPIRE119 | 255.08275493158976 | 64.16220870399037 | 25.6 ± 2.3 | 8.3 ± 1.7 | 0.0 ± 2.3 |
| HS1700-SPIRE120 | 255.13195683894568 | 64.34824390785964 | 24.3 ± 2.2 | 16.4 ± 1.8 | 11.3 ± 2.0 |
| HS1700-SPIRE121 | 255.27122841490217 | 64.05774385749936 | 25.1 ± 2.2 | 17.2 ± 1.8 | 8.5 ± 2.2 |
| HS1700-SPIRE122 | 255.25140674660557 | 64.32406082217207 | 25.5 ± 2.3 | 10.7 ± 1.8 | 3.4 ± 2.1 |
| HS1700-SPIRE123 | 255.061664855774 | 64.32728056438495 | 24.8 ± 2.2 | 25.5 ± 1.9 | 17.7 ± 2.5 |
| HS1700-SPIRE124 | 255.24158932296868 | 63.9819518065892 | 24.5 ± 2.2 | 2.1 ± 1.8 | 0.0 ± 2.5 |
| HS1700-SPIRE125 | 254.9810967103169 | 64.05472051662431 | 23.9 ± 2.2 | 18.3 ± 1.9 | 10.5 ± 2.2 |
| HS1700-SPIRE126 | 255.2482376239971 | 64.40721624843083 | 25.2 ± 2.3 | 11.1 ± 1.8 | 0.0 ± 2.1 |
| HS1700-SPIRE127 | 255.33067496944594 | 64.01566706659209 | 26.9 ± 2.5 | 17.5 ± 1.8 | 6.4 ± 2.5 |
| HS1700-SPIRE128 | 255.40224321462154 | 64.34699067723847 | 24.0 ± 2.2 | 14.7 ± 2.0 | 17.5 ± 2.3 |
| HS1700-SPIRE129 | 255.21105803363105 | 64.10915039642423 | 26.1 ± 2.5 | 13.0 ± 1.8 | 2.6 ± 2.3 |

Table A.7: SPIRE sources catalogue of HS1700 field.

| ID[1] | R.A.[2] (J2000) | Dec.[3] (J2000) | $S_{250}$[4] (mJy) | $S_{350}$[5] (mJy) | $S_{500}$[6] (mJy) |
|---|---|---|---|---|---|
| HS1700-SPIRE130 | 255.0427799532073 | 64.12400653873762 | 24.0 ± 2.3 | 38.2 ± 1.7 | 28.5 ± 2.2 |
| HS1700-SPIRE131 | 255.03208264601471 | 64.29633496992422 | 26.5 ± 2.5 | 40.1 ± 1.7 | 35.7 ± 2.2 |
| HS1700-SPIRE132 | 255.1121500435505 | 64.32237894891821 | 23.3 ± 2.2 | 16.3 ± 1.9 | 4.3 ± 2.3 |
| HS1700-SPIRE133 | 255.30399248808752 | 64.17510560298452 | 23.0 ± 2.2 | 11.8 ± 1.8 | 6.9 ± 2.1 |
| HS1700-SPIRE134 | 255.39430508680312 | 64.21405721492998 | 22.6 ± 2.2 | 12.1 ± 1.9 | 7.8 ± 2.2 |
| HS1700-SPIRE135 | 255.08854430832318 | 64.22103583178021 | 22.7 ± 2.2 | 9.7 ± 1.9 | 0.0 ± 2.0 |
| HS1700-SPIRE136 | 255.08521441305615 | 64.09256479941608 | 22.8 ± 2.2 | 22.7 ± 1.7 | 21.3 ± 2.1 |
| HS1700-SPIRE137 | 255.53065858704403 | 64.27034525115052 | 22.5 ± 2.2 | 19.6 ± 1.8 | 10.5 ± 2.4 |
| HS1700-SPIRE138 | 255.25173239312565 | 64.31059500485742 | 23.4 ± 2.2 | 22.2 ± 1.8 | 10.7 ± 2.2 |
| HS1700-SPIRE139 | 255.69119366551814 | 64.17400595320748 | 24.2 ± 2.3 | 21.9 ± 2.0 | 14.6 ± 2.2 |
| HS1700-SPIRE140 | 255.40677128675262 | 64.16741917511669 | 22.8 ± 2.2 | 21.8 ± 1.9 | 8.3 ± 2.2 |
| HS1700-SPIRE141 | 255.18449669710424 | 64.39321646934938 | 22.1 ± 2.2 | 18.3 ± 1.8 | 7.9 ± 2.4 |
| HS1700-SPIRE142 | 255.26678318975232 | 64.24693808724894 | 22.7 ± 2.2 | 12.0 ± 1.8 | 1.8 ± 2.2 |
| HS1700-SPIRE143 | 255.1347013027577 | 64.17047544804062 | 23.1 ± 2.3 | 21.1 ± 1.8 | 5.0 ± 2.3 |
| HS1700-SPIRE144 | 254.75921126013276 | 64.14489606216179 | 24.6 ± 2.4 | 29.0 ± 2.0 | 12.6 ± 2.5 |
| HS1700-SPIRE145 | 255.74881084087463 | 64.20275554966958 | 24.7 ± 2.4 | 17.8 ± 2.0 | 6.5 ± 2.4 |
| HS1700-SPIRE146 | 254.89137626510535 | 64.157443507805 | 22.1 ± 2.2 | 15.9 ± 1.9 | 5.2 ± 2.2 |
| HS1700-SPIRE147 | 254.8060079089638 | 64.22576079255798 | 24.0 ± 2.4 | 17.0 ± 1.7 | 0.8 ± 2.2 |
| HS1700-SPIRE148 | 255.54008849525687 | 64.12782600674005 | 22.3 ± 2.2 | 17.4 ± 1.9 | 7.1 ± 2.4 |
| HS1700-SPIRE149 | 255.09099642560838 | 64.26794049533011 | 21.7 ± 2.2 | 5.6 ± 1.8 | 5.7 ± 2.1 |
| HS1700-SPIRE150 | 255.33141853599867 | 64.265916679728 | 23.1 ± 2.3 | 17.4 ± 1.8 | 14.2 ± 2.1 |
| HS1700-SPIRE151 | 255.11709002488863 | 64.12822777441606 | 21.5 ± 2.2 | 14.2 ± 1.7 | 4.9 ± 2.1 |
| HS1700-SPIRE152 | 255.21903506655266 | 64.0768806818414 | 21.5 ± 2.2 | 5.9 ± 1.8 | 7.5 ± 2.1 |
| HS1700-SPIRE153 | 255.00988602181386 | 64.34479854561302 | 21.8 ± 2.2 | 2.3 ± 1.9 | 0.0 ± 2.5 |
| HS1700-SPIRE154 | 254.96532540637327 | 64.25568928001114 | 24.4 ± 2.5 | 10.7 ± 1.9 | 0.0 ± 2.2 |
| HS1700-SPIRE155 | 255.14709479257328 | 64.20932771696441 | 22.9 ± 2.3 | 0.0 ± 1.8 | 0.0 ± 2.2 |
| HS1700-SPIRE156 | 255.30946869959723 | 64.38019733313624 | 24.5 ± 2.5 | 13.1 ± 1.9 | 5.8 ± 2.3 |
| HS1700-SPIRE157 | 255.1024305802712 | 64.08819197840525 | 21.0 ± 2.1 | 15.3 ± 1.9 | 15.5 ± 2.2 |
| HS1700-SPIRE158 | 255.5894066697677 | 64.16952340191516 | 21.7 ± 2.2 | 13.3 ± 1.7 | 1.5 ± 2.1 |
| HS1700-SPIRE159 | 254.97013878928092 | 64.1889723175478 | 23.0 ± 2.4 | 11.6 ± 1.8 | 0.9 ± 2.2 |
| HS1700-SPIRE160 | 254.9696684679786 | 64.21593742333039 | 22.9 ± 2.4 | 21.9 ± 1.7 | 14.2 ± 2.1 |
| HS1700-SPIRE161 | 255.16315700038925 | 64.26158150631991 | 20.8 ± 2.1 | 1.9 ± 1.9 | 0.0 ± 2.4 |
| HS1700-SPIRE162 | 255.44586396449097 | 64.31320849870062 | 21.8 ± 2.2 | 18.6 ± 2.0 | 15.5 ± 2.2 |
| HS1700-SPIRE163 | 255.16326882130974 | 64.14964272897505 | 22.2 ± 2.3 | 24.2 ± 1.8 | 13.7 ± 2.2 |
| HS1700-SPIRE164 | 254.74768727543778 | 64.18593943066469 | 21.9 ± 2.3 | 10.8 ± 1.9 | 13.8 ± 2.2 |
| HS1700-SPIRE165 | 255.21813641199375 | 64.02153818572229 | 19.5 ± 2.0 | 20.5 ± 1.8 | 14.1 ± 2.3 |
| HS1700-SPIRE166 | 255.3026229512854 | 64.12567265609698 | 22.6 ± 2.4 | 22.6 ± 1.9 | 25.1 ± 2.2 |
| HS1700-SPIRE167 | 255.26398143622913 | 64.22738023451325 | 21.4 ± 2.3 | 0.0 ± 1.8 | 0.0 ± 2.1 |
| HS1700-SPIRE168 | 255.11785178653625 | 64.43128416067665 | 28.4 ± 3.0 | 5.4 ± 2.7 | 3.1 ± 3.1 |
| HS1700-SPIRE169 | 255.52363820060296 | 64.2631151632022 | 21.0 ± 2.2 | 22.8 ± 1.9 | 12.1 ± 2.5 |
| HS1700-SPIRE170 | 254.9424092596221 | 64.10919374189733 | 21.4 ± 2.3 | 19.1 ± 1.8 | 12.6 ± 2.1 |
| HS1700-SPIRE171 | 254.74920456428228 | 64.23195012544953 | 19.5 ± 2.1 | 22.3 ± 1.8 | 12.5 ± 2.2 |
| HS1700-SPIRE172 | 255.48940673290826 | 64.08407719798309 | 23.5 ± 2.5 | 26.9 ± 1.7 | 15.9 ± 2.3 |
| HS1700-SPIRE173 | 255.09815194748305 | 64.00811880232597 | 21.3 ± 2.3 | 16.3 ± 1.8 | 7.5 ± 2.2 |
| HS1700-SPIRE174 | 255.08580894396212 | 64.23226514526682 | 20.4 ± 2.2 | 13.4 ± 1.7 | 6.6 ± 2.2 |
| HS1700-SPIRE175 | 254.9726482263446 | 64.06968766945158 | 19.7 ± 2.1 | 17.7 ± 1.8 | 16.5 ± 2.3 |
| HS1700-SPIRE176 | 255.0446070554656 | 64.22136421664474 | 19.3 ± 2.1 | 10.0 ± 1.8 | 0.0 ± 2.1 |
| HS1700-SPIRE177 | 255.42154228566932 | 64.09914205087397 | 20.6 ± 2.2 | 23.0 ± 1.8 | 18.9 ± 2.5 |
| HS1700-SPIRE178 | 255.13028702657977 | 64.24532591624873 | 22.0 ± 2.4 | 11.8 ± 1.7 | 7.4 ± 2.3 |
| HS1700-SPIRE179 | 255.37678741933877 | 64.19878113298532 | 19.8 ± 2.2 | 9.4 ± 1.8 | 0.5 ± 2.2 |
| HS1700-SPIRE180 | 255.11366922666747 | 64.42386222220313 | 25.0 ± 2.8 | 18.1 ± 2.3 | 5.8 ± 2.6 |
| HS1700-SPIRE181 | 255.05928188936187 | 64.2477430338451 | 20.4 ± 2.3 | 22.4 ± 1.7 | 11.2 ± 2.0 |
| HS1700-SPIRE182 | 255.15287412989673 | 63.99454460742583 | 19.3 ± 2.1 | 24.7 ± 1.8 | 22.3 ± 2.3 |
| HS1700-SPIRE183 | 255.21633768599472 | 64.32943572683881 | 21.5 ± 2.4 | 17.6 ± 1.8 | 17.2 ± 2.1 |
| HS1700-SPIRE184 | 255.26829006438604 | 64.35977345205534 | 20.9 ± 2.3 | 12.6 ± 1.7 | 0.5 ± 2.3 |
| HS1700-SPIRE185 | 254.6673630918117 | 64.17458062649398 | 26.2 ± 2.9 | 30.4 ± 2.0 | 27.8 ± 2.3 |
| HS1700-SPIRE186 | 255.18768276573823 | 64.19512079316968 | 20.1 ± 2.2 | 12.5 ± 1.8 | 8.4 ± 2.1 |
| HS1700-SPIRE187 | 255.41067612792202 | 64.02952208838677 | 22.8 ± 2.5 | 13.3 ± 2.2 | 10.0 ± 2.8 |
| HS1700-SPIRE188 | 254.96890126794665 | 64.08720265888257 | 19.1 ± 2.2 | 31.7 ± 1.7 | 23.8 ± 2.2 |
| HS1700-SPIRE189 | 254.84035571916777 | 64.11973203999891 | 21.3 ± 2.4 | 28.9 ± 1.9 | 16.4 ± 2.2 |
| HS1700-SPIRE190 | 255.46002098725594 | 64.05682087629236 | 25.5 ± 2.9 | 24.6 ± 2.0 | 8.1 ± 2.6 |
| HS1700-SPIRE191 | 254.95602938696095 | 64.13005210275495 | 19.4 ± 2.2 | 8.7 ± 1.9 | 5.7 ± 2.0 |
| HS1700-SPIRE192 | 255.08686502323275 | 64.34414378439564 | 18.4 ± 2.1 | 10.7 ± 2.0 | 11.5 ± 2.0 |
| HS1700-SPIRE193 | 255.42332625185395 | 64.17804659672366 | 18.5 ± 2.1 | 20.2 ± 1.8 | 6.9 ± 2.3 |
| HS1700-SPIRE194 | 255.70667661526713 | 64.20060836932447 | 18.0 ± 2.1 | 9.1 ± 1.9 | 6.2 ± 2.5 |
| HS1700-SPIRE195 | 255.07379577015138 | 64.07729060568902 | 19.3 ± 2.3 | 19.6 ± 2.1 | 4.0 ± 2.2 |
| HS1700-SPIRE196 | 255.59105094423506 | 64.13028747662462 | 22.6 ± 2.7 | 13.2 ± 1.8 | 0.0 ± 2.2 |
| HS1700-SPIRE197 | 254.88416194149335 | 64.19908167962247 | 19.7 ± 2.3 | 24.8 ± 1.7 | 24.0 ± 2.3 |
| HS1700-SPIRE198 | 254.95151474909784 | 64.32263534746954 | 21.9 ± 2.6 | 15.0 ± 1.8 | 3.5 ± 2.6 |
| HS1700-SPIRE199 | 255.30561675969722 | 63.983105031994214 | 22.1 ± 2.6 | 23.6 ± 2.0 | 2.8 ± 2.5 |
| HS1700-SPIRE200 | 255.32145336398656 | 64.06712739956981 | 17.8 ± 2.1 | 19.1 ± 1.9 | 17.3 ± 2.2 |
| HS1700-SPIRE201 | 255.0292670827424 | 64.03528086621927 | 21.5 ± 2.6 | 6.2 ± 1.8 | 0.0 ± 2.1 |
| HS1700-SPIRE202 | 255.1667771879174 | 64.34162018758381 | 18.3 ± 2.2 | 15.2 ± 1.8 | 6.7 ± 2.2 |
| HS1700-SPIRE203 | 255.0734494441841 | 64.11518580567514 | 18.7 ± 2.2 | 17.0 ± 1.7 | 8.3 ± 2.2 |
| HS1700-SPIRE204 | 255.47274421996633 | 64.31955922662782 | 18.6 ± 2.2 | 38.0 ± 2.0 | 26.0 ± 2.2 |
| HS1700-SPIRE205 | 255.61435913127664 | 64.14583208934694 | 18.9 ± 2.3 | 31.6 ± 1.9 | 36.4 ± 2.2 |

Table A.7: SPIRE sources catalogue of HS1700 field.

| ID[1] | R.A.[2] (J2000) | Dec.[3] (J2000) | $S_{250}$[4] (mJy) | $S_{350}$[5] (mJy) | $S_{500}$[6] (mJy) |
|---|---|---|---|---|---|
| HS1700-SPIRE206 | 255.21407154357078 | 64.05212857056853 | 18.3 ± 2.2 | 25.5 ± 1.7 | 24.6 ± 2.2 |
| HS1700-SPIRE207 | 255.4772558172304 | 64.26331774932586 | 18.4 ± 2.2 | 14.5 ± 1.8 | 1.8 ± 2.3 |
| HS1700-SPIRE208 | 255.0194214156777 | 64.15838307692107 | 21.6 ± 2.6 | 24.1 ± 1.8 | 16.9 ± 2.2 |
| HS1700-SPIRE209 | 255.37668444565176 | 64.0833162106136 | 17.8 ± 2.2 | 9.6 ± 1.8 | 4.2 ± 2.2 |
| HS1700-SPIRE210 | 255.2704039296112 | 63.98701806279157 | 19.9 ± 2.4 | 23.6 ± 1.9 | 18.4 ± 2.3 |
| HS1700-SPIRE211 | 255.1911905908206 | 64.04518549967953 | 16.9 ± 2.1 | 20.9 ± 1.5 | 4.4 ± 2.0 |
| HS1700-SPIRE212 | 255.36150990385352 | 64.00567142360792 | 22.6 ± 2.8 | 9.7 ± 1.9 | 1.1 ± 2.6 |
| HS1700-SPIRE213 | 254.99144496491914 | 64.3614448249524 | 20.1 ± 2.5 | 10.0 ± 2.1 | 2.1 ± 2.6 |
| HS1700-SPIRE214 | 255.11754166001143 | 64.22596183252645 | 18.6 ± 2.3 | 20.9 ± 1.8 | 10.2 ± 2.3 |
| HS1700-SPIRE215 | 255.2922106814531 | 64.05281489411368 | 17.3 ± 2.2 | 26.4 ± 1.8 | 13.3 ± 2.2 |
| HS1700-SPIRE216 | 254.99527763459236 | 64.28678621975106 | 19.4 ± 2.4 | 9.4 ± 1.8 | 0.0 ± 2.4 |
| HS1700-SPIRE217 | 255.10817385919992 | 64.35445821802712 | 17.2 ± 2.2 | 9.7 ± 1.7 | 1.0 ± 2.0 |
| HS1700-SPIRE218 | 255.07740455594526 | 64.13692485235151 | 17.6 ± 2.2 | 10.7 ± 1.8 | 2.2 ± 2.0 |
| HS1700-SPIRE219 | 255.04491988726247 | 64.10168404504381 | 17.5 ± 2.2 | 12.6 ± 1.8 | 3.3 ± 2.1 |
| HS1700-SPIRE220 | 255.32832110439884 | 64.20808993034001 | 16.4 ± 2.1 | 9.4 ± 1.8 | 0.0 ± 2.2 |
| HS1700-SPIRE221 | 255.08800019562395 | 64.20011696506096 | 21.0 ± 2.7 | 9.2 ± 1.9 | 0.0 ± 2.2 |
| HS1700-SPIRE222 | 255.1437837923233 | 64.07933098532088 | 18.0 ± 2.3 | 17.8 ± 1.7 | 4.2 ± 2.2 |
| HS1700-SPIRE223 | 254.90078587844366 | 64.1865170716732 | 16.9 ± 2.2 | 10.3 ± 1.6 | 5.5 ± 2.2 |
| HS1700-SPIRE224 | 255.27336928981535 | 64.14106019686494 | 20.0 ± 2.6 | 25.1 ± 1.9 | 13.7 ± 2.1 |
| HS1700-SPIRE225 | 255.10915044105008 | 64.31637095207034 | 17.2 ± 2.2 | 18.2 ± 1.8 | 11.4 ± 2.2 |
| HS1700-SPIRE226 | 254.9558426459311 | 64.11569870999061 | 17.9 ± 2.3 | 2.7 ± 1.8 | 2.0 ± 2.3 |
| HS1700-SPIRE227 | 255.5348498812314 | 64.13823187395806 | 15.8 ± 2.0 | 7.3 ± 1.9 | 1.0 ± 2.4 |
| HS1700-SPIRE228 | 254.9732933246831 | 64.29820992240815 | 18.1 ± 2.3 | 20.7 ± 1.8 | 19.3 ± 2.3 |
| HS1700-SPIRE229 | 255.29744815459173 | 64.33277416821319 | 16.7 ± 2.2 | 15.8 ± 1.7 | 6.5 ± 2.0 |
| HS1700-SPIRE230 | 254.88243811117982 | 64.26534795202964 | 17.5 ± 2.3 | 17.8 ± 1.9 | 5.7 ± 2.4 |
| HS1700-SPIRE231 | 255.30824932955062 | 64.26929747136347 | 17.5 ± 2.3 | 15.5 ± 1.7 | 7.5 ± 2.1 |
| HS1700-SPIRE232 | 255.22400567488896 | 64.00150433662029 | 16.8 ± 2.2 | 19.5 ± 1.9 | 6.0 ± 2.2 |
| HS1700-SPIRE233 | 255.14413472752605 | 64.40794377194113 | 17.2 ± 2.3 | 11.2 ± 1.8 | 8.5 ± 2.6 |
| HS1700-SPIRE234 | 255.1928368331423 | 63.98531125435708 | 19.4 ± 2.6 | 9.4 ± 1.9 | 2.9 ± 2.2 |
| HS1700-SPIRE235 | 254.99682474657664 | 64.09773724413898 | 15.7 ± 2.1 | 7.3 ± 1.7 | 0.0 ± 2.2 |
| HS1700-SPIRE236 | 255.2567603316837 | 64.07227473831762 | 16.9 ± 2.3 | 20.2 ± 1.6 | 13.3 ± 2.1 |
| HS1700-SPIRE237 | 255.2194407955101 | 63.97785018215934 | 17.7 ± 2.4 | 14.0 ± 1.9 | 2.8 ± 2.4 |
| HS1700-SPIRE238 | 255.27481478961772 | 64.33780692285065 | 16.8 ± 2.3 | 8.7 ± 1.7 | 5.1 ± 2.1 |
| HS1700-SPIRE239 | 255.08057827544803 | 64.41491729836717 | 27.4 ± 3.7 | 12.3 ± 2.5 | 0.0 ± 2.7 |
| HS1700-SPIRE240 | 255.2317956700802 | 63.99014841497874 | 17.4 ± 2.4 | 10.8 ± 1.8 | 3.7 ± 2.3 |
| HS1700-SPIRE241 | 255.4818782913186 | 64.15262372607785 | 14.8 ± 2.0 | 22.9 ± 1.7 | 19.5 ± 2.1 |
| HS1700-SPIRE242 | 255.1999987297114 | 64.22379114831746 | 19.0 ± 2.6 | 19.0 ± 1.8 | 7.5 ± 2.2 |
| HS1700-SPIRE243 | 254.82678046869745 | 64.24565970421001 | 15.9 ± 2.2 | 23.6 ± 1.9 | 15.7 ± 2.2 |
| HS1700-SPIRE244 | 255.30977395282278 | 64.10865902719684 | 14.9 ± 2.0 | 1.9 ± 1.9 | 0.0 ± 2.1 |
| HS1700-SPIRE245 | 255.17876135986452 | 64.06535750984952 | 16.8 ± 2.3 | 21.2 ± 1.8 | 15.5 ± 2.2 |
| HS1700-SPIRE246 | 255.30030121093202 | 64.2879194342231 | 16.6 ± 2.3 | 10.8 ± 1.8 | 3.1 ± 2.5 |
| HS1700-SPIRE247 | 255.0418207195462 | 64.39140308190997 | 18.1 ± 2.5 | 20.3 ± 2.3 | 13.0 ± 2.4 |
| HS1700-SPIRE248 | 255.26264218786164 | 64.32853394484808 | 16.6 ± 2.3 | 9.7 ± 1.8 | 0.0 ± 2.1 |
| HS1700-SPIRE249 | 255.36630585537063 | 64.1174934748239 | 16.0 ± 2.2 | 12.5 ± 1.7 | 2.6 ± 2.2 |
| HS1700-SPIRE250 | 255.52105388017475 | 64.10846028417164 | 16.4 ± 2.3 | 16.7 ± 1.8 | 9.0 ± 2.3 |
| HS1700-SPIRE251 | 254.97024958629706 | 64.12244882522371 | 17.1 ± 2.4 | 16.2 ± 1.8 | 6.7 ± 2.1 |
| HS1700-SPIRE252 | 255.17915708939074 | 64.37499587744892 | 15.9 ± 2.2 | 15.5 ± 1.9 | 0.1 ± 2.1 |
| HS1700-SPIRE253 | 255.382640143575 | 64.1775431908688 | 16.5 ± 2.3 | 20.3 ± 2.0 | 5.6 ± 2.3 |
| HS1700-SPIRE254 | 255.4726788989045 | 64.18977710098626 | 15.8 ± 2.2 | 5.3 ± 1.8 | 5.3 ± 2.1 |
| HS1700-SPIRE255 | 255.1183889777853 | 64.37494938940165 | 14.8 ± 2.1 | 12.9 ± 1.7 | 6.1 ± 2.1 |
| HS1700-SPIRE256 | 254.69830668407462 | 64.16846299115092 | 18.2 ± 2.6 | 22.8 ± 1.9 | 10.4 ± 2.3 |
| HS1700-SPIRE257 | 255.35422697906458 | 64.37048953311019 | 16.1 ± 2.3 | 5.7 ± 1.9 | 2.6 ± 2.5 |
| HS1700-SPIRE258 | 255.47255941643297 | 64.21137533275525 | 19.0 ± 2.7 | 0.0 ± 1.7 | 5.4 ± 2.4 |
| HS1700-SPIRE259 | 255.30611156171685 | 64.31352181196559 | 15.0 ± 2.1 | 6.6 ± 1.7 | 0.0 ± 2.2 |
| HS1700-SPIRE260 | 255.06393176161686 | 64.29120298669206 | 16.9 ± 2.4 | 2.8 ± 1.8 | 0.0 ± 2.3 |
| HS1700-SPIRE261 | 255.4505621661385 | 64.15274321261307 | 15.5 ± 2.2 | 11.2 ± 1.7 | 6.0 ± 2.4 |
| HS1700-SPIRE262 | 255.6062705066117 | 64.18333980673783 | 16.6 ± 2.4 | 16.9 ± 1.7 | 10.0 ± 2.1 |
| HS1700-SPIRE263 | 255.03040247883288 | 64.31121022392557 | 16.3 ± 2.3 | 12.7 ± 1.9 | 7.9 ± 2.1 |
| HS1700-SPIRE264 | 255.2889810201737 | 63.96624005143044 | 20.8 ± 3.0 | 5.4 ± 2.2 | 5.1 ± 3.2 |
| HS1700-SPIRE265 | 255.04886987649917 | 64.30598594516415 | 14.9 ± 2.2 | 0.0 ± 1.8 | 0.0 ± 2.2 |
| HS1700-SPIRE266 | 255.05591498687747 | 64.04405107966375 | 17.1 ± 2.5 | 2.7 ± 1.9 | 0.0 ± 2.1 |
| HS1700-SPIRE267 | 255.15977041142807 | 64.33139788836539 | 14.7 ± 2.1 | 8.9 ± 1.6 | 0.0 ± 2.0 |
| HS1700-SPIRE268 | 255.06719711333406 | 64.05779959179402 | 16.4 ± 2.4 | 27.8 ± 1.8 | 16.2 ± 2.3 |
| HS1700-SPIRE269 | 255.17851626910786 | 64.00585273322497 | 15.9 ± 2.4 | 12.7 ± 1.8 | 8.7 ± 2.3 |
| HS1700-SPIRE270 | 255.23854888197278 | 64.2297536757271 | 15.4 ± 2.3 | 2.2 ± 1.8 | 0.0 ± 2.4 |
| HS1700-SPIRE271 | 254.85946006715528 | 64.17207755778433 | 14.5 ± 2.1 | 9.0 ± 1.8 | 4.6 ± 2.0 |
| HS1700-SPIRE272 | 255.1638748477644 | 64.20374083001816 | 17.1 ± 2.5 | 8.9 ± 1.8 | 5.9 ± 2.2 |
| HS1700-SPIRE273 | 255.14823258419605 | 64.02272410479014 | 14.4 ± 2.1 | 15.9 ± 1.7 | 6.3 ± 2.2 |
| HS1700-SPIRE274 | 255.1834136505459 | 63.98017784518366 | 15.8 ± 2.3 | 12.9 ± 1.8 | 7.0 ± 2.5 |
| HS1700-SPIRE275 | 255.11953775579113 | 64.06110692557317 | 15.4 ± 2.3 | 15.3 ± 1.9 | 8.0 ± 2.2 |
| HS1700-SPIRE276 | 254.838528284223 | 64.19180360588474 | 14.7 ± 2.2 | 2.8 ± 1.9 | 0.0 ± 2.0 |
| HS1700-SPIRE277 | 254.95423934216845 | 64.22808910335192 | 14.5 ± 2.2 | 11.4 ± 2.0 | 8.2 ± 2.3 |
| HS1700-SPIRE278 | 255.13502163977614 | 64.3271649054061 | 15.5 ± 2.3 | 5.9 ± 1.9 | 0.0 ± 2.1 |
| HS1700-SPIRE279 | 254.93137902274842 | 64.2992691942364 | 13.8 ± 2.1 | 10.3 ± 1.8 | 3.7 ± 2.2 |
| HS1700-SPIRE280 | 255.3634713562748 | 64.07398154984072 | 14.8 ± 2.2 | 8.4 ± 1.8 | 6.7 ± 2.4 |
| HS1700-SPIRE281 | 255.06824851678263 | 64.18409020095977 | 15.8 ± 2.4 | 11.5 ± 1.8 | 4.3 ± 2.3 |

Table A.7: SPIRE sources catalogue of HS1700 field.

| ID[1] | R.A.[2] (J2000) | Dec.[3] (J2000) | $S_{250}$[4] (mJy) | $S_{350}$[5] (mJy) | $S_{500}$[6] (mJy) |
|---|---|---|---|---|---|
| HS1700-SPIRE282 | 255.46793090896884 | 64.20017441883402 | 14.9 ± 2.3 | 16.0 ± 1.7 | 9.7 ± 2.1 |
| HS1700-SPIRE283 | 255.6201747119304 | 64.12577259033992 | 14.6 ± 2.2 | 9.9 ± 1.9 | 4.9 ± 2.2 |
| HS1700-SPIRE284 | 255.28669944469374 | 64.38435270130333 | 13.8 ± 2.1 | 7.5 ± 2.0 | 0.0 ± 2.3 |
| HS1700-SPIRE285 | 255.56573741179884 | 64.20707968354168 | 14.2 ± 2.2 | 11.9 ± 1.8 | 5.9 ± 2.0 |
| HS1700-SPIRE286 | 254.84873416880336 | 64.15093030820334 | 14.0 ± 2.2 | 10.3 ± 1.8 | 8.3 ± 2.3 |
| HS1700-SPIRE287 | 255.61097767095262 | 64.15636988071594 | 14.7 ± 2.3 | 2.2 ± 1.8 | 0.0 ± 2.1 |
| HS1700-SPIRE288 | 255.2766224837779 | 64.37143905498684 | 13.5 ± 2.1 | 5.5 ± 1.8 | 0.0 ± 2.3 |
| HS1700-SPIRE289 | 255.2113240112616 | 64.23717121633283 | 15.6 ± 2.5 | 10.3 ± 1.8 | 0.2 ± 2.3 |
| HS1700-SPIRE290 | 255.40372448963547 | 64.1454171066854 | 15.4 ± 2.4 | 12.9 ± 1.8 | 5.2 ± 2.1 |
| HS1700-SPIRE291 | 254.7886979760014 | 64.13211130330548 | 17.7 ± 2.8 | 5.8 ± 2.0 | 0.7 ± 2.6 |
| HS1700-SPIRE292 | 255.35612139863835 | 64.13190339874397 | 14.4 ± 2.3 | 13.3 ± 1.8 | 0.0 ± 2.1 |
| HS1700-SPIRE293 | 255.28894913388413 | 63.99712075913502 | 14.4 ± 2.3 | 16.8 ± 1.9 | 10.4 ± 2.3 |
| HS1700-SPIRE294 | 254.92053160922126 | 64.11620949644251 | 14.0 ± 2.2 | 16.4 ± 1.8 | 15.5 ± 2.4 |
| HS1700-SPIRE295 | 255.24595986684076 | 64.2491869555558 | 15.8 ± 2.5 | 12.2 ± 1.8 | 6.2 ± 2.3 |
| HS1700-SPIRE296 | 255.05329190990523 | 64.03209551379459 | 13.9 ± 2.2 | 6.1 ± 1.8 | 1.1 ± 2.4 |
| HS1700-SPIRE297 | 255.1128590800553 | 64.24400636714402 | 13.7 ± 2.2 | 8.7 ± 1.8 | 0.0 ± 2.2 |
| HS1700-SPIRE298 | 254.85202085461788 | 64.13467320464208 | 13.2 ± 2.1 | 10.5 ± 2.0 | 7.3 ± 2.2 |
| HS1700-SPIRE299 | 255.3126434570494 | 64.13704586521578 | 14.6 ± 2.3 | 9.2 ± 1.8 | 0.0 ± 2.1 |
| HS1700-SPIRE300 | 254.9255937807887 | 64.24645418322154 | 13.5 ± 2.2 | 11.3 ± 1.8 | 2.5 ± 2.3 |
| HS1700-SPIRE301 | 254.7995824091944 | 64.2057994633758 | 13.2 ± 2.1 | 7.8 ± 1.9 | 13.4 ± 2.1 |
| HS1700-SPIRE302 | 255.36942209489317 | 64.35100702303748 | 14.4 ± 2.3 | 16.2 ± 1.8 | 12.9 ± 2.2 |
| HS1700-SPIRE303 | 255.2449297681676 | 64.19062276155381 | 13.9 ± 2.3 | 9.2 ± 1.7 | 4.8 ± 2.2 |
| HS1700-SPIRE304 | 255.26469920046287 | 64.04745824425618 | 14.1 ± 2.3 | 12.0 ± 1.7 | 7.2 ± 2.4 |
| HS1700-SPIRE305 | 255.30139190948762 | 64.25763811757945 | 13.3 ± 2.2 | 5.5 ± 1.8 | 0.0 ± 2.1 |
| HS1700-SPIRE306 | 254.9664361976918 | 64.24316543008196 | 14.2 ± 2.3 | 10.1 ± 1.8 | 6.2 ± 2.2 |
| HS1700-SPIRE307 | 255.38095921935846 | 64.30510593878145 | 15.9 ± 2.6 | 10.8 ± 1.8 | 1.7 ± 2.4 |
| HS1700-SPIRE308 | 255.14040822759804 | 63.992091303797984 | 13.3 ± 2.2 | 17.6 ± 1.8 | 18.6 ± 2.2 |
| HS1700-SPIRE309 | 255.05138396918306 | 64.07963878008043 | 13.2 ± 2.2 | 10.2 ± 2.0 | 4.8 ± 2.1 |
| HS1700-SPIRE310 | 255.21556383889714 | 64.41643535686721 | 12.3 ± 2.1 | 3.1 ± 1.9 | 0.7 ± 2.4 |
| HS1700-SPIRE311 | 255.0495110353008 | 64.37899630049091 | 13.5 ± 2.3 | 12.4 ± 1.8 | 2.5 ± 2.3 |
| HS1700-SPIRE312 | 255.19715655861333 | 64.12804260764638 | 13.4 ± 2.3 | 7.4 ± 1.9 | 0.0 ± 2.5 |
| HS1700-SPIRE313 | 255.6317649410481 | 64.15485461711783 | 13.2 ± 2.3 | 0.0 ± 2.0 | 0.0 ± 2.2 |
| HS1700-SPIRE314 | 254.88431841978846 | 64.30386064698845 | 12.7 ± 2.2 | 15.2 ± 1.8 | 15.6 ± 2.2 |
| HS1700-SPIRE315 | 255.58223699453737 | 64.2733450921526 | 12.4 ± 2.1 | 6.0 ± 1.9 | 6.2 ± 2.4 |
| HS1700-SPIRE316 | 255.3438522953578 | 64.36367144675394 | 13.1 ± 2.2 | 15.5 ± 1.7 | 12.1 ± 2.3 |
| HS1700-SPIRE317 | 254.92391587929538 | 64.12567692572362 | 13.3 ± 2.3 | 16.3 ± 1.9 | 8.6 ± 2.3 |
| HS1700-SPIRE318 | 254.79550913068627 | 64.1796288331929 | 12.6 ± 2.2 | 13.8 ± 1.9 | 10.5 ± 2.2 |
| HS1700-SPIRE319 | 254.77355216933174 | 64.23786713600325 | 12.6 ± 2.2 | 6.9 ± 1.8 | 0.0 ± 2.2 |
| HS1700-SPIRE320 | 255.56568128543552 | 64.22518479186775 | 12.9 ± 2.2 | 15.0 ± 1.8 | 13.3 ± 2.3 |
| HS1700-SPIRE321 | 255.2732211885352 | 64.20456875619097 | 13.7 ± 2.4 | 20.2 ± 1.8 | 15.9 ± 2.1 |
| HS1700-SPIRE322 | 254.8700535422054 | 64.16396153676396 | 12.1 ± 2.1 | 0.2 ± 1.8 | 0.0 ± 2.1 |
| HS1700-SPIRE323 | 255.19371181041015 | 64.28434612741934 | 12.9 ± 2.2 | 11.9 ± 1.8 | 0.0 ± 2.3 |
| HS1700-SPIRE324 | 255.28288511209817 | 64.00546647746297 | 12.7 ± 2.2 | 2.2 ± 1.7 | 6.1 ± 2.0 |
| HS1700-SPIRE325 | 254.98511276103935 | 64.19637162335437 | 12.3 ± 2.1 | 3.5 ± 1.9 | 2.8 ± 2.2 |
| HS1700-SPIRE326 | 254.82071440617233 | 64.11145508391583 | 13.8 ± 2.4 | 5.4 ± 2.2 | 0.0 ± 2.2 |
| HS1700-SPIRE327 | 255.04217369347265 | 64.0936695915759 | 12.2 ± 2.1 | 9.2 ± 1.9 | 11.0 ± 2.2 |
| HS1700-SPIRE328 | 255.44017746002055 | 64.33659612961452 | 12.2 ± 2.1 | 0.5 ± 2.0 | 0.0 ± 2.4 |
| HS1700-SPIRE329 | 255.20930485214237 | 64.33447227945129 | 13.4 ± 2.4 | 16.0 ± 1.6 | 16.7 ± 2.1 |
| HS1700-SPIRE330 | 255.11709695645501 | 64.08029908904382 | 13.9 ± 2.5 | 6.1 ± 1.7 | 0.4 ± 2.2 |
| HS1700-SPIRE331 | 255.09731906631092 | 64.336997859086 | 12.6 ± 2.2 | 19.9 ± 2.0 | 15.0 ± 2.1 |
| HS1700-SPIRE332 | 254.82581709494852 | 64.12987992283975 | 12.9 ± 2.3 | 8.1 ± 1.9 | 0.0 ± 2.3 |
| HS1700-SPIRE333 | 254.98813449777657 | 64.1155318869504 | 12.0 ± 2.1 | 8.9 ± 2.0 | 0.2 ± 2.1 |
| HS1700-SPIRE334 | 255.34366106817046 | 64.04454480945921 | 12.8 ± 2.3 | 7.2 ± 1.8 | 4.5 ± 2.2 |
| HS1700-SPIRE335 | 255.3988821762122 | 64.15526504003682 | 13.0 ± 2.3 | 4.6 ± 1.7 | 0.0 ± 2.3 |
| HS1700-SPIRE336 | 255.19095011772959 | 64.16272086054359 | 11.7 ± 2.1 | 20.0 ± 1.8 | 16.3 ± 2.0 |
| HS1700-SPIRE337 | 255.30981802082357 | 63.96987499391897 | 16.5 ± 3.0 | 11.3 ± 2.3 | 2.8 ± 2.8 |
| HS1700-SPIRE338 | 255.270230963901 | 64.0310466944142 | 13.3 ± 2.4 | 9.3 ± 1.9 | 4.2 ± 2.3 |
| HS1700-SPIRE339 | 255.14235695340065 | 64.05954455176591 | 13.0 ± 2.4 | 13.5 ± 1.7 | 7.5 ± 2.1 |
| HS1700-SPIRE340 | 255.45421807272018 | 64.1980107710728 | 12.9 ± 2.3 | 5.4 ± 1.8 | 0.0 ± 2.1 |
| HS1700-SPIRE341 | 255.2676518748695 | 64.16787571640256 | 12.2 ± 2.2 | 20.3 ± 1.8 | 14.5 ± 2.4 |
| HS1700-SPIRE342 | 254.97761206955735 | 64.17914579920843 | 12.2 ± 2.2 | 11.9 ± 1.9 | 5.8 ± 2.1 |
| HS1700-SPIRE343 | 255.2252089137016 | 64.29649666294672 | 11.5 ± 2.1 | 10.3 ± 1.8 | 12.9 ± 2.1 |
| HS1700-SPIRE344 | 254.70767958407455 | 64.18562083894093 | 14.2 ± 2.6 | 7.9 ± 1.8 | 0.0 ± 2.5 |
| HS1700-SPIRE345 | 255.4858933242717 | 64.05872744779455 | 14.6 ± 2.7 | 4.6 ± 2.0 | 0.0 ± 2.7 |
| HS1700-SPIRE346 | 255.09733610746906 | 64.12151758686409 | 12.0 ± 2.2 | 4.3 ± 1.7 | 1.3 ± 2.3 |
| HS1700-SPIRE347 | 255.305209403197 | 64.36715292222493 | 11.8 ± 2.2 | 12.3 ± 1.8 | 6.9 ± 2.2 |
| HS1700-SPIRE348 | 255.18974821482252 | 63.97239756150806 | 12.3 ± 2.3 | 11.7 ± 1.9 | 2.3 ± 2.2 |
| HS1700-SPIRE349 | 255.0662002982671 | 64.2581769206518 | 12.1 ± 2.3 | 9.0 ± 1.8 | 8.3 ± 2.1 |
| HS1700-SPIRE350 | 255.3227787951508 | 64.19991080269358 | 12.4 ± 2.4 | 7.1 ± 1.9 | 7.4 ± 2.2 |
| HS1700-SPIRE351 | 254.92691284358236 | 64.05797439629247 | 13.2 ± 2.7 | 10.7 ± 2.0 | 1.6 ± 2.5 |
| HS1700-SPIRE352 | 255.39599722226424 | 64.30218611175826 | 12.2 ± 2.5 | 10.5 ± 1.8 | 9.5 ± 2.3 |
| HS1700-SPIRE353 | 254.74375849798344 | 64.15260727142301 | 10.9 ± 2.2 | 15.8 ± 2.0 | 14.1 ± 2.7 |
| HS1700-SPIRE354 | 255.38151080168674 | 64.31708203646991 | 10.9 ± 2.2 | 14.5 ± 2.0 | 2.8 ± 2.3 |
| HS1700-SPIRE355 | 255.02414281518156 | 64.22371556065298 | 10.6 ± 2.2 | 12.9 ± 1.8 | 7.7 ± 2.2 |
| HS1700-SPIRE356 | 255.4302247027845 | 64.06531126682206 | 12.1 ± 2.5 | 13.4 ± 1.8 | 3.0 ± 2.4 |
| HS1700-SPIRE357 | 255.31882668031724 | 64.03069791465623 | 13.2 ± 2.7 | 2.7 ± 1.8 | 4.0 ± 2.2 |

Table A.7: SPIRE sources catalogue of HS1700 field.

| ID[1] | R.A.[2] (J2000) | Dec.[3] (J2000) | $S_{250}$[4] (mJy) | $S_{350}$[5] (mJy) | $S_{500}$[6] (mJy) |
|---|---|---|---|---|---|
| HS1700-SPIRE358 | 255.1830130983343 | 64.13824998638474 | 10.2 ± 2.1 | 12.6 ± 1.9 | 1.4 ± 2.5 |
| HS1700-SPIRE359 | 255.51551241729288 | 64.07856223017363 | 13.5 ± 2.8 | 9.3 ± 1.8 | 7.5 ± 2.4 |
| HS1700-SPIRE360 | 255.00574679344044 | 64.23996340478568 | 10.1 ± 2.1 | 14.5 ± 1.7 | 6.5 ± 2.1 |
| HS1700-SPIRE361 | 255.34842599582024 | 64.29581327757332 | 12.1 ± 2.5 | 10.3 ± 1.8 | 8.1 ± 2.1 |
| HS1700-SPIRE362 | 255.42740675443568 | 64.22840322332893 | 10.2 ± 2.2 | 17.6 ± 1.7 | 0.0 ± 2.4 |
| HS1700-SPIRE363 | 255.72433328626468 | 64.19669455587629 | 10.7 ± 2.3 | 12.8 ± 2.0 | 6.9 ± 2.3 |
| HS1700-SPIRE364 | 255.05908835054356 | 64.1542328258156 | 11.1 ± 2.4 | 12.6 ± 1.7 | 4.1 ± 2.1 |
| HS1700-SPIRE365 | 255.42173610754196 | 64.04854633642826 | 10.9 ± 2.4 | 14.7 ± 1.9 | 0.0 ± 2.6 |
| HS1700-SPIRE366 | 255.3917377466943 | 64.18925157912565 | 9.9 ± 2.3 | 20.1 ± 1.9 | 9.1 ± 2.2 |
| HS1700-SPIRE367 | 255.07344829929494 | 64.40340117186997 | 12.2 ± 2.8 | 2.3 ± 2.1 | 0.0 ± 2.8 |
| HS1700-SPIRE368 | 255.09136314792855 | 64.01512299511784 | 9.6 ± 2.2 | 7.7 ± 1.9 | 14.8 ± 2.2 |
| HS1700-SPIRE369 | 254.89674301936608 | 64.14540357249318 | 9.4 ± 2.2 | 14.1 ± 2.0 | 2.4 ± 2.3 |
| HS1700-SPIRE370 | 255.34700921699394 | 63.988562332210115 | 12.4 ± 3.0 | 2.4 ± 2.2 | 0.0 ± 3.1 |
| HS1700-SPIRE371 | 254.73338629394914 | 64.13990403379256 | 12.5 ± 3.1 | 6.9 ± 2.1 | 0.0 ± 2.8 |
| HS1700-SPIRE372 | 255.31385372452752 | 64.18901944773353 | 8.9 ± 2.2 | 13.2 ± 1.8 | 0.0 ± 2.2 |
| HS1700-SPIRE373 | 255.4999492768274 | 64.24852532255984 | 9.2 ± 2.3 | 16.3 ± 1.8 | 6.1 ± 2.3 |
| HS1700-SPIRE374 | 255.0107259531617 | 64.27555946879103 | 9.0 ± 2.3 | 15.4 ± 1.7 | 1.0 ± 2.4 |
| HS1700-SPIRE375 | 255.23136406374655 | 64.36032180274546 | 9.3 ± 2.5 | 18.7 ± 1.8 | 16.7 ± 2.0 |
| HS1700-SPIRE376 | 255.38417204451346 | 64.04331722321582 | 7.7 ± 2.3 | 11.1 ± 1.9 | 12.2 ± 2.3 |
| HS1700-SPIRE377 | 255.23486637474437 | 64.37562743553654 | 9.1 ± 2.7 | 18.0 ± 1.9 | 8.1 ± 2.3 |
| HS1700-SPIRE378 | 254.93126671598708 | 64.33873184866039 | 8.9 ± 2.7 | 12.8 ± 2.3 | 1.6 ± 2.7 |
| HS1700-SPIRE379 | 255.15411341788638 | 64.17478174732368 | 7.3 ± 2.2 | 9.4 ± 1.8 | 12.1 ± 2.2 |
| HS1700-SPIRE380 | 255.49888624109758 | 64.30164004945671 | 6.8 ± 2.1 | 13.6 ± 1.9 | 9.1 ± 2.1 |
| HS1700-SPIRE381 | 255.1444837718744 | 64.43365766197537 | 7.6 ± 2.6 | 14.6 ± 2.2 | 6.5 ± 2.6 |
| HS1700-SPIRE382 | 254.82026935962313 | 64.25811096082035 | 5.1 ± 2.2 | 14.2 ± 1.8 | 8.1 ± 2.2 |
| HS1700-SPIRE383 | 254.69821536315285 | 64.14857688077629 | 6.4 ± 3.1 | 5.6 ± 2.1 | 25.1 ± 2.7 |

Table A.8: SPIRE sources catalogue of 2QZCluster field.

| ID[1] | R.A.[2] (J2000) | Dec.[3] (J2000) | $S_{250}$[4] (mJy) | $S_{350}$[5] (mJy) | $S_{500}$[6] (mJy) |
|---|---|---|---|---|---|
| SSA22-SPIRE1 | 334.264444128561 | 0.6764415586203842 | 135.3±2.2 | 71.3±1.9 | 30.4±2.3 |
| SSA22-SPIRE2 | 334.57160684240256 | 0.49219161422544583 | 93.3±2.2 | 76.7±1.7 | 48.7±2.3 |
| SSA22-SPIRE3 | 334.344178441303 | 0.3528652232847903 | 79.2±2.2 | 34.4±1.9 | 10.4±2.2 |
| SSA22-SPIRE4 | 334.34457572927244 | 0.607307593915126 | 79.7±2.4 | 56.9±1.7 | 21.9±2.0 |
| SSA22-SPIRE5 | 334.69745115684617 | 0.3983836901706686 | 72.9±2.2 | 29.8±1.9 | 12.8±2.1 |
| SSA22-SPIRE6 | 334.392819716858 | 0.3042332652494624 | 68.9±2.1 | 33.2±1.8 | 0.0±2.1 |
| SSA22-SPIRE7 | 334.23836274598824 | 0.40194158606064945 | 61.8±2.1 | 45.8±1.8 | 8.8±2.1 |
| SSA22-SPIRE8 | 334.55462830631444 | 0.47701863826781765 | 62.9±2.1 | 33.3±1.8 | 18.3±2.0 |
| SSA22-SPIRE9 | 334.3848999033597 | 0.2912395866246295 | 57.5±2.1 | 49.6±1.7 | 45.7±2.2 |
| SSA22-SPIRE10 | 334.58002216598203 | 0.35006798763473185 | 64.3±2.3 | 51.3±2.0 | 30.6±2.3 |
| SSA22-SPIRE11 | 334.5755496003682 | 0.22250417788370147 | 62.1±2.3 | 20.9±1.8 | 14.7±2.2 |
| SSA22-SPIRE12 | 334.43134959402465 | 0.11706176788891216 | 59.2±2.2 | 26.4±1.9 | 10.7±2.1 |
| SSA22-SPIRE13 | 334.6278347214049 | 0.29133392559629395 | 53.2±2.1 | 28.6±1.8 | 8.3±2.5 |
| SSA22-SPIRE14 | 334.4027585675123 | 0.2179536270084429 | 58.2±2.3 | 30.8±1.9 | 15.4±2.1 |
| SSA22-SPIRE15 | 334.6215640701658 | 0.34817151748627767 | 52.3±2.1 | 41.7±1.7 | 25.6±2.2 |
| SSA22-SPIRE16 | 334.2491254313019 | 0.17788257241578864 | 53.0±2.2 | 53.0±2.0 | 35.0±2.2 |
| SSA22-SPIRE17 | 334.5457848924229 | 0.1754391429595643 | 58.9±2.4 | 31.4±1.7 | 8.9±2.1 |
| SSA22-SPIRE18 | 334.37299492364775 | 0.5268242905063404 | 59.0±2.4 | 42.4±1.7 | 20.6±2.2 |
| SSA22-SPIRE19 | 334.3554128271123 | 0.3681810959146735 | 51.9±2.2 | 24.5±1.8 | 9.1±2.4 |
| SSA22-SPIRE20 | 334.1968643724931 | 0.31841437029881636 | 49.5±2.1 | 26.9±1.8 | 11.6±2.2 |
| SSA22-SPIRE21 | 334.2136006462951 | 0.30567471832178333 | 50.6±2.2 | 54.6±2.0 | 43.4±2.1 |
| SSA22-SPIRE22 | 334.47689856565995 | 0.19682107295325102 | 49.1±2.2 | 33.0±1.8 | 15.8±2.1 |
| SSA22-SPIRE23 | 334.23431491828694 | 0.4799891962055718 | 51.3±2.3 | 55.6±1.7 | 51.1±2.4 |
| SSA22-SPIRE24 | 334.4909443492956 | 0.5515964197651031 | 52.4±2.4 | 20.9±1.8 | 0.3±2.2 |
| SSA22-SPIRE25 | 334.4958537939469 | 0.32304139449407426 | 52.6±2.4 | 20.3±1.7 | 5.0±2.3 |
| SSA22-SPIRE26 | 334.67405878369874 | 0.3585819075546096 | 50.2±2.4 | 29.7±1.8 | 10.6±2.1 |
| SSA22-SPIRE27 | 334.1104125900193 | 0.38212160196607753 | 48.2±2.3 | 33.0±1.8 | 6.2±2.2 |
| SSA22-SPIRE28 | 334.2206033150244 | 0.580575698910158 | 47.8±2.3 | 34.1±1.8 | 15.1±2.3 |
| SSA22-SPIRE29 | 334.68007139276364 | 0.42486839496210854 | 41.1±2.0 | 35.1±1.6 | 12.5±2.0 |
| SSA22-SPIRE30 | 334.20875954844786 | 0.37922354558485555 | 44.6±2.2 | 56.6±1.7 | 46.2±2.0 |
| SSA22-SPIRE31 | 334.6420802699643 | 0.40744648984557824 | 48.2±2.4 | 30.3±1.8 | 16.5±2.1 |
| SSA22-SPIRE32 | 334.46811378567406 | 0.5203560190320456 | 43.3±2.2 | 35.5±1.6 | 17.6±2.1 |
| SSA22-SPIRE33 | 334.54451041539545 | 0.5353916976644296 | 43.3±2.2 | 21.1±1.9 | 4.2±2.4 |
| SSA22-SPIRE34 | 334.44333142934164 | 0.48249392011691566 | 46.8±2.4 | 29.7±1.9 | 21.5±2.1 |
| SSA22-SPIRE35 | 334.4833365552271 | 0.26920401551486817 | 40.1±2.1 | 29.9±1.8 | 26.7±2.1 |
| SSA22-SPIRE36 | 334.5908133188132 | 0.5196469026777315 | 46.4±2.4 | 25.0±1.7 | 4.8±2.4 |
| SSA22-SPIRE37 | 334.3497129271324 | 0.28128843517532787 | 44.6±2.3 | 32.4±1.7 | 15.4±2.1 |
| SSA22-SPIRE38 | 334.4525404107452 | 0.3412680896748497 | 43.3±2.3 | 43.0±1.8 | 25.4±2.3 |

Table A.8: SPIRE sources catalogue of 2QZCluster field.

| ID[1] | R.A.[2] (J2000) | Dec.[3] (J2000) | $S_{250}$[4] (mJy) | $S_{350}$[5] (mJy) | $S_{500}$[6] (mJy) |
|---|---|---|---|---|---|
| SSA22-SPIRE39 | 334.51108899229143 | 0.40283447207422063 | 44.8±2.4 | 30.3±1.8 | 10.5±2.2 |
| SSA22-SPIRE40 | 334.5438822802702 | 0.42812243922245485 | 43.6±2.4 | 27.9±1.9 | 11.8±2.0 |
| SSA22-SPIRE41 | 334.3484908639407 | 0.45434133824737294 | 40.9±2.2 | 15.9±1.8 | 5.7±2.2 |
| SSA22-SPIRE42 | 334.40258665302116 | 0.13974198951048514 | 40.7±2.2 | 32.3±1.7 | 26.2±2.2 |
| SSA22-SPIRE43 | 334.5336197422643 | 0.22653913790202754 | 38.8±2.2 | 42.4±1.8 | 19.2±2.4 |
| SSA22-SPIRE44 | 334.31834153284245 | 0.14156930159028283 | 38.2±2.1 | 29.4±1.9 | 12.6±2.3 |
| SSA22-SPIRE45 | 334.57638795026696 | 0.5652045923071393 | 38.7±2.2 | 21.2±2.0 | 9.5±2.4 |
| SSA22-SPIRE46 | 334.4287134579472 | 0.5098571383454719 | 41.7±2.4 | 32.1±1.9 | 2.5±2.3 |
| SSA22-SPIRE47 | 334.423534757171 | 0.5622396298161293 | 38.8±2.2 | 31.0±1.7 | 17.2±2.0 |
| SSA22-SPIRE48 | 334.0596998912589 | 0.26889311642856406 | 36.4±2.1 | 22.5±1.8 | 8.0±2.3 |
| SSA22-SPIRE49 | 334.3993764792089 | 0.45788002222686675 | 40.1±2.3 | 26.8±1.9 | 19.2±2.3 |
| SSA22-SPIRE50 | 334.2183855456978 | 0.5588159377339286 | 37.8±2.2 | 37.7±1.8 | 31.7±2.3 |
| SSA22-SPIRE51 | 334.61333165709976 | 0.3309355278459874 | 36.5±2.1 | 31.1±1.7 | 22.5±2.2 |
| SSA22-SPIRE52 | 334.2070952471623 | 0.47455960931757724 | 40.9±2.4 | 29.3±1.9 | 20.6±2.3 |
| SSA22-SPIRE53 | 334.6284583928753 | 0.32939872556574606 | 35.8±2.1 | 9.7±1.8 | 0.0±2.0 |
| SSA22-SPIRE54 | 334.3317273514648 | 0.16095187876818767 | 36.5±2.2 | 15.3±1.8 | 6.5±2.1 |
| SSA22-SPIRE55 | 334.38295588631837 | 0.4609870294795754 | 36.0±2.1 | 22.3±1.7 | 2.9±2.2 |
| SSA22-SPIRE56 | 334.22341301377304 | 0.3220200895437896 | 38.3±2.3 | 17.2±1.8 | 9.6±2.2 |
| SSA22-SPIRE57 | 334.5471198263948 | 0.5039565360518778 | 38.1±2.3 | 34.0±1.8 | 21.6±2.1 |
| SSA22-SPIRE58 | 334.528459617602 | 0.2131489105180075 | 39.6±2.4 | 42.8±1.7 | 25.5±2.2 |
| SSA22-SPIRE59 | 334.3341362303931 | 0.5331709786040492 | 37.3±2.3 | 20.7±2.0 | 16.5±2.2 |
| SSA22-SPIRE60 | 334.2319195775968 | 0.41379530349189264 | 32.7±2.0 | 41.7±1.6 | 22.7±1.9 |
| SSA22-SPIRE61 | 334.7613898733321 | 0.4490550956425628 | 35.3±2.2 | 18.4±1.9 | 7.8±2.4 |
| SSA22-SPIRE62 | 334.6862451194263 | 0.39009806641379513 | 34.6±2.1 | 19.8±1.8 | 1.8±2.3 |
| SSA22-SPIRE63 | 334.5427365398572 | 0.45027338410247464 | 38.0±2.4 | 28.6±1.8 | 14.2±2.3 |
| SSA22-SPIRE64 | 334.0988124270266 | 0.3600234768746395 | 33.7±2.1 | 29.7±1.8 | 21.6±2.2 |
| SSA22-SPIRE65 | 334.51771024027533 | 0.5994486644652689 | 37.8±2.3 | 25.2±2.1 | 12.8±2.3 |
| SSA22-SPIRE66 | 334.2461297025148 | 0.20932117860693622 | 36.5±2.3 | 36.6±1.7 | 19.0±2.5 |
| SSA22-SPIRE67 | 334.31960342404625 | 0.49597705984394636 | 38.2±2.4 | 34.0±1.9 | 16.4±2.2 |
| SSA22-SPIRE68 | 334.7579593684066 | 0.4271802793556352 | 40.5±2.6 | 37.1±1.8 | 20.9±2.5 |
| SSA22-SPIRE69 | 334.281513478729 | 0.15656241726627412 | 33.5±2.1 | 18.0±1.9 | 0.0±2.2 |
| SSA22-SPIRE70 | 334.0538684563115 | 0.23484726518994797 | 35.6±2.3 | 8.2±2.0 | 2.6±2.1 |
| SSA22-SPIRE71 | 334.5075312830932 | 0.2493828545397405 | 36.7±2.3 | 26.6±1.9 | 20.4±2.4 |
| SSA22-SPIRE72 | 334.42440192246653 | 0.32043319853984364 | 33.5±2.1 | 32.9±1.9 | 23.3±2.3 |
| SSA22-SPIRE73 | 334.35143903948614 | 0.1252740170256821 | 33.2±2.1 | 21.9±1.9 | 16.1±2.2 |
| SSA22-SPIRE74 | 334.1674839489523 | 0.2720558050945857 | 33.7±2.2 | 22.3±1.8 | 10.4±2.2 |
| SSA22-SPIRE75 | 334.07670006037256 | 0.23869065988185822 | 35.7±2.3 | 19.2±1.8 | 7.4±2.3 |
| SSA22-SPIRE76 | 334.6318257024618 | 0.3727128449496398 | 35.2±2.3 | 20.3±1.7 | 9.7±2.3 |
| SSA22-SPIRE77 | 334.22774672395786 | 0.17276532245659323 | 33.3±2.2 | 14.5±1.8 | 4.0±2.4 |
| SSA22-SPIRE78 | 334.298828816217 | 0.47540101794157874 | 34.4±2.2 | 37.8±2.0 | 21.8±2.0 |
| SSA22-SPIRE79 | 334.5913065105346 | 0.24083866571967058 | 33.3±2.2 | 22.2±1.9 | 13.8±2.2 |
| SSA22-SPIRE80 | 334.3864214436095 | 0.4967318519446424 | 32.0±2.1 | 33.8±1.7 | 24.3±2.0 |
| SSA22-SPIRE81 | 334.22639818393725 | 0.21151389336947674 | 34.0±2.2 | 32.8±1.6 | 18.1±2.1 |
| SSA22-SPIRE82 | 334.2179299207901 | 0.41880505975717003 | 33.2±2.2 | 28.8±1.6 | 11.8±2.2 |
| SSA22-SPIRE83 | 334.28831795241285 | 0.3337606865209588 | 33.6±2.2 | 15.2±1.8 | 5.3±2.2 |
| SSA22-SPIRE84 | 334.60133954981984 | 0.40273220906548607 | 34.8±2.3 | 30.1±1.9 | 30.8±2.1 |
| SSA22-SPIRE85 | 334.23212115165336 | 0.5739282797253542 | 32.3±2.1 | 35.4±1.8 | 21.3±2.5 |
| SSA22-SPIRE86 | 334.44762768019353 | 0.13502566971986574 | 36.4±2.4 | 50.8±1.9 | 26.0±2.2 |
| SSA22-SPIRE87 | 334.5996146381847 | 0.23655453516203023 | 31.6±2.1 | 21.6±1.9 | 12.8±2.2 |
| SSA22-SPIRE88 | 334.4066026177318 | 0.200415566246098 | 32.1±2.2 | 32.0±1.8 | 11.2±2.5 |
| SSA22-SPIRE89 | 334.5680084416561 | 0.4147964490528236 | 33.2±2.2 | 33.1±1.7 | 17.9±2.1 |
| SSA22-SPIRE90 | 334.2949128261823 | 0.38151906340756825 | 31.4±2.1 | 24.7±1.8 | 15.2±2.0 |
| SSA22-SPIRE91 | 334.08752082867903 | 0.3335484177684095 | 32.8±2.2 | 26.8±1.8 | 23.6±2.4 |
| SSA22-SPIRE92 | 334.5469368143001 | 0.4058969853629003 | 34.0±2.3 | 23.7±1.7 | 10.1±2.2 |
| SSA22-SPIRE93 | 334.33627495411196 | 0.21239590486826632 | 34.4±2.3 | 20.5±1.7 | 6.3±2.1 |
| SSA22-SPIRE94 | 334.3282107948312 | 0.3021542277006582 | 40.6±2.8 | 42.6±1.8 | 37.0±2.2 |
| SSA22-SPIRE95 | 334.62215553003375 | 0.5294949987303228 | 32.8±2.3 | 27.6±1.7 | 15.8±2.2 |
| SSA22-SPIRE96 | 334.51734717984573 | 0.47857277265509984 | 33.6±2.3 | 34.0±1.8 | 20.0±2.1 |
| SSA22-SPIRE97 | 334.49683072851263 | 0.48436693840054806 | 30.6±2.1 | 10.1±1.8 | 0.0±2.2 |
| SSA22-SPIRE98 | 334.4056902675419 | 0.40628310299948545 | 33.3±2.3 | 18.1±1.8 | 6.0±2.2 |
| SSA22-SPIRE99 | 334.51960213908626 | 0.17205313047769832 | 30.9±2.2 | 13.7±1.9 | 11.5±2.1 |
| SSA22-SPIRE100 | 334.5155751097287 | 0.5622684827274208 | 33.2±2.3 | 32.4±1.9 | 15.8±2.3 |
| SSA22-SPIRE101 | 334.188360405849 | 0.27041877759207794 | 32.0±2.3 | 21.1±1.9 | 18.7±2.4 |
| SSA22-SPIRE102 | 334.24710931963256 | 0.14877594891556897 | 33.1±2.3 | 28.2±1.9 | 11.9±2.2 |
| SSA22-SPIRE103 | 334.36679635489764 | 0.48047052999574463 | 31.5±2.2 | 33.2±1.8 | 24.9±2.2 |
| SSA22-SPIRE104 | 334.0966906971447 | 0.3434368264284261 | 29.5±2.1 | 24.5±1.9 | 5.6±2.3 |
| SSA22-SPIRE105 | 334.4228100323802 | 0.17918329996523535 | 30.3±2.2 | 31.3±1.9 | 12.6±2.1 |
| SSA22-SPIRE106 | 334.23462203007887 | 0.427487449652578 | 31.2±2.2 | 22.9±1.6 | 6.7±2.1 |
| SSA22-SPIRE107 | 334.52407872223483 | 0.2765601704100953 | 31.4±2.3 | 33.6±1.9 | 13.5±2.2 |
| SSA22-SPIRE108 | 334.2728870283139 | 0.3293461641639451 | 31.5±2.3 | 26.4±1.8 | 13.2±2.2 |
| SSA22-SPIRE109 | 334.3468196956325 | 0.3204358071576784 | 32.9±2.4 | 30.9±1.9 | 6.8±2.3 |
| SSA22-SPIRE110 | 334.27731199253793 | 0.29028152485784375 | 30.1±2.2 | 40.7±1.7 | 22.6±2.1 |
| SSA22-SPIRE111 | 334.1485824374597 | 0.4198880397415793 | 29.1±2.1 | 26.9±1.8 | 19.3±2.4 |
| SSA22-SPIRE112 | 334.1709555443369 | 0.31442110482790164 | 30.4±2.2 | 36.8±1.7 | 22.7±2.1 |
| SSA22-SPIRE113 | 334.41567603814406 | 0.6263006266483344 | 30.9±2.3 | 9.9±1.9 | 2.1±2.2 |
| SSA22-SPIRE114 | 334.2944891124376 | 0.4069295775008844 | 30.4±2.2 | 30.3±1.8 | 20.0±2.1 |

Table A.8: SPIRE sources catalogue of 2QZCluster field.

| ID[1] | R.A.[2] (J2000) | Dec.[3] (J2000) | $S_{250}$[4] (mJy) | $S_{350}$[5] (mJy) | $S_{500}$[6] (mJy) |
|---|---|---|---|---|---|
| SSA22-SPIRE115 | 334.4229629550191 | 0.5433826877395354 | 28.0±2.1 | 20.0±1.7 | 8.8±2.1 |
| SSA22-SPIRE116 | 334.5628414817463 | 0.2914350249569934 | 30.9±2.3 | 15.1±1.7 | 4.3±2.3 |
| SSA22-SPIRE117 | 334.60366258878156 | 0.3222495354282699 | 30.0±2.2 | 34.1±1.8 | 25.1±2.4 |
| SSA22-SPIRE118 | 334.17002180707897 | 0.38478845672843764 | 30.6±2.3 | 21.2±1.9 | 5.1±2.1 |
| SSA22-SPIRE119 | 334.2239058082972 | 0.5129096908120522 | 32.5±2.4 | 20.7±1.8 | 3.4±2.2 |
| SSA22-SPIRE120 | 334.5836146406482 | 0.536636696400224 | 30.4±2.3 | 30.0±1.9 | 14.9±2.2 |
| SSA22-SPIRE121 | 334.2732991559811 | 0.4618944089321916 | 28.0±2.1 | 19.0±1.8 | 14.1±2.4 |
| SSA22-SPIRE122 | 334.39851766698484 | 0.5513878596217229 | 28.3±2.1 | 12.8±1.7 | 7.2±2.1 |
| SSA22-SPIRE123 | 334.520848442146 | 0.34732817596503507 | 28.3±2.2 | 13.9±1.8 | 0.0±2.1 |
| SSA22-SPIRE124 | 334.27596759241914 | 0.6472304843107454 | 28.4±2.2 | 18.2±1.8 | 18.0±2.2 |
| SSA22-SPIRE125 | 334.44074157097424 | 0.505719201521876 | 34.8±2.7 | 26.1±1.8 | 16.2±2.3 |
| SSA22-SPIRE126 | 334.38552978637824 | 0.19144135161257644 | 32.3±2.5 | 28.7±1.9 | 20.3±2.1 |
| SSA22-SPIRE127 | 334.2343156332541 | 0.5538551955376773 | 34.7±2.7 | 23.2±1.8 | 10.9±2.2 |
| SSA22-SPIRE128 | 334.59426774753223 | 0.5532563345665636 | 28.4±2.2 | 16.0±2.0 | 10.1±2.1 |
| SSA22-SPIRE129 | 334.4130030705576 | 0.48501692342800284 | 27.2±2.1 | 27.6±1.9 | 15.7±2.1 |
| SSA22-SPIRE130 | 334.4586657368944 | 0.3812150783058228 | 28.5±2.2 | 21.6±1.8 | 8.2±2.4 |
| SSA22-SPIRE131 | 334.3864133923612 | 0.4840280215850618 | 30.0±2.3 | 18.0±1.7 | 6.3±2.1 |
| SSA22-SPIRE132 | 334.6075634939119 | 0.28240864844245916 | 30.8±2.4 | 29.1±1.7 | 20.3±2.1 |
| SSA22-SPIRE133 | 334.3537675325221 | 0.30237830412670597 | 29.8±2.3 | 30.1±1.8 | 13.1±2.4 |
| SSA22-SPIRE134 | 334.39006853606446 | 0.13288181838455634 | 27.2±2.1 | 16.1±1.6 | 0.8±2.2 |
| SSA22-SPIRE135 | 334.32021254977946 | 0.5546204849668697 | 26.9±2.1 | 14.3±1.8 | 8.3±2.2 |
| SSA22-SPIRE136 | 334.6039690005555 | 0.36376896393603997 | 29.5±2.3 | 25.7±1.7 | 10.7±2.3 |
| SSA22-SPIRE137 | 334.2992186124408 | 0.5835160854666533 | 30.4±2.4 | 23.6±1.9 | 17.3±2.0 |
| SSA22-SPIRE138 | 334.41458260460763 | 0.1151669156682154 | 26.2±2.1 | 25.0±1.8 | 15.0±2.1 |
| SSA22-SPIRE139 | 334.3874944172351 | 0.15152164002295654 | 29.4±2.4 | 26.4±1.8 | 6.9±2.0 |
| SSA22-SPIRE140 | 334.4052213720607 | 0.6423225172119716 | 28.5±2.3 | 14.1±1.9 | 8.2±2.2 |
| SSA22-SPIRE141 | 334.22947482976974 | 0.3613904382929383 | 27.0±2.2 | 9.4±1.8 | 6.6±2.3 |
| SSA22-SPIRE142 | 334.5335878405184 | 0.1755752498599096 | 25.8±2.1 | 18.4±1.7 | 10.2±2.0 |
| SSA22-SPIRE143 | 334.2643365866803 | 0.4029439453164923 | 25.8±2.1 | 5.9±1.9 | 0.0±2.2 |
| SSA22-SPIRE144 | 334.56614564129825 | 0.5708792042950576 | 26.4±2.2 | 15.2±1.9 | 6.4±2.3 |
| SSA22-SPIRE145 | 334.7014685362106 | 0.42172292060090927 | 25.3±2.1 | 14.0±1.8 | 7.9±2.2 |
| SSA22-SPIRE146 | 334.280789292262 | 0.26891148785517643 | 26.8±2.2 | 8.6±1.9 | 1.1±2.2 |
| SSA22-SPIRE147 | 334.5151184330032 | 0.2533512436618365 | 27.6±2.3 | 11.2±1.9 | 8.0±2.3 |
| SSA22-SPIRE148 | 334.257795286942 | 0.5296270634163822 | 27.5±2.3 | 20.5±1.9 | 13.0±2.3 |
| SSA22-SPIRE149 | 334.27805464759143 | 0.1797144119666992 | 26.2±2.2 | 15.2±1.7 | 6.7±2.0 |
| SSA22-SPIRE150 | 334.277955460448 | 0.5248281117202276 | 26.7±2.2 | 23.1±1.7 | 13.7±2.4 |
| SSA22-SPIRE151 | 334.3677636981975 | 0.6178386734837007 | 25.1±2.1 | 20.5±1.8 | 10.4±2.4 |
| SSA22-SPIRE152 | 334.3545232148711 | 0.6291983510378699 | 26.3±2.2 | 17.1±1.8 | 10.4±2.1 |
| SSA22-SPIRE153 | 334.33189468202215 | 0.27919799842835735 | 29.5±2.5 | 13.6±1.7 | 0.0±2.1 |
| SSA22-SPIRE154 | 334.6880398531809 | 0.5289350342792862 | 29.3±2.4 | 26.5±2.0 | 17.5±2.5 |
| SSA22-SPIRE155 | 334.51948706048677 | 0.520638080619377 | 27.0±2.3 | 25.5±1.7 | 15.2±2.1 |
| SSA22-SPIRE156 | 334.20327245367815 | 0.39270833831169893 | 26.2±2.2 | 18.8±1.7 | 1.2±2.3 |
| SSA22-SPIRE157 | 334.3154136085122 | 0.3664102276251471 | 24.2±2.0 | 22.0±1.8 | 7.5±2.0 |
| SSA22-SPIRE158 | 334.45279789632445 | 0.3072447732887595 | 26.4±2.2 | 26.1±1.8 | 16.6±2.1 |
| SSA22-SPIRE159 | 334.43401358780034 | 0.38743644308710423 | 26.5±2.2 | 21.6±1.7 | 21.2±2.2 |
| SSA22-SPIRE160 | 334.2707516256328 | 0.6995364976082926 | 29.6±2.5 | 20.5±2.2 | 6.5±2.4 |
| SSA22-SPIRE161 | 334.1114322965925 | 0.31521206509239147 | 27.2±2.3 | 19.9±1.9 | 11.6±2.1 |
| SSA22-SPIRE162 | 334.5399086389454 | 0.6005937391562238 | 29.6±2.5 | 31.1±1.9 | 15.4±2.4 |
| SSA22-SPIRE163 | 334.2699495847096 | 0.1490615680982239 | 27.2±2.3 | 25.6±1.7 | 20.2±2.4 |
| SSA22-SPIRE164 | 334.4051492076298 | 0.1732526493647733 | 26.3±2.2 | 26.2±1.9 | 22.7±2.2 |
| SSA22-SPIRE165 | 334.4901507548892 | 0.5123305400138726 | 26.4±2.2 | 28.5±1.7 | 21.7±2.2 |
| SSA22-SPIRE166 | 334.3271026226081 | 0.36346406391090674 | 24.8±2.1 | 17.8±1.8 | 10.1±2.1 |
| SSA22-SPIRE167 | 334.4055887987355 | 0.4563181296839242 | 27.0±2.3 | 16.3±1.9 | 10.2±2.3 |
| SSA22-SPIRE168 | 334.5000587013419 | 0.4951130165736352 | 23.7±2.0 | 17.0±1.8 | 18.8±2.0 |
| SSA22-SPIRE169 | 334.34210222130554 | 0.6400991201575016 | 25.8±2.2 | 21.0±1.7 | 8.9±2.4 |
| SSA22-SPIRE170 | 334.2525773361816 | 0.18891575126699123 | 26.0±2.2 | 29.7±1.8 | 15.5±2.1 |
| SSA22-SPIRE171 | 334.2535599835562 | 0.5035600527287462 | 26.9±2.3 | 19.0±1.9 | 10.2±2.1 |
| SSA22-SPIRE172 | 334.29279132088607 | 0.5146262813887026 | 27.0±2.3 | 31.6±1.8 | 23.6±2.0 |
| SSA22-SPIRE173 | 334.33397418328514 | 0.11210808518327352 | 29.6±2.6 | 10.5±1.9 | 5.2±2.3 |
| SSA22-SPIRE174 | 334.3524097376433 | 0.21321313745353077 | 25.4±2.2 | 22.4±1.8 | 14.4±2.3 |
| SSA22-SPIRE175 | 334.4915442161405 | 0.2759590000169102 | 26.1±2.3 | 16.7±1.8 | 5.2±2.2 |
| SSA22-SPIRE176 | 334.50895015548815 | 0.4327158329817197 | 28.3±2.5 | 23.4±1.8 | 11.0±2.1 |
| SSA22-SPIRE177 | 334.3222519652916 | 0.5265623476206347 | 26.3±2.3 | 27.8±1.8 | 24.7±2.1 |
| SSA22-SPIRE178 | 334.13844487897376 | 0.3912829214827451 | 25.3±2.2 | 13.8±1.9 | 13.5±2.0 |
| SSA22-SPIRE179 | 334.2333655943735 | 0.3030100058031791 | 25.5±2.2 | 19.8±1.9 | 8.3±2.0 |
| SSA22-SPIRE180 | 334.5972576176873 | 0.33720596335652026 | 27.3±2.4 | 5.4±1.7 | 0.1±2.1 |
| SSA22-SPIRE181 | 334.3860248603755 | 0.21880727658418297 | 26.4±2.3 | 27.6±2.0 | 18.4±2.1 |
| SSA22-SPIRE182 | 334.4347820955337 | 0.13978345061456204 | 25.4±2.3 | 28.5±1.7 | 19.0±2.3 |
| SSA22-SPIRE183 | 334.2084083781158 | 0.3186651678804012 | 24.3±2.2 | 10.3±1.7 | 0.0±2.1 |
| SSA22-SPIRE184 | 334.2175362111473 | 0.5006159991363184 | 28.6±2.6 | 25.6±1.9 | 17.9±2.3 |
| SSA22-SPIRE185 | 334.3225370081864 | 0.6137799940897299 | 26.7±2.4 | 26.1±1.8 | 15.3±2.1 |
| SSA22-SPIRE186 | 334.1552432833247 | 0.3548141153165248 | 24.8±2.2 | 11.2±1.7 | 11.0±2.3 |
| SSA22-SPIRE187 | 334.24623146001676 | 0.25401453924647815 | 24.3±2.2 | 13.8±1.7 | 4.4±2.1 |
| SSA22-SPIRE188 | 334.485125983953 | 0.47110467727854954 | 23.4±2.1 | 27.2±1.7 | 14.4±2.2 |
| SSA22-SPIRE189 | 334.7443204051687 | 0.39313511428656245 | 26.4±2.4 | 18.8±1.9 | 6.8±2.6 |
| SSA22-SPIRE190 | 334.45622354690084 | 0.18589890055702368 | 24.4±2.2 | 16.1±1.9 | 3.3±2.4 |

Table A.8: SPIRE sources catalogue of 2QZCluster field.

| ID[1] | R.A.[2] (J2000) | Dec.[3] (J2000) | $S_{250}$[4] (mJy) | $S_{350}$[5] (mJy) | $S_{500}$[6] (mJy) |
|---|---|---|---|---|---|
| SSA22-SPIRE191 | 334.1735155912016 | 0.2255837724488139 | 26.4±2.4 | 25.6±1.7 | 10.9±2.0 |
| SSA22-SPIRE192 | 334.20827607524745 | 0.18426073791069345 | 24.3±2.2 | 21.4±1.7 | 16.7±2.2 |
| SSA22-SPIRE193 | 334.7060166437043 | 0.4402771151369646 | 25.0±2.3 | 14.3±1.7 | 10.1±2.2 |
| SSA22-SPIRE194 | 334.55766779913137 | 0.4523422370564958 | 26.9±2.4 | 25.4±1.9 | 15.1±2.2 |
| SSA22-SPIRE195 | 334.5350707636686 | 0.5659992776840205 | 23.1±2.1 | 14.8±1.7 | 5.9±2.2 |
| SSA22-SPIRE196 | 334.3267045369965 | 0.5339250954150513 | 26.0±2.4 | 2.3±1.8 | 13.4±2.2 |
| SSA22-SPIRE197 | 334.36766460140655 | 0.4263410952274448 | 23.9±2.2 | 18.4±1.8 | 10.5±2.3 |
| SSA22-SPIRE198 | 334.13826200680234 | 0.333452501300957 | 23.6±2.2 | 13.7±1.9 | 13.9±2.0 |
| SSA22-SPIRE199 | 334.4997784927171 | 0.19088985828677643 | 23.6±2.2 | 17.5±1.8 | 9.5±1.9 |
| SSA22-SPIRE200 | 334.7358057268622 | 0.4740325222966418 | 24.3±2.2 | 13.9±1.8 | 9.4±2.3 |
| SSA22-SPIRE201 | 334.5267809059953 | 0.19251452632248434 | 25.3±2.3 | 23.1±1.8 | 27.2±2.1 |
| SSA22-SPIRE202 | 334.54574311056984 | 0.28230908514812875 | 27.6±2.5 | 38.1±1.7 | 29.9±2.3 |
| SSA22-SPIRE203 | 334.63069898730237 | 0.23681964316173781 | 26.6±2.4 | 27.9±1.7 | 21.9±2.2 |
| SSA22-SPIRE204 | 334.25907404110814 | 0.2647372679700501 | 22.2±2.0 | 24.3±1.7 | 18.7±2.2 |
| SSA22-SPIRE205 | 334.31628054778326 | 0.28453880165967627 | 26.8±2.5 | 27.9±1.8 | 17.6±2.2 |
| SSA22-SPIRE206 | 334.3838738437232 | 0.3521183453654886 | 26.2±2.4 | 20.8±1.7 | 7.6±2.2 |
| SSA22-SPIRE207 | 334.45931610338135 | 0.25375640286403733 | 23.7±2.2 | 18.6±1.7 | 9.0±2.2 |
| SSA22-SPIRE208 | 334.6175984846612 | 0.2459948083012943 | 23.9±2.2 | 14.5±1.9 | 10.5±2.2 |
| SSA22-SPIRE209 | 334.35868224198026 | 0.07708762760520842 | 25.3±2.3 | 24.6±1.8 | 12.2±2.4 |
| SSA22-SPIRE210 | 334.3633217084487 | 0.22702863632558082 | 22.7±2.1 | 13.2±1.9 | 3.0±2.2 |
| SSA22-SPIRE211 | 334.5985060885882 | 0.5228338504621515 | 24.8±2.3 | 7.5±2.0 | 6.6±2.1 |
| SSA22-SPIRE212 | 334.5427124586213 | 0.3947049203380887 | 24.3±2.3 | 15.4±1.8 | 4.8±2.2 |
| SSA22-SPIRE213 | 334.6853045094415 | 0.5138075472173385 | 25.1±2.4 | 11.5±2.1 | 2.6±2.1 |
| SSA22-SPIRE214 | 334.26230665726195 | 0.41331784236506225 | 23.9±2.2 | 22.3±1.8 | 12.7±2.2 |
| SSA22-SPIRE215 | 334.60952534535477 | 0.3403763109160239 | 22.7±2.1 | 29.7±1.9 | 14.6±2.1 |
| SSA22-SPIRE216 | 334.613413024629 | 0.49854675377891716 | 24.5±2.3 | 22.8±1.7 | 10.8±2.0 |
| SSA22-SPIRE217 | 334.46723690499925 | 0.5432656441866781 | 24.9±2.4 | 22.2±1.8 | 16.6±2.3 |
| SSA22-SPIRE218 | 334.46431107275424 | 0.4568101426442481 | 23.2±2.2 | 15.8±1.7 | 11.5±2.1 |
| SSA22-SPIRE219 | 334.11649093828436 | 0.28264192986610914 | 27.6±2.6 | 27.0±1.7 | 16.7±2.2 |
| SSA22-SPIRE220 | 334.46391695108576 | 0.35425154858361246 | 25.8±2.5 | 21.7±1.8 | 10.5±2.0 |
| SSA22-SPIRE221 | 334.54446704924703 | 0.16369923230775332 | 22.0±2.1 | 13.3±1.8 | 6.0±2.1 |
| SSA22-SPIRE222 | 334.16320355671496 | 0.2625422311339393 | 23.8±2.3 | 5.7±1.7 | 1.4±2.3 |
| SSA22-SPIRE223 | 334.59445422971686 | 0.4348877714321818 | 23.3±2.2 | 0.0±1.8 | 0.0±2.4 |
| SSA22-SPIRE224 | 334.08522043385415 | 0.2195105405847669 | 24.0±2.3 | 11.7±1.9 | 3.9±2.3 |
| SSA22-SPIRE225 | 334.47774781089976 | 0.3236192515851488 | 23.5±2.3 | 22.4±1.7 | 24.2±2.2 |
| SSA22-SPIRE226 | 334.57145887511115 | 0.27974655975634705 | 23.3±2.2 | 13.4±1.8 | 8.9±2.1 |
| SSA22-SPIRE227 | 334.287032250666 | 0.6966654334697933 | 21.4±2.1 | 14.4±1.9 | 0.0±2.4 |
| SSA22-SPIRE228 | 334.46253317374584 | 0.23478937099075145 | 24.2±2.3 | 20.6±1.7 | 12.1±2.1 |
| SSA22-SPIRE229 | 334.2161785133694 | 0.28038386878933946 | 23.3±2.2 | 21.0±1.8 | 13.2±2.2 |
| SSA22-SPIRE230 | 334.1315648265994 | 0.32540210432802047 | 24.7±2.4 | 15.2±1.8 | 0.0±2.2 |
| SSA22-SPIRE231 | 334.4507614126582 | 0.21953933838470724 | 22.6±2.2 | 11.4±1.6 | 5.7±2.1 |
| SSA22-SPIRE232 | 334.287973993992 | 0.4544710299657594 | 22.7±2.2 | 2.4±1.9 | 4.6±2.4 |
| SSA22-SPIRE233 | 334.4954221194837 | 0.29293873412388366 | 20.7±2.0 | 26.3±1.6 | 17.3±2.0 |
| SSA22-SPIRE234 | 334.51831150067096 | 0.36479663815491487 | 23.7±2.3 | 23.0±1.8 | 17.4±2.5 |
| SSA22-SPIRE235 | 334.4485028301401 | 0.1559378117489092 | 22.6±2.2 | 20.1±1.8 | 16.4±2.2 |
| SSA22-SPIRE236 | 334.55656373270773 | 0.1874612152151463 | 22.8±2.2 | 19.2±1.7 | 8.6±2.3 |
| SSA22-SPIRE237 | 334.53499110508005 | 0.5777844074945347 | 21.7±2.1 | 18.1±1.9 | 5.4±2.0 |
| SSA22-SPIRE238 | 334.60151566611927 | 0.5672345842395575 | 23.7±2.3 | 8.9±1.9 | 0.0±2.2 |
| SSA22-SPIRE239 | 334.36937260553543 | 0.6302080978974247 | 21.3±2.1 | 14.4±1.8 | 5.1±2.4 |
| SSA22-SPIRE240 | 334.52739690614703 | 0.39681884170799875 | 24.8±2.4 | 30.2±1.8 | 13.6±2.2 |
| SSA22-SPIRE241 | 334.42839718907993 | 0.28427017845141817 | 27.8±2.8 | 54.4±1.9 | 54.4±2.3 |
| SSA22-SPIRE242 | 334.3015244312238 | 0.564756797348531 | 20.8±2.1 | 17.7±1.7 | 5.8±2.4 |
| SSA22-SPIRE243 | 334.625342061734 | 0.39911550480542446 | 22.7±2.3 | 32.2±1.8 | 25.4±2.3 |
| SSA22-SPIRE244 | 334.54188160084607 | 0.4158867848688038 | 23.6±2.4 | 21.6±1.8 | 6.8±2.1 |
| SSA22-SPIRE245 | 334.49171192988564 | 0.5772916293093892 | 23.0±2.3 | 14.9±1.8 | 5.1±2.3 |
| SSA22-SPIRE246 | 334.3760070272529 | 0.12262622133255163 | 22.7±2.3 | 15.5±2.0 | 12.5±2.0 |
| SSA22-SPIRE247 | 334.56673384662906 | 0.3827663944766183 | 21.9±2.2 | 4.1±1.8 | 0.0±2.4 |
| SSA22-SPIRE248 | 334.2293024429927 | 0.6325557220632083 | 24.9±2.5 | 23.4±1.9 | 12.7±2.2 |
| SSA22-SPIRE249 | 334.52718731493525 | 0.16959507939070428 | 21.5±2.2 | 11.8±1.8 | 14.4±2.0 |
| SSA22-SPIRE250 | 334.75875203368236 | 0.49694992703739743 | 23.4±2.4 | 17.0±2.0 | 11.9±2.5 |
| SSA22-SPIRE251 | 334.7294683064092 | 0.43411386980902444 | 22.6±2.3 | 35.9±1.8 | 29.6±2.1 |
| SSA22-SPIRE252 | 334.243889215681 | 0.4772949763238862 | 22.6±2.3 | 12.4±1.8 | 13.4±2.3 |
| SSA22-SPIRE253 | 334.26046084711066 | 0.393639246835847 | 21.4±2.2 | 15.0±2.0 | 9.1±2.1 |
| SSA22-SPIRE254 | 334.4784387827381 | 0.22131801711429777 | 21.9±2.2 | 27.9±1.8 | 13.8±2.3 |
| SSA22-SPIRE255 | 334.657149476976 | 0.3337220808938893 | 21.8±2.2 | 11.1±1.7 | 2.9±2.1 |
| SSA22-SPIRE256 | 334.4228612216957 | 0.4447852200176837 | 22.0±2.2 | 29.6±1.7 | 24.1±2.2 |
| SSA22-SPIRE257 | 334.4800802215759 | 0.38367362959642204 | 21.6±2.2 | 10.1±1.9 | 0.0±2.2 |
| SSA22-SPIRE258 | 334.16399040209785 | 0.22489914839743722 | 21.2±2.2 | 23.4±1.9 | 17.7±2.3 |
| SSA22-SPIRE259 | 334.2186496093971 | 0.23672568724983659 | 24.6±2.5 | 2.3±1.8 | 0.0±2.1 |
| SSA22-SPIRE260 | 334.4871554913514 | 0.41549940704956245 | 22.4±2.3 | 20.6±1.8 | 8.3±2.3 |
| SSA22-SPIRE261 | 334.4222893971154 | 0.25516341371378487 | 22.1±2.3 | 6.1±1.8 | 3.9±2.1 |
| SSA22-SPIRE262 | 334.5871718400545 | 0.2456803263458217 | 20.8±2.1 | 21.1±1.7 | 8.5±2.1 |
| SSA22-SPIRE263 | 334.55359804568747 | 0.27391247488693493 | 21.6±2.2 | 9.9±1.8 | 0.0±2.1 |
| SSA22-SPIRE264 | 334.4123329497454 | 0.2593680541002806 | 23.6±2.4 | 23.8±1.8 | 10.9±2.1 |
| SSA22-SPIRE265 | 334.57631915648096 | 0.520323398297768 | 21.8±2.3 | 18.6±1.9 | 7.2±2.1 |
| SSA22-SPIRE266 | 334.57500056415597 | 0.5055029586961567 | 22.9±2.4 | 11.2±1.8 | 0.0±2.3 |

Table A.8: SPIRE sources catalogue of 2QZCluster field.

| ID[1] | R.A.[2] (J2000) | Dec.[3] (J2000) | $S_{250}$[4] (mJy) | $S_{350}$[5] (mJy) | $S_{500}$[6] (mJy) |
|---|---|---|---|---|---|
| SSA22-SPIRE267 | 334.3784574105292 | 0.5579946890394614 | 20.7±2.2 | 11.3±1.7 | 7.4±2.1 |
| SSA22-SPIRE268 | 334.19755839289405 | 0.2739978524247776 | 22.2±2.3 | 12.2±1.9 | 6.9±2.2 |
| SSA22-SPIRE269 | 334.52680263103355 | 0.28771541418206076 | 21.9±2.3 | 17.1±1.9 | 3.5±2.1 |
| SSA22-SPIRE270 | 334.3675744986949 | 0.4473103933997581 | 20.8±2.2 | 25.2±1.8 | 29.2±2.1 |
| SSA22-SPIRE271 | 334.38854712442355 | 0.6660428201691831 | 21.4±2.2 | 19.0±2.0 | 6.9±2.3 |
| SSA22-SPIRE272 | 334.4490324840386 | 0.38884895862342905 | 21.6±2.3 | 28.3±1.8 | 15.7±2.2 |
| SSA22-SPIRE273 | 334.6376005265192 | 0.44889462375447 | 22.5±2.4 | 26.1±1.8 | 11.2±2.2 |
| SSA22-SPIRE274 | 334.6984474164843 | 0.35710719016430564 | 23.3±2.4 | 16.0±1.8 | 9.1±2.2 |
| SSA22-SPIRE275 | 334.4618642624161 | 0.19689065060904476 | 20.6±2.2 | 15.5±1.9 | 6.2±2.2 |
| SSA22-SPIRE276 | 334.1117643522606 | 0.23953383188662355 | 19.8±2.1 | 15.6±1.9 | 10.4±2.1 |
| SSA22-SPIRE277 | 334.6158944069376 | 0.3828408476895649 | 25.1±2.6 | 15.4±1.8 | 1.3±2.2 |
| SSA22-SPIRE278 | 334.66818527603976 | 0.4803199153189568 | 20.7±2.2 | 8.6±1.8 | 2.0±2.2 |
| SSA22-SPIRE279 | 334.5206433092702 | 0.3700167152912165 | 21.8±2.3 | 10.5±1.9 | 14.5±2.2 |
| SSA22-SPIRE280 | 334.03250433554535 | 0.23661248741536015 | 21.0±2.2 | 24.6±2.0 | 15.0±2.5 |
| SSA22-SPIRE281 | 334.28163235545156 | 0.5787880532209033 | 21.1±2.2 | 20.7±1.8 | 12.4±2.4 |
| SSA22-SPIRE282 | 334.37420100732595 | 0.1715064358743166 | 23.6±2.5 | 28.5±1.8 | 22.7±2.2 |
| SSA22-SPIRE283 | 334.4159900754225 | 0.5002528300196661 | 20.8±2.2 | 18.1±1.9 | 3.2±2.4 |
| SSA22-SPIRE284 | 334.45482099344014 | 0.49756425041482283 | 22.1±2.4 | 10.4±1.8 | 1.9±2.3 |
| SSA22-SPIRE285 | 334.61834950682413 | 0.28965050244923235 | 20.4±2.2 | 28.8±1.8 | 26.0±2.2 |
| SSA22-SPIRE286 | 334.3910965342107 | 0.32297183392508005 | 20.1±2.1 | 17.2±1.8 | 10.6±2.1 |
| SSA22-SPIRE287 | 334.39379246323483 | 0.5593392497542103 | 22.5±2.4 | 13.9±1.8 | 9.0±2.1 |
| SSA22-SPIRE288 | 334.2916024853946 | 0.46177616889009676 | 19.7±2.1 | 19.5±1.9 | 15.1±2.3 |
| SSA22-SPIRE289 | 334.14568253282937 | 0.4524178123881159 | 20.6±2.2 | 13.8±1.7 | 8.6±2.0 |
| SSA22-SPIRE290 | 334.5073438595216 | 0.3800887749374608 | 19.1±2.1 | 17.3±1.9 | 7.3±2.2 |
| SSA22-SPIRE291 | 334.2421255344159 | 0.350196917666382 | 22.3±2.4 | 7.5±1.8 | 5.1±2.1 |
| SSA22-SPIRE292 | 334.35928998121983 | 0.12923405302825644 | 20.0±2.2 | 23.0±1.9 | 6.1±2.1 |
| SSA22-SPIRE293 | 334.6129374563156 | 0.4332873719774979 | 20.0±2.2 | 0.0±2.0 | 10.1±2.3 |
| SSA22-SPIRE294 | 334.58595684523823 | 0.3186815897651611 | 20.5±2.2 | 8.4±1.8 | 8.7±2.4 |
| SSA22-SPIRE295 | 334.556900824868 | 0.254513895064679 | 21.1±2.3 | 22.0±1.9 | 11.4±2.0 |
| SSA22-SPIRE296 | 334.3950153178788 | 0.5172654198850305 | 20.5±2.2 | 18.1±1.7 | 10.7±2.1 |
| SSA22-SPIRE297 | 334.54214911847487 | 0.26493449469356833 | 19.4±2.1 | 17.6±1.9 | 13.4±2.1 |
| SSA22-SPIRE298 | 334.5808022042657 | 0.46799629346487903 | 19.0±2.1 | 12.9±1.6 | 2.2±2.1 |
| SSA22-SPIRE299 | 334.56128734914785 | 0.5927535076691385 | 21.0±2.3 | 25.2±1.9 | 17.1±2.3 |
| SSA22-SPIRE300 | 334.3386011881636 | 0.5550909989198349 | 20.3±2.2 | 16.4±2.0 | 9.4±2.2 |
| SSA22-SPIRE301 | 334.59720210002985 | 0.444399024637839 | 19.0±2.1 | 29.7±1.9 | 21.6±2.1 |
| SSA22-SPIRE302 | 334.2254017020133 | 0.19800251515951992 | 20.5±2.2 | 18.4±1.8 | 5.9±2.1 |
| SSA22-SPIRE303 | 334.22691780259385 | 0.34394119776103355 | 22.4±2.5 | 23.4±1.8 | 13.2±2.2 |
| SSA22-SPIRE304 | 334.3123977370562 | 0.41113795891501603 | 22.3±2.5 | 20.1±1.8 | 13.7±2.1 |
| SSA22-SPIRE305 | 334.28931874707285 | 0.32413447268603174 | 20.7±2.3 | 15.9±1.6 | 8.6±2.0 |
| SSA22-SPIRE306 | 334.3891194660002 | 0.33629909943802355 | 20.2±2.2 | 14.8±1.9 | 3.9±2.1 |
| SSA22-SPIRE307 | 334.7401163465271 | 0.4580144702215775 | 20.7±2.3 | 15.6±2.1 | 8.9±2.2 |
| SSA22-SPIRE308 | 334.3643244636881 | 0.24142397062487375 | 19.3±2.1 | 9.8±1.8 | 6.9±2.1 |
| SSA22-SPIRE309 | 334.37016695448415 | 0.6554217379204682 | 19.2±2.1 | 23.5±1.9 | 10.0±2.1 |
| SSA22-SPIRE310 | 334.3654500601511 | 0.5524852333436847 | 21.8±2.4 | 7.3±1.9 | 2.1±2.2 |
| SSA22-SPIRE311 | 334.42193958723504 | 0.052587504478533345 | 21.1±2.4 | 15.8±1.9 | 14.2±2.2 |
| SSA22-SPIRE312 | 334.2698095643515 | 0.6202228477742817 | 20.4±2.3 | 25.4±1.8 | 13.9±2.3 |
| SSA22-SPIRE313 | 334.3915756963511 | 0.23006767192809138 | 19.8±2.2 | 31.7±2.1 | 16.1±2.1 |
| SSA22-SPIRE314 | 334.45896174928953 | 0.3711029947434112 | 20.7±2.3 | 17.1±1.9 | 5.9±2.1 |
| SSA22-SPIRE315 | 334.3805143422246 | 0.3335611300120771 | 21.0±2.4 | 8.7±2.0 | 1.8±2.0 |
| SSA22-SPIRE316 | 334.5997027248518 | 0.4684272367163788 | 20.1±2.3 | 16.3±1.7 | 11.2±2.1 |
| SSA22-SPIRE317 | 334.1815140914588 | 0.24693295500630683 | 19.9±2.3 | 20.5±1.9 | 14.7±2.1 |
| SSA22-SPIRE318 | 334.63070194683394 | 0.5407288735994193 | 19.7±2.2 | 9.6±1.8 | 0.0±2.1 |
| SSA22-SPIRE319 | 334.40004564020353 | 0.5991228987948153 | 20.0±2.3 | 15.1±1.9 | 1.3±2.1 |
| SSA22-SPIRE320 | 334.69985325537704 | 0.5061826933141778 | 20.4±2.3 | 17.2±2.0 | 8.9±2.1 |
| SSA22-SPIRE321 | 334.23330445797103 | 0.33023204145592877 | 25.0±2.9 | 14.5±1.9 | 0.0±2.3 |
| SSA22-SPIRE322 | 334.4784328171711 | 0.49972770909079284 | 18.0±2.1 | 10.8±2.0 | 0.0±2.0 |
| SSA22-SPIRE323 | 334.6857380059234 | 0.47241550429869006 | 20.2±2.3 | 23.3±1.9 | 19.9±2.2 |
| SSA22-SPIRE324 | 334.6217265657504 | 0.3181794489594713 | 18.9±2.2 | 25.7±1.7 | 13.9±2.2 |
| SSA22-SPIRE325 | 334.18289229209813 | 0.27425299214545973 | 19.1±2.2 | 19.7±1.9 | 18.4±2.2 |
| SSA22-SPIRE326 | 334.42961283007463 | 0.14941486490570804 | 20.6±2.4 | 10.9±1.8 | 11.4±2.1 |
| SSA22-SPIRE327 | 334.2893037257142 | 0.42286811407532576 | 22.9±2.6 | 14.7±1.8 | 1.1±2.3 |
| SSA22-SPIRE328 | 334.3285325389057 | 0.33885609304070197 | 19.7±2.3 | 18.6±1.8 | 28.1±2.2 |
| SSA22-SPIRE329 | 334.24819404593256 | 0.38810198301893123 | 18.6±2.2 | 5.8±1.9 | 1.1±2.0 |
| SSA22-SPIRE330 | 334.1208571652619 | 0.3943614291432219 | 20.3±2.4 | 15.0±1.8 | 0.0±2.2 |
| SSA22-SPIRE331 | 334.5380565316497 | 0.5412383881928761 | 18.1±2.1 | 9.0±1.8 | 4.5±2.3 |
| SSA22-SPIRE332 | 334.4307948037288 | 0.20921951111287873 | 18.7±2.2 | 24.1±1.8 | 21.5±2.2 |
| SSA22-SPIRE333 | 334.3392953348331 | 0.14419539144777038 | 18.7±2.2 | 22.0±1.9 | 17.3±2.2 |
| SSA22-SPIRE334 | 334.2746513134086 | 0.48155672481615125 | 18.1±2.1 | 14.1±1.8 | 12.0±2.0 |
| SSA22-SPIRE335 | 334.39800162937917 | 0.16408032650000495 | 22.1±2.6 | 19.2±1.9 | 5.6±2.1 |
| SSA22-SPIRE336 | 334.4718896022783 | 0.4249965896660705 | 19.0±2.2 | 8.9±1.8 | 2.6±2.2 |
| SSA22-SPIRE337 | 334.50754738352407 | 0.5138362426645172 | 18.6±2.2 | 14.1±1.7 | 0.0±2.1 |
| SSA22-SPIRE338 | 334.52578486396277 | 0.259721598253632 | 21.9±2.6 | 17.8±1.9 | 7.4±2.3 |
| SSA22-SPIRE339 | 334.4543512839912 | 0.3582840322866202 | 19.6±2.3 | 4.3±1.9 | 0.0±2.1 |
| SSA22-SPIRE340 | 334.569809846071 | 0.4346701307748476 | 17.3±2.1 | 8.7±1.7 | 0.0±2.2 |
| SSA22-SPIRE341 | 334.25385300938586 | 0.5585917879488647 | 20.3±2.4 | 30.1±1.9 | 30.2±2.4 |
| SSA22-SPIRE342 | 334.3849028336227 | 0.6329925010898872 | 18.0±2.1 | 6.9±1.9 | 0.0±2.2 |

Table A.8: SPIRE sources catalogue of 2QZCluster field.

| ID[1] | R.A.[2] (J2000) | Dec.[3] (J2000) | $S_{250}$[4] (mJy) | $S_{350}$[5] (mJy) | $S_{500}$[6] (mJy) |
|---|---|---|---|---|---|
| SSA22-SPIRE343 | 334.234829100636 | 0.3678937435151981 | 18.2±2.2 | 24.8±1.9 | 24.3±2.1 |
| SSA22-SPIRE344 | 334.6836135300965 | 0.3601381876648053 | 19.3±2.3 | 1.0±1.9 | 0.0±2.2 |
| SSA22-SPIRE345 | 334.18386621441505 | 0.5095300201456046 | 17.8±2.1 | 16.6±1.8 | 10.3±2.5 |
| SSA22-SPIRE346 | 334.62622278681243 | 0.44387320311882966 | 18.3±2.2 | 24.4±1.9 | 9.0±2.0 |
| SSA22-SPIRE347 | 334.42067910537384 | 0.6480029743243073 | 19.1±2.3 | 12.9±1.8 | 2.4±2.2 |
| SSA22-SPIRE348 | 334.613411331921 | 0.45263900063251916 | 18.0±2.2 | 24.0±1.7 | 13.6±2.0 |
| SSA22-SPIRE349 | 334.53480563447147 | 0.31601295086211356 | 19.0±2.3 | 18.8±1.8 | 18.0±2.2 |
| SSA22-SPIRE350 | 334.3787392586509 | 0.0765064006944189 | 19.4±2.3 | 11.5±1.7 | 10.6±2.0 |
| SSA22-SPIRE351 | 334.53547985723117 | 0.586231880896037 | 17.4±2.1 | 19.4±1.8 | 15.2±2.3 |
| SSA22-SPIRE352 | 334.37914316224146 | 0.31979072844986506 | 18.6±2.2 | 14.3±1.8 | 7.3±2.3 |
| SSA22-SPIRE353 | 334.20443240807043 | 0.5884755100318009 | 20.2±2.4 | 14.3±2.0 | 6.6±2.4 |
| SSA22-SPIRE354 | 334.63743985893865 | 0.30999198846231496 | 18.1±2.2 | 16.7±1.8 | 15.3±2.5 |
| SSA22-SPIRE355 | 334.2077800080186 | 0.21102970354364217 | 17.3±2.1 | 16.5±1.7 | 13.9±2.0 |
| SSA22-SPIRE356 | 334.69702591672154 | 0.44437424513357915 | 19.6±2.4 | 13.7±1.7 | 6.5±2.1 |
| SSA22-SPIRE357 | 334.1663220372652 | 0.1731547203021038 | 19.7±2.4 | 13.4±1.8 | 10.3±2.3 |
| SSA22-SPIRE358 | 334.5105220571564 | 0.4945476058876593 | 18.2±2.2 | 13.3±1.8 | 0.5±2.1 |
| SSA22-SPIRE359 | 334.19733582909333 | 0.18483175881029262 | 18.4±2.2 | 26.3±1.7 | 8.2±2.4 |
| SSA22-SPIRE360 | 334.40442320968856 | 0.3057630996579073 | 18.2±2.2 | 30.3±1.8 | 24.2±2.3 |
| SSA22-SPIRE361 | 334.13530160221484 | 0.3977878802268622 | 17.9±2.2 | 15.6±1.8 | 20.3±2.2 |
| SSA22-SPIRE362 | 334.10863765145695 | 0.3468946385287244 | 17.7±2.2 | 18.0±1.9 | 12.1±2.1 |
| SSA22-SPIRE363 | 334.3331622621108 | 0.5789319618053831 | 16.9±2.1 | 17.7±1.7 | 13.3±2.1 |
| SSA22-SPIRE364 | 334.6913420349737 | 0.35085070938591345 | 21.2±2.6 | 26.9±1.8 | 19.6±2.2 |
| SSA22-SPIRE365 | 334.657595480927 | 0.5306473922465786 | 18.2±2.2 | 14.2±1.9 | 3.7±2.2 |
| SSA22-SPIRE366 | 334.1256328644733 | 0.21649891993305556 | 18.1±2.2 | 14.6±1.8 | 8.7±2.2 |
| SSA22-SPIRE367 | 334.1246560677858 | 0.3486892021457336 | 17.8±2.2 | 15.5±2.0 | 5.9±2.2 |
| SSA22-SPIRE368 | 334.7438720178419 | 0.4687270366453854 | 18.5±2.3 | 11.7±1.9 | 1.5±2.4 |
| SSA22-SPIRE369 | 334.1599644520173 | 0.40320101296658434 | 18.5±2.3 | 18.5±1.8 | 9.4±2.3 |
| SSA22-SPIRE370 | 334.3446487716635 | 0.5929093883015212 | 17.7±2.2 | 18.4±1.7 | 9.6±2.1 |
| SSA22-SPIRE371 | 334.55336627160466 | 0.5154048131726046 | 18.7±2.3 | 19.8±1.8 | 9.7±2.1 |
| SSA22-SPIRE372 | 334.1958581332435 | 0.4520053392377362 | 19.2±2.4 | 14.0±1.8 | 0.0±2.2 |
| SSA22-SPIRE373 | 334.3792498280392 | 0.6519273614715104 | 17.4±2.2 | 7.1±2.0 | 1.7±2.2 |
| SSA22-SPIRE374 | 334.54272039013705 | 0.199898367164837 | 18.3±2.3 | 14.1±1.7 | 1.8±2.1 |
| SSA22-SPIRE375 | 334.1438906496083 | 0.38293567856951527 | 19.4±2.4 | 23.3±1.9 | 20.8±2.2 |
| SSA22-SPIRE376 | 334.4000947523159 | 0.5404469450953286 | 16.5±2.1 | 15.8±1.8 | 7.4±2.1 |
| SSA22-SPIRE377 | 334.62250050534396 | 0.4089130408363089 | 18.5±2.3 | 3.6±1.9 | 0.8±2.2 |
| SSA22-SPIRE378 | 334.4259457257346 | 0.3685784473662933 | 17.4±2.2 | 18.2±1.7 | 11.5±2.0 |
| SSA22-SPIRE379 | 334.4922199915053 | 0.14092699121929975 | 18.4±2.3 | 5.7±1.8 | 0.0±2.1 |
| SSA22-SPIRE380 | 334.37363809383857 | 0.6675041107635064 | 17.2±2.2 | 7.1±1.7 | 3.4±2.1 |
| SSA22-SPIRE381 | 334.2634829615406 | 0.17223590857025534 | 18.4±2.3 | 21.8±1.9 | 13.4±2.0 |
| SSA22-SPIRE382 | 334.36945315508586 | 0.12799836401213321 | 18.1±2.3 | 18.0±1.8 | 15.5±2.2 |
| SSA22-SPIRE383 | 334.5394793405797 | 0.4956592881775439 | 18.5±2.3 | 9.4±1.9 | 0.0±2.2 |
| SSA22-SPIRE384 | 334.2185499296076 | 0.45113328647783707 | 19.4±2.4 | 5.3±1.6 | 6.0±2.3 |
| SSA22-SPIRE385 | 334.10630666514703 | 0.2980790580435267 | 20.3±2.6 | 20.9±1.8 | 11.1±2.2 |
| SSA22-SPIRE386 | 334.4469770447859 | 0.4075628501862815 | 16.7±2.1 | 21.1±1.8 | 11.7±2.0 |
| SSA22-SPIRE387 | 334.4040159138834 | 0.06142966182487461 | 18.6±2.4 | 27.9±1.9 | 23.1±2.4 |
| SSA22-SPIRE388 | 334.40714977611054 | 0.6332526105756809 | 17.7±2.3 | 4.8±1.9 | 0.1±2.2 |
| SSA22-SPIRE389 | 334.6855173931013 | 0.31895480458084197 | 17.9±2.3 | 18.4±1.8 | 7.8±2.2 |
| SSA22-SPIRE390 | 334.30328321936946 | 0.14335837798499645 | 16.9±2.2 | 12.3±1.8 | 3.7±2.2 |
| SSA22-SPIRE391 | 334.23394162587124 | 0.18174910773175998 | 16.8±2.2 | 7.3±1.8 | 1.8±2.3 |
| SSA22-SPIRE392 | 334.46316764663965 | 0.5764241375396091 | 16.6±2.1 | 14.5±1.8 | 1.0±2.1 |
| SSA22-SPIRE393 | 334.50801983903443 | 0.13251782815752136 | 16.6±2.1 | 21.5±1.9 | 14.2±2.1 |
| SSA22-SPIRE394 | 334.31248850469854 | 0.1998498531353794 | 18.7±2.4 | 17.7±1.8 | 16.4±2.2 |
| SSA22-SPIRE395 | 334.2807637333553 | 0.21879354092725947 | 20.7±2.7 | 19.1±1.8 | 11.4±2.2 |
| SSA22-SPIRE396 | 334.2178427473951 | 0.2289067633889885 | 16.8±2.2 | 28.0±1.8 | 24.7±2.2 |
| SSA22-SPIRE397 | 334.4151190929765 | 0.6046400993981161 | 17.4±2.2 | 11.1±1.8 | 6.3±2.2 |
| SSA22-SPIRE398 | 334.1404604196384 | 0.40398259512171747 | 17.3±2.2 | 22.6±1.8 | 11.6±2.3 |
| SSA22-SPIRE399 | 334.3449989666648 | 0.24086629839035514 | 16.7±2.2 | 10.3±1.9 | 11.6±2.0 |
| SSA22-SPIRE400 | 334.22927749946075 | 0.5927669286579482 | 17.0±2.2 | 25.6±1.8 | 13.3±2.4 |
| SSA22-SPIRE401 | 334.6478220704281 | 0.31538661367071386 | 17.1±2.2 | 6.8±1.8 | 0.0±2.1 |
| SSA22-SPIRE402 | 334.44221908418154 | 0.19114284390061573 | 16.7±2.2 | 24.4±1.9 | 11.5±2.2 |
| SSA22-SPIRE403 | 334.5438178870068 | 0.3677744389803693 | 17.6±2.3 | 4.5±1.8 | 2.9±2.0 |
| SSA22-SPIRE404 | 334.5030284252964 | 0.47610582281218444 | 16.8±2.2 | 13.5±1.8 | 1.2±2.3 |
| SSA22-SPIRE405 | 334.04758446946914 | 0.22732152569772032 | 17.1±2.2 | 6.8±1.9 | 9.4±2.2 |
| SSA22-SPIRE406 | 334.4370475351623 | 0.20190880365750022 | 16.1±2.1 | 7.3±1.9 | 0.0±2.1 |
| SSA22-SPIRE407 | 334.4251158067288 | 0.6271579014410057 | 16.3±2.1 | 5.0±1.9 | 0.0±2.2 |
| SSA22-SPIRE408 | 334.69491780295215 | 0.48260433178771367 | 17.1±2.2 | 11.4±1.9 | 3.8±2.4 |
| SSA22-SPIRE409 | 334.3066640657022 | 0.46226730057366533 | 19.1±2.5 | 2.9±1.9 | 0.0±2.3 |
| SSA22-SPIRE410 | 334.2412265981277 | 0.41675667253379745 | 17.0±2.2 | 25.0±1.7 | 30.0±2.1 |
| SSA22-SPIRE411 | 334.44694373473413 | 0.17928414097931963 | 16.5±2.2 | 10.2±1.8 | 4.7±2.4 |
| SSA22-SPIRE412 | 334.6213273482786 | 0.2253086078567393 | 17.4±2.3 | 10.1±1.9 | 3.3±2.2 |
| SSA22-SPIRE413 | 334.4861830137655 | 0.5962408335621321 | 17.4±2.3 | 23.1±2.1 | 20.7±2.2 |
| SSA22-SPIRE414 | 334.2659882208496 | 0.6911763540146921 | 17.9±2.4 | 15.5±2.1 | 9.2±2.6 |
| SSA22-SPIRE415 | 334.2894431959571 | 0.22593115373477862 | 18.9±2.5 | 5.2±1.8 | 0.0±2.3 |
| SSA22-SPIRE416 | 334.18768098652566 | 0.5248681911325953 | 16.8±2.2 | 7.3±1.9 | 0.0±2.2 |
| SSA22-SPIRE417 | 334.26259162078054 | 0.2025894019277201 | 17.8±2.4 | 11.9±1.8 | 0.9±2.4 |
| SSA22-SPIRE418 | 334.3588461384398 | 0.38317872471944153 | 17.2±2.3 | 8.7±1.8 | 8.2±2.3 |

Table A.8: SPIRE sources catalogue of 2QZCluster field.

| ID[1] | R.A.[2] (J2000) | Dec.[3] (J2000) | $S_{250}$[4] (mJy) | $S_{350}$[5] (mJy) | $S_{500}$[6] (mJy) |
|---|---|---|---|---|---|
| SSA22-SPIRE419 | 334.43919532037813 | 0.3089221725670777 | 17.0±2.3 | 6.9±1.9 | 9.1±2.1 |
| SSA22-SPIRE420 | 334.28741622331404 | 0.4813734413084476 | 16.9±2.2 | 12.9±1.9 | 7.3±2.2 |
| SSA22-SPIRE421 | 334.41709465976624 | 0.40497561138196325 | 17.4±2.3 | 23.4±1.7 | 12.1±2.3 |
| SSA22-SPIRE422 | 334.55462298978574 | 0.5677657523754517 | 15.6±2.1 | 4.1±1.8 | 0.0±2.2 |
| SSA22-SPIRE423 | 334.55939346205435 | 0.347081546933012 | 17.5±2.3 | 11.6±1.9 | 4.6±2.3 |
| SSA22-SPIRE424 | 334.2083543151611 | 0.41834807206157343 | 17.2±2.3 | 9.2±1.9 | 0.0±2.0 |
| SSA22-SPIRE425 | 334.3540536870753 | 0.09868927107751406 | 18.8±2.5 | 12.5±1.7 | 1.8±2.2 |
| SSA22-SPIRE426 | 334.5206542910307 | 0.14589599270918424 | 16.9±2.3 | 18.7±1.6 | 18.8±2.2 |
| SSA22-SPIRE427 | 334.2358341276901 | 0.6405546750053616 | 18.4±2.5 | 19.5±1.9 | 20.8±2.3 |
| SSA22-SPIRE428 | 334.6522973925839 | 0.2927213496189878 | 17.0±2.3 | 16.1±1.9 | 16.5±2.2 |
| SSA22-SPIRE429 | 334.305687497942 | 0.5401083489339816 | 16.2±2.2 | 15.7±1.7 | 0.0±2.1 |
| SSA22-SPIRE430 | 334.33670055273495 | 0.5069251723521995 | 18.1±2.4 | 9.9±1.8 | 0.2±2.3 |
| SSA22-SPIRE431 | 334.33638569687605 | 0.44494739148931217 | 16.3±2.2 | 17.3±1.9 | 10.1±2.2 |
| SSA22-SPIRE432 | 334.3599951003655 | 0.3511950572851227 | 16.9±2.3 | 19.9±1.8 | 12.9±2.1 |
| SSA22-SPIRE433 | 334.28030315030054 | 0.4869370081491596 | 15.9±2.2 | 0.0±1.8 | 0.0±2.1 |
| SSA22-SPIRE434 | 334.55625872556095 | 0.24259231184479552 | 16.3±2.2 | 33.3±1.9 | 18.9±2.2 |
| SSA22-SPIRE435 | 334.45947647533995 | 0.6409605589438487 | 17.0±2.3 | 7.1±1.9 | 3.9±2.4 |
| SSA22-SPIRE436 | 334.3148347246877 | 0.6661630813285514 | 17.1±2.3 | 10.2±1.9 | 5.5±2.4 |
| SSA22-SPIRE437 | 334.48007911991385 | 0.29072740720616996 | 15.9±2.2 | 15.8±1.7 | 15.9±2.2 |
| SSA22-SPIRE438 | 334.3601902398472 | 0.08918714856857499 | 15.9±2.2 | 9.2±1.9 | 0.0±2.3 |
| SSA22-SPIRE439 | 334.7283924286807 | 0.46555116560511617 | 15.4±2.1 | 14.6±1.9 | 2.9±2.3 |
| SSA22-SPIRE440 | 334.50377091649614 | 0.3663164788206191 | 16.6±2.3 | 17.2±1.7 | 9.9±2.3 |
| SSA22-SPIRE441 | 334.5864886570426 | 0.21539811911593276 | 15.4±2.1 | 21.7±1.8 | 9.4±2.5 |
| SSA22-SPIRE442 | 334.33174937520414 | 0.22411042448541546 | 15.5±2.1 | 16.2±1.7 | 12.5±2.4 |
| SSA22-SPIRE443 | 334.34343067533126 | 0.4266139765450884 | 15.4±2.1 | 15.7±1.7 | 8.6±2.2 |
| SSA22-SPIRE444 | 334.26304308079483 | 0.4325971245488402 | 15.9±2.2 | 22.6±1.8 | 15.8±2.2 |
| SSA22-SPIRE445 | 334.4482541393764 | 0.5690523350096057 | 16.1±2.2 | 15.9±1.7 | 6.5±2.2 |
| SSA22-SPIRE446 | 334.30941084662993 | 0.42183422780943286 | 16.5±2.3 | 9.3±1.8 | 11.2±2.2 |
| SSA22-SPIRE447 | 334.23333697391536 | 0.264806498458423 | 16.9±2.4 | 10.7±1.9 | 2.3±2.2 |
| SSA22-SPIRE448 | 334.6095155034302 | 0.4754561560662736 | 16.1±2.2 | 7.3±1.7 | 0.0±2.1 |
| SSA22-SPIRE449 | 334.41950587661256 | 0.22223692919251062 | 14.5±2.0 | 7.3±1.7 | 0.0±2.1 |
| SSA22-SPIRE450 | 334.4316273127872 | 0.13085900998664549 | 16.5±2.3 | 11.9±1.7 | 0.0±2.1 |
| SSA22-SPIRE451 | 334.3112827947125 | 0.1323266674747156 | 15.2±2.1 | 5.1±1.8 | 6.0±2.3 |
| SSA22-SPIRE452 | 334.3704421109648 | 0.18009532937111783 | 19.4±2.7 | 18.0±1.8 | 15.0±2.1 |
| SSA22-SPIRE453 | 334.20529307431406 | 0.25104415822193216 | 17.4±2.4 | 13.1±1.8 | 7.7±2.1 |
| SSA22-SPIRE454 | 334.33633894493016 | 0.5961713864425641 | 15.4±2.2 | 20.3±1.7 | 9.6±2.0 |
| SSA22-SPIRE455 | 334.272233715514 | 0.441055931809475 | 16.5±2.3 | 8.2±1.8 | 2.0±2.1 |
| SSA22-SPIRE456 | 334.6590684857938 | 0.290436402125955 | 17.2±2.4 | 11.5±1.8 | 3.7±2.5 |
| SSA22-SPIRE457 | 334.1649644957122 | 0.23652402288064855 | 15.3±2.1 | 21.8±1.9 | 14.2±2.1 |
| SSA22-SPIRE458 | 334.60222045474507 | 0.508208207945168 | 15.8±2.2 | 7.8±1.7 | 2.7±2.3 |
| SSA22-SPIRE459 | 334.44373626912056 | 0.30191015283782 07 | 16.4±2.3 | 9.5±1.9 | 2.7±2.2 |
| SSA22-SPIRE460 | 334.3286680964309 | 0.43288261821316065 | 15.8±2.2 | 7.1±1.9 | 0.0±2.1 |
| SSA22-SPIRE461 | 334.4306535632793 | 0.33739073712582285 | 16.1±2.3 | 4.1±1.7 | 0.0±2.4 |
| SSA22-SPIRE462 | 334.29980312897914 | 0.15513519369802625 | 14.2±2.0 | 5.7±1.8 | 6.9±2.0 |
| SSA22-SPIRE463 | 334.4748594794794 | 0.6020824287998899 | 15.9±2.2 | 2.0±1.9 | 0.0±2.2 |
| SSA22-SPIRE464 | 334.35942283260744 | 0.5425077812513804 | 17.7±2.5 | 6.3±1.8 | 1.6±2.3 |
| SSA22-SPIRE465 | 334.73186396985466 | 0.49578584782318874 | 16.1±2.3 | 24.3±2.0 | 18.1±2.2 |
| SSA22-SPIRE466 | 334.2951151179939 | 0.6518975547960724 | 15.5±2.2 | 12.9±1.9 | 12.1±2.3 |
| SSA22-SPIRE467 | 334.29084516911365 | 0.4741397080900095 | 16.2±2.3 | 2.4±1.9 | 10.3±2.2 |
| SSA22-SPIRE468 | 334.4670469966386 | 0.18599134840139514 | 15.5±2.2 | 12.0±1.9 | 2.6±2.0 |
| SSA22-SPIRE469 | 334.20526780744655 | 0.44638893901813426 | 16.3±2.3 | 5.8±1.8 | 5.8±2.1 |
| SSA22-SPIRE470 | 334.42420744151 | 0.65442918991938 | 17.7±2.5 | 3.7±1.9 | 1.3±2.4 |
| SSA22-SPIRE471 | 334.1993374945812 | 0.35074199890239977 | 17.2±2.4 | 10.5±1.7 | 0.6±2.1 |
| SSA22-SPIRE472 | 334.4467316142162 | 0.08557695342331775 | 15.8±2.2 | 13.0±1.8 | 11.2±2.2 |
| SSA22-SPIRE473 | 334.6119404741436 | 0.36194679416946246 | 16.6±2.4 | 23.3±1.6 | 18.3±2.4 |
| SSA22-SPIRE474 | 334.1146206639813 | 0.22286644680889706 | 14.7±2.1 | 8.9±1.8 | 6.1±2.1 |
| SSA22-SPIRE475 | 334.2688118309474 | 0.5175362753885044 | 16.1±2.3 | 10.9±1.8 | 0.0±2.4 |
| SSA22-SPIRE476 | 334.17414051331605 | 0.4754064557029177 | 16.9±2.4 | 16.8±1.8 | 13.4±2.1 |
| SSA22-SPIRE477 | 334.66334446197726 | 0.40233458310701997 | 14.5±2.1 | 18.1±1.7 | 13.3±2.2 |
| SSA22-SPIRE478 | 334.3673736560081 | 0.3403394941507098 | 15.6±2.3 | 5.5±1.9 | 4.4±2.0 |
| SSA22-SPIRE479 | 334.55530965957377 | 0.2948068818240376 | 16.2±2.3 | 11.1±1.7 | 0.0±2.2 |
| SSA22-SPIRE480 | 334.6621847991523 | 0.48975977232383106 | 17.1±2.5 | 14.6±1.8 | 8.8±2.3 |
| SSA22-SPIRE481 | 334.33182976853726 | 0.4900607439640587 | 16.5±2.4 | 4.8±1.8 | 0.7±2.2 |
| SSA22-SPIRE482 | 334.4818747133843 | 0.39298093988733057 | 15.0±2.2 | 1.8±2.0 | 3.4±2.1 |
| SSA22-SPIRE483 | 334.4943500867115 | 0.3135756334573868 | 15.2±2.2 | 14.3±1.7 | 10.3±2.2 |
| SSA22-SPIRE484 | 334.2561481650671 | 0.4607774796930902 | 15.1±2.2 | 9.7±1.7 | 9.2±2.1 |
| SSA22-SPIRE485 | 334.4391451316761 | 0.3275239295663537 | 16.4±2.4 | 17.2±1.9 | 8.0±2.1 |
| SSA22-SPIRE486 | 334.6638367729862 | 0.3011902577105226 | 15.9±2.3 | 13.0±1.9 | 11.4±2.4 |
| SSA22-SPIRE487 | 334.41432746433156 | 0.6570405884925784 | 17.8±2.6 | 11.5±2.0 | 9.3±2.3 |
| SSA22-SPIRE488 | 334.1801076494678 | 0.20519028134380404 | 15.7±2.3 | 20.3±1.8 | 15.1±2.1 |
| SSA22-SPIRE489 | 334.27930387632523 | 0.31685157865649216 | 15.9±2.3 | 22.4±1.8 | 6.0±2.1 |
| SSA22-SPIRE490 | 334.61617778956605 | 0.42661691700147586 | 15.6±2.3 | 20.3±1.9 | 20.2±2.3 |
| SSA22-SPIRE491 | 334.3902436038466 | 0.10194524618570028 | 14.2±2.1 | 16.9±1.7 | 9.9±2.2 |
| SSA22-SPIRE492 | 334.6310632151826 | 0.27027539205861 | 16.8±2.5 | 15.0±1.8 | 12.1±2.3 |
| SSA22-SPIRE493 | 334.27714644266644 | 0.5603252072227881 | 14.5±2.1 | 6.7±1.9 | 3.7±2.3 |
| SSA22-SPIRE494 | 334.5250411656594 | 0.24185760089291583 | 16.0±2.4 | 10.0±1.8 | 3.1±2.3 |

Table A.8: SPIRE sources catalogue of 2QZCluster field.

| ID[1] | R.A.[2] (J2000) | Dec.[3] (J2000) | $S_{250}$[4] (mJy) | $S_{350}$[5] (mJy) | $S_{500}$[6] (mJy) |
|---|---|---|---|---|---|
| SSA22-SPIRE495 | 334.4788429175537 | 0.2849155318764119 | 14.5±2.2 | 15.8±1.8 | 8.7±2.1 |
| SSA22-SPIRE496 | 334.6345930224202 | 0.37846528937872775 | 15.0±2.2 | 13.8±1.8 | 18.9±2.2 |
| SSA22-SPIRE497 | 334.2451649402795 | 0.28654718589978617 | 15.3±2.3 | 4.4±2.0 | 3.7±2.0 |
| SSA22-SPIRE498 | 334.3135454504068 | 0.45543657106567365 | 15.6±2.3 | 15.8±1.8 | 8.7±2.3 |
| SSA22-SPIRE499 | 334.1260099061218 | 0.36598443542260034 | 15.4±2.3 | 19.7±1.8 | 5.6±2.3 |
| SSA22-SPIRE500 | 334.49973091971447 | 0.3541160214909132 | 14.9±2.2 | 17.8±1.8 | 10.8±2.1 |
| SSA22-SPIRE501 | 334.558610694119 | 0.5371079137634046 | 15.8±2.4 | 23.4±1.9 | 18.1±2.2 |
| SSA22-SPIRE502 | 334.3150419065522 | 0.5474352022642756 | 14.7±2.2 | 11.8±1.7 | 7.3±2.3 |
| SSA22-SPIRE503 | 334.64649223465 | 0.2842952369883467 | 15.3±2.3 | 4.3±1.9 | 4.6±2.2 |
| SSA22-SPIRE504 | 334.36539645092137 | 0.14429949898366456 | 15.7±2.3 | 14.5±1.7 | 11.6±2.0 |
| SSA22-SPIRE505 | 334.13418435562 | 0.4224454751916438 | 15.0±2.2 | 6.3±1.8 | 8.9±2.3 |
| SSA22-SPIRE506 | 334.1764571120003 | 0.3359083033581151 | 14.0±2.1 | 4.9±1.7 | 3.2±2.1 |
| SSA22-SPIRE507 | 334.60075046001316 | 0.30223663852556215 | 14.3±2.1 | 5.9±1.8 | 2.7±2.3 |
| SSA22-SPIRE508 | 334.6909292631965 | 0.41773910457056007 | 14.1±2.1 | 4.3±1.7 | 1.2±2.1 |
| SSA22-SPIRE509 | 334.2313494881642 | 0.3168352277189254 | 15.5±2.3 | 13.1±1.8 | 3.5±2.2 |
| SSA22-SPIRE510 | 334.39595223775177 | 0.11231287177366092 | 13.7±2.1 | 6.9±1.8 | 0.5±2.0 |
| SSA22-SPIRE511 | 334.32865572866 | 0.19214524055630727 | 14.3±2.2 | 5.2±1.7 | 4.5±2.0 |
| SSA22-SPIRE512 | 334.19824617286866 | 0.39840190832381894 | 14.2±2.1 | 23.9±1.8 | 11.1±2.2 |
| SSA22-SPIRE513 | 334.30660856004954 | 0.697472046366028 | 15.3±2.3 | 15.6±1.8 | 10.2±2.2 |
| SSA22-SPIRE514 | 334.62120283582317 | 0.4727857239188639 | 14.2±2.2 | 10.6±1.8 | 1.5±2.2 |
| SSA22-SPIRE515 | 334.4418297010263 | 0.5429754776626786 | 14.9±2.3 | 9.1±1.7 | 4.4±2.3 |
| SSA22-SPIRE516 | 334.2448241104956 | 0.31053665298588246 | 15.5±2.4 | 10.5±1.8 | 7.0±2.3 |
| SSA22-SPIRE517 | 334.14129850456413 | 0.35884983512630636 | 16.1±2.5 | 15.8±1.7 | 5.8±2.4 |
| SSA22-SPIRE518 | 334.49058500738437 | 0.16263654470634129 | 14.4±2.2 | 4.9±1.8 | 2.4±2.3 |
| SSA22-SPIRE519 | 334.05874884555163 | 0.2559089162978464 | 14.6±2.2 | 10.7±1.9 | 6.7±2.3 |
| SSA22-SPIRE520 | 334.53667361368724 | 0.26900359198727225 | 14.3±2.2 | 9.0±1.9 | 1.7±2.2 |
| SSA22-SPIRE521 | 334.1926556428607 | 0.42077470045601534 | 14.0±2.1 | 13.2±1.8 | 0.7±2.1 |
| SSA22-SPIRE522 | 334.1304523303541 | 0.19237068996643092 | 14.2±2.2 | 21.9±1.8 | 7.7±2.4 |
| SSA22-SPIRE523 | 334.5109018212088 | 0.5442991101758813 | 15.5±2.4 | 8.3±1.7 | 0.0±2.2 |
| SSA22-SPIRE524 | 334.20797633700795 | 0.43135713217934646 | 15.8±2.4 | 13.4±1.7 | 2.9±2.2 |
| SSA22-SPIRE525 | 334.29482027736117 | 0.5992479083405639 | 14.8±2.3 | 13.3±1.7 | 3.4±2.2 |
| SSA22-SPIRE526 | 334.53102864177964 | 0.5553661004724288 | 13.9±2.1 | 7.7±1.8 | 3.2±2.1 |
| SSA22-SPIRE527 | 334.4412090075895 | 0.4018136800106649 | 13.6±2.1 | 0.0±1.7 | 5.1±2.2 |
| SSA22-SPIRE528 | 334.35275408902146 | 0.6826158999078871 | 15.8±2.5 | 12.3±2.0 | 9.6±2.3 |
| SSA22-SPIRE529 | 334.1673180482023 | 0.19913573642493335 | 15.3±2.4 | 14.2±1.8 | 1.2±2.3 |
| SSA22-SPIRE530 | 334.2514074301019 | 0.6269730152834535 | 14.3±2.2 | 6.7±1.7 | 2.6±2.4 |
| SSA22-SPIRE531 | 334.1644682493926 | 0.4243305081397475 | 14.4±2.2 | 11.3±1.9 | 12.6±2.2 |
| SSA22-SPIRE532 | 334.12669270717197 | 0.4163992182804598 | 14.5±2.3 | 0.0±1.9 | 0.0±2.2 |
| SSA22-SPIRE533 | 334.1918549503418 | 0.24737610831927764 | 15.9±2.5 | 8.7±1.7 | 0.8±2.3 |
| SSA22-SPIRE534 | 334.32854524835477 | 0.3958130477636632 | 14.5±2.3 | 12.9±1.6 | 1.7±2.2 |
| SSA22-SPIRE535 | 334.4588155046812 | 0.1567535367102567 | 14.2±2.2 | 19.3±1.9 | 11.2±2.3 |
| SSA22-SPIRE536 | 334.7117601969682 | 0.3564968582581304 | 14.5±2.3 | 11.3±1.8 | 4.6±2.4 |
| SSA22-SPIRE537 | 334.4163393095319 | 0.639800855160064 | 13.6±2.1 | 10.1±1.9 | 0.0±2.2 |
| SSA22-SPIRE538 | 334.24417423552114 | 0.5749336625317986 | 13.5±2.1 | 9.6±2.1 | 12.2±2.1 |
| SSA22-SPIRE539 | 334.2525665145726 | 0.4879967943492369 | 13.7±2.2 | 8.0±1.9 | 0.0±2.3 |
| SSA22-SPIRE540 | 334.4619685477293 | 0.1183584170009199 | 15.0±2.4 | 11.4±1.8 | 0.0±2.0 |
| SSA22-SPIRE541 | 334.4040360151863 | 0.6236972927087795 | 14.8±2.3 | 16.3±1.8 | 13.4±2.3 |
| SSA22-SPIRE542 | 334.1340837709863 | 0.2415123315697641 | 13.0±2.1 | 13.3±1.7 | 7.9±2.0 |
| SSA22-SPIRE543 | 334.30609255324094 | 0.32371483963031 | 13.7±2.2 | 18.4±1.9 | 22.4±2.2 |
| SSA22-SPIRE544 | 334.4620299670457 | 0.13106749419871852 | 15.8±2.5 | 24.8±1.8 | 13.0±2.2 |
| SSA22-SPIRE545 | 334.358866665735 | 0.4704665953573043 | 14.5±2.3 | 10.1±1.6 | 0.0±2.3 |
| SSA22-SPIRE546 | 334.31904811570257 | 0.32027818592041785 | 14.2±2.3 | 11.4±1.9 | 7.4±2.2 |
| SSA22-SPIRE547 | 334.6066913886979 | 0.2551521129235171 | 13.2±2.1 | 13.3±1.7 | 8.4±2.4 |
| SSA22-SPIRE548 | 334.31278790074924 | 0.6215450495100481 | 14.4±2.3 | 0.0±1.7 | 0.0±2.3 |
| SSA22-SPIRE549 | 334.3888902273649 | 0.3809016059125342 | 15.2±2.4 | 15.9±1.8 | 7.2±2.1 |
| SSA22-SPIRE550 | 334.67773156389575 | 0.49290589106041566 | 14.3±2.3 | 10.2±1.8 | 0.0±2.4 |
| SSA22-SPIRE551 | 334.54790035920286 | 0.582912169290803 | 12.9±2.1 | 7.5±1.8 | 0.0±2.1 |
| SSA22-SPIRE552 | 334.3372219508791 | 0.30836776763108653 | 14.1±2.3 | 1.3±1.9 | 0.0±2.2 |
| SSA22-SPIRE553 | 334.5706201373252 | 0.29593320452449773 | 14.7±2.4 | 8.9±1.8 | 18.0±2.3 |
| SSA22-SPIRE554 | 334.59518706568053 | 0.49274753993115133 | 14.7±2.4 | 14.5±1.7 | 6.9±2.2 |
| SSA22-SPIRE555 | 334.4440100589277 | 0.44408388303789137 | 14.9±2.4 | 11.7±1.9 | 5.7±2.1 |
| SSA22-SPIRE556 | 334.48076886641445 | 0.13915737425936883 | 15.1±2.4 | 21.4±1.9 | 14.8±2.3 |
| SSA22-SPIRE557 | 334.6275149181289 | 0.42413064935409917 | 13.9±2.2 | 1.7±1.9 | 0.0±2.3 |
| SSA22-SPIRE558 | 334.1564580979003 | 0.3460198822216086 | 12.9±2.1 | 3.3±1.8 | 0.9±2.2 |
| SSA22-SPIRE559 | 334.328305474672 | 0.25022607025768884 | 13.8±2.2 | 14.7±1.8 | 1.6±2.1 |
| SSA22-SPIRE560 | 334.5151826568796 | 0.5842848512776043 | 15.0±2.4 | 4.7±1.7 | 5.2±2.2 |
| SSA22-SPIRE561 | 334.29775143257103 | 0.48444674841806934 | 13.6±2.2 | 15.1±1.8 | 7.5±2.1 |
| SSA22-SPIRE562 | 334.7086618550108 | 0.4563981723946564 | 14.3±2.3 | 11.4±1.8 | 5.1±2.1 |
| SSA22-SPIRE563 | 334.3950878328938 | 0.6420175671399563 | 13.1±2.1 | 18.1±2.0 | 16.2±2.2 |
| SSA22-SPIRE564 | 334.1291747142277 | 0.3481090423627161 | 13.4±2.2 | 13.6±1.9 | 5.7±2.1 |
| SSA22-SPIRE565 | 334.4045834926907 | 0.5110175928643532 | 13.2±2.2 | 3.2±1.8 | 5.2±2.2 |
| SSA22-SPIRE566 | 334.4274597918637 | 0.08589511523020527 | 16.3±2.7 | 11.3±1.8 | 9.3±2.3 |
| SSA22-SPIRE567 | 334.2426864360744 | 0.21866163237903585 | 13.5±2.2 | 8.4±1.8 | 0.0±2.1 |
| SSA22-SPIRE568 | 334.2565834507684 | 0.3307629731283852 | 15.2±2.5 | 13.3±1.7 | 9.9±2.3 |
| SSA22-SPIRE569 | 334.62868765748965 | 0.38994952187080917 | 14.6±2.4 | 8.8±1.7 | 3.1±2.1 |
| SSA22-SPIRE570 | 334.3767700289332 | 0.632359976038 | 13.3±2.2 | 3.5±1.8 | 0.0±2.5 |

Table A.8: SPIRE sources catalogue of 2QZCluster field.

| ID[1] | R.A.[2] (J2000) | Dec.[3] (J2000) | $S_{250}$[4] (mJy) | $S_{350}$[5] (mJy) | $S_{500}$[6] (mJy) |
|---|---|---|---|---|---|
| SSA22-SPIRE571 | 334.3422623775726 | 0.6544369001380174 | 14.3±2.4 | 12.8±1.8 | 9.8±2.2 |
| SSA22-SPIRE572 | 334.3018068847733 | 0.5520398350248041 | 12.9±2.1 | 4.5±1.8 | 0.0±2.2 |
| SSA22-SPIRE573 | 334.38393050246583 | 0.12771569001943422 | 13.1±2.2 | 12.3±1.9 | 10.5±2.2 |
| SSA22-SPIRE574 | 334.72476929706255 | 0.391163024185624 | 13.5±2.2 | 8.1±2.0 | 2.0±2.1 |
| SSA22-SPIRE575 | 334.20787308199004 | 0.4543759586827882 | 15.0±2.5 | 17.7±1.8 | 12.9±2.1 |
| SSA22-SPIRE576 | 334.50121414716415 | 0.26010092870964313 | 12.7±2.1 | 7.0±1.8 | 0.0±2.4 |
| SSA22-SPIRE577 | 334.3532347731767 | 0.44248260218602387 | 12.4±2.1 | 8.8±1.7 | 0.0±2.1 |
| SSA22-SPIRE578 | 334.2539708848391 | 0.21719514557773845 | 13.3±2.2 | 5.7±1.7 | 2.6±2.4 |
| SSA22-SPIRE579 | 334.280725829254 | 0.6613904803509686 | 13.6±2.3 | 14.4±1.9 | 7.5±2.3 |
| SSA22-SPIRE580 | 334.50451419966794 | 0.42562801156439717 | 14.6±2.4 | 8.0±1.7 | 4.1±2.1 |
| SSA22-SPIRE581 | 334.2877941643009 | 0.40814851448017797 | 13.3±2.2 | 6.5±1.8 | 2.4±2.1 |
| SSA22-SPIRE582 | 334.4523858645481 | 0.48918288128358084 | 14.0±2.3 | 2.7±1.8 | 0.0±2.3 |
| SSA22-SPIRE583 | 334.7354661746737 | 0.39160857267365046 | 13.6±2.3 | 10.9±1.9 | 10.3±2.4 |
| SSA22-SPIRE584 | 334.66153251742435 | 0.3497569022926601 | 12.7±2.1 | 17.3±1.8 | 8.4±2.3 |
| SSA22-SPIRE585 | 334.38358177935197 | 0.47614693718087625 | 13.9±2.3 | 4.9±1.7 | 0.0±2.2 |
| SSA22-SPIRE586 | 334.43406286121365 | 0.35336163260641396 | 13.2±2.2 | 18.2±1.8 | 14.4±2.1 |
| SSA22-SPIRE587 | 334.481271690022 | 0.30454851265797783 | 12.5±2.1 | 9.9±1.7 | 5.2±2.1 |
| SSA22-SPIRE588 | 334.5809958618645 | 0.4069091839530742 | 13.7±2.3 | 15.3±1.8 | 0.3±2.3 |
| SSA22-SPIRE589 | 334.3526100237255 | 0.18972228357046947 | 13.6±2.3 | 4.2±1.8 | 1.2±2.2 |
| SSA22-SPIRE590 | 334.49246827936327 | 0.43550338684269707 | 13.2±2.2 | 22.4±1.8 | 18.9±2.1 |
| SSA22-SPIRE591 | 334.69578291312047 | 0.40729417621079017 | 12.7±2.2 | 3.3±1.8 | 0.9±2.2 |
| SSA22-SPIRE592 | 334.6414013194246 | 0.34353821412672353 | 12.8±2.2 | 7.7±1.8 | 3.8±2.1 |
| SSA22-SPIRE593 | 334.26027027823613 | 0.6359161375382208 | 13.1±2.2 | 8.4±1.8 | 2.0±2.2 |
| SSA22-SPIRE594 | 334.4705416682414 | 0.4644907451499131 | 12.9±2.2 | 8.1±1.8 | 3.6±2.2 |
| SSA22-SPIRE595 | 334.38358953833284 | 0.5517220304049335 | 12.8±2.2 | 12.6±1.8 | 7.9±2.2 |
| SSA22-SPIRE596 | 334.05536483834214 | 0.2447095427169325 | 13.9±2.4 | 12.2±1.9 | 8.5±2.2 |
| SSA22-SPIRE597 | 334.48757391975033 | 0.34398331114454594 | 13.9±2.4 | 11.9±1.8 | 0.0±2.3 |
| SSA22-SPIRE598 | 334.23651842086923 | 0.28249711651684606 | 13.3±2.3 | 8.7±1.8 | 0.0±2.2 |
| SSA22-SPIRE599 | 334.59464099627013 | 0.4245687291413499 | 12.5±2.1 | 6.3±1.8 | 0.0±2.4 |
| SSA22-SPIRE600 | 334.5437556358152 | 0.3392133479860648 | 12.7±2.2 | 14.7±1.8 | 10.3±2.4 |
| SSA22-SPIRE601 | 334.1157635428262 | 0.3534362379036504 | 13.1±2.2 | 5.0±1.9 | 1.4±2.0 |
| SSA22-SPIRE602 | 334.22230013080747 | 0.4884425939730719 | 13.3±2.3 | 9.1±1.8 | 3.1±2.2 |
| SSA22-SPIRE603 | 334.65037025811233 | 0.4515547738441176 | 14.0±2.4 | 10.6±1.8 | 0.8±2.2 |
| SSA22-SPIRE604 | 334.3920056316466 | 0.43226350350206605 | 12.6±2.2 | 15.2±2.0 | 20.6±2.1 |
| SSA22-SPIRE605 | 334.3421141164269 | 0.6799139329368231 | 13.0±2.2 | 4.9±2.0 | 0.0±2.2 |
| SSA22-SPIRE606 | 334.34332325420075 | 0.15406360085543286 | 13.3±2.3 | 19.6±1.7 | 9.2±2.2 |
| SSA22-SPIRE607 | 334.7201533463177 | 0.4006421060928195 | 13.2±2.3 | 4.3±1.9 | 0.0±2.3 |
| SSA22-SPIRE608 | 334.41069747898734 | 0.5224425674080866 | 12.5±2.2 | 5.8±1.8 | 0.0±2.1 |
| SSA22-SPIRE609 | 334.4685623736369 | 0.6123572326813215 | 12.6±2.2 | 12.8±2.0 | 15.5±2.2 |
| SSA22-SPIRE610 | 334.3787192329035 | 0.599525076489724 | 13.6±2.4 | 13.9±1.8 | 11.6±2.1 |
| SSA22-SPIRE611 | 334.23938552158035 | 0.15163340339511913 | 12.5±2.2 | 6.0±1.9 | 16.5±2.1 |
| SSA22-SPIRE612 | 334.4612112740702 | 0.6140110550764727 | 12.8±2.2 | 11.5±1.9 | 17.5±2.1 |
| SSA22-SPIRE613 | 334.47664802132175 | 0.1203066497858752 | 14.3±2.5 | 14.2±1.6 | 6.8±2.3 |
| SSA22-SPIRE614 | 334.2950311739614 | 0.14828405759364954 | 12.5±2.2 | 11.4±1.8 | 4.9±2.2 |
| SSA22-SPIRE615 | 334.220573923172 | 0.408920446023983 | 12.2±2.1 | 18.2±1.8 | 5.4±2.0 |
| SSA22-SPIRE616 | 334.30298708459185 | 0.30924328200733725 | 13.4±2.3 | 11.6±1.7 | 0.0±2.2 |
| SSA22-SPIRE617 | 334.2173727097316 | 0.25608142114257987 | 12.8±2.2 | 6.6±1.8 | 1.2±2.3 |
| SSA22-SPIRE618 | 334.2307202112398 | 0.24033006194996157 | 13.0±2.3 | 11.2±1.7 | 2.3±2.2 |
| SSA22-SPIRE619 | 334.5945845851547 | 0.5744564496666805 | 14.7±2.6 | 14.9±2.1 | 5.3±2.5 |
| SSA22-SPIRE620 | 334.5189867486424 | 0.3317164264632873 | 12.1±2.1 | 19.6±1.7 | 15.1±2.0 |
| SSA22-SPIRE621 | 334.6512833356974 | 0.3706425184775063 | 12.5±2.2 | 12.3±1.7 | 8.9±2.0 |
| SSA22-SPIRE622 | 334.5102317611003 | 0.41302278464544784 | 13.1±2.3 | 15.0±1.7 | 5.1±2.1 |
| SSA22-SPIRE623 | 334.36431299673217 | 0.44139484957210484 | 12.4±2.2 | 14.8±1.8 | 11.5±2.0 |
| SSA22-SPIRE624 | 334.2351979222735 | 0.4972674520663925 | 12.9±2.3 | 22.4±1.9 | 8.0±2.2 |
| SSA22-SPIRE625 | 334.65774222212667 | 0.42302718321658583 | 11.9±2.1 | 12.8±1.9 | 4.7±2.1 |
| SSA22-SPIRE626 | 334.3235305792159 | 0.44446055200619106 | 12.5±2.2 | 11.9±1.7 | 1.2±2.4 |
| SSA22-SPIRE627 | 334.7258839172008 | 0.36998989536050125 | 13.2±2.3 | 15.3±1.8 | 11.5±2.6 |
| SSA22-SPIRE628 | 334.4183809154473 | 0.3410198135754659 | 12.7±2.3 | 10.2±1.7 | 5.7±2.2 |
| SSA22-SPIRE629 | 334.4036217238124 | 0.39438713116343005 | 13.5±2.4 | 13.6±1.9 | 1.6±2.3 |
| SSA22-SPIRE630 | 334.29510963691934 | 0.707257286639086 | 13.2±2.3 | 15.1±2.0 | 11.4±2.5 |
| SSA22-SPIRE631 | 334.2784686099547 | 0.6027186627675782 | 12.1±2.2 | 10.4±1.7 | 3.1±2.1 |
| SSA22-SPIRE632 | 334.30538077017303 | 0.28262338277767146 | 13.4±2.4 | 9.7±1.8 | 3.5±2.3 |
| SSA22-SPIRE633 | 334.28413688184304 | 0.5394028090622563 | 14.1±2.5 | 19.8±1.8 | 13.0±2.2 |
| SSA22-SPIRE634 | 334.31184529236594 | 0.5172340619158359 | 12.4±2.2 | 10.1±1.8 | 0.0±2.3 |
| SSA22-SPIRE635 | 334.6649792842616 | 0.4991459579150149 | 12.6±2.3 | 6.5±1.8 | 5.1±2.4 |
| SSA22-SPIRE636 | 334.4369369335861 | 0.10937328901692217 | 12.1±2.2 | 10.9±1.7 | 5.7±2.0 |
| SSA22-SPIRE637 | 334.4513472086358 | 0.27047083340489264 | 12.6±2.3 | 4.9±1.7 | 5.1±2.2 |
| SSA22-SPIRE638 | 334.31900464376764 | 0.6880433412252877 | 12.7±2.3 | 7.9±2.0 | 10.9±2.1 |
| SSA22-SPIRE639 | 334.2183324844446 | 0.24665431489777637 | 13.0±2.3 | 6.3±1.8 | 0.3±2.1 |
| SSA22-SPIRE640 | 334.32955606660175 | 0.6624307695976359 | 12.4±2.2 | 11.9±1.9 | 1.9±2.4 |
| SSA22-SPIRE641 | 334.695950795914 | 0.49628986617873116 | 13.6±2.5 | 11.4±1.9 | 3.7±2.2 |
| SSA22-SPIRE642 | 334.11606962329927 | 0.4069339611555634 | 12.4±2.3 | 24.1±1.9 | 18.5±2.2 |
| SSA22-SPIRE643 | 334.3188776418221 | 0.2729332139857584 | 12.8±2.3 | 11.1±1.7 | 8.2±2.1 |
| SSA22-SPIRE644 | 334.46827604130175 | 0.2465224545910436 | 12.9±2.3 | 20.6±1.7 | 5.8±2.0 |
| SSA22-SPIRE645 | 334.50378825525377 | 0.5429933313601525 | 12.5±2.3 | 7.4±1.8 | 6.8±2.1 |
| SSA22-SPIRE646 | 334.5083347988228 | 0.31264258366344677 | 12.1±2.2 | 8.7±1.8 | 4.9±2.0 |

Table A.8: SPIRE sources catalogue of 2QZCluster field.

| ID[1] | R.A.[2] (J2000) | Dec.[3] (J2000) | $S_{250}$[4] (mJy) | $S_{350}$[5] (mJy) | $S_{500}$[6] (mJy) |
|---|---|---|---|---|---|
| SSA22-SPIRE647 | 334.72601043320395 | 0.3613463227431588 | 14.1±2.6 | 5.6±2.0 | 7.7±2.5 |
| SSA22-SPIRE648 | 334.1772836493689 | 0.39600344759150274 | 12.8±2.3 | 2.8±1.8 | 0.0±2.3 |
| SSA22-SPIRE649 | 334.50057589804334 | 0.14545511054977267 | 12.4±2.3 | 14.0±1.9 | 6.4±2.2 |
| SSA22-SPIRE650 | 334.7100291315308 | 0.39095349778746546 | 14.8±2.7 | 8.8±1.9 | 2.6±2.2 |
| SSA22-SPIRE651 | 334.3575036503603 | 0.344434707422731 | 12.7±2.3 | 20.7±1.9 | 16.3±2.1 |
| SSA22-SPIRE652 | 334.6604996536647 | 0.2804977298992863 | 12.9±2.4 | 16.8±2.0 | 12.9±2.2 |
| SSA22-SPIRE653 | 334.715152250471 | 0.42169507214903545 | 12.4±2.3 | 15.8±1.8 | 4.0±2.4 |
| SSA22-SPIRE654 | 334.2009438268595 | 0.43567259946528697 | 12.8±2.4 | 8.9±1.7 | 4.5±2.2 |
| SSA22-SPIRE655 | 334.5253005688389 | 0.5070399078325806 | 12.5±2.3 | 9.8±1.8 | 4.1±2.5 |
| SSA22-SPIRE656 | 334.41087760073555 | 0.15676277636777922 | 13.0±2.4 | 8.4±1.8 | 0.0±2.0 |
| SSA22-SPIRE657 | 334.50966515920595 | 0.1641992977825809 | 12.7±2.3 | 14.1±1.8 | 5.1±2.0 |
| SSA22-SPIRE658 | 334.4848653312656 | 0.5225120509186243 | 12.2±2.2 | 8.7±1.7 | 12.6±2.1 |
| SSA22-SPIRE659 | 334.1738817057527 | 0.4095001237498779 | 12.7±2.4 | 5.2±1.8 | 3.9±2.3 |
| SSA22-SPIRE660 | 334.3086795616829 | 0.6325753539921674 | 13.2±2.4 | 10.6±1.8 | 5.5±2.1 |
| SSA22-SPIRE661 | 334.4790550127434 | 0.6275264519541572 | 13.1±2.4 | 4.4±2.0 | 6.0±2.4 |
| SSA22-SPIRE662 | 334.31537662702664 | 0.4365360562753683 | 12.7±2.4 | 2.1±1.9 | 3.5±2.2 |
| SSA22-SPIRE663 | 334.4142521779223 | 0.4257035429007088 | 12.5±2.3 | 14.5±1.9 | 9.2±2.1 |
| SSA22-SPIRE664 | 334.2266724690479 | 0.2896962613255827 | 12.3±2.3 | 5.7±1.9 | 0.0±2.1 |
| SSA22-SPIRE665 | 334.6820640045845 | 0.32496499976062222 | 12.8±2.4 | 11.6±1.8 | 16.3±2.2 |
| SSA22-SPIRE666 | 334.2036913722439 | 0.40997150984911235 | 12.0±2.2 | 19.7±1.9 | 12.9±2.0 |
| SSA22-SPIRE667 | 334.3373234406613 | 0.3830487766983032 | 12.6±2.3 | 15.2±1.7 | 9.7±2.2 |
| SSA22-SPIRE668 | 334.3626650983188 | 0.1517286424232382 | 13.5±2.5 | 19.3±1.8 | 16.7±2.2 |
| SSA22-SPIRE669 | 334.3391522160012 | 0.09632666254100988 | 13.2±2.5 | 1.9±1.9 | 0.0±2.2 |
| SSA22-SPIRE670 | 334.7440376868953 | 0.41710974956504 | 12.2±2.3 | 8.0±1.8 | 9.8±2.3 |
| SSA22-SPIRE671 | 334.480774454018 | 0.5426786626539674 | 13.4±2.5 | 29.6±1.7 | 13.0±2.1 |
| SSA22-SPIRE672 | 334.4307513466747 | 0.6380612810356768 | 11.8±2.2 | 17.3±1.9 | 15.4±2.2 |
| SSA22-SPIRE673 | 334.0488305327562 | 0.253167778046107 | 11.6±2.2 | 19.1±1.8 | 15.7±2.4 |
| SSA22-SPIRE674 | 334.4366923984954 | 0.5690148438901299 | 13.0±2.4 | 3.7±1.7 | 0.0±2.0 |
| SSA22-SPIRE675 | 334.66956261282 | 0.43020544420569984 | 10.9±2.1 | 14.4±1.6 | 11.8±2.1 |
| SSA22-SPIRE676 | 334.118410447019 | 0.257447747224852 | 12.2±2.3 | 22.1±1.8 | 15.1±2.0 |
| SSA22-SPIRE677 | 334.44923195108794 | 0.6444010958821557 | 11.9±2.2 | 7.1±2.0 | 13.6±2.4 |
| SSA22-SPIRE678 | 334.22496972717533 | 0.2529070491887176 | 12.4±2.3 | 11.9±1.9 | 11.5±2.1 |
| SSA22-SPIRE679 | 334.6993616355506 | 0.3875177736243527 | 12.0±2.3 | 9.3±1.9 | 5.3±2.4 |
| SSA22-SPIRE680 | 334.30059392366076 | 0.1956980787498092 | 12.8±2.4 | 6.8±1.7 | 3.1±2.1 |
| SSA22-SPIRE681 | 334.36739643071076 | 0.6818106040323657 | 12.2±2.3 | 11.1±1.8 | 0.0±2.5 |
| SSA22-SPIRE682 | 334.42294973055766 | 0.23691033376562567 | 12.3±2.3 | 16.5±1.8 | 0.5±2.4 |
| SSA22-SPIRE683 | 334.32416986881213 | 0.4536984896756 38 | 12.2±2.3 | 10.4±1.9 | 6.7±2.4 |
| SSA22-SPIRE684 | 334.25109017537505 | 0.33197960798224924 | 12.3±2.4 | 13.2±1.7 | 13.0±2.1 |
| SSA22-SPIRE685 | 334.2150537983702 | 0.34368076175067713 | 12.1±2.3 | 7.0±1.7 | 1.3±2.3 |
| SSA22-SPIRE686 | 334.44375569909545 | 0.22620280743515428 | 11.6±2.2 | 13.4±1.7 | 8.2±2.4 |
| SSA22-SPIRE687 | 334.32094891618465 | 0.1963965545072171 | 12.8±2.5 | 1.5±1.8 | 0.0±2.1 |
| SSA22-SPIRE688 | 334.40159709817556 | 0.5342948169663295 | 10.7±2.1 | 13.6±1.9 | 9.6±2.0 |
| SSA22-SPIRE689 | 334.3297690657412 | 0.26122607138748927 | 10.8±2.1 | 12.6±1.8 | 8.4±2.1 |
| SSA22-SPIRE690 | 334.6925905831552 | 0.33794106541890223 | 12.0±2.3 | 15.2±1.8 | 9.7±2.3 |
| SSA22-SPIRE691 | 334.222906219859 | 0.6140166995266039 | 12.3±2.4 | 13.6±2.2 | 10.0±2.3 |
| SSA22-SPIRE692 | 334.23937040146456 | 0.32273019124380525 | 11.9±2.3 | 13.4±1.8 | 15.3±2.1 |
| SSA22-SPIRE693 | 334.4037747420677 | 0.38434541877183853 | 12.6±2.5 | 5.5±1.7 | 0.4±2.2 |
| SSA22-SPIRE694 | 334.36049961251956 | 0.40377311641759545 | 11.1±2.2 | 16.6±1.8 | 10.8±2.2 |
| SSA22-SPIRE695 | 334.36367835593035 | 0.10099944148347421 | 12.1±2.4 | 8.3±1.9 | 1.9±2.2 |
| SSA22-SPIRE696 | 334.64427973352804 | 0.42937175450881093 | 12.2±2.4 | 11.6±2.0 | 7.4±2.2 |
| SSA22-SPIRE697 | 334.31576493756234 | 0.5705126204000787 | 11.4±2.2 | 14.8±1.7 | 7.6±2.0 |
| SSA22-SPIRE698 | 334.33588648747826 | 0.4742690266332529 | 12.0±2.3 | 15.8±1.7 | 5.3±2.2 |
| SSA22-SPIRE699 | 334.4142327920479 | 0.47289430808615757 | 12.7±2.5 | 7.4±1.8 | 0.0±2.2 |
| SSA22-SPIRE700 | 334.33708860378414 | 0.335573535346617 | 11.2±2.2 | 8.6±1.9 | 27.0±2.3 |
| SSA22-SPIRE701 | 334.395685048047 | 0.0839681211017246 | 10.8±2.1 | 12.3±1.9 | 4.9±2.2 |
| SSA22-SPIRE702 | 334.4990035776788 | 0.4151646473668758 | 11.8±2.4 | 12.1±1.8 | 13.5±2.2 |
| SSA22-SPIRE703 | 334.2986328378474 | 0.44625624038673756 | 13.7±2.7 | 12.2±1.9 | 7.8±2.3 |
| SSA22-SPIRE704 | 334.362356064727 | 0.3059886037533692 | 12.3±2.5 | 7.5±1.8 | 6.5±2.2 |
| SSA22-SPIRE705 | 334.6984690361977 | 0.3019366051947561 | 13.9±2.8 | 13.9±2.1 | 10.7±2.6 |
| SSA22-SPIRE706 | 334.25121998140594 | 0.3461780025017109 | 11.4±2.3 | 13.1±1.9 | 4.6±2.1 |
| SSA22-SPIRE707 | 334.43830639687616 | 0.2435931608463835 | 12.5±2.5 | 9.5±1.7 | 7.9±2.2 |
| SSA22-SPIRE708 | 334.6574814457453 | 0.47179212829863515 | 12.1±2.4 | 1.7±1.9 | 0.0±2.1 |
| SSA22-SPIRE709 | 334.50666974141774 | 0.5709935022620208 | 11.4±2.3 | 13.9±1.7 | 1.0±2.4 |
| SSA22-SPIRE710 | 334.21880496460346 | 0.16117929448515986 | 11.2±2.3 | 12.6±1.9 | 5.1±2.3 |
| SSA22-SPIRE711 | 334.3254086590514 | 0.3103384286349216 | 12.2±2.5 | 7.5±2.0 | 4.5±2.1 |
| SSA22-SPIRE712 | 334.6000705191302 | 0.39117727727425644 | 14.9±3.0 | 18.4±1.8 | 14.9±2.3 |
| SSA22-SPIRE713 | 334.2726578713182 | 0.34642970792601313 | 12.9±2.6 | 10.6±1.7 | 5.7±2.2 |
| SSA22-SPIRE714 | 334.63659558788925 | 0.3168308741229456 | 10.1±2.1 | 9.7±1.9 | 16.0±2.3 |
| SSA22-SPIRE715 | 334.1830715013427 | 0.3268720530681967 | 9.4±1.9 | 15.6±1.7 | 6.4±2.0 |
| SSA22-SPIRE716 | 334.56165616838985 | 0.5172301668979087 | 12.3±2.5 | 12.9±1.8 | 13.2±2.2 |
| SSA22-SPIRE717 | 334.2523796284157 | 0.16356524239813336 | 12.7±2.6 | 5.1±1.9 | 0.0±2.4 |
| SSA22-SPIRE718 | 334.4522739595525 | 0.3244922645923525 | 14.0±2.9 | 11.3±1.7 | 0.0±2.3 |
| SSA22-SPIRE719 | 334.3992509992332 | 0.6130697835178459 | 11.6±2.4 | 14.0±1.9 | 1.5±2.3 |
| SSA22-SPIRE720 | 334.2715966410657 | 0.4305372424428567 | 11.4±2.4 | 17.2±1.8 | 23.5±2.1 |
| SSA22-SPIRE721 | 334.07226649164096 | 0.21383700300904265 | 11.5±2.4 | 24.6±1.9 | 21.3±2.2 |
| SSA22-SPIRE722 | 334.6772929055635 | 0.2787252108063868 | 12.0±2.5 | 11.3±1.9 | 13.9±2.7 |

Table A.8: SPIRE sources catalogue of 2QZCluster field.

| ID[1] | R.A.[2] (J2000) | Dec.[3] (J2000) | $S_{250}$[4] (mJy) | $S_{350}$[5] (mJy) | $S_{500}$[6] (mJy) |
|---|---|---|---|---|---|
| SSA22-SPIRE723 | 334.6212849563693 | 0.258753763984327 | 10.6±2.2 | 12.5±1.9 | 2.0±2.1 |
| SSA22-SPIRE724 | 334.18816762617394 | 0.38858029804210426 | 10.1±2.1 | 18.9±1.9 | 8.3±2.1 |
| SSA22-SPIRE725 | 334.32406771110345 | 0.5176720008109987 | 11.0±2.3 | 26.0±1.9 | 14.8±2.2 |
| SSA22-SPIRE726 | 334.56715189626925 | 0.5525446782654587 | 10.9±2.3 | 14.8±1.9 | 7.5±2.4 |
| SSA22-SPIRE727 | 334.6398772301036 | 0.29596404486823363 | 10.4±2.2 | 23.2±1.9 | 11.2±2.2 |
| SSA22-SPIRE728 | 334.4511840665961 | 0.2068431006651706 | 9.5±2.0 | 12.8±1.7 | 1.7±2.0 |
| SSA22-SPIRE729 | 334.29740849477554 | 0.18391816649190926 | 11.6±2.5 | 19.1±1.8 | 17.2±2.2 |
| SSA22-SPIRE730 | 334.2351223371565 | 0.6510769174503582 | 12.9±2.8 | 7.0±1.8 | 3.5±2.5 |
| SSA22-SPIRE731 | 334.73264449011015 | 0.4478893946453595 | 10.2±2.2 | 14.2±1.9 | 5.2±2.2 |
| SSA22-SPIRE732 | 334.46888511043517 | 0.27325883813268553 | 10.3±2.3 | 12.0±1.7 | 10.5±2.4 |
| SSA22-SPIRE733 | 334.3025038805183 | 0.33470506376936227 | 10.3±2.3 | 12.6±1.8 | 1.3±2.1 |
| SSA22-SPIRE734 | 334.3842106414945 | 0.42909282688058287 | 10.2±2.3 | 17.8±2.0 | 9.3±2.2 |
| SSA22-SPIRE735 | 334.16742004100945 | 0.2917452612060907 | 9.4±2.1 | 13.5±1.9 | 4.2±2.2 |
| SSA22-SPIRE736 | 334.42381601972914 | 0.09890395637274545 | 9.9±2.3 | 17.9±1.9 | 7.2±2.2 |
| SSA22-SPIRE737 | 334.4244755412057 | 0.4646905963970229 | 9.9±2.3 | 10.9±1.8 | 14.7±2.3 |
| SSA22-SPIRE738 | 334.2760333740995 | 0.2561734456853286 | 8.9±2.1 | 15.0±1.8 | 16.3±2.5 |
| SSA22-SPIRE739 | 334.2523154998761 | 0.22353556620713042 | 9.6±2.3 | 17.3±1.8 | 11.4±2.2 |
| SSA22-SPIRE740 | 334.27691204585994 | 0.3829317776538938 | 9.3±2.2 | 14.1±1.9 | 12.1±2.1 |
| SSA22-SPIRE741 | 334.3704007416281 | 0.33053684921044785 | 9.2±2.2 | 17.9±1.8 | 4.6±2.3 |
| SSA22-SPIRE742 | 334.2780323273875 | 0.2081649262981295 | 11.1±2.6 | 14.1±1.8 | 8.1±2.3 |
| SSA22-SPIRE743 | 334.63251799914354 | 0.4809819077703643 | 10.3±2.4 | 16.9±1.8 | 12.0±2.1 |
| SSA22-SPIRE744 | 334.71699117585206 | 0.3435556681914645 | 11.3±2.7 | 19.9±2.0 | 9.0±2.4 |
| SSA22-SPIRE745 | 334.3525767140105 | 0.5409560248098466 | 10.5±2.5 | 16.6±1.9 | 11.8±2.4 |
| SSA22-SPIRE746 | 334.09907012241786 | 0.30668687168427994 | 9.3±2.2 | 13.0±1.8 | 9.1±2.2 |
| SSA22-SPIRE747 | 334.2204693344558 | 0.5338468244395221 | 9.2±2.3 | 16.8±1.8 | 12.5±2.1 |
| SSA22-SPIRE748 | 334.4186920852893 | 0.13306229181951335 | 9.1±2.3 | 14.0±1.8 | 0.0±2.3 |
| SSA22-SPIRE749 | 334.5631160498753 | 0.3332027682333343 | 8.6±2.2 | 12.2±1.9 | 11.3±2.3 |
| SSA22-SPIRE750 | 334.4891567114401 | 0.6169243262063007 | 9.0±2.3 | 20.5±2.0 | 14.5±2.2 |
| SSA22-SPIRE751 | 334.4958596252892 | 0.18435590619032238 | 8.8±2.3 | 12.2±1.9 | 4.7±2.1 |
| SSA22-SPIRE752 | 334.58015231751284 | 0.39294297985228066 | 10.0±2.6 | 20.2±1.7 | 14.1±2.2 |
| SSA22-SPIRE753 | 334.32437833363036 | 0.6002987939318869 | 8.5±2.3 | 13.2±1.7 | 5.2±2.2 |
| SSA22-SPIRE754 | 334.1394577545074 | 0.29524813191781424 | 8.7±2.3 | 9.4±1.9 | 14.0±2.3 |
| SSA22-SPIRE755 | 334.71006855578946 | 0.40431735033091204 | 8.2±2.3 | 14.6±2.0 | 3.4±2.1 |
| SSA22-SPIRE756 | 334.39511354989025 | 0.648422040632885 | 7.6±2.1 | 12.5±2.0 | 10.4±2.2 |
| SSA22-SPIRE757 | 334.1889595068943 | 0.5539469819745917 | 9.4±2.7 | 13.0±2.0 | 6.7±2.4 |
| SSA22-SPIRE758 | 334.47075501723543 | 0.21301199679947008 | 7.9±2.2 | 14.2±1.7 | 10.5±2.4 |
| SSA22-SPIRE759 | 334.4825404403322 | 0.40211292445241353 | 7.8±2.3 | 21.5±1.9 | 9.2±2.2 |
| SSA22-SPIRE760 | 334.6405288705976 | 0.46688662390331526 | 9.1±2.7 | 12.2±1.8 | 10.5±2.2 |
| SSA22-SPIRE761 | 334.6409753717408 | 0.358759840338069 | 7.4±2.2 | 14.3±1.7 | 17.4±2.1 |
| SSA22-SPIRE762 | 334.3358601778361 | 0.3320507818172157 | 7.3±2.3 | 17.8±1.9 | 9.5±2.3 |
| SSA22-SPIRE763 | 334.2911671540028 | 0.5557397335131653 | 6.8±2.3 | 12.6±1.9 | 2.9±2.3 |
| SSA22-SPIRE764 | 334.52435525974624 | 0.44727628702143873 | 7.3±2.5 | 12.8±1.9 | 12.4±2.2 |
| SSA22-SPIRE765 | 334.3988821585665 | 0.3701244848228838 | 6.7±2.4 | 15.2±1.8 | 11.2±2.1 |
| SSA22-SPIRE766 | 334.55061823031235 | 0.3839224997607248 | 6.5±2.3 | 18.5±1.7 | 14.7±2.0 |
| SSA22-SPIRE767 | 334.5296756035935 | 0.14725096941952445 | 6.2±2.3 | 13.6±1.8 | 5.9±2.3 |
| SSA22-SPIRE768 | 334.5488164901507 | 0.3157227237696726 | 6.3±2.4 | 13.9±1.9 | 8.5±2.1 |
| SSA22-SPIRE769 | 334.17702914150567 | 0.3755974201203453 | 6.8±2.7 | 12.4±1.7 | 8.1±2.2 |
| SSA22-SPIRE770 | 334.3145190988717 | 0.2973550214545609 | 5.8±2.4 | 12.0±1.8 | 0.0±2.3 |
| SSA22-SPIRE771 | 334.2916160268147 | 0.23664253810975625 | 5.8±2.4 | 16.9±2.0 | 13.7±2.2 |
| SSA22-SPIRE772 | 334.5069646447244 | 0.27698000761694663 | 4.6±2.2 | 14.0±1.9 | 8.5±2.2 |
| SSA22-SPIRE773 | 334.4486644383346 | 0.3740824316457329 | 4.6±2.3 | 6.3±1.8 | 22.5±2.2 |
| SSA22-SPIRE774 | 334.15032126442424 | 0.47598352216815387 | 3.0±2.4 | 7.1±1.7 | 12.7±2.3 |

# Bibliography


Adelberger K. L., Steidel C. C., Shapley A. E., Pettini M., 2003, ApJ, 584, 45

Alexander D. M., et al., 2016, MNRAS, 461, 2944

Ao Y., et al., 2018, ApJ, 850, 178

Aravena M., et al., 2016, ApJ, 833, 68
Bai L., et al., 2007, ApJ, 664, 181

Barger A. J., Cowie L. L., Wold I. G. B., 2012, ApJ, 749, 106

Beelen A., et al., 2008, A&A, 485, 645

Bell E. F., 2003, ApJ, 586, 794

Bertin E., Arnouts S., 1996, A&AS, 117, 393

Béthermin M., et al., 2012, A&A, 542, AA58

Bhattacharya S., Habib S., Heitmann K., Vikhlinin A., 2013, ApJ, 766, 32

Blain A. W., Barnard V. E., Chapman S. C., 2003, MNRAS, 338, 733

Blain A. W., Chapman S. C., Smail I., Ivison R., 2004, ApJ, 611, 725

Bogosavljević M., 2010, PhDT, California Institute of Technology

Borgani S., Kravtsov A., 2011, ASL, 4, 204

Bothwell M. S., et al., 2013, MNRAS, 429, 3047

Bouché N., Murphy M. T., Kacprzak G. G., Péroux C., Contini T., Martin C. L., Dessauges-Zavadsky M., 2013, Sci, 341, 50

Bouché N., et al., 2016, ApJ, 820, 121

Braglia F. G., et al., 2011, MNRAS, 412, 1187

Brammer G. B., van Dokkum P. G., Coppi P., 2008, ApJ, 686, 1503-1513

Brodwin M., et al., 2013, ApJ, 779, 138

Bruzual G., Charlot S., 2003, MNRAS, 344, 1000

Calzetti D., Armus L., Bohlin R. C., Kinney A. L., Koornneef J., Storchi-Bergmann T., 2000, ApJ, 533, 682

Carilli C. L., Walter F., 2013, ARA&A, 51, 105

Casey C. M., et al., 2012, ApJ, 761, 140

Casey C. M., 2012, MNRAS, 425, 3094

Casey C. M., Narayanan D., Cooray A., 2014, PhR, 541, 45

Casey C. M., et al., 2015, ApJ, 808, L33

Casey C. M., 2016, ApJ, 824, 36

Ceverino D., Sánchez Almeida J., Muñoz Tuñón C., Dekel A., Elmegreen B. G., Elmegreen D. M., Primack J., 2016, MNRAS, 457, 2605

Chabrier G., 2003, PASP, 115, 763

Chapin E. L., et al., 2011, MNRAS, 411, 505

Chapman S. C., Lewis G. F., Scott D., Richards E., Borys C., Steidel C. C., Adelberger K. L., & Shapley A. E., 2001, ApJ, 548, L17

Chapman S. C., Scott D., Windhorst R. A., Frayer D. T., Borys C., Lewis G. F., & Ivison R. J., 2004, ApJ, 606, 85

Chapman S. C., et al., 2015, MNRAS, 449, L68

Chiang Y.-K., Overzier R., Gebhardt K., 2013, ApJ, 779, 127

Chiang C.-W., Senaha E., 2017, PhLB, 774, 489

Chung S. M., Gonzalez A. H., Clowe D., Markevitch M., Zaritsky D., 2010, ApJ, 725, 1536

Clements D. L., et al., 2014, MNRAS, 439, 1193

Clements D. L., et al., 2017, arXiv, arXiv:1712.04843

Cortese L., et al., 2014, MNRAS, 440, 942

Croom S. M., Smith R. J., Boyle B. J., Shanks T., Loaring N. S., Miller L., Lewis I. J., 2001, MNRAS, 322, L29

Croom S. M., Smith R. J., Boyle B. J., Shanks T., Miller L., Outram P. J., Loaring N. S., 2004, MNRAS, 349, 1397

da Cunha E., et al., 2015, ApJ, 806, 110

Daddi E., et al., 2009, ApJ, 694, 1517

Daddi E., et al., 2010, ApJ, 714, L118

Dannerbauer H., et al., 2014, A&A, 570, AA55

Dekel A., et al., 2009, Nature, 457, 451

Demyk K., et al., 2017, A&A, 600, A123

Dey A., et al., 2005, ApJ, 629, 654

Digby-North J. A., et al., 2010, MNRAS, 407, 846

Downes A. J. B., Peacock J. A., Savage A., Carrie D. R., 1986, MNRAS, 218, 31

Downes D., Solomon P. M., 1998, ApJ, 507, 615

Dunne L., Eales S. A., Edmunds M. G., 2003, MNRAS, 341, 589

Elbaz D., et al., 2011, A&A, 533, A119

Ellis R. S., Smail I., Dressler A., Couch W. J., Oemler A., Jr., Butcher H., Sharples R. M., 1997, ApJ, 483, 582

Emonts B. H. C., et al., 2016, Sci, 354, 1128

Engel H., et al., 2010, ApJ, 724, 233

Erb D. K., Bogosavljević M., Steidel C. C., 2011, ApJ, 740, L31

Erb D. K., et al., 2014, ApJ, 795, 33

Fadda D., Elbaz D., Duc P.-A., Flores H., Franceschini A., Cesarsky C. J., Moorwood A. F. M., 2000, A&A, 361, 827

Faucher-Giguère C.-A., Hopkins P. F., Kereš D., Muratov A. L., Quataert E., Murray N., 2015, MNRAS, 449, 987

Faucher-Giguère C.-A., Feldmann R., Quataert E., Kereš D., Hopkins P. F., Murray N., 2016, MNRAS, 461, L32

Geach J. E., et al., 2005, MNRAS, 363, 1398

Geach J. E., et al., 2006, ApJ, 649, 661

Geach J. E., et al., 2009, ApJ, 700, 1

Geach J. E., et al., 2014, ApJ, 793, 22

Geach J. E., et al., 2016, ApJ, 832, 37

Ginolfi M., et al., 2017, MNRAS, 468, 3468

Goerdt T., Dekel A., Sternberg A., Ceverino D., Teyssier R., & Primack J. R., 2010, MNRAS, 407, 613

Gottlöber S., Klypin A., Kravtsov A. V., 2001, ApJ, 546, 223

Governato F., Baugh C. M., Frenk C. S., Cole S., Lacey C. G., Quinn T., Stadel J., 1998, Natur, 392, 359

Granato G. L., Ragone-Figueroa C., Domínguez-Tenreiro R., Obreja A., Borgani S., De Lucia G., Murante G., 2015, MNRAS, 450, 1320

Greve T. R., et al., 2005, MNRAS, 359, 1165

Greve T. R., et al., 2014, ApJ, 794, 142

Griffin M. J., et al., 2010, A&A, 518, L3

Haiman Z., Spaans M., Quataert E., 2000, ApJ, 537, L5

Haines C. P., Smith G. P., Egami E., Okabe N., Takada M., Ellis R. S., Moran S. M., Umetsu K., 2009, MNRAS, 396, 1297

Hashimoto T., Ouchi M., Shimasaku K., Ono Y., Nakajima K., Rauch M., Lee J., Okamura S., 2013, ApJ, 765, 70

Hashimoto T., et al., 2015, ApJ, 812, 157

Hayashino T., et al., 2004, AJ, 128, 2073

Hickox R. C., et al., 2012, MNRAS, 421, 284

Hildebrand R. H., 1983, QJRAS, 24, 267

Hine N. K., Geach J. E., Alexander D. M., Lehmer B. D., Chapman S. C., Matsuda Y., 2016a, MNRAS, 455, 2363

Hine N. K., et al., 2016b, MNRAS, 460, 4075

Hung C.-L., et al., 2013, ApJ, 778, 129

Israel H., Reiprich T. H., Erben T., Massey R. J., Sarazin C. L., Schneider P., Vikhlinin A., 2014, A&A, 564, A129

Ivison R. J., Dunlop J. S., Smail I., Dey A., Liu M. C., Graham J. R., 2000, ApJ, 542, 27

Ivison R. J., et al., 2013, ApJ, 772, 137

Kartaltepe J. S., et al., 2010, ApJ, 721, 98

Kartaltepe J. S., et al., 2012, ApJ, 757, 23

Kato Y., et al., 2016, MNRAS, 460, 3861

Kennicutt R. C., Jr., 1998, ARA&A, 36, 189

Kennicutt R. C., & Evans N. J., 2012, ARA&A, 50, 531

Kereš D., Katz N., Weinberg D. H., Davé R., 2005, MNRAS, 363, 2

Kodama T., Tanaka M., Tanaka I., Kajisawa M., 2007, ASPC, 379, 202

Koyama Y., Kodama T., Tadaki K.-i., Hayashi M., Tanaka M., Smail I., Tanaka I., Kurk J., 2013, MNRAS, 428, 1551

Kriek M., van Dokkum P. G., Labbé I., Franx M., Illingworth G. D., Marchesini D., Quadri R. F., 2009, ApJ, 700, 221

Kubo M., et al., 2013, ApJ, 778, 170

Kubo M., Yamada T., Ichikawa T., Kajisawa M., Matsuda Y., Tanaka I., 2015, ApJ, 799, 38

Kulas K. R., et al., 2013, ApJ, 774, 130

Lagache G., Puget J.-L., Dole H., 2005, ARA&A, 43, 727

Lawrence A., et al., 2007, MNRAS, 379, 1599

Lee K.-G., et al., 2016, ApJ, 817, 160

Lee M. M., et al., 2017, ApJ, 842, 55

Lehmer B. D., et al., 2009a, ApJ, 691, 687

Lehmer B. D., et al., 2009b, MNRAS, 400, 299

Lehmer B. D., et al., 2013, ApJ, 765, 87

Leitherer C., Heckman T. M., 1995, ApJS, 96, 9

Lilly S. J., Tresse L., Hammer F., Crampton D., Le Fevre O., 1995, ApJ, 455, 108

Lilly S., et al., 1998, ApJ, 500, 75

Lutz D., et al., 2001, A&A, 378, 70

Ma C.-J., et al., 2015, ApJ, 806, 257

Madau P., Dickinson M., 2014, ARA&A, 52, 415

Martin D. C., Chang D., Matuszewski M., Morrissey P., Rahman S., Moore A., Steidel C. C., Matsuda Y., 2014, ApJ, 786, 107

Matsuda Y., et al., 2004, AJ, 128, 569

Matsuda Y., et al., 2011a, MNRAS, 416, 2041

Matsuda Y., et al., 2011b, MNRAS, 410, L13

McDermid R. M., et al., 2015, yCat, 744,

McMullin J. P., Waters B., Schiebel D., Young W., Golap K., 2007, ASPC, 376, 127

Meusinger H., Brunzendorf J., Krieg R., 2000, A&A, 363, 933

Miley G. K., et al., 2006, ApJ, 650, L29

Mori, M., & Umemura, M. 2006, Nature, 440, 644

Narayanan D., et al., 2015, Natur, 525, 496

Newman S. F., et al., 2012, ApJ, 761, 43

Nelson E. J., et al., 2016, ApJ, 828, 27

Nguyen H. T., et al., 2010, A&A, 518, LL5

Oguri M., 2010, PASJ, 62, 1017

Oliver S. J., et al., 2012, MNRAS, 424, 1614

Oteo I., Zwaan M. A., Ivison R. J., Smail I., Biggs A. D., 2016, ApJ, 822, 36

Oteo I., Zwaan M. A., Ivison R. J., Smail I., Biggs A. D., 2017a, ApJ, 837, 182

Oteo I., et al., 2017b, arXiv, arXiv:1709.02809

Ouchi M., et al., 2005, ApJ, 635, L117

Pallottini A., Ferrara A., Gallerani S., Vallini L., Maiolino R., Salvadori S., 2017, MNRAS, 465, 2540

Peter A. H. G., Shapley A. E., Law D. R., Steidel C. C., Erb D. K., Reddy N. A., Pettini M., 2007, ApJ, 668, 23

Pilbratt G. L., et al., 2010, A&A, 518, L1

Planck Collaboration, et al., 2015, A&A, 582, A30

Polletta M., et al., 2007, ApJ, 663, 81

Rahmati A., Schaye J., Bower R. G., Crain R. A., Furlong M., Schaller M., Theuns T., 2015, MNRAS, 452, 2034

Ricci L., Testi L., Natta A., Neri R., Cabrit S., Herczeg G. J., 2010, A&A, 512, A15

Rigby E. E., et al., 2014, MNRAS, 437, 1882

Rudie G. C., et al., 2012, ApJ, 750, 67

Saito T., et al., 2015, MNRAS, 447, 3069

Salpeter E. E., 1955, ApJ, 121, 161

Sánchez Almeida J., Morales-Luis A. B., Muñoz-Tuñón C., Elmegreen D. M., Elmegreen B. G., Méndez-Abreu J., 2014, ApJ, 783, 45

Scoville N., et al., 2016, ApJ, 820, 83

Shapley A. E., Steidel C. C., Erb D. K., Reddy N. A., Adelberger K. L., Pettini M., Barmby P., Huang J., 2005, ApJ, 626, 698

Sharda P., Federrath C., Lima da Cunha E., Swinbank M., Dye S., 2017, arXiv, arXiv:1712.03661

Simpson J. M., et al., 2012, MNRAS, 426, 3201

Simpson J. M., et al., 2015, ApJ, 807, 128

Smail I., Ivison R. J., Blain A. W., Kneib J.-P., 1998, ApJ, 507, L21

Smail I., et al., 2014, ApJ, 782, 19

Smith A. J., et al., 2012, MNRAS, 419, 377

Smith D. J. B., et al., 2013, MNRAS, 436, 2435

Solomon P. M., Sage L. J., 1988, ApJ, 334, 613

Solomon P. M., Vanden Bout P. A., 2005, ARA&A, 43, 677

Speagle J. S., Steinhardt C. L., Capak P. L., Silverman J. D., 2014, ApJS, 214, 15

Steidel C. C., Adelberger K. L., Dickinson M., Giavalisco M., Pettini M., Kellogg M., 1998, ApJ, 492, 428

Steidel C. C., Adelberger K. L., Shapley A. E., Pettini M., Dickinson M., Giavalisco M., 2000, ApJ, 532, 170

Steidel C. C., Adelberger K. L., Shapley A. E., Pettini M., Dickinson M., Giavalisco M., 2003, ApJ, 592, 728

Steidel C. C., Adelberger K. L., Shapley A. E., Erb D. K., Reddy N. A., Pettini M., 2005, ApJ, 626, 44

Steidel C. C., Erb D. K., Shapley A. E., Pettini M., Reddy N., Bogosavljević M., Rutdie G. C., Rakic O., 2010, ApJ, 717, 289

Steidel C. C., et al., 2014, ApJ, 795, 165

Stevens J. A., et al., 2003, Natur, 425, 264

Stevens J. A., Jarvis M. J., Coppin K. E. K., Page M. J., Greve T. R., Carrera F. J., Ivison R. J., 2010, MNRAS, 405, 2623

Swinyard B. M., et al., 2010, A&A, 518, L4

Swinbank A. M., et al., 2014, MNRAS, 438, 1267

Tacconi L. J., et al., 2017, arXiv, arXiv:1702.01140

Tadaki K.-i., et al., 2015, ApJ, 811, L3

Tadaki K.-i., et al., 2017, ApJ, 841, L25

Takeuchi T. T., Buat V., Burgarella D., 2005, A&A, 440, L17

Tamura Y., et al., 2009, Natur, 459, 61

Tamura Y., et al., 2013, MNRAS, 430, 2768

Taniguchi, Y., & Shioya, Y. 2000, ApJL, 532, L13

Thomas D., Maraston C., Bender R., Mendes de Oliveira C., 2005, ApJ, 621, 673

Toshikawa J., et al., 2017, arXiv, arXiv:1708.09421

Tumlinson J., Peeples M. S., Werk J. K., 2017, ARA&A, 55, 389

Uchimoto Y. K., et al., 2012, ApJ, 750, 116

Ueda J., et al., 2014, ApJS, 214, 1

Umehata H., et al., 2014, MNRAS, 440, 3462

Umehata H., et al., 2015, ApJ, 815, L8

Umehata H., et al., 2017a, ApJ, 835, 98

Umehata H., et al., 2017b, ApJ, 834, L16

Valtchanov I., et al., 2013, MNRAS, 436, 2505

van der Burg R. F. J., et al., 2013, A&A, 557, A15

Vogelsberger M., et al., 2014, MNRAS, 444, 1518

Walter F., et al., 2012, Natur, 486, 233

Webb T. M. A., Yamada T., Huang J.-S., Ashby M. L. N., Matsuda Y., Egami E., Gonzalez M., & Hayashino T., 2009, ApJ, 692, 1561

Webb T., et al., 2015, ApJ, 809, 173

Whitaker K. E., et al., 2017, ApJ, 838, 19

Wilson C. D., et al., 2008, ApJS, 178, 189-224

Wisnioski E., et al., 2015, ApJ, 799, 209

Yajima H., Umemura M., & Mori M., 2012, MNRAS, 420, 3381

Yamada T., Nakamura Y., Matsuda Y., Hayashino T., Yamauchi R., Morimoto N., Kousai K., Umemura M., 2012, AJ, 143, 79

Yamaguchi Y., et al., 2016, PASJ, 68, 82

Yang M., Phillips T., 2007, ApJ, 662, 284

Yang Y., Walter F., Decarli R., Bertoldi F., Weiss A., Dey A., Prescott M. K. M., Bădescu T., 2014, ApJ, 784, 171

Zabl J., Nørgaard-Nielsen H. U., Fynbo J. P. U., Laursen P., Ouchi M., Kjærgaard P., 2015, MNRAS, 451, 2050